TEMPORAL VARIATIONS OF MONSOON SYSTEMS

A Thesis
Presented to
The Academic Faculty

by

Sara C. Vieira Agudelo

In Partial Fulfillment
of the Requirements for the Degree
Doctor of Philosophy in the
School of Earth and Atmospheric Sciences

Georgia Institute of Technology
December 2010

TEMPORAL VARIATIONS OF MONSOON SYSTEMS

Approved by:

Dr. Peter Webster, Advisor
School of Earth and Atmospheric Sciences
Georgia Institute of Technology

Dr. Annalisa Bracco
School of Earth and Atmospheric Sciences
Georgia Institute of Technology

Dr. Judith A. Curry
School of Earth and Atmospheric Sciences
Georgia Institute of Technology

Dr. Yi Deng
School of Earth and Atmospheric Sciences
Georgia Institute of Technology

Dr. Marshall Shepherd
Department of Geography/Atmospheric Sciences
University of Georgia

Date Approved: 19 July 2010

To my family

ACKNOWLEDGEMENTS

First, I would like to show my gratitude to my academic advisor, Dr. Peter Webster, whose encouragement, guidance and support enabled me to complete my Ph.D. studies at Georgia Tech. I am truly privileged to have worked with and learned from him. I will always admire his passion for the field and the excellence in his work.

Furthermore, I want to extend my gratitude to the members of my dissertation committee: Drs. Judith Curry, Annalisa Bracco, Yi Deng and Marshall Shepherd for their valuable comments during the defense process. Their ideas and critical suggestions were a key factor for the completion of my dissertation.

Thanks to my research group fellows for all their constant help and support. Special thanks to Hai-Ru, who assisted me in many different ways. Violeta Toma's help with the WRF model was crucial for the development of my research. Carlos Hoyos' comments were always very valuable. Thanks to my officemate, Matthew, who I was fortunate to share office with and share ideas.

I am indebted to my first year graduate student fellows Vincent Combes and Dana Ionita for their friendship from the initial to the final stages of my PhD adventure. Jason Furtado and Intan Nuharti were also very supportive people during these years. I will miss our fun bimonthly lunch times. I cannot forget to mention about Jud Partin. His encouragement and company were very important to me. Thanks for sharing with me this experience.

I am also very grateful to the LASPAU personnel for assisting me trough the application process to the PhD program and for administering my fellowship. Thanks to the Fulbright-COLCIENCIAS grant for sponsoring the first three years of my doctoral studies.

I would like to offer my regards to my tango friends. Thanks guys for all the fun moments. Special thanks to Fredda, who is no longer with us. I will never forget the wise words you share with me in your office. I also offer my regards to all of those friends in Atlanta, Medellin, and in many other places in the word, who supported me in any respect during the completion of this work.

It is a pleasure to thank my dear friends Paola, Lina, Yuley, Jessica and Manuel for all the shared experiences. I will miss their company and the great moments we had. They were a great support during difficult and happy times. Thanks for sharing your lives with me during these years. Cheers for the "alegria total" moments.

I am deeply grateful to my family for supporting me from afar. Thanks to my father for his interest in my academic experience and for his support. Thanks Mom for your trust and wise words. She accompanied me during all the process and was always there to listen to my excitements and frustrations. Thanks Sis for sharing these years from the other side of the screen and for showing me other views of the world.

Finally, I owe my deepest gratitude to Douglas for his unconditional support and constant encouragement. His company, care and love kept me sane during the last months of this journey. Thanks for your patiente and understanding. Thanks for you enthusiasm. Thanks for accompanying me.

TABLE OF CONTENTS

LIST OF TABLES

LIST OF FIGURES

SUMMARY

Part I

It has been proposed that the Asian-Australasian monsoon system is influenced by large-scale sea-surface temperature (SST) variability in the three tropical oceans although how this influence is manifested has remained a largely open question. Closure of this issue is important because it is needed to explain trends in monsoon precipitation and circulation that have occurred in the last 30 years. Using an atmospheric general circulation model, we run a series of experiments with different configurations of global SST relating to various epochs occurring during the last century to evaluate their influence on the monsoon. Comparisons of circulation fields show that a colder SST configuration generates a weaker large-scale monsoonal circulation. On the other hand, warmer SST states generate stronger large scale circulations with more vigorous centers of divergence and convergence. Warmer SST configurations are associated with positive anomalies of precipitation in the eastern Bay of Bengal, Eastern Indian Ocean and South East Asia. Cooler SST configurations are associated with negative anomalies of precipitation in the Arabian Sea and Indian peninsula, especially at the beginning of the summer. Since SST gradients determine, to a large degree, the low level flow, they are also going to influence the transport of atmospheric moisture. Comparison of vertically integrated moisture transport fields between the different experiments show that cold SST configuration favors an increased inter-hemispheric flow of moisture but decreases in the westerly moisture flow in to the Bay of Bengal and India. Warm SST configurations, on the other hand, strengthens westerly flow into the eastern Indian Ocean. An increasing availability of moisture in a region

of stronger convergence constitutes a favorable environment for the production of monsoonal precipitation.

Part II

African easterly waves (AEW) constitute an important component of the African and tropical Atlantic Ocean climate during the boreal summer. An understanding of this component is essential since AEW are closely related with tropical Atlantic storm activity. We adopt an idealized modeling approach using the WRF model initialized with ERA-40 reanalysis data to study the mechanisms that trigger the formation and maintenance of AEW. The model domain includes the African continent, central and eastern Atlantic Ocean and the western Indian Ocean. Experiments are designed to test the relative importance of the thermal effect of the eastern African topography and the influence of the cross-equatorial pressure gradient, induced by the sea surface temperature (SST) on the origins and maintenance of AEW. Topography and SST variation are selectively added and removed. The control experiment shows that the model reproduces many of the mean features observed during the boreal summer. Westward propagating disturbances of 3 – 8 day period that originate between 30° and 40°E at the surface levels and in the mid troposphere are well depicted. In addition, the model provides a reasonable representation of the AEJ. When all topographic features are removed, there is a weakening of the AEJ over land and ocean, however, longitude – time sections of meridional velocity still exhibit westward propagating disturbances that reach the western African coast at the surface and at the jet level with the same 3 – 8 day period. Spectral analysis of meridional velocity show that the variability associated with AEWs is reduced over East Africa and West Africa at 850-hPa and is reduced west of 20°E along the southern flank of the jet and over northern Africa at the jet level. Maximum amplitude of the disturbances occurs right at the coast. The spatial distribution of barotropic and baroclinic energy conversions explains the reduction in AEWs over land and the intensification of these features at

the coast. When the zonal SST gradient is removed, a weaker AEJ displaces southward and a weaker monsoon flow ensues. Spectral analysis of meridional velocity displays a variance reduction in the 3 – 8 day band at the 850-hP a level in western and eastern Africa and at the coast. At the 650-hPa level significant changes are not observed at the latitude of the AEJ (15°N), however, a decrease in the variance associated with AEW occurs at the southern flank of the jet. A southward displacement of the jet favors a weakening of the baroclinic energy conversions. Barotropic conversions also appear to be weaker when the SST gradient is removed. The present study suggests that orography plays an important role in determining the variability of meridional wind associated with AEW over Eastern Africa at the lower levels. Further, zonal SST gradients over the Atlantic favor intensification of waves when they reach the coast and the maintenance of disturbances across the Ocean. Also, results could suggest that SST gradients support genesis of AEW just off the coast of Africa.

CHAPTER I

INTRODUCTION

Monsoons are a response of the coupled land-ocean-atmosphere system to annual variations of solar radiation forcing. The major monsoon systems in the world are the Asia-Australian, African and the American monsoon. These systems are characterized by seasonal reversals in atmospheric circulation and associated precipitation (Webster et al. 1998). Due to regional differences, each of these monsoons sustains distinct circulation characteristics and intensity.

The Asian monsoon is a major component of the general atmospheric circulation. During the boreal summer, winds flow from the Southern Indian Ocean, transporting moisture and producing large amounts of precipitation over South Asia and the adjacent ocean regions (Hoyos and Webster 2007). During the winter, dry winds flow from the cold land areas of Asia and converge over the warm Southern Indian Ocean, Indonesia and the north of Australia, generating the precipitation of the Australian monsoon.

The African monsoon is characterized by a poleward migration of peak rainfall up to about August, followed by a more rapid retreat. During the boreal summer months, a southwesterly wind coming off the Gulf of Guinea brings humid air over West Africa. A zone of surface wind convergence develops where the southwest monsoon meets the dry desert air. South of this region of convergence, a zone of deep convection forms. This zone of precipitation brings large amounts of rainfall over the Sahel/Guinea coast region (Nicholson 2009).

These monsoon systems exhibit variability on various timescales. This variability is manifested in large-scale aspects of the monsoon and also in its associated weather

systems. The variability of the monsoons is largely determined by the slowly varying boundary conditions from the underlying oceans and land (Charney and Shukla 1981). Perhaps, the leading impacting factor is the sea surface temperature. Many studies have attempted to explain how the sea surface temperature modulates the monsoon variability. However, due to the complexities of the systems, this modulation is still not well understood.

Variability of the monsoon systems on these various timescales has major socioeconomic impacts in Asia and Africa. Climatic extremes, such as flooding and drought, have a direct impact on agricultural production and livelihoods. In addition, it also affects the management of water resources and it is directly related to societal health issues.

The South Asian and West African societies are particularly vulnerable to the variability of rainfall associated with the monsoon. Understanding how monsoon changes on different time scales and how it responds to actual and future changes in SST is a key scientific issue.

Thesis outline

This study centers on the understanding of the variability of the monsoon systems on diverse time scales. In Part 1 we study the interdecadal variability of the Asian monsoon noting the importance of SST variability on the monsoon's evolving nature. For this purpose, we utilized an atmospheric general circulation model and designed a number of experiments in which only the sea surface temperature fields are modified. Chapter 2 discusses relevant aspects of the variability of the Asian monsoon. Chapter 3 describes the model and the observational data set used in this study. In Chapter 4, we describe the changes in the monsoon circulation forced by changes in the distribution of sea surface temperature. Finally, in Chapter 5, we explore the interconnection that exists between sea surface temperature, atmospheric circulation and moisture availability over the main Asian monsoon regions.

In Part 2 we look at the most rapid variability of a monsoon circulation associated with dynamic instabilities of the mean flow. We use a regional model to explore the role of orography and cross-equatorial pressure gradients induced by SST in the genesis and maintenance of African easterly waves. These features are an important component of the African monsoon and are linked to the generation of rainfall over West Africa. Chapter 6 describes the large-scale features of the African monsoon climate and reviews relevant studies concerned with the origin and dynamics of African easterly waves. Chapter 7 describes the regional model and the experimental design. Chapter 8 discusses changes in African easterly wave variability associated with orography and sea surface temperature gradients. Chapter 9 concentrates on the instability mechanisms and energy conversions that lead to the development of African easterly waves and how they are modified when orography and sea surface temperature gradients are removed. Finally, Chapter 10 summarizes salient conclusions from Part 1 and Part 2.

CHAPTER II

VARIABILITY OF THE ASIAN MONSOON

A monsoon is a large-scale circulation system characterized by seasonal reversals in both atmospheric circulation and precipitation, typically wet during the summer and dry in the winter. This distinctive annual cycle arises essentially from the development of cross-equatorial pressure gradients produced by the differential heating of land and ocean, the consequent generation of meridional pressure-gradient forces resulting from the differential heating and the modification of the differential heating by moist processes (Webster 1987; Webster and Fasullo 2003). To understand the physical nature of a particular monsoon system, each of these processes has to be considered in conjunction with planetary rotation and the influence of regional effects such as the geographical distribution of land and ocean and orography.

The major monsoon systems in the world are the Asia-Australian, African and the American monsoon. Although the latter has not been identified with wind reversals, it qualifies as a monsoon in terms of precipitation (Webster et al. 1998). Due to regional differences, each of these systems sustains distinct circulation characteristics and intensity. Compared to the Asian-Australian monsoon, the African and the American monsoon are relatively weak. Perhaps the greater difference between the Asian monsoon and the two other systems is the existence of major orographic features around the Indian Ocean basin that act as mechanical barriers and elevated heat sources. The impact of these differences is rather profound. The African and Australian monsoons possess maximum precipitation that decreases more or less linearly from about 10 degrees of latitude towards the poles. The Asian monsoon, on the other hand, possesses elongated precipitation maxima that extend from the equator

to 30 – 35°N (Hoyos and Webster 2007).

The Indian Ocean is bordered to the west by the East African Highlands and to the north by the Himalayas and the Tibetan Plateau. The East African Highlands act as a mechanical barrier to the low level cross-equatorial flow from the Southern Indian Ocean, providing a western boundary intensification known as the Somali jet (Findlater 1969a,b; Krishnamurti et al. 1976; Hart 1977). The Tibetan Plateau and the Himalayas act as an elevated heat source during summer that induces upward motion and sustained rainfall over South East Asia (Flohn 1957; Flohn and Reiter 1968; Hahn and Manabe 1975; Yanai et al. 1992; Yanai and Li 1994) , Riehl 1969). These geographical features clearly influence the establishment, strength and maintenance of the monsoon circulation (Webster et al. 1998). Flohn (1957) postulated that the seasonal heating of the elevated surface of the Tibetan Plateau and the consequent reversal of meridional temperature and pressure gradients south of the Plateau trigger a large-scale change of the general circulation over East Asia and the monsoon burst over the Indian subcontinent. Later, Hahn and Manabe (1975) performed numerical experiments to study the effect of the Himalayas on the establishment of the monsoon circulation and found that the presence of the mountains is essential in maintaining the South Asian low pressure system. Yanai et al. (1992) suggested that the time evolution of the general circulation over Asia from mid-spring to summer can be described in terms of an interaction of the vertical circulation induced by the heated Tibetan Plateau with the principal monsoon system that migrates northward.

The Asian monsoon is a major component of the general atmospheric circulation. During the boreal summer, winds flow from the South Indian Ocean, transporting moisture and producing large amounts of precipitation over South Asia and the adjacent ocean regions (Hoyos and Webster 2007). During the winter, dry winds flow from the cold land areas of Asia and converge over the warm Southern Indian Ocean, Indonesia and the north of Australia, generating the precipitation of the Australian

monsoon. Overall, the monsoon precipitation provides the main source of fresh water for over a third of the world's population and is crucial for the economy and livelihood of the Asian and African countries.

Monsoon rainfall is thus essential to human life. Variations in monsoon rainfall affect agriculture, drinking water, transportation, health, power and the subsistence of billions of people. Understanding how monsoon changes, not only from year to year, but also as a response to actual and future changes in SST is a key scientific issue.

In the following sections, relevant aspects of the variability of the Asian monsoon are discussed. Special attention is given to the influence of sea surface temperature (SST) on the Asian monsoon.

2.1 Internannual variability of the Asian monsoon

The Asian monsoon exhibits significant variability on a wide range of timescales ranging from the intraseasonal to the interannual (Hoyos and Webster 2007). On interannual time scales, the monsoon displays variability in three major frequency bands. According to Webster et al. (1998) these bands are the biennial period (e.g. Yasunari 1987, 1991; Webster et al. 1999), multiyear variability associated with El Nino and Southern Oscillation (ENSO; e.g. Shukla and Paolino 1983; Shukla 1987) and interdecadal variability (e.g. Mooley and Parthasarathy 1984; Kripalani et al. 1997; Mehta and Lau 1997). Charney and Shukla (1981) suggested that the long-term variability of the monsoon is determined by slowly varying components of the climate system such as the SST rather than by synoptic-scale instabilities.

Extensive studies have been carried out to understand the relationship between ENSO-monsoon and the responsible physical mechanisms for the connection (e.g. Webster and Yang 1992; Lau and Nath 2000; Slingo and Annamalai 2000). One of the most important results is that warm ENSO events are often accompanied by

below normal monsoon rain over Indian, whereas wetter than normal conditions occur during cold events. Furthermore, the summer monsoon circulation over South Asia is generally weaker than normal during an El Nino and stronger during a La Nina (e.g. Shukla and Paolino 1983; Webster and Yang 1992; Lau and Yang 1997).

The statistical relationship between ENSO and the monsoon provides evidence that the Pacific Ocean sea surface temperature (SST) anomalies influence the Asian monsoon. The specific effect of tropical central eastern Pacific SST variability on the monsoon has been the object of study of a number of numerical studies with atmospheric general circulation models (e.g. Palmer et al. 1992; Webster and Yang 1992; Soman and Slingo 1997; Arpe et al. 1998; Yang and Lau 1998; Lau and Nath 2000). All these studies have been carried out to understand a variety of aspects of the ENSO-monsoon relationship and the underlying physical mechanisms.

Soman and Slingo (1997) explored the sensitivity of the Asian summer monsoon (ASM) to SST variability in the tropical Pacific Ocean using two particular case studies for years 1983 (a weak monsoon year) and 1984 (a strong monsoon year). Their sensitivity experiments demonstrated that the modulation of the Walker circulation by SST variations in the equatorial Pacific is the dominant mechanism by which the ASM is weakened during warm ENSO events. During cold events, the modulation of the Walker circulation appears not to be a dominant factor, suggesting that cold SST anomalies in the central/east Pacific may not affect the strength of the monsoon. On the other hand, warm anomalies in the west Pacific associated with La Nina events enhance convective activity over the western Pacific leading to stronger monsoons (Soman and Slingo 1997).

Yang and Lau (1998) also found a nonlinear response of the monsoon circulation to warm and cold SST anomalies in the central-eastern tropical Pacific. Moreover, they noticed that the diminution of monsoon circulation associated with the warm eastern Pacific SST anomalies was accompanied by a broad-scale reduction in water

vapor convergence over Asia and the consequent decrease of monsoon rainfall.

Although there is a clear connection between the Asian monsoon and ENSO, it is not possible to predict the strength of the monsoon from the phase of ENSO alone, because the monsoon-ENSO correlations have variable lead-lag times (Webster and Yang 1992)). In addition, Torrence and Webster (1999) showed that the ENSO-Asian monsoon relationship has experienced changes on the interdecadal and decadal time scales. Moreover, there are other factors besides ENSO that modulate the interannual variability of the monsoon such as regional SST variability, residual soil moisture and land surface processes (e.g. Medina et al. 2010) and remote impacts from the Atlantic Ocean (e.g. Kucharski et al. 2007, 2008, 2009) and higher latitudes (e.g. Yasunari and Seki 1992; Krishnan and Sugi 2003; Lu et al. 2006; Li et al. 2008).

2.1.1 Role of the Indian Ocean

The variability of SST in the Indian Ocean and other coastal water domains also influences the Asian monsoon (e.g. Shukla 1975; Arpe et al. 1998; Clark et al. 2000; Slingo and Annamalai 2000; Rajeevan et al. 2008) although these SST variations are not always independent of ENSO. However, there is evidence that the Indian Ocean SST often varies differently from the SST over the central-eastern Pacific on interannual time scales. Regional SSTs influence the Asian monsoon through changes in land-sea meridional thermal contrast, surface heat and moisture fluxes, and direct moisture supply. A rise in SST can enhance rainfall through an increase in surface evaporation and moisture supply in the atmosphere. Additionally, an increase in temperature over the ocean during summer reduces the land-sea thermal contrast. This reduction decreases the cross-equatorial pressure gradient and the intensity of the monsoon circulation (Shukla 1975; Meehl 1987; Clark et al. 2000).

Chandrasekar and Kitoh (1998) performed numerical experiments to assess the relative importance of local SST forcing and moisture supply effects on the ASM.

Their results suggested that positive SST anomalies over the equatorial Indian Ocean intensify precipitation locally but favor a weakening in monsoon rainfall over the South Asian land areas. The Chandrasekar-Kitoh study illustrates the importance of location of Indian Ocean SST anomalies to ensuing monsoon rainfall.

Observational studies (e.g. Clark et al. 2000; Terray et al. 2003) have also highlighted the importance of the location of SST anomalies in the Indian Ocean on the ASM. Clark et al. (2000) found that winter SSTs over the Arabian Sea and northwest Australia and autumn SSTs over the central equatorial Indian Ocean are positively correlated with Indian monsoon rainfall in the following summer. The studies also noted that these correlations exhibited interdecadal variation associated with changes on the background climate, affecting the predictive relationships between the Indian Ocean SST and the monsoon rainfall. Terray et al. (2003) found that winter SSTs over the southern Indian Ocean are strongly linked to the Indian summer monsoon.

Another interesting aspect of the relationship between Indian Ocean SST and the Indian monsoon is the biennial nature of this variability. Strong tropospheric biennial oscillations (TBO) signals are evident in the variability of both precipitation and circulation of the Asian monsoon (e.g. Mooley and Parthasarathy 1984; Meehl 1987; Yasunari 1990; Webster et al. 1998; Li et al. 2001). In the context of the TBO, warm SST anomalies throughout the tropical Indian Ocean favor enhanced precipitation over the ocean and South Asian land areas leading to a strong Australian monsoon in the subsequent boreal winter (Meehl and Arblaster 2002b). Yu et al. (2003) demonstrated that the Indian Ocean plays a more crucial role than the Pacific Ocean in the TBO transition from a strong Australian monsoon to a weak Indian summer monsoon.

The discovery of the Indian Ocean dipole (IOD, e.g. Webster et al. 1999; Saji et al. 1999) as an important mode of variability of the Indian Ocean, suggested the

possibility of interactions between the IOD and the ASM. Ashok et al. (2001) suggests that IOD events enhance ISM rainfall through a modification of the meridional circulation cell over the Indian sector in summer. Li et al. (2003) suggested that a strong ASM seems capable of forcing an IOD. Webster et al. (2002) developed a more general theory of the regulation of the coupled ocean-atmospheric monsoon system, in which the slow dynamics of the IOD are an inherent feature of the Asian summer monsoon and the TBO. This theory explains how changes in the monsoons winds between strong and weak monsoon create zonal wind anomalies leading to anomalies in the SST distribution, forcing a negative or positive dipole in the fall (Loschnigg et al. 2003)

Overall, the Indian Ocean SST plays an important role in influencing the ASM. Modeling studies (Yang and Lau 1998; Meehl and Arblaster 2002a) demonstrated that the effect of anomalous SST over the Indian Ocean, in conjunction with SST anomalies over the Pacific, was dominant over the effect of land surface processes. Furthermore, variations of the Indian Ocean SST exhibit complex patterns, preventing a clear understanding of the relationship between the ASM and the Indian Ocean SST. In addition, the study of the impact of localized SST Indian Ocean anomalies on the ASM provides a partial understanding of the connection between these two entities. Since the ASM is a climate system that affects the global climate, it is likely to be driven by SST anomalies over large oceanic regions.

2.1.2 Interdecadal variability

The economy of India is still highly dependent on agriculture, which is why rainfall related events such as drought and flood lead to significant crop failure and societal distress across the country. Most recently, in 2002 and 2009, the average rainfall over India was >20% below average. Each year over 40 million Indians are affected directly by flooding. Consequently, it is important to understand when precipitation

variability has occurred and why it has occurred as preludes to prediction of long-term rainfall variability.

Precipitation over South Asia and atmospheric circulation fields show variability from one year to another. The most dominant mode of interannual variability of summer monsoon precipitation is associated with a dipole-like variation of rainfall between South Asia and South East Asia (Goswami et al. 1999). Principal component analysis of zonal winds at 200-hPa reveals that variability in the mean easterlies-westerlies and the south Asian High represents an important element of the nature of principal monsoon modes (Yang and Lau 2006; see Figure 2.1).

In an attempt to quantify interannual monsoon variability, a series of monsoon indices have been developed to measure different components of the monsoon system (Wang and Fan 1999). Perhaps the mostly widely used index is the "all-India" monsoon rainfall (AIMR) index, which is defined by the seasonally averaged precipitation over all the Indian subdivisions from June to September (Mooley and Parthasarathy 1984). In spite of the spatial differences in rainfall within the country, AIMR appears as a good indicator of the variability of the large scale monsoon over India. Other indices that are widely used are the Webster and Yang monsoon index (Webster and Yang 1992) and the meridional monsoon index (Goswami et al. 1999). The definition of these indexes is based on dynamical assumptions (see Appendix A for a list of indices and their respective definitions).

Several components of the Asian monsoon also exhibit significant interdecadal variability. Figure 2.2 displays normalized anomalies of June-September (JJAS) rainfall over all India based on AIMR index. The mean AIMR rainfall for the summer season is 851.8 millimeters and the standard deviation is 82.63 millimeters. June-September rainfall contributes to more than 70% of the annual rainfall (Guhathakurta and Rajeevan 2008; Parthasarathy et al. 1993). The solid curve in Figure 2.2 represents the normalized 11-year running mean of the AIMR. The normalized rainfall

during the periods 1878 - 1898 and 1931 - 1960 is above the long term mean while during the periods 1898 - 1929 and 1961 - 2000 is below the long term mean. Such epochal variation of the Indian summer monsoon rainfall with multidecadal quasi-periodicity has been documented in previous studies (Parthasarathy et al. 1994; Kripalani and Kulkarni 1997; Krishnamurthy and Goswami 2000; Guhathakurta and Rajeevan 2008). Interdecadal variability has also been noted in other monsoon components such as the frequency of cyclones in the Indian monsoon region (Joseph 1976) and the position of the 500-hPa ridge (Kripalani et al. 1997).

Goswami (2006) studied the interdecadal variability of the summer season mean maximum and minimum surface temperature, and its relation to rainfall variability. His analysis showed that after detrending the time series, both minimum and maximum temperature show significant interdecadal variability similar to that of the monsoon rainfall over India. The interdecadal variation of the maximum summer surface temperature was highly negatively correlated with that of the AIMR and the interdecadal variation of summer minimum temperature was positively correlated with that of AIMR. These results suggest that there is coherent evolution of precipitation and surface temperature over India on interdecadal time scales.

The interdecadal variability of the monsoon associated with ENSO interdecadal variability has received most attention. Mehta and Lau (1997) showed that interdecadal variability of AIMR is negatively coherently correlated with the Nino-3 SST (area averaged SST over the eastern Pacific region 5°S-5°N, 90°-150°W), suggesting that there is a strong link between interdecadal variability of Pacific SST and that of the Indian summer monsoon. Wavelet analysis by Torrence and Webster shows that the annual cycle variance of the ASM is negatively correlated with ENSO variance on interdecadal time scales. In addition, the coherency between these two climate components has undergone interdecadal changes (Torrence and Webster 1999) with ENSO-monsoon relationship weakening during the last 20 years (e.g. Torrence and

Webster 1999; Krishna Kumar et al. 1999). Recently, a number of studies have attempted to understand the reasons for the long-term change of the ENSO-ASM relationship (e.g. Krishnamurthy and Goswami 2000; Wu and Kirtman 2003). Krishnamurthy and Goswami (2000) presented empirical evidence to support the hypothesis that the interdecadal variations of the Indian monsoon are an integral part of a coupled monsoon-SST mode. Wu and Kirtman (2003) used a general circulation model to analyze the impacts of monsoon variability on ENSO evolution. They demonstrated that a strong or weak monsoon has significant effects on an ongoing warm ENSO event. The monsoon impacts are manifested in the surface zonal wind-stress anomalies in the western central equatorial Pacific. Cold events, on the other hand, experience much weaker impacts from monsoon anomalies. The also found no apparent relationship between the long-term changes of the monsoon-ENSO correlation and the long-term changes of anomalies in the monsoon and tropical Pacific regions.

2.1.3 Trends in precipitation and sea surface temperature in the Asian monsoon region

A trend analysis of the AIMR index was performed using the Mann-Kendall test (Hirsch et al. 1982). The 11-year running mean of the AIMR shows a long term insignificant decreasing trend. Values of the Mann-Kendall test statistic are indicated in Figure 2.2. The declining trend in monsoon rainfall over India is also not significant if the summer rainfall is analyzed from 1925 onwards.

A closer look at the AIMR time series during the last "dry" epoch shows that during the period 1981 - 2000 there were five years with less precipitation than the mean value minus one standard deviation (deficit years) and three years with more precipitation than the mean value plus one standard deviation (excess years). During the period 1961 - 1980 there were six deficit years and three excess years. Decadal means from 1961 to 2000 exhibit negative departures from the long term mean (see

Table 2.1: Decadal rainfall departure from long term mean

Decade	Departure from long term mean(%)
1961-1970	-0.8
1971-1980	-1.317
1981-1990	-2.33
1991-2000	-1.04

Table 2.1).

It has been suggested that India as a whole covers too large of a geographic area to be studied as a single unit (e.g. Normand 1953; Webster et al. 1998; Ghosh et al. 2009) and variability at the regional scale should be considered when investigating trends (Guhathakurta and Rajeevan 2008). For this reason, a trend analysis of summer precipitation (JJAS) was carried out for the 30 meteorological subdivisions of India.

Results for the subdivision analysis from 1871 onwards are shown in Table 2.2 and Figure 2.3. Over the entire period, decreasing trends are observed in 20 subdivisions. Of these subdivisions, three exhibit significant decreasing trends, namely Naga Mani Mizo & Tripura at 99% significance level; East MP at 95% significance level; Chattisgarh at 99% significance level. Increasing significant trends are observed in four subdivisions such as Coastal Karnataka (90%); Konan & Goa (90%); Punjab (95%); and Haryana (90%). Figure 2.3 depicts considerable variations on the regional scale.

When the trend analysis is performed from 1925 onwards, the number of subdivisions with significant decreasing trend increases from three to eight. Most of these subdivisions are located in central India and north-east India. Subdivisions located over West India have not significant decreasing trends. Guhathakurta and Rajeevan (2008) observed significant decreasing trends over Chattisgrah, Jharkhand and Kerala during the monsoon season, using a different dataset. Krishnakumar et al. (2009) also reported a significant decrease is south-west monsoon rainfall over Kerala. Kerala State is located in the west side of the southern tip of India and it is popularly

known as the "Gateway of summer monsoon" over India.

An examination of monsoon rainfall time series over Kerala and other subdivisions located over west India and south-west India (Figure 2.4) shows that rainfall over Kerala was mostly less than the long term mean from 1980 to 2005. Monsoon rainfall over North Karnataka, South Karnataka, Konan & Goa and Coastal Karnataka depict less rainfall than the long term mean mostly after 1990.

In a recent study based on daily gridded rainfall, Dash et al. (2009) found significant changes in frequencies of different categories of rainfall over India as a whole and over six homogenous rainfall zones. In particular, they found a decreasing trend in the occurrences of long rain spells. Long term decreasing trends in summer rainfall over regions of India has also been reported by Kumar et al. (1992), Dash et al. (2007) and Krishnakumar et al. (2009).

The shift in the rainfall patterns over India during the last 20 years has been attributed to a weakening of the monsoon circulation over South Asia (Kripalani et al. 2007; Dash et al. 2009). Figure 2.5 shows the shear monsoon index designed by Webster and Yang (1992). This index is defined by a time-mean zonal wind shear between 850 and 200-hPa, averaged over south Asia from the equator to 20°N and from 40° to 110°E. The index corresponds to the first baroclinic mode which is supposedly forced by monsoon convective heating. An examination of the evolution of this index shows a change in the mean of the index around 1971. Before this year the mean was positive (0.8) and after this year the mean has a negative value (-0.6). Since this index is an indicator of the strength of the monsoon, a change in the mean to a negative value suggests that the monsoon circulation is weakening.

Some studies have reported a southward shift in the location of the low level westerly jet that brings moisture over India during summer (e.g. Joseph and Simon 2005) while others suggest that there is a decreasing trend in monsoon depression frequency during the last century (Joseph and Xavier 1999; Dash et al. 2004). Chung

Table 2.2: Trend analysis for 30 subdivisions of India

Subdivision	Slope	M-K statistic
Assam & Meghalaya	-0.638	-1.543
Naga.Mani.Mizo.&Trip.	-1	-2.716*
Sub-Hima. W. Bengal	-0.575	-0.805
Gangetic W. Bengal	0.579	1.507
Orissa	-0.451	-1.252
Jharkhand	-0.442	-1.242
Bihar	-0.518	-1.08
East Uttar Pra.	-0.134	-0.308
West U.P. Plains	-0.389	-0.991
Haryana	0.567	1.752*
Punjab	0.846	2.184**
West Rajasthan	-0.03	-0.114
East Rajasthan	-0.537	-1.419
West Madhya Pradesh	-0.493	-1.354
East Madhya Pradesh	-0.89	-2.081*
Gujarat	-0.284	-0.43
Saurashtra & Kutch	-0.054	-0.107
Konkan And Goa	1.557	1.731*
Madhya Maharashtra	0.001	0.01
Marathwada	-0.208	-0.496
Vidarbha	-0.581	-1.299
Chattisgarh	-1.288	-2.836**
Coastal Andhra Pra.	0.369	1.638
Telangana	0.3	0.801
Rayalaseema	0.214	0.715
Tamil Nadu	-0.02	-0.146
Coastal Karnataka	1.807	1.659*
North Int. Karnataka	-0.055	-0.196
South Int. Karnataka	0.184	0.689
Kerala	-1.276	-1.556

Red values indicate negative significant trends at a 95 %(*) and 99% (**) level. Blue values indicate positive significant trends at a 90% (*)and 95% (**) level

and Ramanathan (2006) showed a summertime weakening of the North Indian Ocean meridional SST gradient for the period 1950 - 2002, which could lead to a weakening of the monsoon circulation and the subsequent diminution of summer rainfall over India. Meehl et al. (2008) suggested that the radiative effects of black carbon aerosols over South Asia could explain the changes in SST over the Northern Indian Ocean during the summer season.

From the discussion above it is clear that several factors control monsoon variability. Among all the external causes of interannual and interdecadal variability of the ASM, SST variability appears to be the leading impacting factor (Chao and Chen 2001). Time series of summertime (June-September) SST anomalies for the tropical oceans (Figure 2.6a) reveal that they have warmed substantially since the 1960s. The temporal evolution of SST anomalies is similar for all the tropical oceanic regions. A period of negative anomalies is evident before 1935, a shorter period of sudden warming occurs around 1940 and increasing SST anomalies are evident after 1970. Figure 2.6b shows the temporal evolution of the annual cycle of SST anomalies over the Indian Ocean from 20°S to 20°N. The most prominent feature of this diagram is the continuous increase in SST anomalies since 1970. Periods of cooling and sudden warming are also evident. Furthermore, the temporal evolution of SST is coherent across all the seasons.

Figure 2.7 shows the evolution of normalized 11 year running mean AIMR index time series and low-pass filtered SST anomalies over the tropical oceans and over the tropical Indian Ocean from 1871 to 2000. While the AIMR index depicts interdecadal variability, SSTs anomalies exhibit a very clear increasing trend since the early 1990's. One remarkable feature is that during the last "dry" epoch (approximately since 1960) SSTs anomalies are positive and continually increasing. This behavior suggests that SSTs over the tropical oceans play a role in determining the

atmospheric circulation during the summer season, ultimately affecting the convergence of moisture into peninsular India. A reduction (or increase) in the available moisture over India would impact the development and growth of convective processes in the region. We hypothesize that increasing SSTs in the tropics decrease rainfall in the monsoon regions.

Both modeling and empirical studies have demonstrated that the SST variability of the tropical oceans influence the ASM. However, it is still unclear how the SST variability modulates the monsoon circulation and it is not well understood how changes in SST translate into changes in convective processes over South Asia and the Indian Ocean.

Given the complexity of the system, experiments with general circulations models constitute a useful tool to improve our knowledge of the mechanisms responsible for the influence of SST on the monsoon. In this study we aim to investigate the response of the large scale features of the mean state of the summer monsoon to different configurations of SST observed during periods in the last century, using an atmospheric general circulation model. To keep the experimental design as simple as possible, a number of experiments were designed in which the only the SST fields are modified. More detail about the experimental design is given in the following chapter.

Chapter 3 describes the atmospheric general circulation model and the observational dataset used in this study. Chapter 4 describes the mean state of the large scale monsoon circulation for the control simulation and discusses the differences between each of the experiments and the control simulations. A detailed analysis of changes in the monsoon circulation forced by changes in the distribution of SST is presented. Chapter 5 discusses in more detail the long term variability in the monsoon precipitation and the interconnection that exists between SSTs, atmospheric circulation and moisture availability are evaluated to help explain the variations in monsoon precipitation during the last century.

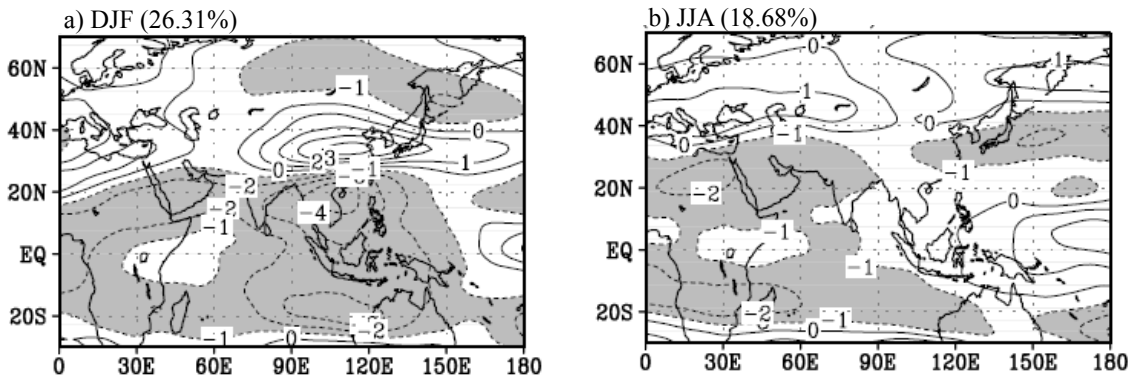

Figure 2.1: First EOF Modes of U200 for DJF and JJA based on the NCEP/NCAR reanalysis for 1968-2003. Note that the variability of the upper tropospheric monsoon easterlies and the westerlies to the north are pronounced. From Yang and Lau (2006).

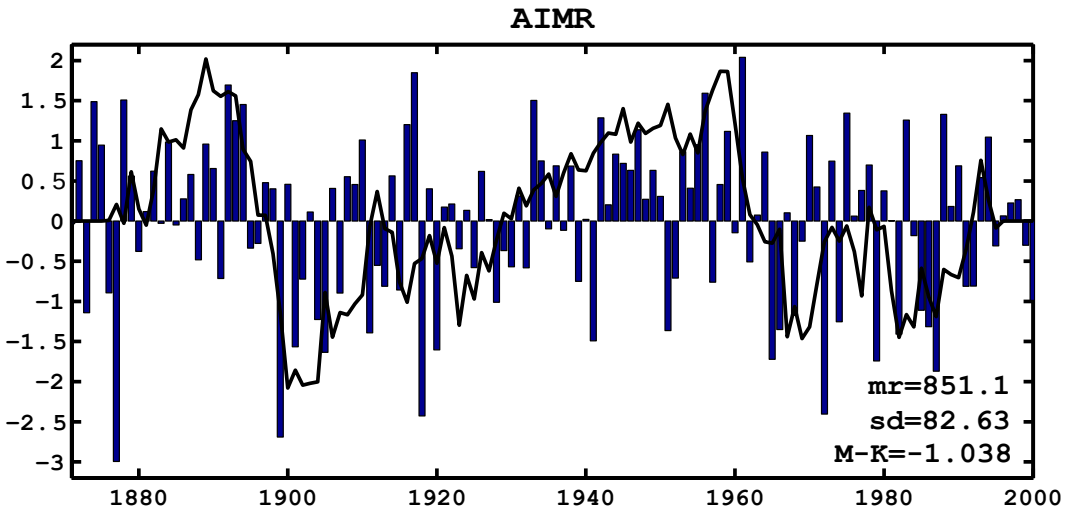

Figure 2.2: Normalized anomalies (bars) of All india monsoon rainfall index and normalized 11-year running mean (solid curve) of AIMR. Long term mean seasonal rainfall (mr, in mm), standard deviation (sd, in mm), and Mann-kendall statistic (M-K) associated with the trend test are also shown.

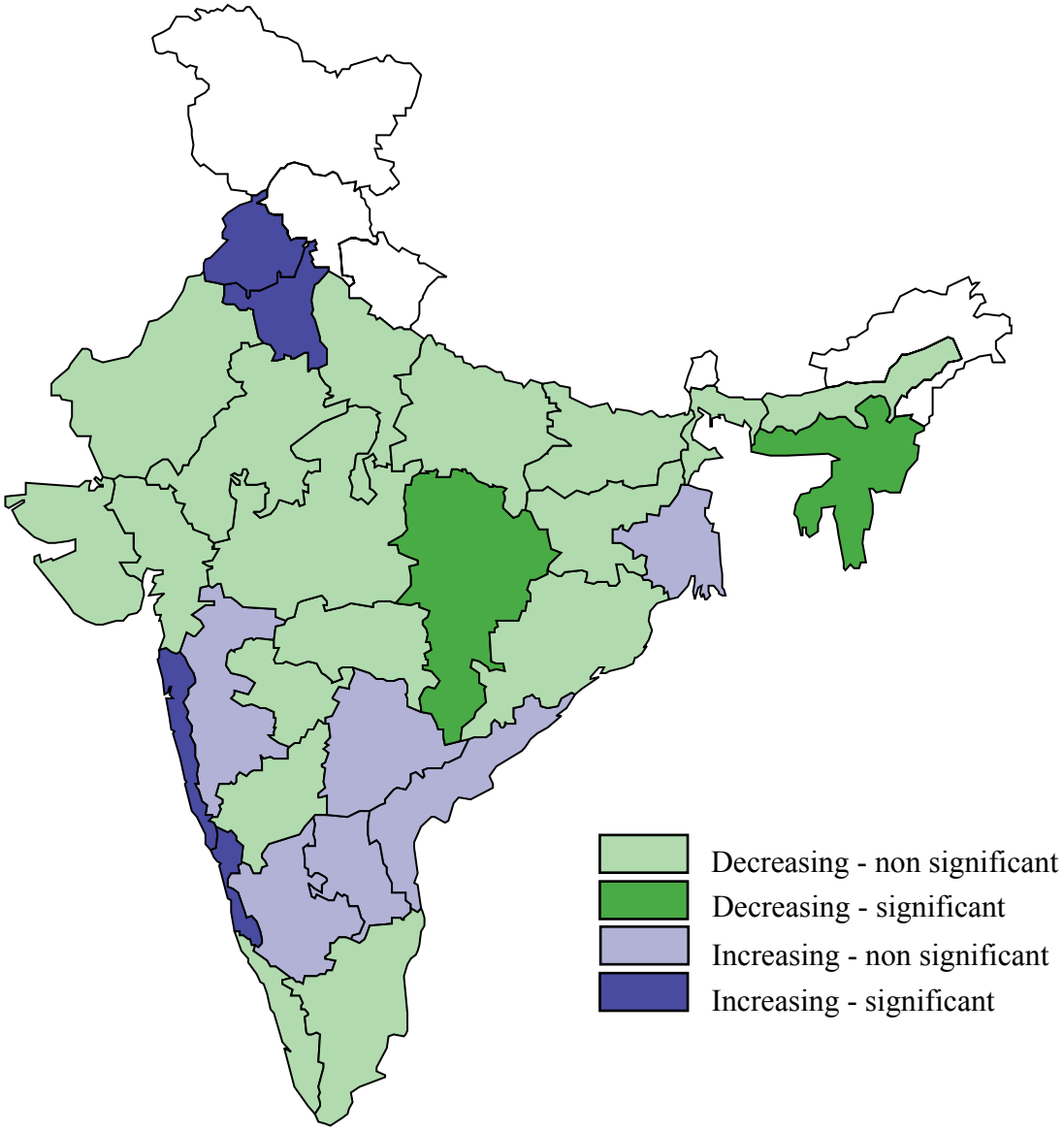

Figure 2.3: Decreasing – Increasing trends in rainfall for 30 meteorological subdivisions of India during the summer season. Significant and non-significant trends are indicated with color shading.

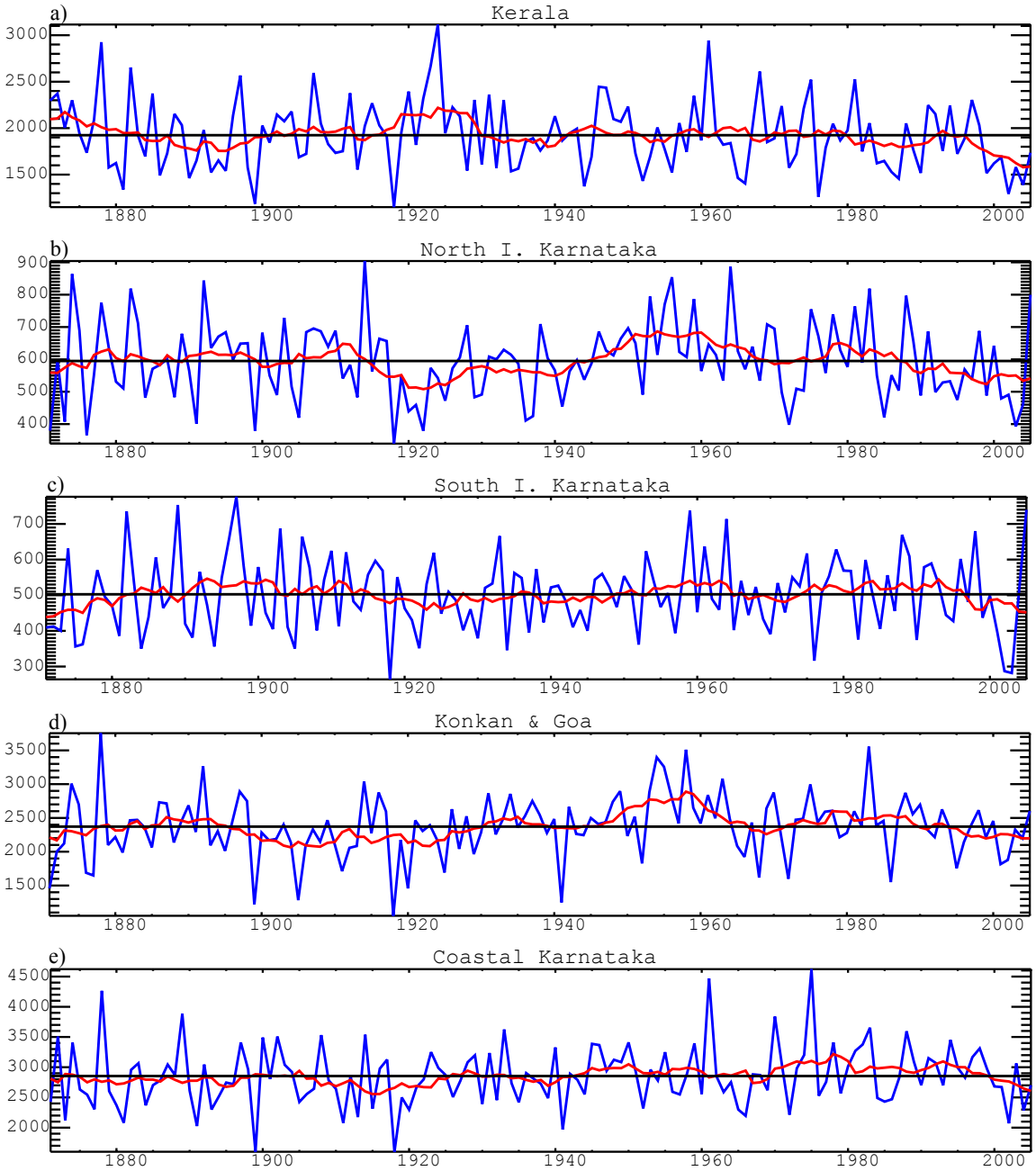

Figure 2.4: Time series of summer monsoon rainfall over a)Kerala, b) North I. Karnataka, c)South I. Karnataka, d) Konan & Goa, and e) Coastal Karnataka (mm). The red line represents the 11-year running mean for each time series. The horizontal black line denotes the long term mean for each time series.

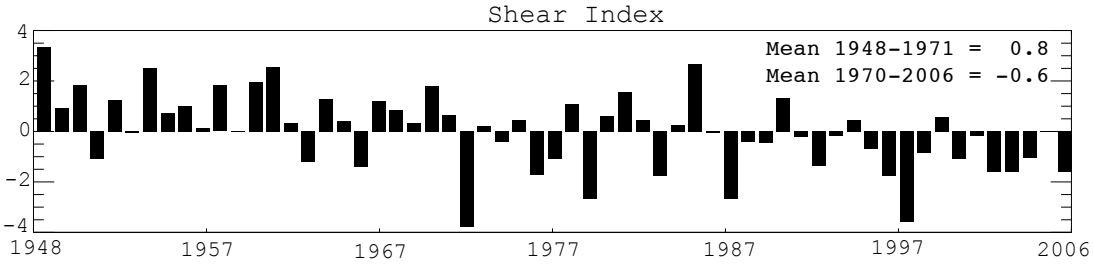

Figure 2.5: Temporal evolution of the shear monsoon index after Webster and Yang (1992) from 1948 - 2006. The index is defined by the time mean zonal wind (U) shear between 850 and 200-hPa, U850-U200, averaged from the equator to 20°N and from 40°E to 110°E.

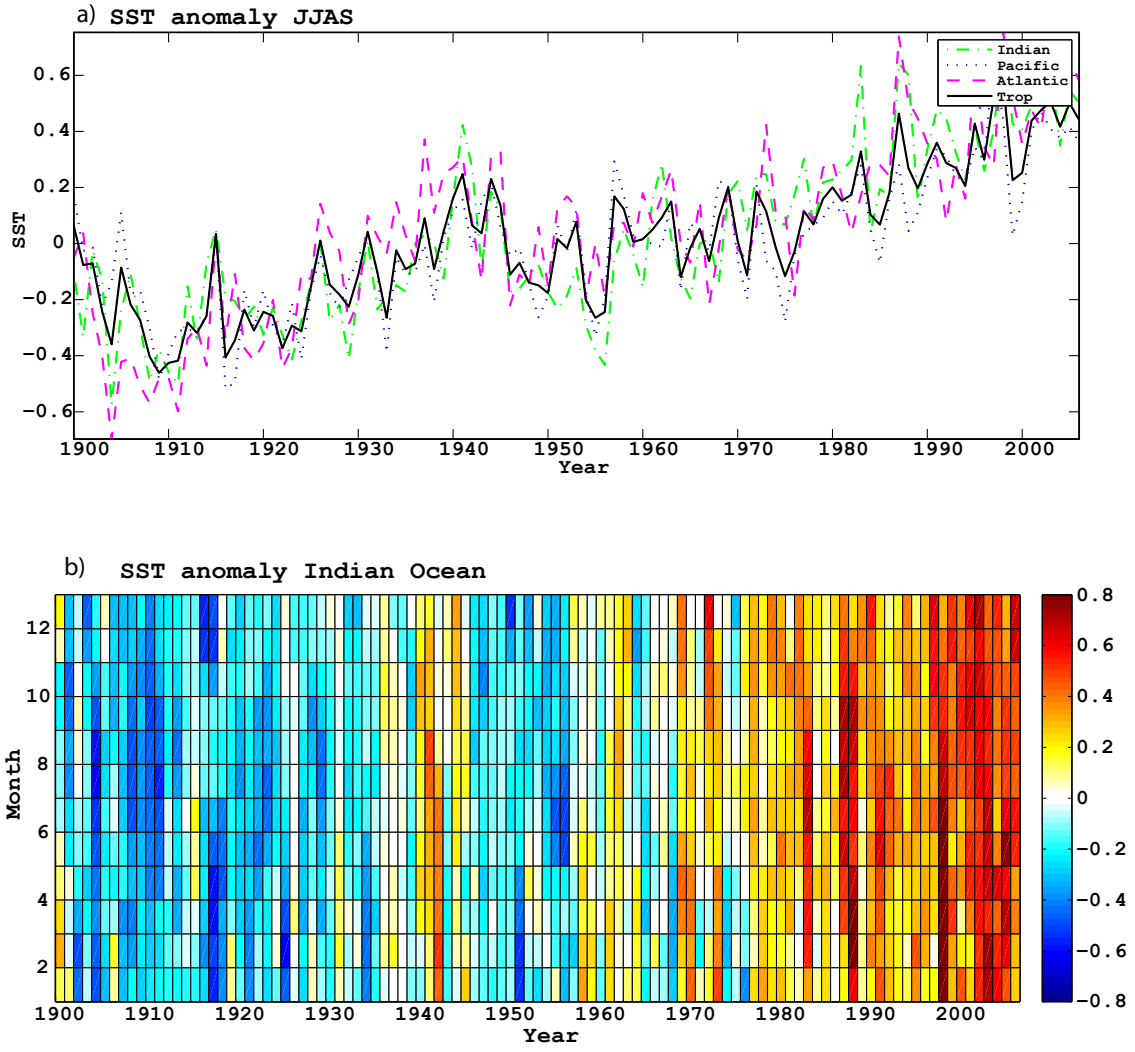

Figure 2.6: a) Time series of SST anomalies for the June - September season from 1900 to 2006. Time series for the whole tropical ocean band and for each of the tropical ocean basins are plotted. b) Temporal evolution of the annual cycle of SST anomalies over the tropical Indian Ocean from 1900 to 2006. Units are °C.

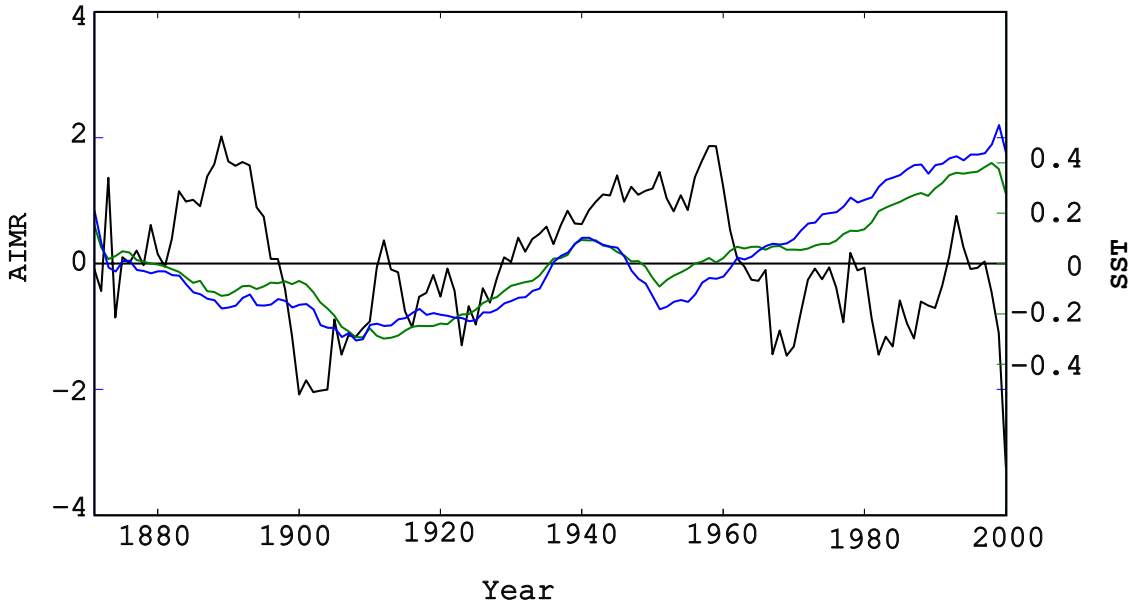

Figure 2.7: Normalized low-pass filtered AIMR index (black line, in mm) and low-pass filtered SST anomalies (°C) over the tropical oceans (green line) and over the tropical Indian Ocean (blue line).

CHAPTER III

METHODOLOGY

3.1 Data and model description

The atmospheric general circulation model (AGCM) used in this work is the International Centre for Theoretical Physics (ICTP) AGCM (Molteni 2003 for details). The model is based on a hydrostatic spectral dynamical core, a σ vertical coordinate system and a number of physical parameterizations schemes. A σ surface is defined as a pressure level normalized by the surface pressure and is thus terrain following. The parameterized processes include convection, large-scale condensation, clouds, shortwave and long-wave radiation, surface fluxes of momentum and energy, and vertical diffusion (Molteni 2003).

Convection is represented by a simplified mass-flux scheme that is activated where conditional instability is present, and where boundary layer humidity exceeds a defined threshold. Large-scale condensation is modeled as a relaxation of humidity relative to a reference value, which occur whenever relative humidity exceeds a σ-dependent threshold. Clouds properties are defined diagnostically from the values of relative humidity in the tropospheric air column and the amount of total precipitation. The shortwave radiation scheme uses two spectral bands (one corresponds to the visible part and the other to the near-infrared). For each band and for each tropospheric layer, shortwave transmissivity is a function of the layer mass, specific humidity and cloud properties. The longwave radiation scheme uses four spectral bands, one for the infrared window and the other ones for the spectral regions of carbon dioxide and water vapor. The effect of clouds is represented as a decrease in the transmissivity in the window band. Transmissivity for each band and model layer

is computed as a function of layer mass and humidity. Surface fluxes are obtained by bulk aerodynamic formulas with different exchange coefficients between land and sea. Land skin temperature is defined from the surface energy balance. The vertical diffusion scheme models three processes: shallow convection; a slow diffusion of moisture in stable conditions and a fast redistribution of dry static energy occurring when the lapse rate is close to the dry-adiabatic limit. A detailed description of the parameterization schemes used in the model can be found in the ICTP website (`http://users.ictp.it/$\sim$kucharsk/speedy-net.html`).

Molteni (2003) described the ICTP AGCM response to tropical and extratropical SST anomalies for a configuration with five vertical levels. In this study, Molteni (2003) compared the model mean state from an ensemble of three multi-decadal integrations for the period 1952 to 1992 with the European Centre for Medium Range Weather Forecasts reanalysis (ERA; Gibson et al. 1997) data.

An examination of the mean state during boreal summer (June-July-August) showed that there are model biases. For example, the model overestimates the strength of the 500-hPa meridional temperature gradient in the extratropical regions. In the Northern Hemisphere the model depicts a cold bias in the polar mid-troposphere. Large temperature biases were also found over Antarctica. Zonal-mean wind distribution exhibit a strong westerly bias at 250-hPa between 15°S and 25°N. This westerly bias decreased almost linearly with increasing pressure in the vertical. An easterly bias is also found in the southern extratropics around 60°S, which results in a northward shift of the simulated jet. Near-surface zonal wind maps showed that the model reproduces the location of westerly and easterly winds well qualitatively. However, the simulated wind intensity is weaker than the observed in the Southern Ocean and some regions of the tropical oceans. Specifically, the intensity of the low level westerlies was underestimated over the Arabian Sea, India and Bay of Bengal

(Molteni 2003). Additionally, the model also revealed deficiencies in the representation of summer rainfall. The model does not reproduce the observed maximum over the Bay of Bengal and the rainfall maxima associated with the tropical convergence zone in the Indian Ocean was restricted to a latitudinal band around 10°N. Furthermore, rainfall over the southern slopes of the Himalayas was overestimated, and rainfall over the west Pacific was underestimated. In general, the simulated summer tropical rainfall exhibited a narrower latitudinal distribution compared to the observations.

An examination of the mean state during the boreal winter (December – January – February), showed that the model provides a more realistic representation of the atmospheric circulation during winter than its summer counterpart. The model reproduced the structure of the meridional temperature gradient satisfactorily. The representation of zonal mean wind was quite realistic, showing an amplitude and location of the upper tropospheric jet maxima very close to observations in both hemispheres. Regions of easterly and westerly flow in the surface were well represented in the near surface zonal winds. Distribution of rainfall was in good agreement with observations. Zonal mean rainfall comparisons between the model, ERA (Gibson et al. 1997) and CMAP (Climate Prediction Center Merged Analysis of Precipitation; Xie and Arkin 1997), showed that in many regions the difference between the model and CMAP distributions is comparable to the difference between CMAP and ERA.

Molteni (2003), stated that despite the limitations imposed by the parameterization of physical processes, and the coarse vertical resolution, the model is computationally very efficient and constitutes a useful tool for academic purposes. The simplicity of the model is an advantage that allows the user to design a series of experiments in a "controlled" manner, allowing a diversity of climatological problems to be addressed.

Bracco et al. (2004) used a seven-layer version of the ICTP AGCM to study

decadal climate variability in the second half of the 20^{th} century. This version of the model was significantly improved with respect to the five-layer one, in aspects as the stationary wave pattern over the Pacific Ocean and the response to ENSO-type SST anomalies. In their analysis they found that the model reproduces moderately well the structure of climate variability in the second half of the twentieth century and was able to reproduce the structure of the observed trend.

An eight-layer version of the model was used in Kucharski et al. (2006) to investigate the influence of the decadal variations in the SST on the North Atlantic Oscillation (NAO) from 1870 to 2002. Compared with the previous versions, the model climatology showed an improved structure and strength of stationary waves in the Atlantic region and a more realistic representation of the main features in the rainfall pattern during boreal winter. Bracco et al. (2007) used the eight-layer version of the model to investigate the relationship between SST anomalies in the Pacific and Indian Ocean and anomalies in wind and rainfall patterns associated with the South Asian summer monsoon. Comparison of model climatology with rainfall data from the CMAP and wind climatology from the NCEP reanalysis showed that when the model is forced by prescribed SST, it underestimates the strength of the Somali jet and the westerlies that blow from the ocean into the Indian peninsula. The AGCM also overestimates precipitation over the Equatorial Indian Ocean and produces less precipitation than observed over the Indian peninsula. In their work they performed six ensemble experiments that included uncoupled and coupled versions of the AGCM and their results confirm the importance of a coupled modeling strategy to simulate the interannual and interdecadal variability of the Asian monsoon.

Kucharski et al. (2009) also used the eight-layer ITCP AGCM to study the physical mechanism by which the tropical Atlantic Ocean impacts the summer (July–August–September) monsoon rainfall over Africa and India. A comparison of simulated climatology with observations, showed that despite some differences in rainfall intensity

the model reproduces the overall features of precipitation and low-level winds over the African-Indian monsoon regions. In their work they demonstrated that observational evidence supports the existence of a teleconnection between the southern tropical Atlantic and the Indian monsoon. Using the results from a set of sensitivity experiments they proposed that a "Gill-Matsuno" type (Matsuno 1966; Webster 1972; Gill 1980) quadrupole response explains the teleconnection between the tropical Atlantic and the Indian basin.

The configuration of the model used in the present study has eight vertical layers with boundaries at σ values of 0, 0.05, 0.14, 0.26, 0.42, 0.60, 0.77, 0.90 and 1. The prognostic variables (vorticity, divergence and absolute temperature) are specified at σ levels intermediate between the upper and lower boundaries, at σ values 0.025, 0.095, 0.20, 0.34, 0.51, 0.685, 0.835 and 0.95. In the horizontal, the model uses a triangular spectral truncation at total wave number 30 (T30), with a standard Gaussian grid of 96 by 48 points, which corresponds approximately to a 3.7° grid (about 400 Km).

3.1.1 Observational data

The eight layers T30 ICTP AGCM is forced by monthly varying SST from the National Oceanic Atmospheric Administration (NOAA) Extended Reconstructed SST dataset (Smith et al. 2008). This monthly mean analysis extends from January 1854 to the present, with a horizontal resolution of 2° in latitude and longitude. In this study only the period from 1925 to 2000 is considered to create forcing fields for the AGCM. The data are obtained from:

`http://www.esrl.noaa.gov/psd/data/gridded/data.noaa.ersst.html`

To evaluate the ICTP AGCM performance, summer rainfall and surface wind mean fields from the model are compared with observations. Estimates of precipitation are obtained from a satellite-based global precipitation analysis provided by the Global Precipitation Climatology Project (GPCP; Arkin and Meisner 1987; Adler

et al. 2003; Bolvin et al. 2009; Huffman et al. 2009). Monthly mean rainfall data is available on a 2.5-degree global grid from 1979 to the present and can be obtained from `http://precip.gsfc.nasa.gov/`. Monthly mean wind data from the 40-year European Centre for Medium-Range Weather Forecast (ECMWF) Re-Analysis (ERA40; Uppala et al. 2005) was also used. ERA-40 data is available from 1957 to 2002 for 18 pressure levels and it has a horizontal resolution of 1° x 1°.

Finally, All-India (rainfall averaged over the entire Indian subcontinent) and 30 different meteorological subdivisional summer monsoon rainfall time series are used to perform a trend analysis of precipitation over India. These time series are area-weighted estimates based on rainfall observations at 306 land stations uniformly distributed over India. A detailed discussion on how these datasets were prepared is found in Mooley and Parthasarathy (1984) and Parthasarathy et al. (1987, 1990, 1995). An updated version of these datasets from 1871 and onwards can be obtained from `http://www/tropmet.res.in`.

3.1.2 Experimental design

The ICTP AGCM simulated climatology for the control experiment, forced by an average annual cycle of SST determined over the period 1930 to 2000, is used to evaluate the model's ability to reproduce the large scale atmospheric features observed during the period of the Asian summer monsoon. Figure 3.1 compares the model and the ERA-40 relanalysis 925-hPa summer winds. An examination of the two data sets reveals that low-level circulation over the summer monsoon region is simulated reasonably well. Figure 3.2 shows a comparison of precipitation between the model and GPCP data. As described by Bracco et al. (2007), the AGCM reproduces the overall spatial structure of the observed monsoonal precipitation during the summer months. Larger differences with precipitation observations are seen over the equatorial Indian Ocean and over the Indian peninsula. The use of the optional mixed

layer ocean does not improve considerably the modeled climatology (Bracco et al. 2007). Furthermore, the simplicity of the AGCM allows us to make several controlled simulations with prescribed SST, with a fair representation of the large scale features of the summer monsoon.

In addition to the Control experiment, four major ensemble experiments have been carried out with different SST forcing representative of epochs chosen from the last century. In all cases, the model was run in ensemble mode with 10 members. The experiments were designed to investigate the response of the large scale features of the mean state of the summer monsoon to different configurations of observed SST observed during the last century. In the control runs (CTRL), the model is forced by monthly SST climatology averaged from 1935 to 1945. In Experiment 1 runs (COLD), the AGCM is forced by monthly SST climatology averaged from 1925 to 1935. In Experiment 2 (MODERATE), the model is forced by monthly SST climatology averaged from 1950 to 1960. In Experiment 3 (WARM), the model is forced by monthly SST averaged from 1950 to 1960. In Experiment 4 (BUMP), the model is forced by monthly SST averaged from 1938 – 1942. Figure 3.3 shows SST anomalies time series for the summer season for the experiments COLD, MODERATE, WARM and BUMP. Table 3.1 provides a summary of the experiments.

The four periods that are the basis of the experiments are chosen to allow the largest changes in boundary forcing occurring in the last century to be isolated and to test if there is any influence of these various global SST signatures on ASM precipitation. COLD, MODERATE and WARM are assumed typical of periods in the last century as the globe heats up towards its current configuration. The BUMP experiment uses as boundary conditions that period where there may have been a large scale global oscillation in the SST.

Figure 3.4 shows the June–September (JJAS) forcing field differences between each of the experiments and the control run. The COLD – CTRL SST forcing field

Table 3.1: List of experiments

Experiment	Ensembles	Forced by
CTRL	10 members	Monthly climatology of SST averaged from 1930 – 2000
EXP1 (COLD)	10 members	Monthly climatology of SST averaged from 1925 – 1935 – coldest scenario
EXP2 (MODERATE)	10 members	Monthly climatology of SST averaged from 1950 – 1960 – cold scenario
EXP3 (WARM)	10 members	Monthly climatology of SST averaged from 1990 – 2000 – warmest scenario
EXP4 (BUMP)	10 members	Monthly climatology of SST averaged from 1938 – 1942. – bump scenario

differences (Fig 3.4a) exhibit negative anomalies in the tropical band. Largest negative anomalies are observed in the western northern Indian Ocean and the eastern Indian Ocean. The MODERATE – SST differences (Fig. 3.4b) also display negative anomalies in the tropical ocean band, but the magnitude of the anomalies is smaller than in the COLD experiment. The WARM SST forcing field differences with CTRL (Fig 3.4c) are characterized by generalized positive anomalies in the tropical ocean band. Largest positive anomalies are observed in eastern equatorial Pacific Ocean. Finally, the BUMP forcing field differences with CTRL (Fig. 3.4d) exhibit slight negative anomalies in the northern Indian Ocean and in the western tropical Pacific. Slight positive anomalies are observed in the eastern tropical Pacific and the southern Indian Ocean.

For each of the above forcing scenarios, the model is run for 30 years. The first five years of the simulations are used as spin-up time. To account for the uncertainties due to internal atmospheric dynamics, 10 member ensemble simulations are conducted for each of the experiments including the control run. Ensembles differ from each other only in the initial conditions. To produce an ensemble, a random perturbation is applied to the diabatic forcing in the first time step. Sensitivity analyses described in

this study are based on 25 year averages. Unless otherwise mentioned, model results presented here focus on the JJAS season.

3.2 Forced and internal variability in the AGCM

In our experiments, the variability of seasonal means in the AGCM may be considered as due to a combination of internal atmospheric variability and to the variability imposed by boundary conditions. In this section, we take advantage of our experimental set up and compare the variability that can be ascribed to changes in SST during the summer season with that due to internal variability of the system.

Following Rowell et al. (1995) and Straus and Shukla (2000), the total AGCM variance, ${\sigma^2}_{TOT}$, can be separated into two components: the variance due to SST forcing, ${\sigma^2}_{SST}$, and the variance due to internal atmospheric dynamics, ${\sigma^2}_{INT}$. The former is calculated in a manner that takes into account the finite size of the ensemble and the latter arises from examining the model's sensitivity to differing initial atmospheric conditions.

Consider a generalized case of Nensembles (number of experiments with different SST forcing), each with n ensemble members. The internal component of the variability can be estimated by computing the variance of deviations of each data point about the ensemble mean as follows:

$$\sigma^2_{INT} = \frac{1}{N\,(n-1)} \sum_{i=1}^{N} \sum_{j=1}^{n} \left(x_{ij} - \bar{x_i}\right)^2$$

where

$$\bar{x_i} = \frac{1}{n} \sum_{j=1}^{n} x_{ij} \text{ (the ensemble mean for the } i\text{th experiment)}$$

The variability due to SST forcing, ${\sigma^2}_{SST}$, is related to the ensemble mean variance and the internal variance in the following manner:

$$\sigma^2_{SST} = \sigma^2_{EM} - \frac{1}{n}\sigma^2_{INT}$$

where ${\sigma^2}_{EM}$ is the variance of the ensemble means and is estimated as:

$$\sigma^2_{EM} = \frac{1}{N-1}\sum_{i=1}^{N}(\bar{x}_i - \bar{x})^2$$

and:

$$\bar{x} = \frac{1}{nN}\sum_{i=1}^{N}\sum_{j=1}^{n} x_{ij} \text{ (the mean of all data)}$$

Finally, the total variance ${\sigma^2}_{TOT}$ is expressed as:

$$\sigma^2_{TOT} = \sigma^2_{EM} + \sigma^2_{INT}$$

and the signal to noise ratio as:

$$\frac{\sigma^2_{SST}}{\sigma^2_{INT}}$$

Here we use N= 5 (number of experiments with different SST forcing: CTRL, COLD, MODERATE, WARM, BUMP) and n= 10 (the size of the family of ensembles for each experiment) to compare the SST forced variance of the simulated large scale circulation of the Asian summer monsoon to its internal variability. The signal to noise ratio for velocity potential at 850 and 200-hPa is displayed in Figure 3.5. We choose these diagnostics because they provide a valuable measure of monsoon activity and are directly linked to precipitation.

At 850-hPa (Fig 3.5a), the ratio ${\sigma^2}_{SST}/{\sigma^2}_{INT}$ exceeds 1.0 in South Asia, the northern Indian Ocean, the tropical Pacific and in a large portion of the tropical Atlantic Ocean. At 200-hPa (Fig 3.5b), the signal to noise ratio exceeds 1.0 in a large portion of the tropical band, and is even larger over India and the central Indian Ocean.

According to standard analysis of variance methods (Scheffe 1959), the statistical significance of this ratio can be assessed by testing the null hypothesis that

$\sigma^2{}_{SST}$=$\sigma^2{}_{INT}$. The corresponding F statistic is given by the ratio of the SST-forced variance to its uncertainty due to the presence of internal noise and is defined as:

$$F = \frac{\sigma^2_{INT} + n * \sigma^2_{SST}}{\sigma^2_{INT}}$$

with $N-1$ and $N\,(n-1)$ degrees of freedom, at the α level of significance. Figure 3.6 shows estimates of the F statistic for velocity potential at 850 and 200-hPa. For our experimental design, a value of F equal to 3.83 corresponds to 99% statistical significance.

In Figure 3.6 values of the F statistic greater than 3.83 are evident almost everywhere and in particular across the entire tropical band. In these regions the null hypothesis can be rejected at a 99% significant level. Results of the statistical analysis in conjunction with the distribution of the signal to noise ratio shown in Figure 3.5a,b demonstrate that the SST-forced variance exceeds the internal variance over almost the entire tropical band and in particular over the Asian monsoon region. These results are consistent with the Charney and Shukla (1981) hypothesis that a major part of the low-latitude variability is due to boundary anomalies. In summary, in our simulations the monsoon circulation is relatively insensitive to atmospheric initial conditions and most of its variability is due to the underlying SST distribution.

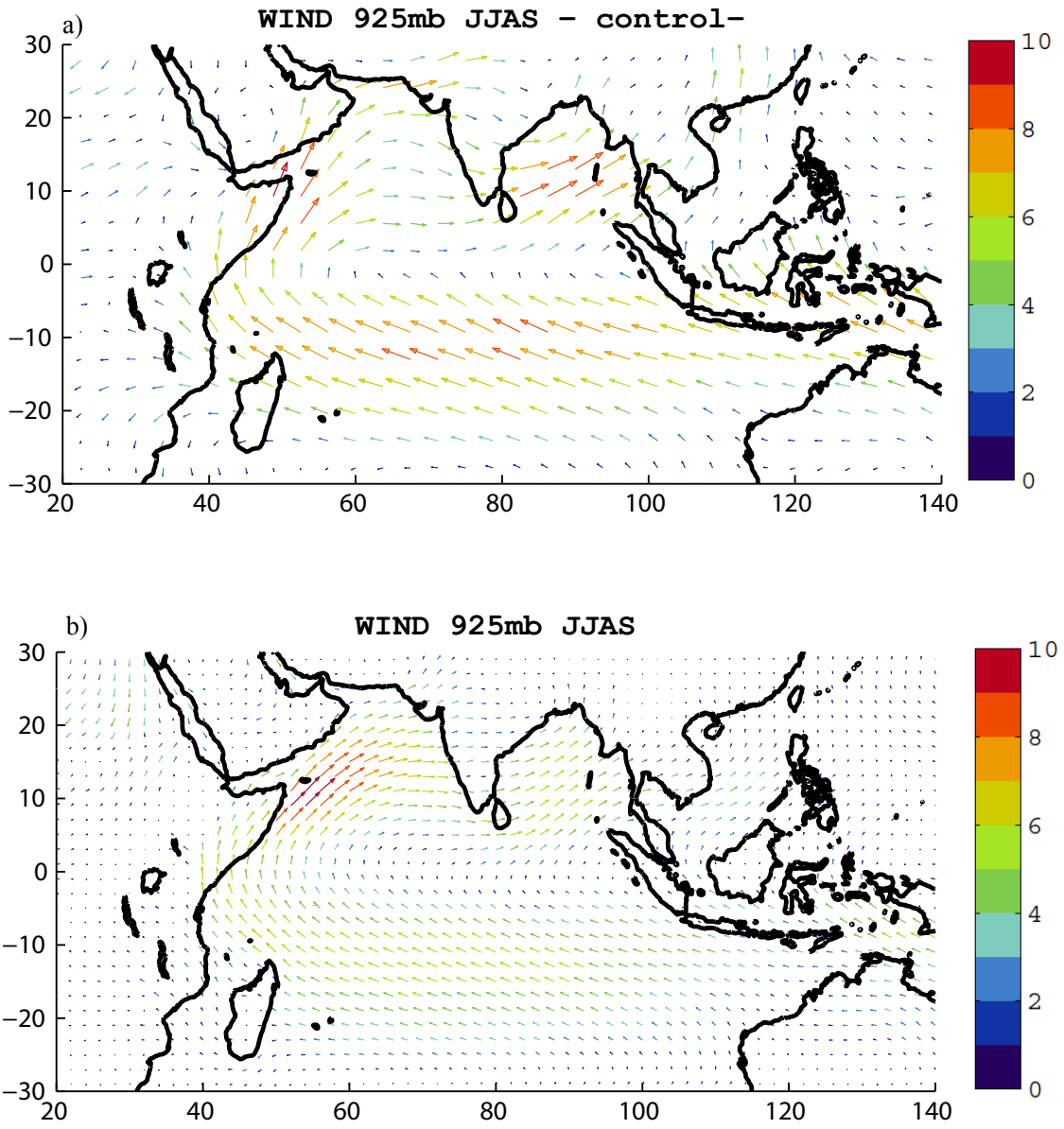

Figure 3.1: a) Mean JJAS wind field at 925-hPa from model CTRL run. b) Mean JJAS wind field at 925-hPa from ECMWF reanalysis for the period 1958 - 2000. Units are ms^{-1}.

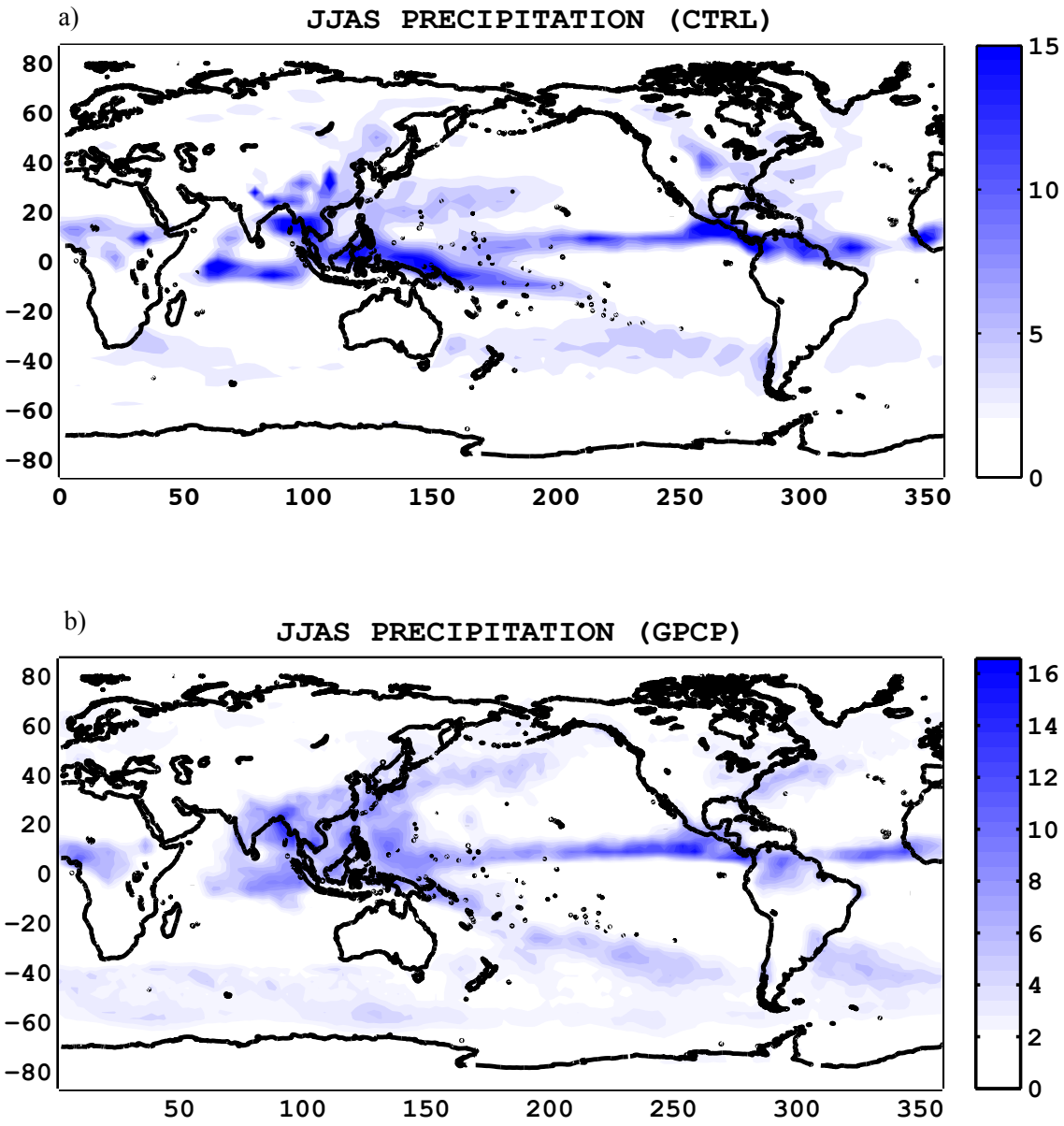

Figure 3.2: a) Mean JJAS precipitation from model CTRL run. b) Observed JJAS precipitation from GPCP (1979 - 2006). Units are mmday^{-1}.

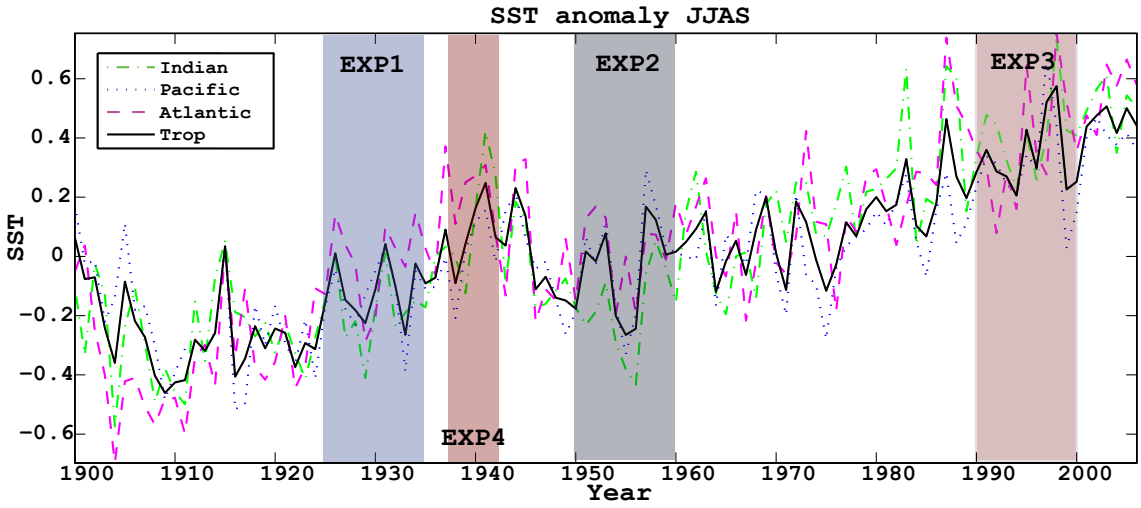

Figure 3.3: Summer SST anomalies for the tropical ocean band with COLD (EXP1), MODERATE (EXP2), WARM (EXP3) and BUMP (EXP4) experiments indicated. Units are °C.

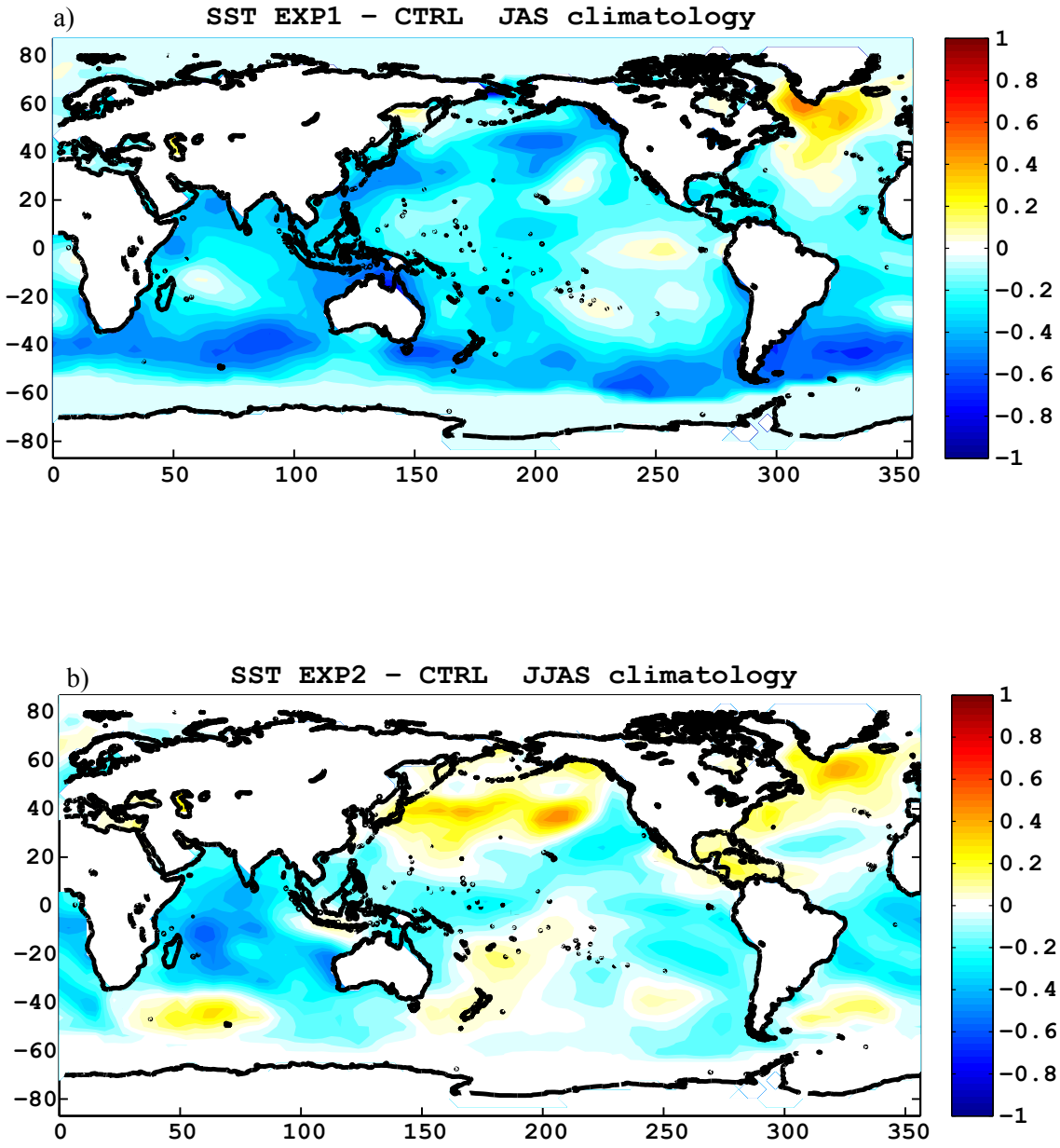

Figure 3.4: SST forcing field differences between each of the experiments and the control run. a) COLD - CTRL. b) MODERATE - CTRL. c) WARM - CTRL. d) BUMP - CTRL. Units are °C.

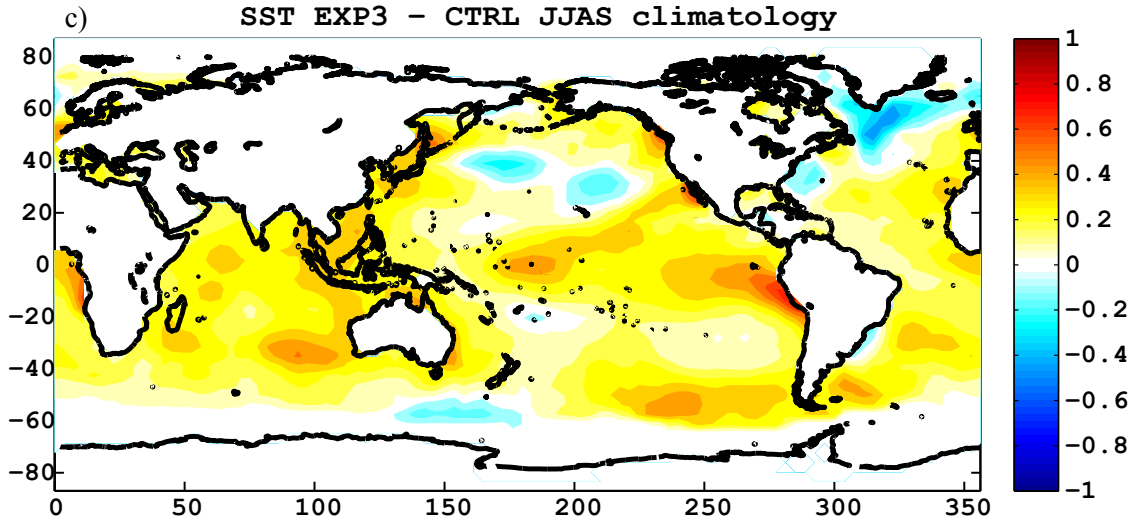

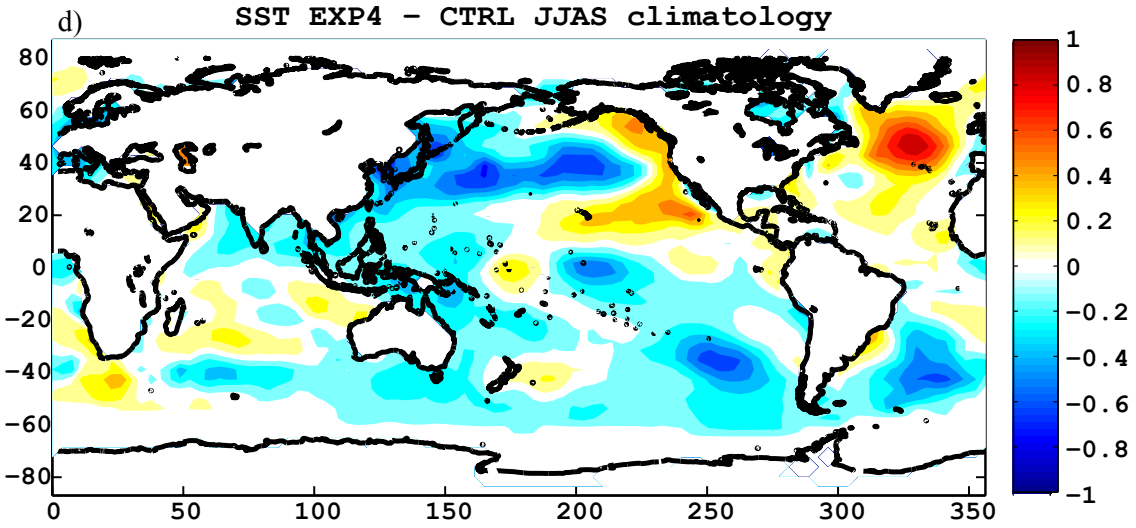

Figure 3.4 (continued)

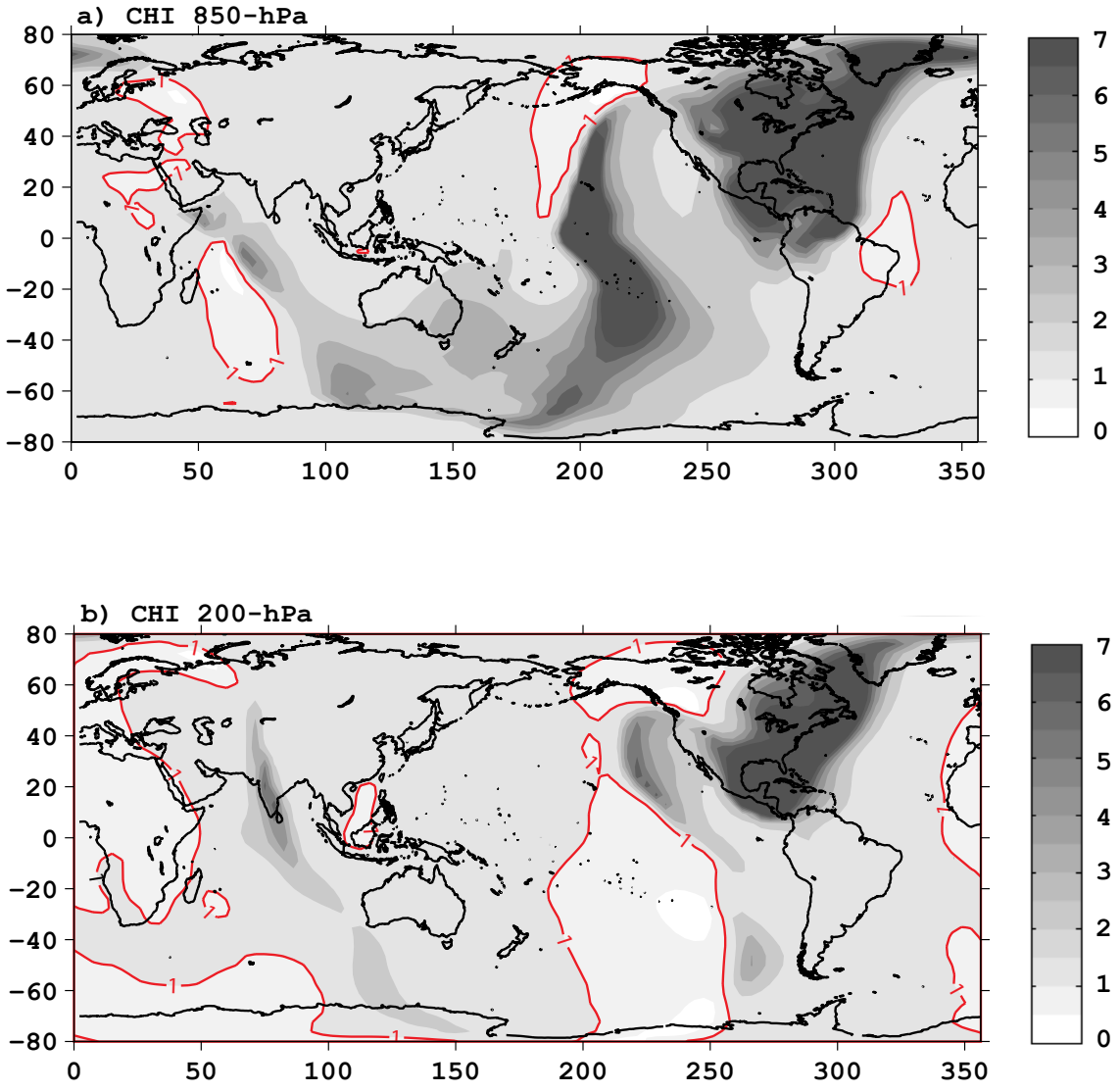

Figure 3.5: Ratio of the SST-forced variance to the internal variance for a) Velocity potential at 850-hPa. b) Velocity potential at 200-hPa. Red contours correspond to a ratio equal to 1.0.

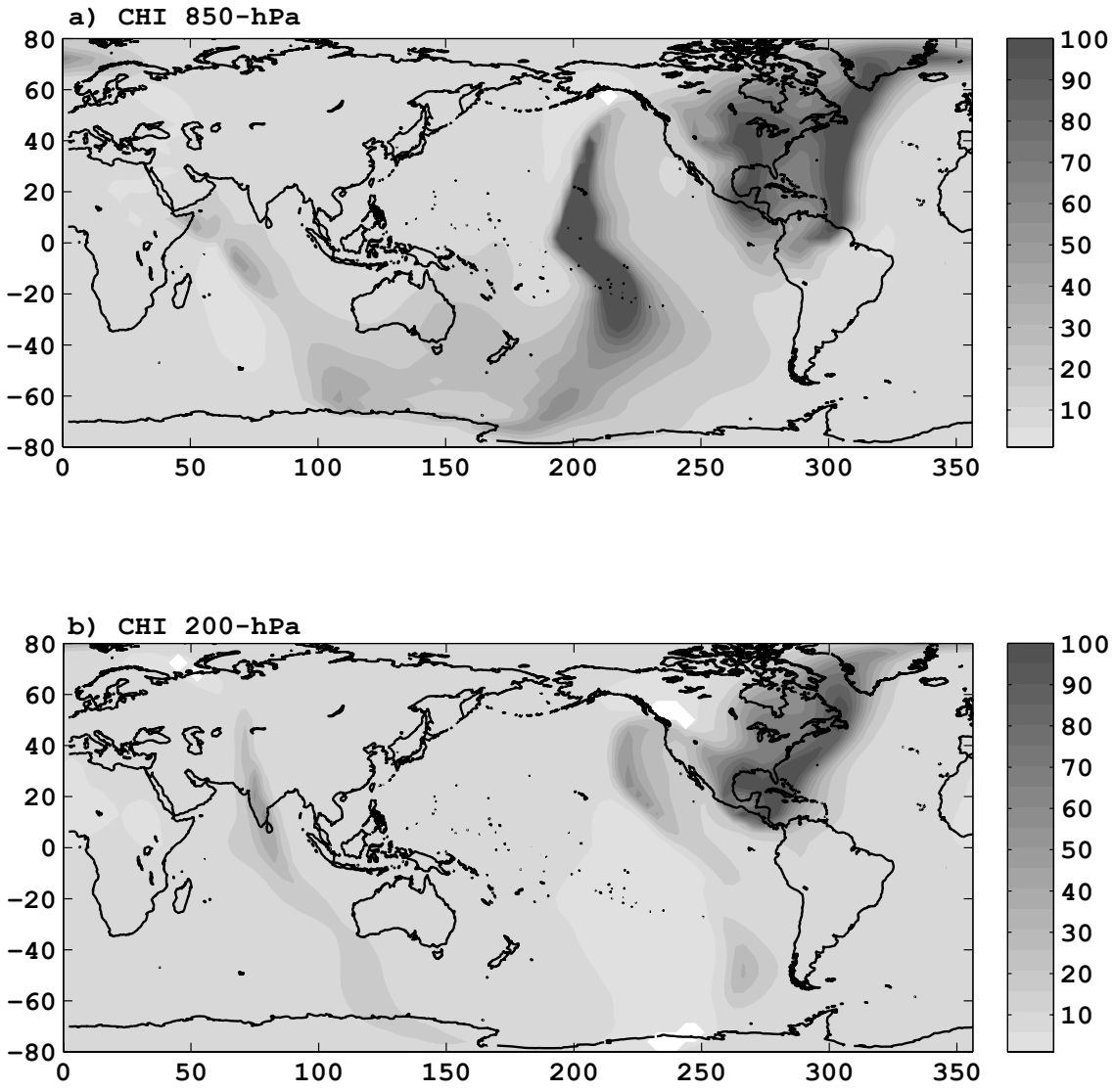

Figure 3.6: Corresponding F statistic for a) Velocity potential at 850-hPa. b) Velocity potential at 200-hPa. F = 3.83 corresponds to 99% statistical significance. Regions in white correspond to values less than 3.83.

CHAPTER IV

EVALUATION OF MONSOON RESPONSE TO SEA SURFACE TEMPERATURE CHANGES

The Asian monsoon is characterized by a seasonal reversal of winds and the associated wet and dry seasons caused by changes in the distribution of surface heating caused principally by land-sea contrasts. Numerous studies have described the mean state of the annual cycle of the monsoon (e.g. Krishnamurti 1985; Fein and Stephens 1987; Webster et al. 1998) discussing the role of land sea-differences exacerbated by the elevated Himalayan-Tibet Plateau mountain complex (Hahn and Manabe 1975; Kuo and Qian 1982; Yanai et al. 1992; Webster et al. 1998) that acts as an elevated heat source (Yanai et al. 1992). This elevated heat source acts as the main determiner of the differences between the weaker African and Australian summer monsoons where elevated heat sources do not exist. The boreal summer season of South Asia is of particular importance since low level southwesterly cross equatorial flow over the Indian Ocean, brings moisture over the continent generating large amounts of rain over India and southeast Asia.

The orographic features of the continents are fixed whereas the other component of land-sea temperature contrasts, the sea-surface temperature, is evolving on inter-annual and interdecadal time scales (Shukla and Paolino 1983; Clark et al. 2000, 2003). The distribution of SST is one of the dominant and variable factors impacting the Asian monsoon circulation (e.g. Clark et al. 2000, 2003; Chao and Chen 2001). Webster and Fasullo (2003) have shown that the amplitude of the monsoon annual cycle depends on the SST gradient over the Indian Ocean. However, not only regional SST influences the Asian summer monsoon. Remote Ocean SST anomalies over the

eastern Pacific and the Atlantic Ocean also modulate the monsoon circulation trough modifications in the Walker and transverse circulations (e.g. Soman and Slingo 1997; Slingo and Annamalai 2000; Kucharski et al. 2009).

4.1 Summer monsoon model climatology: Control runs

In the following paragraphs we describe the mean state of the monsoon averaged over the period June, July August, September (JJAS). The analysis is based on the climatology obtained from the control experiment (see Table 3.1). The mean monsoon is described in terms of zonal wind (U), meridional wind (V) and velocity potential (χ) at 200 and 850-hPa levels, the vertical velocity in pressure coordinates (ω=dp/dt) at 500-hPa level, out-going long-wave radiation (OLR) as a proxy for deep convection and precipitation.

4.1.1 Atmospheric circulation

The boreal summer SST and surface air temperature over land are plotted in Figure 4.1a. In general, tropical oceans and land regions are warmer than 20°C (∼293K). The primordial driving mechanisms of the monsoon, the differential heating of the land and ocean, is evident from the figure. Differential heating arises from differences in specific heat and effective heat capacity of ocean compared to the land. For the same values of insolation, the land heats quicker than the ocean as the only process of heat storage is that produced by conduction to greater depths. On the other hand, the ocean can store heat to great depths due to wind mixing. During summer, land surface heats rapidly leading to the development of thermal low pressure regions which serve to bring in air from the surrounding regions in a shallow circulation. However, due to the radiation to space from these hot land regions, the low pressure anomaly is shallow and the radiative cooling of the column is compensated by the adiabatic warming from large scale subsidence. However, if the converging air is moisture laden, convection may ensue with a wetting of the land surface. Even though this produces a

decrease in soil temperature, the moist land becomes a source of atmospheric moisture through evaporation (Webster 1983; Srinivasan et al. 1993). Land surface hydrological processes complicate the monsoon and lead to intraseasonal oscillations of monsoon systems (Webster 1983).

Boreal summer and winter differences in surface temperature (Figure 4.1b) show clearly the land-sea temperature contrasts and the relative small annual changes over the ocean. The largest variations occur over Asia and, to a slightly less extent, over North America, Africa and Australia. Differences between summer and winter temperatures can be seen to exceed 30°C.

There are a number of prominent features in the mean JJAS sea level pressure (Fig 4.1c). In the northern hemisphere summer subtropics, the oceans are dominated by areas of high pressure in both the Atlantic and Pacific. In the southern hemisphere, the band of high pressure extends across the subtropics. Low pressure exists over the northern continents extending across south Asia to North Africa. In conjunction with the southern hemisphere high pressure regimes, large cross-equatorial pressure gradients are produced. Of particular importance for this study is the pressure gradient between the Mascarene High, located in the south Indian Ocean and the low-pressure over South Asia.

The 850-hPa boreal summer zonal and meridional wind fields are shown in Figure 4.2a, b. Westerlies dominate the northern Indian Ocean, Bay of Bengal and the Arabian Sea while easterly winds are observed in the southern Indian Ocean, northern Australia, subtropical northern region around 40°N and the Equatorial Pacific Ocean. The meridional component (Fig 4.2b) shows northward winds along the eastern African coast, indicating a strong cross-equatorial flow. This cross-equatorial flow is one of the components of a low level jet known as the Somali or Findlater jet (Findlater 1969a,b; Krishnamurti and Bhalme 1976) constrained vertically and horizontally by the East African Highlands (Webster and Fasullo 2003). In the northern

hemisphere, the jet turns anticyclonically to become the monsoon westerlies (Figure 4.2a, 4.2b, and 4.3b) bringing moisture over the Arabian Sea and India.

Figure 4.3a shows a cross section of the meridional wind component averaged between 5°S and 5°N for the JJAS period. Peak cross-equatorial southerlies of 8 ms^{-1} occur at 45°E and 925-hPa. This peak is somewhat weaker ($\sim$27%) than the 11 ms^{-1} in the ERA-40 reanalysis. In the upper troposphere a northerly maximum is evident over the western Indian Ocean at 300-hPa, reaching values of 4 ms^{-1}. Northerlies are also evident over the eastern Indian Ocean and the western Pacific. The strength of the jet is evaluated using two indexes of jet intensity. Following Boos and Emanuel (2009), we defined the first index (SOM1) as the square root of the area mean wind speed at 850-hPa in the region 5°S - 20°N, 50°E - 70°E (this region is outlined in Figure 4.3b in red), which is the same spatial domain used by Krishnamurti et al. (1981). SOM1 describes the intensity of the southwesterly jet. In addition, we created a scalar index of cross–equatorial jet intensity (SOM2) by computing the area mean meridional wind at 925-hPa in the region 5°S - 5°N, 40°E - 60°E (this region is outlined in Figure 4.3b in green). For the control experiment SOM1 has a value of 3.7 ms^{-1} and SOM2 has a value of 2.9 ms^{-1} (see Table 4.1).

Figure 4.4a,b shows the upper tropospheric flow for the boreal summer. Strong westerlies extend around the winter hemisphere subtropics and middle latitudes while weaker westerlies with much more meridional variability prevail in the summer hemisphere. Easterlies blow over the northern Indian Ocean, Arabian Sea and Bay of Bengal. This band of strong easterlies is known as the Tropical Easterly jet, and extends from Southeast Asia to Africa and exists on the southern flank of the upper tropospheric Tibetan anticyclone. This jet has mean winds of about 10 – 20 ms^{-1}, with the strongest wind located to the south of the southern tip of India and is the thermal wind response to the reversed upper tropospheric temperature gradient. Webster and Yang (1992) showed that zonal winds are negatively correlated in the

Table 4.1: Circulation monsoon indices*

EXPERIMENT	SOM1		SOM2		WYI		MHI		WSI		CEPG	
	M	SD	M	SD	M	SD	M	SD	M	SD	M	SD
CTRL	3.7	0.05	2.9	0.02	17.7	0.18	2.8	0.03	17.3	0.24	12.6	0.09
COLD	3.6	0.07	2.4	0.04	17.1	0.2	2.6	0.04	16.2	0.29	12.2	0.09
MODERATE	3.4	0.06	3.3	0.06	17.9	0.29	2.7	0.05	17.6	0.27	12.9	0.11
WARM	3.9	0.06	2.9	0.04	18.0	0.17	2.6	0.05	17.3	0.23	12.5	0.09
BUMP	3.2	0.03	2.5	0.03	15.9	0.15	2.5	0.07	15.1	0.17	11.6	0.11

* For each experiment, M corresponds to the ensemble mean value of the index and SD to the standard deviation

vertical over South Asia and the Indian Ocean and used the magnitude of this shear as an indicator of monsoon strength. The meridional winds at the 200-hPa level are northerly winds over south East Asia and eastern Indian Ocean (Figure 4.4b and Figure 4.3a). Differences between the lower and the upper levels show positive values along the western Indian Ocean boundary and the eastern Indian Ocean, indicating a cross-equatorial circulation or a lateral monsoon circulation (Webster et al. 1998).

The divergent part of the flow is shown in the form of velocity potential in Figure 4.5. Low level convergence at 850-hPa (positive values in Figure 4.5a) is accompanied by upper level divergence at 200-hPa (negative values in Figure 4.5b). In the lower level, regions of convergence are located over Southeast Asia and the western Pacific and regions of divergence are located over the equatorial Atlantic, eastern Pacific and Africa. As expected, the reverse pattern is observed in the upper level. The distribution of velocity potential during boreal summer indicates the major monsoonal circulations referred as lateral monsoon, transverse monsoon and Walker circulation in Webster et al. (1998). Figure 4.6 displays a schematic of the major divergent circulation associated with the monsoon system.

One of the interesting features of Figure 4.5 is the location of the velocity potential maxima relative to the South Asian monsoon region. The climatological maxima are located over the western Pacific warm pool while the Indian region is located at the transition of positive and negative velocity potential. It would seem that small shifts in the location of the velocity potential extrema (e.g., associated with El Nino) could cause changes in the environment over the South Asian monsoon region perhaps changing the region from weak convergence to weak divergence.

The divergent circulations in the upper and lower troposphere shown in Figure 4.5 are coupled through fields of vertical circulations. The field of vertical motion (or ω) at 500-hPa is displayed in Figure 4.7. As vertical velocity depends on the gradients of velocity potential, the fields possess much more detail than the χ fields shown in Figure 4.5. Regions of upward motion (negative values) exist over Africa, Central America and Asia. Areas of rising motion over the south Asian region are located in the Bay of Bengal, southeast Asia, the equatorial Indian Ocean and western equatorial Pacific. Regions of subsidence or downward motion (positive values of ω) are found over the Southern Indian Ocean and North and South of the equator in the eastern Pacific Ocean and eastern Atlantic Ocean.

A three dimensional and more complete view of the mean monsoon circulation can be achieved through a detailed description of the divergent circulations shown in Figure 4.6. The lateral monsoon or the regional Hadley cell has been described in previous works (Das 1986; Fein and Stephens 1987; Webster et al. 1998; Trenberth et al. 2000). This cross-equatorial cell is a thermally driven cell, with rising motion in the summer hemisphere, around 10°N, and descending motion over the subtropical Indian Ocean. The transverse monsoon circulation is an east-west cell that flows between the arid North African regions and the tropical Asian region. This east-west circulation is maintained by the large differences in radiative and latent heating between North Africa and South Asia (Yang et al. 1992; Webster et al. 1998). The

Walker circulation is an east-west cell that extends across the Pacific Ocean (Krishnamurti 1971a,b). This cell, also thermally driven, has received a great deal of attention due to its association with interannual variability of the coupled ocean-atmosphere system and especially with the phenomenon of El Niño-Southern Oscillation (ENSO) (e.g. Bjerknes 1969; Philander 1990; Webster and Chang 1988). During the summer season the ascending regions of the three circulations, the Walker circulation and the lateral and transverse monsoon described above, are collocated over southeast Asia and the Indo-Pacific equatorial warm pool. Figure 4.6 suggests that the influences on the South Asian monsoon circulation are widespread and may exist on very large scales.

The divergent part of the wind and the vertical motion fields can be used to identify the circulation cells associated with the summer monsoon. Figure 4.8a shows the transverse cell, estimated by averaging the divergent wind and vertical velocity between 5.5° and 16°N across the longitudinal section from 0°E to 115°E. The air ascends over Southeast Asia (near 100°E), flows westward in the upper troposphere, descends over Arabian Sea, and moves toward the east in the lower troposphere. Zonal–vertical cross sections of divergent zonal wind and vertical motion associated with this cell are shown in Figure 4.8b. Ascending air is also observed over Africa (Figure 4.8c; note that in Figures 4.8c -10c the vertical velocity is taken as the negative of the pressure vertical velocity in the model) and is associated with the convective activity that occurs in this region (Fig 4.7; Fig 4.11). Model simulations show that subsidence over Africa takes place between 20°E and 0°. The descending air over East Africa is the subsident part of the transverse circulation shown schematically in Figure 4.6.

Figure 4.9 shows longitudinal cross-sections of the Walker circulation along the equator. Here, the divergent zonal wind and the vertical velocity are averaged between 5.5°S and 5.5°N in the longitudinal section from 100°E and 360°E. Panel a) shows

ascending air in the West Pacific – East Asian region between 100°E and 150°E in the vicinity of the warm pool and descending air in the eastern Pacific near 260°E. Air flows westward in the lower troposphere and flows eastward in the upper troposphere (Figure 4.9a and Figure 4.9b). Additional ascending motion is observed around 280°E (Figure 4.9c) and is part of another Walker type circulation in the Americas-Atlantic sector (Trenberth et al. 2000).

The lateral monsoon or local Hadley circulation is obtained by averaging the divergent meridional wind and the vertical velocity between longitudes 80° - 110°E. Based on the velocity potential patterns (Figure 4.5) and the vertical velocity distribution at 500-hPa (Figure 4.7a) it is clear that the meridional circulation in the eastern Indian Ocean and southeast Asia is different from that in the western Indian Ocean and East Africa. To differentiate between these two circulations, a meridional circulation was plotted in the east (80°E - 115°E) and another was plotted in the west (45°E - 75°E). Over the eastern Indian Ocean (Figure 4.10a), air rises in the northern hemisphere from 0° to 25°N and descends in the southern hemisphere (Figure 4.10c). The meridional component flows northward in the lower troposphere and southward in the upper troposphere (Figure 4.10b). The western meridional cell is not as strong as its eastern counterpart. Ascending air is observed between 10°S and 0° and descending air is observed in the northern hemisphere around 22°N and in the southern hemisphere around 20°S (Figure 4.10d). Rising motion close to the equator is associated with the convective activity over the equatorial Indian Ocean (Figure 4.7a and 4.10f). The zonal divergent wind section (Figure 4.10e) shows southerly wind in the lower troposphere and northerly wind in the upper levels.

The overturning circulations just described, constitute a great proportion of the lower tropospheric mass flux. Table 4.2 enumerates the mass fluxes associated with each of the circulations. The mass flux was calculated by vertically integrating the

Table 4.2: Mass fluxes associated with the divergent circulations*

Mass Flux Gkg s^{-1}	TM		WC		LM (E)		LM (W)	
	M	SD	M	SD	M	SD	M	SD
CTRL	7.6	0.10	5.4	0.05	6.2	0.10	3.8	0.09
COLD	7.3	0.14	5.5	0.09	6.3	0.11	3.3	0.05
MODERATE	7.2	0.16	4.5	0.07	5.4	0.09	4.7	0.14
WARM	7.9	0.14	5.5	0.09	5.7	0.06	3.6	0.13
BUMP	6.6	0.14	6.4	0.10	4.8	0.06	3.0	0.09

* For each experiment, M corresponds to the ensemble mean value of the mass flux and SD to the standard deviation

divergent wind in a layer from the lower model level to 500-hPa, and across a 1000-km sector through the center of the circulation in question (TM: transverse monsoon; WC: Walker circulation; LM(E): lateral monsoon or local Hadley circulation over the eastern Indian Ocean; LM(W): lateral monsoon or local Hadley circulation over the western Indian Ocean). These values will be used to compare the changes in the strength of the monsoon during periods of different background SST.

A positive mass flux in TM means that mass is being transported from west to east into the region of ascending motion over southeast Asia ($\sim$100°E). Similarly, a positive mass flux in WC means that mass is being transported from east (East Pacific) to west into the western Pacific Ocean and Southeast Asia. A positive mass flux in LM(E) is associated with a transport of mass from the southern Indian Ocean into Bay of Bengal and southeast Asia. A positive LM(W) means that mass is being transported over the western Indian Ocean from the southern region into the northern Indian Ocean. Figure 4.6 indicates the direction of the circulations used to estimate

TM, WC and LM(E).

4.1.2 Precipitation and OLR

OLR and precipitation fields from the control integration are plotted in Figure 4.11. OLR values <240 Wm^{-2} are used to indicate regions of deep convection (Richards and Arkin 1981). The equatorial Indian Ocean, the western equatorial Pacific Ocean, Central and South America and Central Africa are major regions of convection. The precipitation field is consistent with OLR field, showing large precipitation rates in these regions (see Fig 4.11 panel b). A high degree of correspondence can be seen between OLR, precipitation fields and the omega 500-hPa field.

A regional map of precipitation and sea level pressure (Figure 4.12) in the South Asian monsoon region reveals that organized convection is not collocated with the sea level pressure minima. Tomas and Webster (1997) showed that in regions where there is a strong cross-equatorial pressure gradient, convection occurs in the equatorward side of the sea level pressure minima. This is also the case of the Asian summer monsoon and also the Australian and African monsoons. In general, in regions of strong cross-equatorial pressure gradient, the location of convection is determined by inertial-instability processes. However, in south Asia, convection also occurs in latitudes near the monsoon trough. These collocations are due to the strong intraseasonal variability associated with monsoon active and break periods as convection forms near the equator and moves slowly northward over South Asia. This migration results in two major maxima: one near the equator and the second across South Asia and the Bay of Bengal.

4.2 Response of the South Asian monsoon to large scale sea surface temperature variability

Continued research has shown that the monsoon system is influenced by local and remote variations of SST and that there is long-term variability in the annual precipitation. However, it is still unclear how SST variability modulates the monsoon circulation perhaps because of some of the complexities described in the last section. In this work, the experimental set-up is kept as simple as possible to isolate changes in the monsoon circulation due to SST variability. For this reason, only variations in SST are considered.

The following results describe the response of the mean state of the South Asian summer monsoon circulation to different configurations of SST. In this section, differences between each of the experiments listed in Table 3.1 (see also Figure 3.3) and the control experiment (CTRL) are described. Statistical significance of the differences was evaluated using a t-test. In the figures presented below, shading indicates regions that are significant at a 95% level.

4.2.1 Circulation and precipitation differences for Experiment 1 ("COLD" 1925-1935)

In the following paragraphs, differences between Experiment 1 (hereafter COLD) and CTRL are described. In this experiment the model is forced by monthly SST averaged from 1925 to 1935 (see Table 3.1 and Figure 3.3).

4.2.1.1 Circulation patterns

Figure 4.13a presents seasonal mean surface temperature differences fields for JJAS. In general, negative anomalies occur in the tropical oceans and tropical land areas. In the tropical band, negative anomalies as large as -0.4°C are observed across the northern Indian Ocean and around northern Australia. Even greater anomalies are noted in the austral winter extratropics. Only in the North Atlantic were there

conditions during COLD, warmer than the long term mean.

The sea level pressure differences (COLD – CTRL) associated with these temperature differences are displayed in Figure 4.13b. Positive pressure anomalies of about 0.4 hPa extend over the northern Indian Ocean and the Indian subcontinent. Slight positive anomalies are also present over the Mascarene high region but lower by 1-1.5 hPa further to the south. Since the increase in SLP is larger over the northern Indian Ocean, the pressure gradient between these two regions decreases suggesting a possible decline in the cross-equatorial wind intensity. Table 4.1 shows the cross-equatorial pressure gradient (CEPG) measured along 60°E between 20°S and 20°N for all the experiments. Indeed, the CEPG decreases from 12.5 hPa in CTRL to 12.2 hPa in COLD.

Figure 4.14a shows the differences in the 850-hPa zonal winds between COLD and CTRL. Negative anomalies are evident in the northwestern Indian Ocean and extend into the southern Indian peninsula, suggesting that zonal winds are weaker than in CTRL. Maximum negative anomalies in the area reach values of 0.6 ms^{-1}. South from this region of negative anomalies, a region of positive anomalies is observed, implying a change in the direction of the Somali jet. Positive anomalies are also found in southeast Asia (0.6 – 0.8 ms^{-1}), indicating that westerlies are stronger than in CTRL. At the 200-hPa level (Fig 4.14b), differences in zonal wind show a region of positive anomalies over the western Indian Ocean, extending into the southern India and Bay of Bengal, suggesting a weakening of the Tropical Easter Jet. Anomalies reach values of 1.5 m s^{-1} off the Somali coast.

Table 4.1 also shows three additional monsoon circulation indices (WYI, MHI, WSI) for all the experiments. These indices will be used to provide a simple characterization of the state of the monsoon and to compare the changes in the strength of the monsoon circulation between experiments. For the COLD case, Table 4.1 shows that the mean Webster and Yang index (WYI; Webster and Yang 1992) and the

mean westerly shear index (WSI; Wang and Fan 1999) are both smaller compared to the CTRL values, suggesting a weakening of zonal vertical shear and of the monsoon circulation (Appendix A shows the definition of the monsoon related indices).

Figure 4.15 shows differences in meridional wind between COLD and CTRL. At the 850-hPa level, negative differences (~ 0.4 m s^{-1}) are found in the western Indian Ocean along the African coast and in Bay of Bengal. Negative differences along the Somali coast indicate a weakening of the Somali jet. At the 200-hPa level positive anomalies are observed in the central Indian Ocean and over Bay of Bengal. Anomalous southerly wind reaches maximum values of 0.4 m s^{-1}. The weaker meridional wind anomalies pattern is consistent with a diminished cross-equatorial flow and a weaker lateral circulation. Table 4.1 shows a decrease in the mean monsoon lateral circulation index (MHI, Goswami et al. 1999) from 2.8 m s^{-1} in CTRL to 2.6 m s^{-1} in COLD, further confirming a weakening of the local Hadley circulation.

Figure 4.16 shows a longitude-height section along the equator of the differences in the meridional flow between the COLD and control. The cross-equatorial Somali jet is about 10-15% weaker than its long-term climatological value with negative lower tropospheric anomalies along the eastern African coast from 40°E to 80°E. In the upper troposphere, positive anomalies are found between 400-hPa and 200-hPa over the central Indian Ocean and over eastern Africa. Anomalies over the central Indian Ocean reach values of 0.6 m s^{-1}. In the COLD case, SOM1 has a value of 3.6 ms^{-1} (2.7% less than CTRL), suggesting a decrease in intensity of the southwesterly jet. SOM2 has a value of 2.4 ms^{-1} (7.4% less than CTRL), confirming the decline in the cross-equatorial flow over the western Indian Ocean (see Table 4.1).

The differences in the velocity potential at 850 and 200-hPa between COLD and CTRL experiments are plotted in Figure 4.17. The magnitude of the differences is about 10% of the control experiment (see Figure 4.5). At the 850-hPa level, negative differences over the South Asian monsoon region and positive differences over the

equatorial eastern Pacific Ocean suggest that large scale monsoonal circulations are weaker than in the CTRL. Velocity potential anomalies at the 200-hPa level depict positive differences over South Asia (increased upper level convergence) and negative anomalies over the Atlantic Ocean and Africa, which are consistent with the anomalies observed in the lower level, and indicate a weakening of the large scale circulation. Overall, the impact of the changes in SST is to cause a large scale shift of divergence and convergence along the equator.

Figure 4.18 displays omega differences between COLD and CTRL at 500-hPa. The figure shows weaker upward motion over the Indian Peninsula, western-central equatorial Indian Ocean and Bay of Bengal. However, stronger upward motion is found over southeast Asia and the western Pacific Ocean consistent with a shift of the large scale circulation cells evident in Figure 4.17. These features are consistent with a weaker South Asian monsoon.

The anomalous transverse circulation (COLD-CTRL) is plotted in Figure 4.19a. Anomalous downward motion is found over India (80°E) and over the Arabian Sea (60°E) again consistent with a weaker monsoon. On the other hand, anomalous upward motion is found over southeast Asia (110°E) consistent with an eastward shift of the circulation cells. To illustrate the magnitude of the differences in the transverse circulation with CTRL, longitude-height cross sections of the zonal divergent wind and the vertical motion are displayed in Figure 4.19b and Figure 4.19c (note that in Figures 4.19c -22c the vertical velocity is taken the negative of the pressure vertical velocity in the model). In the vertical velocity section, negative anomalies, reaching a maximum value of 0.01 Pas^{-1}, are found at 80°E. Negative anomalies ($\sim$0.007 Pas^{-1}) are also observed at 60°E. Positive anomalies ($\sim$0.009 Pas^{-1}) are found over Southeast Asia (110°E). The zonal divergent wind section displays positive anomalies in the upper troposphere, confirming the weakening of the easterly jet again consistent with a weaker monsoon. Zonal wind anomalies in the upper troposphere reach values

of 0.5 ms^{-1} in the upper troposphere.

Figure 4.20a shows the anomalous Walker circulation (COLD – CTRL) in a section along the equator. Anomalous downward motion is evident over the eastern Asia – western Pacific region (100°E - 150°E) while upward motion is found over the eastern Pacific (∼270°E). The ascending branch of the Walker type circulation over the Americas–Atlantic sector appears to be strengthening, since anomalous upward motion exists over the Americas. The vertical velocity section (Figure 4.20c) shows negative anomalies, reaching values of 0.006 Pas^{-1}, between 110°E and 140°E. Slightly positive anomalies (0.003 Pas^{-1}) are evident at 270°E. Positive anomalies (0.006 Pas^{-1}) are also found over the Americas. Zonal wind cross section (Figure 4.20b) suggests a weakening of the upper westerlies, showing negative anomalies reaching values of 0.2 ms^{-1}. These changes between the CTRL and COLD are consistent with an eastward shift of the Walker Circulation and subsidence over the equatorial eastern Indian Ocean.

Figure 4.21a depicts a meridional section of the anomalous local Hadley circulation over the eastern Indian Ocean. Anomalous downward motion is evident over the northern Bay of Bengal. Negative vertical velocity anomalies over this region reach 0.003 Pas^{-1} (Figure 4.21c). Anomalous downward motion is also observed in the southern hemisphere. In this region of subsidence, vertical anomalies reach values of 0.002 Pas^{-1}. In the cross section of the meridional divergent wind the main features are the upper troposphere negative anomalies (∼0.1 ms^{-1}) in the northern hemisphere and the upper troposphere positive anomalies (∼0.1 ms^{-1}) in the southern hemisphere (Figure 4.21b). This pattern of anomalies suggests a weakening of the northern portion of the ascending branch of the meridional circulation over the northern hemisphere, again consistent with an anomalous weakening of the monsoon.

The anomalous local Hadley circulation over the western Indian Ocean (Figure 4.22a) displays anomalous upward motion at 8°S and anomalous downward motion

at 2°N. In the vertical velocity cross section (Figure 4.22c), negative anomalies (associated with anomalous downward motion) reach values of 0.012 Pas^{-1} and positive anomalies (associated with anomalous upward motion) reach values of 0.01 Pas^{-1}. Meridional divergent wind anomalies are negative in the lower troposphere from 5°S to 15°N and positive between 0° and 20°S in the upper troposphere (Figure 4.22b).

Mass fluxes associated with each one of the circulations described above are listed in Table 4.2. Larger differences with CTRL are observed for the transverse monsoon and the western Indian Ocean local Hadley circulation. The mass flux associated with TM is 4% weaker than in CTRL, again consistent with a weakening of the monsoon circulation. Moreover, the mass flux associated with LM(W) is also weaker in COLD than in CTRL (15% less), which is consistent with a reduction in the cross-equatorial flow.

4.2.1.2 Precipitation patterns

Figure 4.23 shows differences in OLR (Fig 4.23a) and precipitation (Fig 4.23b) between COLD and CTRL. Whereas the patterns of change are complicated, there is a large decrease in regional precipitation over the Indian sector. Larger differences exist over Bay of Bengal, Indian Subcontinent, southeast Asia and Indonesia. Positive differences in OLR, consistent with decreases in precipitation are evident over the Indian Peninsula, Bay of Bengal and Indonesia. One the other hand, precipitation has increased over southeast Asia consistent with an eastward shift of the circulation patterns. These anomalies are consistent with the observed long interdecadal changes in AIMR (Figure 2.2).

4.2.2 Circulation and precipitation differences for Experiment 2 ("MODERATE" 1950-1960)

In this section, differences between Experiment 2 (hereafter MODERATE) and CTRL are described. In this experiment the model is forced by monthly SST averaged from

1950 to 1960 (refer to Table 3.1 and Figure 3.3).

4.2.2.1 Circulation patterns

Surface JJAS temperature differences for JJAS are shown in Figure 4.24a. Slight negative anomalies of about -0.2°C are observed in the tropical oceans and tropical land areas. Largest negative anomalies are found in the central Indian Ocean and they reach a maximum value of 0.6°C east from Madagascar. The southern oceans are anomalously warmer but it is difficult to determine the fidelity of these anomalies as data during the 1950 - 60 period was still relatively scarce.

Figure 4.24b shows sea level pressure differences for MODERATE. Positive pressure anomalies develop over the western-central Indian Ocean, with maximum values approaching 0.5 hPa east from Madagascar. A slight increase in SLP is observed over the Indian peninsula. However, since the increase in pressure is higher over the south-western Indian Ocean, the pressure gradient between India and the southern ocean increases. This is further confirmed by the CEPG index, which shows an increase from 12.5 hPa in CTRL to 12.9 hPa in MODERATE (see Table 3.1). There are substantial differences between the anomalous surface temperature and pressure fields between COLD and MODERATE. Whereas COLD showed an almost universally lower surface temperature, MODERATE finds increases in surface temperature across the northern subtropics and a corresponding decrease in surface pressure. In the monsoon region, surface temperatures are lower in most of the Indian Ocean together with generally higher surface pressures.

Plots of the differences of the zonal wind between MODERATE and CTRL in the lower and upper troposphere are shown in Figure 4.25. At the 850-hPa level, negative anomalies are evident over western-central equatorial Indian Ocean and Bay of Bengal, indicating that westerlies in MODERATE are weaker than in CTRL by >1 ms^{-1}. Positive anomalies >1 ms^{-1} are found over the central equatorial Pacific

Ocean indicating a slowing of the Walker Circulation associated with the slightly lower surface pressure in the eastern Pacific Ocean. At 200-hPa (Fig 4.25b), positive anomalies extend over central equatorial/southern Indian Ocean, approaching values of 1 ms^{-1}, meaning that easterlies are weaker than in CTRL. Easterly anomalies over Bay of Bengal and Southeast Asia of about 1 ms^{-1}, suggest that easterly winds are stronger in MODERATE over this region. Easterly anomalies are also found over the tropical Pacific Ocean. Both zonal shear indexes, (WYI and WSI; see Table 4.1), show a slight increase compared with the CTRL experiment. This increase is consistent with easterly wind intensification over the Bay of Bengal and India in the upper level.

Figure 4.26 shows differences in meridional wind between MODERATE and CTRL. At the 850-hPa level negative anomalies ($\sim$ -0.4 ms^{-1}) are found in the western Indian Ocean along the Tanzania-Kenya coast. North of the Equator positive anomalies approaching 0.4 ms^{-1} are observed near 60°E, 10°N. Slightly negative differences ($\sim$ 0.2 ms^{-1}) are also found over Bay of Bengal. At the 200 h-Pa level slightly positive anomalies ($\sim$ 0.2 ms^{-1}) exist over Bay of Bengal and the eastern Indian Ocean. The weaker meridional wind anomaly pattern over the eastern Indian Ocean is consistent with a weaker lateral circulation. This result is further confirmed by the MHI (see Table 4.1), which shows a decrease from 2.8 ms^{-1} in CTRL to 2.7 ms^{-1} in MODERATE.

The longitude-height section along the equator of the differences in the meridional wind is plotted in Figure 4.27. In the lower levels, southerly anomalies, approaching 0.4 ms^{-1} are found from 50°E to 80°E and northerly anomalies ($\sim$ 0.2 ms^{-1}) are found near 40°E, suggesting that the cross-equatorial flow weakens right off the coast and intensifies further east. In the upper troposphere, northerly anomalies (reaching values of -0.5 m s^{-1}) prevail over the central Indian Ocean and southerly anomalies (reaching values of 0.5 m s^{-1}) exist over the Eastern Indian Ocean. In MODERATE, SOM1 has a value of 3.4 ms^{-1} (8.1% less than in CTRL), accounting for the decrease

in westerly intensity north of the equator. SOM2 has a value of 3.3 ms^{-1} (14% more than in CTRL), accounting for the increase in southerly winds north of the Equator (see Table 4.1).

Figure 4.28 displays differences in velocity potential between MODERATE and CTRL. The difference fields parallel those found between COLD and the CTRL although somewhat stronger. At the lower level, negative differences over south Asia and the west Pacific, and positive differences over the eastern Pacific and the American continent indicate a weakening in convergence and divergence regions, which implies that the large scale circulation is weaker than in CTRL. This result is supported by the differences pattern at the 200-hPa level. Upper level differences display positive anomalies (anomalous convergence) over the region where CTRL shows divergence and negative differences (anomalous divergence) over the region where CTRL shows convergence. In general, the SST distribution in MODERATE causes a larger impact on the large scale divergence and convergence than in the COLD case. The anomalies in Figure 4.28 are consistent with a weakening of the monsoon circulation. It will be shown that a larger impact is also observed in the Walker Circulation and in the lateral circulation over the eastern Indian Ocean.

Figure 4.29 plots the differences in upward motion between MODERATE and CTRL. Positive anomalies, associated with weaker vertical motion than in CTRL, exist over Bay of Bengal and central equatorial Indian Ocean. Negative anomalies, associated with stronger vertical motion than in CTRL, are evident over Indonesia. These will be shown to be consistent with precipitation patterns in Figure 4.34b.

The anomalous transverse circulation (MODERATE- CTRL) is presented in Figure 4.30. Anomalous downward motion is observed around 80°E. A slightly anomalous upward motion is found over the western Indian Ocean (60°E). A detailed distribution of the anomalies in vertical motion and zonal divergent wind associated with

the transverse circulation is displayed in Figure 4.30b and Figure 4.30c . The vertical velocity section shows negative anomalies, reaching a maximum value of 0.012 Pas^{-1}, between 80°E to 100°E. Slight positive velocity anomalies reaching values of 0.003 Pas^{-1} are found at 60°E. Zonal divergent wind anomalies over the central Indian Ocean show westerly anomalies ($\sim$0.4 ms^{-1}) in the upper levels and easterly anomalies ($\sim$ 0.15 ms^{-1}) in the lower levels. These changes between the CTRL and MODERATE are consistent with a weakening of the transverse circulation.

Figure 4.31 displays the anomalous Walker circulation. Anomalous downward motion is found over the western–central Pacific (150°E - 200°E) and over the Americas (300°E). Anomalous upward motion is found over the eastern Indian Ocean and over the eastern Pacific. The vertical velocity cross section (Fig 4.31c) indicates that negative anomalies (associated with anomalous downward motion) between 150°E and 200°E reach values of 0.01 Pas^{-1}. Negative vertical velocity anomalies over the Americas are weaker than over the western Pacific, approaching 0.004 Pas^{-1}. Weak positive anomalies over the eastern Indian Ocean reach 0.004 Pas^{-1}. The zonal divergent cross section (Fig. 4.31b) shows negative anomalies (0.3 ms^{-1}) in the upper troposphere, which is consistent with a decrease in upper level divergent westerlies. A weakening of the low level easterlies is also evident in the central Pacific, with positive anomalies reaching 0.2 ms^{-1}. This pattern of anomalies is consistent with a weakening of the Walker circulation and in particular with a weakening of the ascending branch over the western Pacific.

The anomalous local Hadley circulation over the eastern Indian Ocean is plotted in Figure 4.32. Anomalous downward motion over the Bay of Bengal (10°N - 20°N) reach values of 0.007 Pas^{-1} (Fig. 4.32c). In the upper trosposphere, the meridional divergent cross section (Fig. 4.32b) shows positive anomalies ($\sim$ 0.2 ms^{-1}), indicating a weakening of the upper northerly divergent winds between 10°N and 0°. The meridional wind section also shows a decrease in the lower level southerlies over this

same region. An anomalous upward motion is observed south of the equator (10°S - 0°), indicating that this portion of the ascending branch intensifies. Positive vertical velocity anomalies reach values of 0.007 Pas^{-1} over this region. This pattern of anomalies suggests a weakening of the ascending branch of the meridional circulation over the Bay of Bengal, again consistent with a weaker monsoon.

Figure 4.33 shows the anomalous local Hadley circulation over the western Indian Ocean. The largest anomalies are found between 10°S and the equator, a region of ascending motion in CTRL. Anomalous downward motion exists around 10°S, reaching values of 0.01 Pas^{-1}. Around the equator, positive vertical velocities (Fig 4.33c) have values of 0.008 Pas^{-1}. The meridional divergent wind cross section shows a weakening of the southerly winds in the lower troposphere and the northerly winds in the upper levels south of 10°S. North of 10°S the reverse situation is observed. This pattern of anomalies suggests decay in the southern portion of the ascending branch of the circulation, which could result in decreased convective activity over the western-central equatorial Indian Ocean.

Mass fluxes associated with each one of the circulations described above are listed in Table 4.2. For this experiment, all the circulations exhibit a decrease in the mass transport compared with the CTRL, but the western Hadley circulation. Larger differences with CTRL are observed for the Walker circulation and the lateral circulation over the eastern Indian Ocean. These results are consistent with a weakening of the ascending branch over Bay of Bengal and the western Pacific Ocean. Overall, the monsoon circulation is weaker in MODERATE than in CTRL.

4.2.2.2 Precipitation patterns

Precipitation and OLR differences between MODERATE and CTRL are displayed in Figure 4.34. Positive anomalies in OLR, consistent with decreases in precipitation are seen over Bay of Bengal and the central equatorial Indian Ocean. Negative differences

in OLR, consistent with increases in precipitation are evident over Indonesia. This anomaly pattern further confirms the weakening of the monsoon circulation and in particular, the decline in the ascending branch over southeast Asia and Bay of Bengal.

4.2.3 Circulation and precipitation differences for Experiment 3 ("WARM" 1990 -2000)

In this section, differences between Experiment 3 (hereafter WARM) and CTRL are described. In this experiment the model is forced by monthly SST averaged from 1990 to 2000 (see Table 3.1 and Figure 3.3).

4.2.3.1 Circulation patterns

Summer SST differences are displayed in Figure 4.35a. With the exception of the North Pacific the surface temperatures are almost universally warmer. Small positive anomalies of about 0.2°C are found in the tropical oceans and tropical land areas. The largest positive anomalies are located in the eastern Pacific and eastern Atlantic oceans, reaching values of 0.6°C. This warmer world is consistent with a reduced surface pressure throughout the tropics and subtropics except in the western sectors of the North and South Pacific. Negative pressure differences of about 0.2 hPa extend over the eastern Indian Ocean and Bay of Bengal. Slightly negative pressure anomalies are observed over the central equatorial Pacific Ocean and the western Indian Ocean. The CEPG index has the same value than in CTRL (12.5 hPa; see Table 4.1) suggesting no intensification or decline in the cross-equatorial flow.

Figure 4.36 shows differences in the zonal wind between WARM and CTRL. At the 850-hPa level, positive anomalies over the equatorial Indian Ocean and southeast Asia indicate that westerly winds are stronger than in CTRL. Maximum westerly anomalies reach values of 0.8 ms^{-1} over Indonesia. Positive anomalies ($\sim$0.6 ms^{-1}) are also found in the western equatorial Pacific Ocean. At the 200-hPa level (Fig. 4.36b), easterly anomalies exist over the central equatorial Indian Ocean, implying

strengthening of easterlies over this region compared with the CTRL case. Negative anomalies reach values of 0.5 ms^{-1}. Easterly anomalies area also found over the central equatorial Pacific Ocean, approaching 1 ms^{-1}. The WYI shear index is larger than in CTRL (see Table 4.1), which is consistent with intensification of westerlies in the lower troposphere and of the easterlies in the upper atmosphere south of 10°N. The WSI index is the same as in CTRL, also consistent with the small magnitude of the zonal wind anomalies north of 10°N.

Differences in meridional wind between WARM and CTRL are plotted in Figure 4.37. At the 850-hPa level, negative differences ($\sim$0.2 ms^{-1}) over western Bay of Bengal indicate that southerly winds are weaker in WARM than in CTRL over this region. Southerly anomalies ($\sim$0.2 ms^{-1}) are evident over the South China Sea. At the 200-hPa level, no significant differences are evident over Bay of Bengal. A region of negative anomalies, reaching values of 0.4 ms^{-1}, exists over the south–western Indian Ocean. The MHI index is smaller than in CTRL (see Table 4.1), accounting for the reduction in low-level southerly winds over Bay of Bengal.

Figure 4.38 shows the longitude-height section of the cross-equatorial anomalous meridional flow (WARM - CTRL). The magnitude of the cross equatorial Somali jet is very similar in both experiments. In fact, SOM2 has a value of 2.9 ms^{-1}(same value as in CTRL, see Table 4.1), confirming that the cross-equatorial flow in the western Indian Ocean show no significant changes in WARM. In the upper troposphere, negative anomalies, reaching values of 0.2 ms^{-1}, are evident over the eastern Indian Ocean. In WARM, SOM1 has a value of 3.9 ms^{-1} (5.4% more than CTRL), consistent with westerlies intensification over the northern Indian Ocean.

Figure 4.39 shows differences in velocity potential between WARM and CTRL. At the 850-hPa level positive differences (anomalous convergence) exist over southeast Asia and the western Pacific Ocean and negative differences (anomalous divergence) exist over the Atlantic Ocean and South America. This anomaly pattern is opposite

to the patterns observed in COLD and MODERATE, and suggests that both convergence and divergence is enhanced at the lower level, implying that the large scale circulation is stronger than in CTRL. Anomalies leveling the upper troposphere confirm this behavior. At the 200-hPa level negative anomalies are observed in regions of mean divergence (South Asia) and positive anomalies exist over regions of mean convergence (Atlantic Ocean). Overall, the impact of the changes in SST is to cause a strengthening of the large scale circulation and a shift in the centers of convergence and divergence.

Differences in omega at 500-hPa are plotted in Figure 4.40. Slightly negative anomalies exist over the eastern Bay of Bengal and southeast Asia, meaning that upward motion over this region is stronger than in CTRL. Negative differences are also observed over the western-central equatorial Pacific Ocean. Stronger upward motion in a region of anomalous convergence implies an intensification of the ascending branch of the divergent circulations over southeast Asia.

Transverse circulation differences (WARM - CTRL) are displayed in Figure 4.41. Anomalous upward motion is found over eastern Bay of Bengal and southeast Asia (90°E - 100°E). Anomalous downward motion is found over Africa, India and the western Indian Ocean. Differences in zonal divergent wind and vertical velocity (Fig. 4.41b and Fig 4.41c) show in more detail the anomalous circulation. Vertical velocity differences show positive anomalies (associated with upward motion) around 100°E, approaching values of 0.006 Pas^{-1}. Between 20°E and 60°E, negative anomalies reach values of 0.002 Pas^{-1}. Zonal divergent wind differences show negative anomalies reaching values of 0.3 ms^{-1} in the upper troposphere. Slightly positive anomalies ($\sim$0.01 ms^{-1}) are found in the lower troposphere over the eastern Indian Ocean. This pattern of anomalies is consistent with a strengthening of the transverse circulation and a stronger monsoon.

Figure 4.42 shows the anomalous Walker circulation WARM - CTRL. Anomalous upward motion is evident over the western-central Pacific Ocean. Anomalous downward motion is observed over the eastern Indian Ocean and over the Americas. The vertical velocity cross section (Fig 4.42c) shows positive anomalies (associated with upward motion) reaching values of 0.01 Pas^{-1} around 175°E. Negative vertical velocity anomalies over the eastern Indian Ocean reach 0.006 Pas^{-1}. Downward motion anomalies over the eastern Pacific and the Americas are about 0.004 Pas^{-1}. The zonal divergent cross section over the central Pacific shows westerly anomalies in the upper troposphere and easterly anomalies in the lower troposphere. This anomaly pattern is consistent with an eastward shift of the Walker circulation and subsidence over the eastern Indian Ocean.

Figure 4.43 depicts the anomalous local Hadley circulation over the eastern Indian Ocean. Anomalous upward motion is evident in the northern hemisphere over Bay of Bengal and in the southern hemisphere around 8°S. A region of anomalous downward motion exists between these two anomalous upward branches. Vertical velocity differences (Fig 4.43c) confirm this anomalous pattern, with positive anomalies around 10°N reaching 0.005 Pas^{-1} and around 10°S approaching 0.003 Pas^{-1}. Negative anomalies around 0° reach 0.005 Pas^{-1}. The meridional wind divergent section (Fig 4.43b) shows northerly anomalies in the upper levels. The magnitude of the anomalies in the lower level is small. This anomaly pattern suggests an intensification of the ascending branch over the Bay of Bengal.

The anomalous local Hadley circulation over the western Indian Ocean is plotted in Figure 4.44. Weak anomalous upward motion is found around 10°N, reaching values of 0.003 Pas^{-1} (Fig. 4.44c). Weak anomalous downward motion is observed north and south of this region. The meridional divergent wind anomalies (Fig 4.44c) are also small, suggesting that the western Hadley circulation exhibits no significant changes relative to the CTRL.

Mass fluxes associated with each one of the circulations described above are listed in Table 4.2. The mass flux associated with the transverse circulation is larger in WARM than in CTRL, indicating an increase in the mass transport into southeast Asia and consistent with a strengthening of this circulation. The mass flux associated with the eastern local Hadley circulation is smaller than in CTRL indicating that the meridional divergent wind anomalies are smaller than in CTRL through the center of the circulation. Thus, the mass flux alone is not a good indicator of the strength of the anomalous circulation.

4.2.3.2 Precipitation patterns

Figure 4.45 displays differences in precipitation and OLR. Regions of negative differences in OLR are consistent with regions of positive differences in precipitation. Increased precipitation is observed over eastern Bay of Bengal and southeast Asia, consistent with a strengthening of the ascending branch over southeast Asia and with a stronger transverse circulation. Slightly negative differences in precipitation and positive differences in OLR exist over the Indian peninsula, consistent with increased subsidence near 80°E and an eastward shift of the circulation pattern and possibly the weaker AIRI for the period shown in Figure 2.2.

4.2.4 Circulation and precipitation differences for Experiment 4 ("BUMP" 1938– 1942)

In this section, differences between Experiment 4 (hereafter BUMP) and CTRL are described. In this experiment the model is forced by monthly SST averaged from 1938 to 1942 (see Table 3.1 and Figure 3.3).

4.2.4.1 Circulation patterns

Seasonal mean surface temperature differences fields for JJAS are shown in Figure 4.46a. Negative anomalies of about 0.3°C are found over the northern Indian Ocean, south Asia and the western equatorial Pacific Ocean. Warm anomalies of about

0.2°C exists over the southern Indian Ocean and the equatorial eastern Pacific. One prominent feature of this period is the co-occurrence of the positive phases of the Pacific decadal oscillation (PDO) and the Atlantic Multidecadal oscillation (AMO).

Figure 4.46b shows sea level pressure differences for BUMP. Positive pressure anomalies reaching 1.5 hP extend over India, Arabian Sea and the Bay of Bengal. Slightly positive anomalies are also observed over the western Pacific Ocean. Negative anomalies (~ 0.3 hPa) are present in the southern Indian Ocean east from Madagascar and over the eastern Pacific. The increase in SLP over south Asia is larger than the decrease in SLP in the southern Indian Ocean so that the pressure gradient between these two regions decreases. This is further confirmed by the CEPG index, which shows a decrease from 12.5 hPa in CTRL to 11.6 hPa in BUMP (see Table 4.1). The SLP pattern associated with the SST BUMP distribution exhibit the largest pressure anomalies over India and the northern Indian Ocean, relative to the other experiments.

Differences in the 850-hPa zonal winds between BUMP and CTRL are plotted in Figure 4.47a. Negative anomalies are evident in the northern Indian Ocean, including the Arabian Sea and Bay of Bengal, and the Indian peninsula, indicating that zonal winds are weaker than in CTRL. Maximum easterly anomalies in the area reach values > 1.5 ms^{-1}. South from this region, a region of positive anomalies ($\sim$0.8 ms^{-1}) is observed. Positive anomalies are also found in the central equatorial Pacific Ocean, approaching values of 1.5 ms^{-1}. At the 200-hPa level (Fig 4.47b), differences in zonal wind show a region of positive anomalies over the western Indian Ocean, extending into the southern tip of India and Bay of Bengal, suggesting a weakening of the Tropical Easterly Jet. Anomalies reach values of 2.5 m s^{-1} off the Somali coast. Over the western equatorial Pacific Ocean, negative anomalies reach values of 1.5 ms^{-1}. The circulation indices, WYI and WSI, are both smaller than in CTRL (see Table 4.1), confirming the weakening of the zonal vertical shear and suggesting a weakening

of the monsoon circulation.

Differences in meridional wind between BUMP and CTRL are shown in Figure 4.48. At the 850-hPa level, negative differences are found in the western Indian Ocean along the Somali coast and in Bay of Bengal. Negative differences along the Somali coast reach vales of -1 ms^{-1} and indicate a weakening of the Somali jet. Positive anomalies approaching 0.4 ms^{-1} are found over the Arabian Sea. At the 200-hPa level positive anomalies are observed in the eastern Indian Ocean and over Bay of Bengal. Anomalous southerly wind reaches maximum values of 0.8 m s^{-1}. The pattern of meridional wind anomalies suggests a diminished low level cross-equatorial flow and a weaker lateral circulation. The MHI decreases relative to the CTRL case (see Table 4.1) which is again consistent with a weakening of the local Hadley circulation.

Figure 4.29 shows a longitude-height section of the cross-equatorial meridional wind differences averaged between 5°S and 5°N. In the lower troposphere, negative anomalies from 40°E to 70°E confirm the weakening of the cross-equatorial Somali jet. Northerly anomalies in the lower levels are also found over the eastern India Ocean. Maximum negative anomalies reach values of 1 ms^{-1}. In the upper troposphere, positive anomalies are found between 400-hPa and 200-hPa over the central – eastern Indian Ocean. Anomalies over the eastern India Ocean reach values of 0.7 ms^{-1}. In BUMP SOM1 has a value of 3.2 ms^{-1} (13% less than CTRL), suggesting a decrease in intensity of the southwesterly jet. SOM2 has a value of 2.5 ms^{-1} (16% less than CTRL), confirming the decay in the cross-equatorial flow over the western Indian Ocean.

Velocity potential differences between BUMP and CTRL are plotted in Figure 4.50. At the 850-hPa level, negative differences are found over South Asia and the western Pacific and positive differences are observed over the eastern Pacific Ocean, the Americas and the Atlantic Ocean. Velocity potential anomalies at the 200-hPa

level show positive differences over South Asia and negative anomalies over the Atlantic Ocean, Africa and eastern Pacific. This anomaly pattern is similar to that found in MODERATE although somewhat stronger and suggests that large scale monsoonal circulations are weaker than in CTRL.

Figure 4.51 displays omega differences between BUMP and CTRL at 500-hPa. Weaker upward motion than in CTRL exists over the Indian Peninsula, western equatorial Indian Ocean and Bay of Bengal. Stronger upward motion is found over the western-central Pacific Ocean (170°E). Weaker upward motion in a region of anomalous divergence suggests a possible decline in the ascending branch of the divergent monsoon circulations over Southeast Asia.

The anomalous transverse circulation (Figure 4.52a) shows anomalous downward motion over the Bay of Bengal ($\sim$ 90°E), Arabian Sea and Indian peninsula. The vertical velocity cross sections (Figure 4.52c) shows negative anomalies (associated with anomalous downward motion) around 90°E, reaching 0.024 Pas^{-1}. Negative anomalies between 60°E and 80°E reach 0.01 Pas^{-1}. In the western Indian Ocean positive anomalies reach 0.006 Pas^{-1}. The zonal divergent wind section (Fig 4.52b) displays positive anomalies ($\sim$ 0.8 ms^{-1}) over the central-western Indian Ocean in the upper troposphere. Weaker easterly anomalies ($\sim$ 0.3 m s^{-1}) are evident in the lower levels. This anomaly pattern is consistent with a weakening of the circulation and a weaker monsoon.

The anomalous Walker circulation is presented in Figure 4.53a. Anomalous downward motion is observed over the western Pacific Ocean near 150°E, and strong anomalous upward motion is found near 170°E. The vertical velocity cross section (Fig 4.53c) shows negative anomalies west of 160°E and near 200°E. Maximum negative anomalies reach values of 0.012 Pas^{-1} at 200°E. A region of strong positive anomalies is found around 170°E, reaching values of 0.02 Pas^{-1}. Whereas the zonal divergent wind (Figure 4.53b) anomalous pattern exhibits a complex structure, it

suggests a weakening of the westerlies in the upper troposphere and a weakening of the easterlies in the lower levels over the central Pacific Ocean. This anomaly pattern is consistent with an eastward shift of the Walker circulation and a weakening of the ascending branch over Indonesia.

Figure 4.54a depicts the anomalous local Hadley circulation over the eastern Indian Ocean. Anomalous downward motion is evident over the Bay of Bengal and anomalous upward motion is found in the southern hemisphere around 10°S. Vertical velocity cross section (Fig 4.54c) anomalies support these findings showing downward anomalies between 10°N and 20°N, approaching 0.02 Pas^{-1} and upward anomalies around 10°S reaching 0.007 Pas^{-1}. Meridional divergent wind anomalies (Fig 4.54b) show a weakening of the low level southerlies, with negative anomalies in the lower levels ($\sim$ 0.8 ms^{-1}) and a weakening of the upper level northerlies, with positive anomalies at 200hPa approaching 0.4 ms^{-1}. This pattern of anomalies is consistent with a decline in the ascending branch of the meridional circulation over southeast Asia and Bay of Bengal and with a weaker monsoon.

The anomalous local Hadley circulation over the western Indian Ocean (Figure 4.55a) displays anomalous upward motion at 10°S and anomalous downward motion in the northern hemisphere. Vertical velocity anomalies (Fig 4.55c) show downward anomalies approaching 0.006 Pas^{-1} around 17°N. In the southern hemisphere positive anomalies reach 0.008 Pas^{-1} around 10°S. Meridional divergent wind anomalies are negative in the lower troposphere from 10°S to 20°N and positive between 10°N and 20°S in the upper troposphere (Figure 4.55b). This anomaly pattern suggests a weakening of the ascending branch around 5°S and increasing subsidence in the northern hemisphere.

For this experiment, largest negative differences (BUMP - CTRL) in mass fluxes are observed for the transverse circulation and lateral monsoon over the eastern Indian Ocean (see Table 4.2), indicating a decrease in the transport of mass into the southeast

Asian region, again consistent with a weaker monsoon. Transport associated to the lateral monsoon over the western Indian Ocean also decreases.

4.2.4.2 Precipitation patterns

Figure 4.56 shows differences in OLR and precipitation between BUMP and CTRL. Large positive differences in OLR (Fig 4.56a), consistent with negative differences in precipitation (Fig 4.56b) are evident over the Indian Peninsula, Bay of Bengal and the western Indian Ocean. More precipitation than in CTRL is found south of the equator in the eastern Indian Ocean. Over the Pacific Ocean, large positive precipitation anomalies are found around 170°E. Negative precipitation anomalies occur west of this region. The anomalous precipitation pattern is consistent with an overall weakening of the divergent circulations.

4.3 Summary

The results described in the previous sections demonstrate that the mean large scale monsoonal circulation responds to changes in the SST distribution. The colder SST (COLD) configuration, leads to a reduced pressure gradient between the northern land and the southern ocean causing weaker cross-equatorial flow and weaker westerlies in the lower level. The indexes used to describe the Somali jet strength confirm the weakening of the cross–equatorial flow, showing a decrease in intensity across the equator and over the western Indian Ocean. A reduced Somali jet suggests a decline in the amount of momentum and water vapor that is transported into India and Bay of Bengal.

In general, regions of active convection are located in the vicinity of areas of low level convergence and upper level divergence (Krishnamurti, 1971, Krishnamurti, 1973). Velocity potential fields for the COLD experiment display a weakening of the center of convergence at the lower level and a weakening of the center of divergence at the upper level over south Asia, suggesting a large scale weakening of the monsoon

circulation. A modification in the convergence and divergence patterns, imply a modification in the vertical velocities and convection patterns.

Since COLD depicts a weaker large scale circulation, weaker vertical velocities are expected. Omega 500 h-Pa fields show reduced vertical velocities over Bay of Bengal and the Indian peninsula, suggesting a decline in the ascending branch of the divergent circulations associated with the summer monsoon.

A detailed examination of the circulations shows a decrease in the upward motion over India and Bay of Bengal. This decrease is more evident in the ascending branch of the transverse circulation. Moreover, the Walker Circulation exhibits an eastward shift which brings subsidence over the equatorial eastern Indian Ocean. The reduction in upward motion over India and Bay of Bengal is further confirmed by the reduction in convective activity and precipitation over these areas. Increased vertical velocities over southeast Asia and the South China Sea are associated with an eastward shift of the ascending branch of the transverse circulation. These conditions favor an increase in convective activity and enhanced precipitation over these areas.

In MODERATE, SSTs anomalies are negative in the tropical band but in less magnitude than in COLD. The central equatorial Indian Ocean is the region that exhibits larger negative anomalies in the tropics. The SLP associated with this SST distribution shows a larger increase in pressure over the southern ocean than over the land to the north. Resulting pressure gradients generate decreased southerlies along the coast of Tanzania and Kenya and increased southerlies off the Somali coast. SLP gradients between the western Indian Ocean and the eastern Indian Ocean induce decreased low level westerlies over the central and western equatorial Indian Ocean and over the Bay of Bengal. The Somali jet indexes for MODERATE support these results showing an increase in SOM2 (14% more than in CTRL) and a decrease in SOM1 (8.1 less than CTRL value). The increase in SOM2 accounts for the increased southerlies north of the Equator and further out off the African coast. The decrease

in SOM1 is explained by the reduction in westerlies over the western Indian Ocean.

Moreover, the cross-equatorial wind section displays negative anomalies over the eastern Indian Ocean. This reduction in meridional flow is also observed in the low level wind field over the Bay of Bengal. The wind pattern, just described, favors decreased convergence over south Asia, especially over Bay of Bengal and the eastern Indian Ocean. Upper level fields are consistent with the low level circulation showing decreased easterlies over the central Indian Ocean and weaker divergence over South Asia. Furthermore, the zonal vertical shear decreases in the northern-central Indian Ocean and the meridional vertical shear is diminished over the eastern Indian Ocean.

An evaluation of the divergent circulations shows a diminished ascending branch over the Bay of Bengal and southeastern Asia in the transverse circulation and over the north-eastern Indian Ocean in the local Hadley circulation. The decrease in the upward motion is stronger in the transverse circulation. Moreover, the magnitude of the negative anomalies is larger in MODERATE than in COLD. In the Walker circulation, a reduction in the upward motion is more visible over the west Pacific. As a result, vertical velocities (omega) decrease over Bay of Bengal, southeastern Asia and the western equatorial Pacific, giving rise to increased OLR and decreased precipitation. Similarly, negative precipitation anomalies over the western equatorial Indian Ocean are explained by a weakening of the southern portion of the local western Hadley circulation. Overall, the circulation patterns associated with the MODERATE SST distribution are consistent with a weakening of the monsoon circulation.

A warmer SST configuration (WARM) is associated with a decrease in sea level pressure throughout the tropics. Over the Indian Ocean the decrease in SLP is larger over the eastern side than over the western side, favoring an increase in low level westerlies over the equatorial Indian Ocean. In the upper level, easterly winds intensify over the tropical Indian Ocean. As a result, the zonal vertical shear increases relative to the CTRL case.

A closer examination of the cross-equatorial flow shows that the magnitude of the anomalies is small compared with the other cases. The index SOM2 has the same value as in CTRL. SOM1, on the other hand, has the largest value of all the experiments (see Table 4.1), accounting for an increase in westerly intensity over the northern Indian Ocean.

In a consistent manner, velocity potential fields display an increase in low-level and upper level divergence over the eastern Bay of Bengal and southeast Asia, consistent with a stronger monsoon circulation. This circulation pattern favors intensification of the ascending branch of the divergent circulations over southeast Asia. An examination of the transverse and local eastern Hadley circulations confirms this intensification, showing increased upward velocities over Bay of Bengal and southeast Asia. The Walker circulation, on the other hand, reveals increased upward motion over the west Pacific. The strengthening of the ascending branch reflects in the precipitation field, showing enhanced precipitation over Bay of Bengal and southeast Asia and the west Pacific. Again, the pattern of the anomalous circulation is consistent with a stronger monsoon.

In the BUMP experiment, SSTs anomalies are slightly negative in the northern Indian Ocean and slightly positive in the southern tropical Indian Ocean. In the northern subtropical oceans, SSTs anomalies resemble the positive phases of the PDO and AMO. The SLP associated with these SSTs depicts strong positive anomalies over India, the Arabian Sea and Bay Bengal. The increase in SLP over land in conjunction with a slight decrease in pressure over the southern ocean results in a reduced cross-equatorial pressure gradient.

The resulting wind fields show decreased low level westerlies over the northern Indian Ocean and decreased southerlies along the African coast. In the upper level, the tropical easterly jet weakens and the meridional flow over the Bay of Bengal and the eastern Indian Ocean is reduced. The BUMP experiment displays the largest wind

anomalies of all the experiments over these regions. The meridional cross-section along the equator shows a decrease in the cross equatorial flow along the African coast and the eastern Indian Ocean. SOM2 in the BUMP case has the smallest value compared to the other experiments, accounting for the decreased southerly flow. SOM1 has also the smallest value, which is consistent with a larger decrease in westerlies over the western Indian Ocean. This wind pattern favors decreased low level convergence and decreased upper level divergence over South Asia, and a weakening of the large scale circulation.

An examination of the divergent circulations related to the monsoon shows a large decrease in the ascending branch over the Bay of Bengal and southeast Asia. The BUMP experiment depicts the largest downward anomalies over Bay of Bengal and East Asia in the transverse circulation and in the local eastern Hadley circulation relative to the other experiments. Precipitation decreases accordingly over these regions.

In the BUMP experiment, the magnitude of the local SSTs anomalies and "remote" SSTs tropical anomalies is small compared with the other experiments. However, the response of the monsoon circulation to these anomalies is the largest. This behavior suggests that not only local but remote SSTs impact the monsoon circulation. In this particular case, large SST negative anomalies over the north Pacific and large SST positive anomalies over the North Atlantic Ocean also modulate the large scale tropical circulations.

In summary, the previous results confirm the importance of SST distribution in regulating the strength of the Asian monsoon. SST gradients constitute a key factor for controlling the intensity of the monsoonal winds and the strength of the divergent circulations. Modified circulations could result in an increase or decrease of moisture convergence into continental regions, ultimately impacting the development of convective processes over these regions. In the next chapter, we investigate the

association between SSTs, atmospheric circulation and moisture availability.

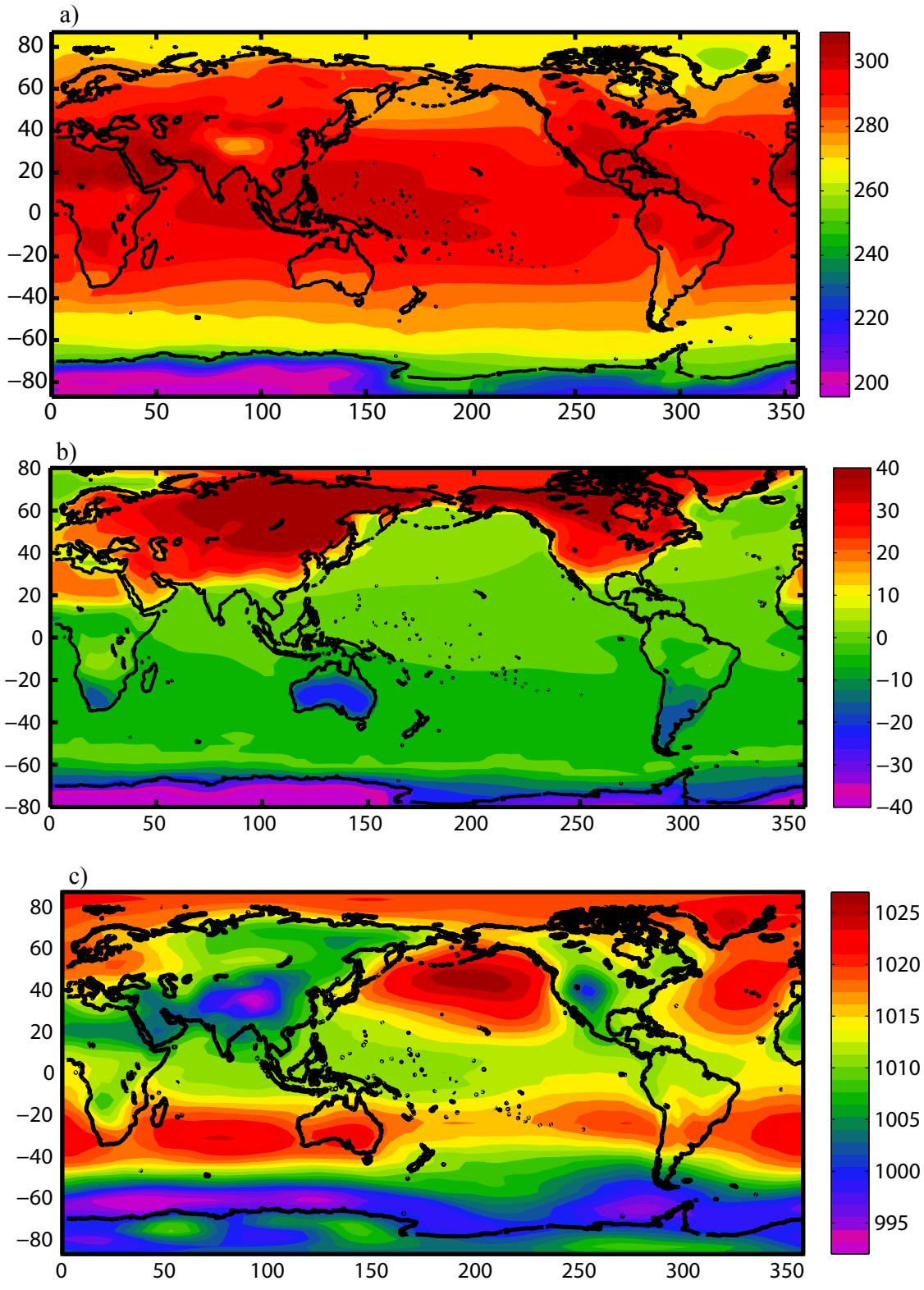

Figure 4.1: a) Mean summer surface air temperature and SST from CTRL run. b) Surface temperature differences between summer and winter season. Units are °C. c) Mean summer sea level pressure from CTRL run. Units are hPa.

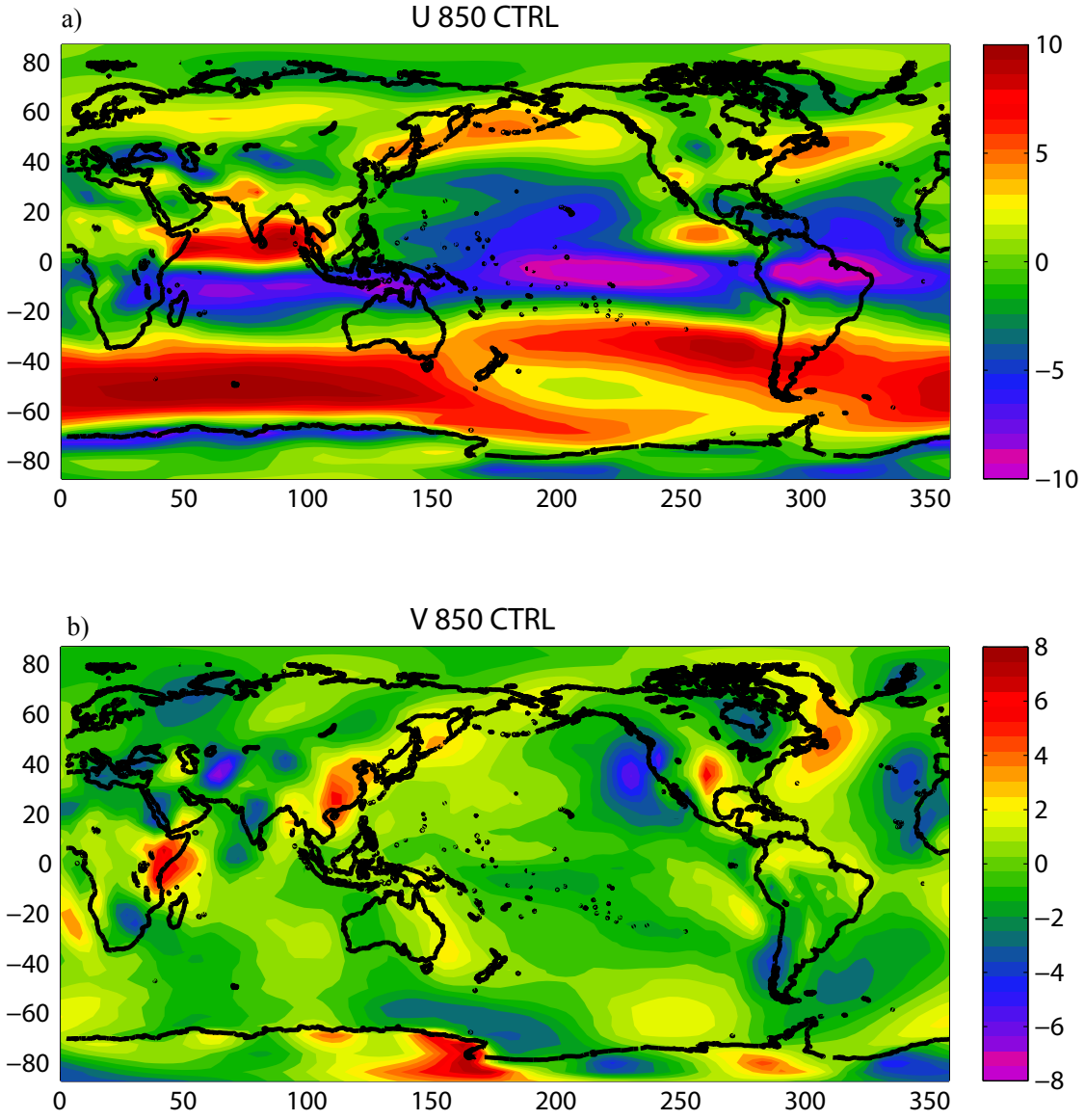

Figure 4.2: a) Mean summer zonal wind field at 850-hPa level from CTRL run. b) Mean summer meridional wind field at 850-hPa level from CTRL run. Units are ms^{-1}.

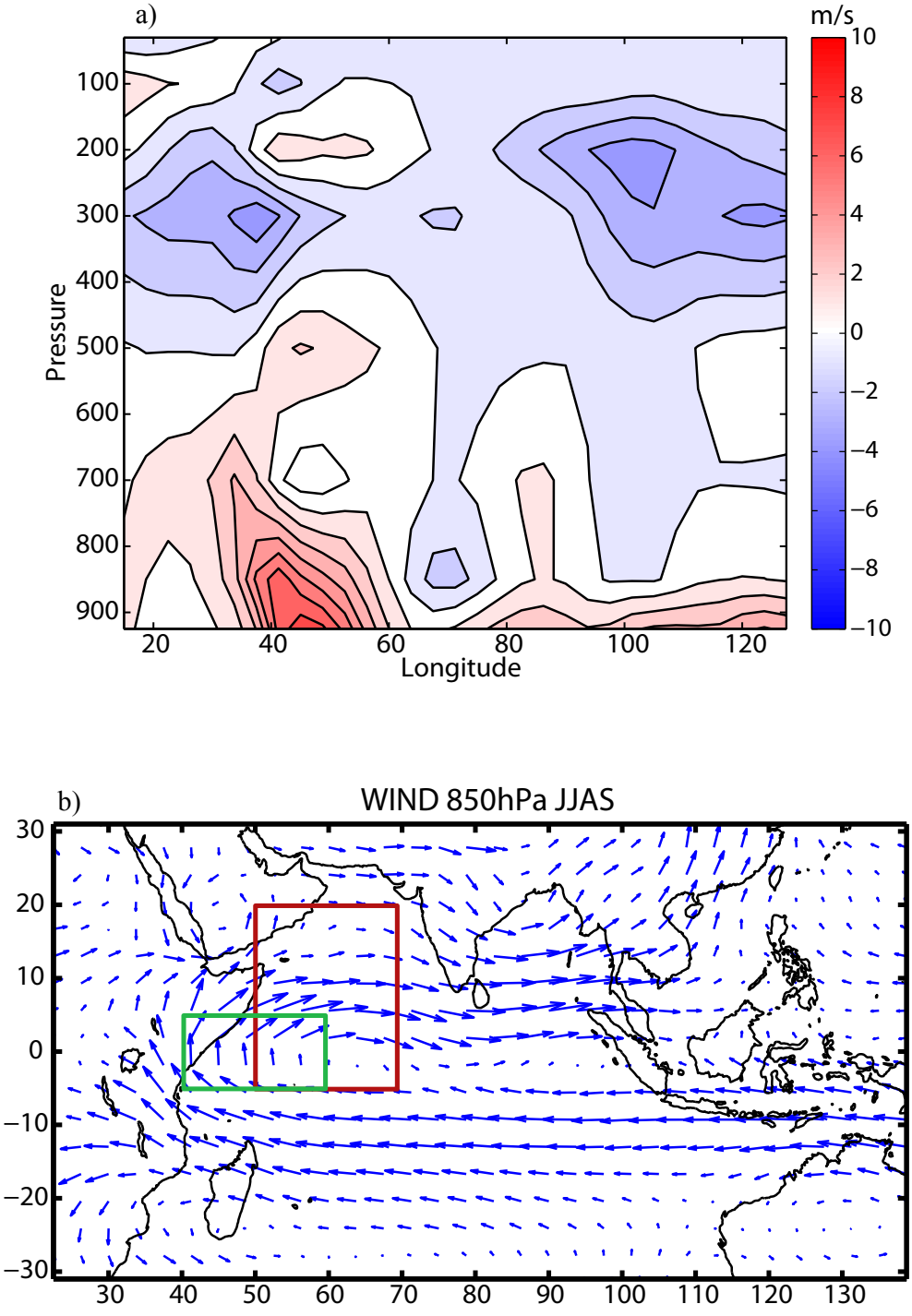

Figure 4.3: a) Meridional wind averages for JJAS between 5°S and 5°N from CTRL. Units are ms^{-1} b) Wind field at 850-hPa for JJAS.

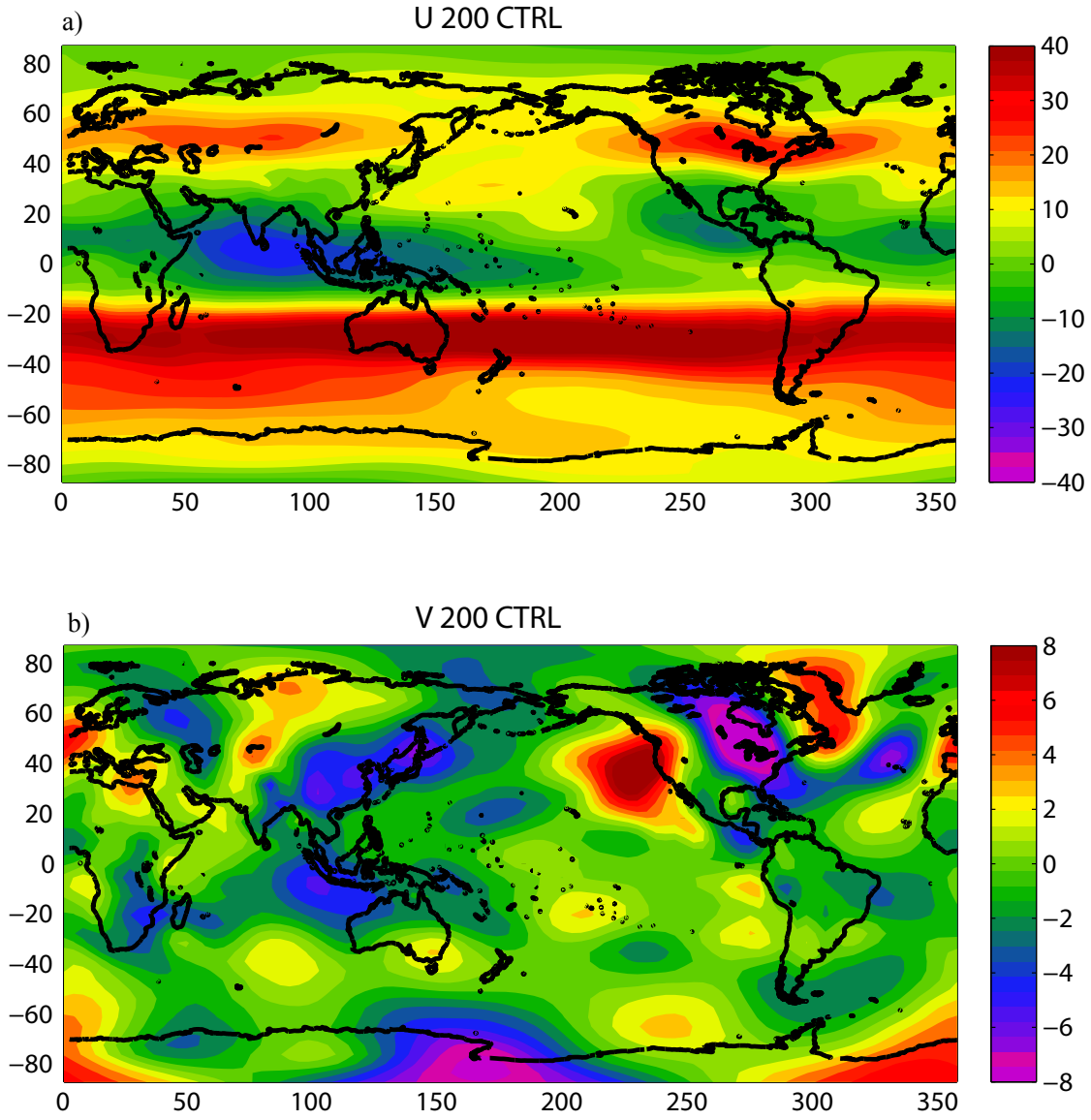

Figure 4.4: a) Mean summer zonal wind field at 200-hPa level from CTRL run. b) Mean summer meridional wind field at 200-hPa from CTRL. Units are ms^{-1}.

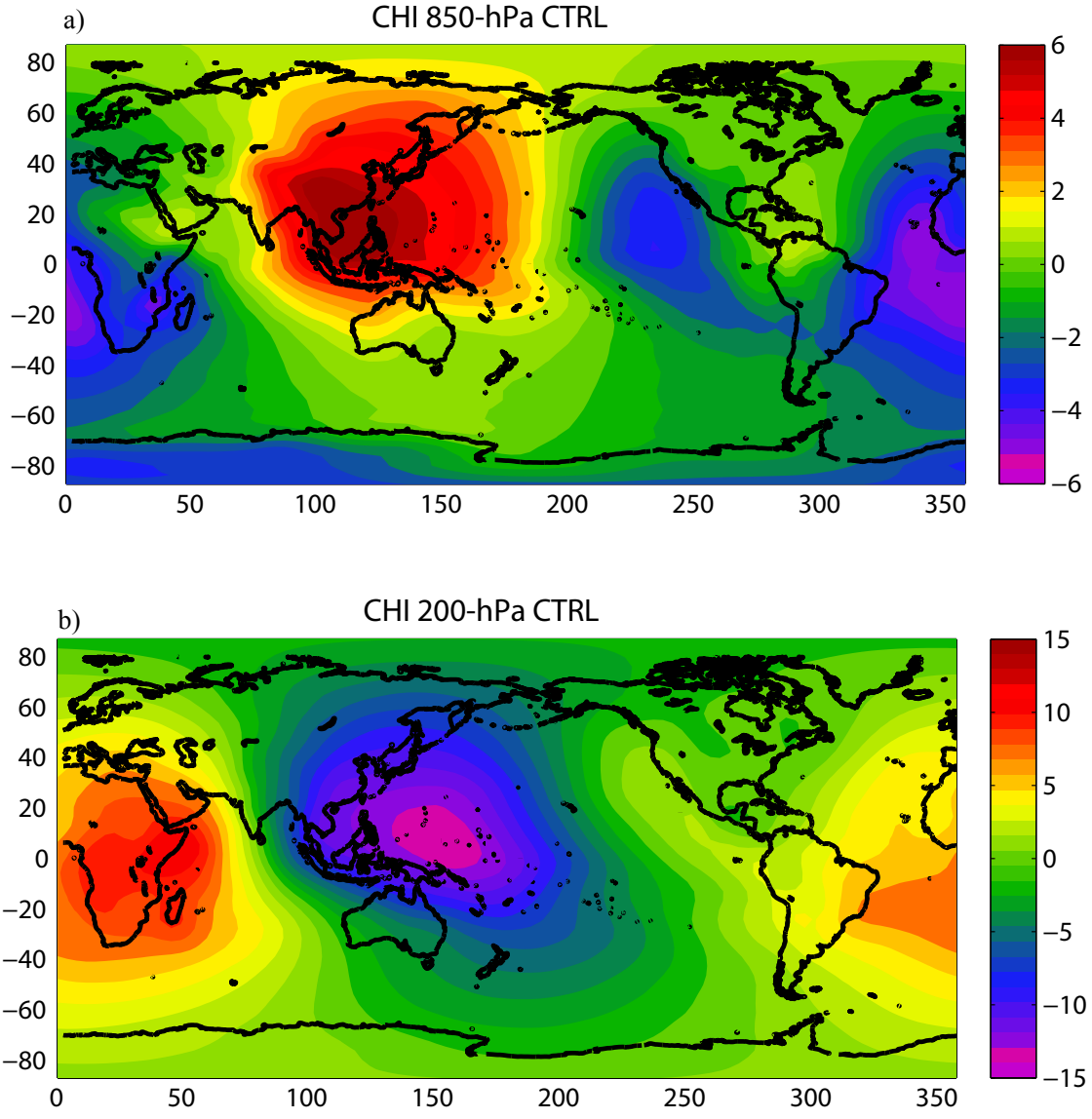

Figure 4.5: Mean summer velocity potential from CTRL run at: a) 850-hPa level; b) 200-hPa. Units are $10^6 \mathrm{m}^2\mathrm{s}^{-1}$.

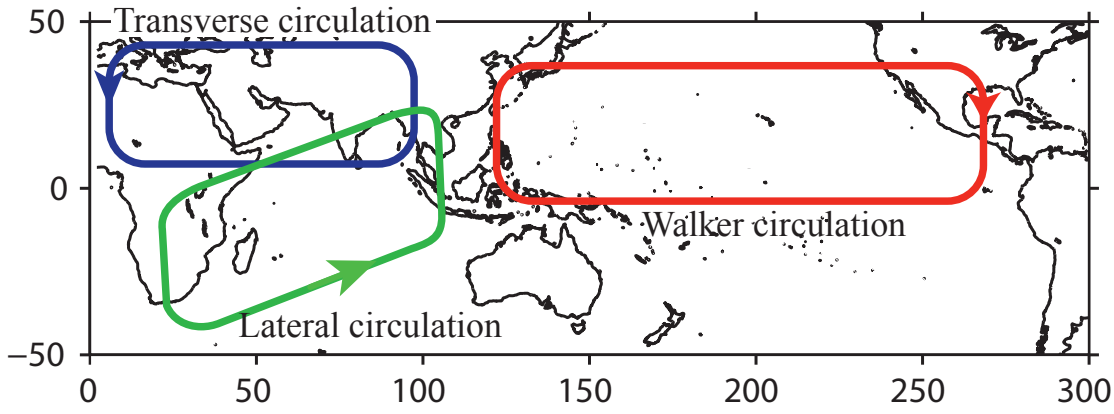

Figure 4.6: Schematic of the major divergent circulations associated with the south Asian monsoon during the summer season.

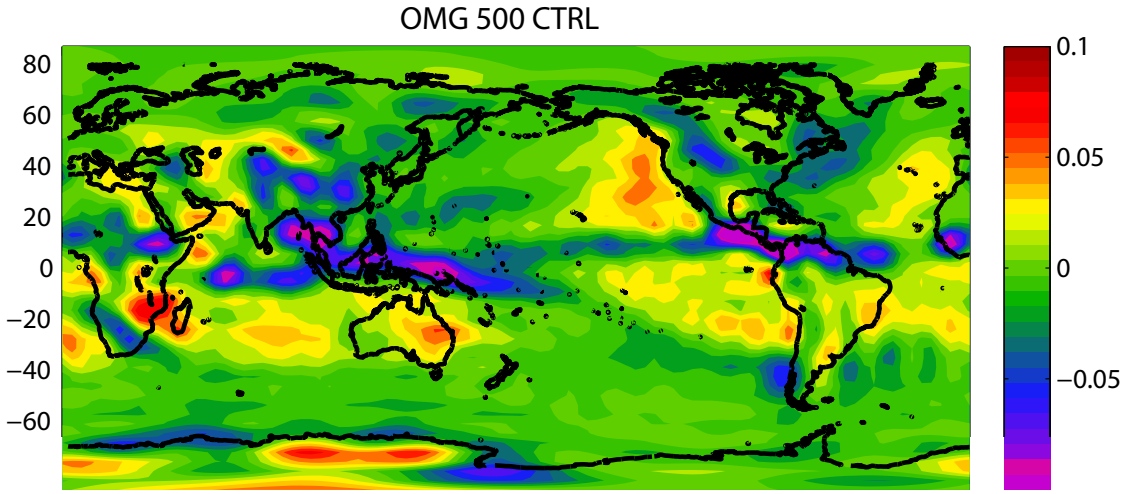

Figure 4.7: Mean summer omega at 500-hPa from CTRL sun. Units are Pa s^{-1}.

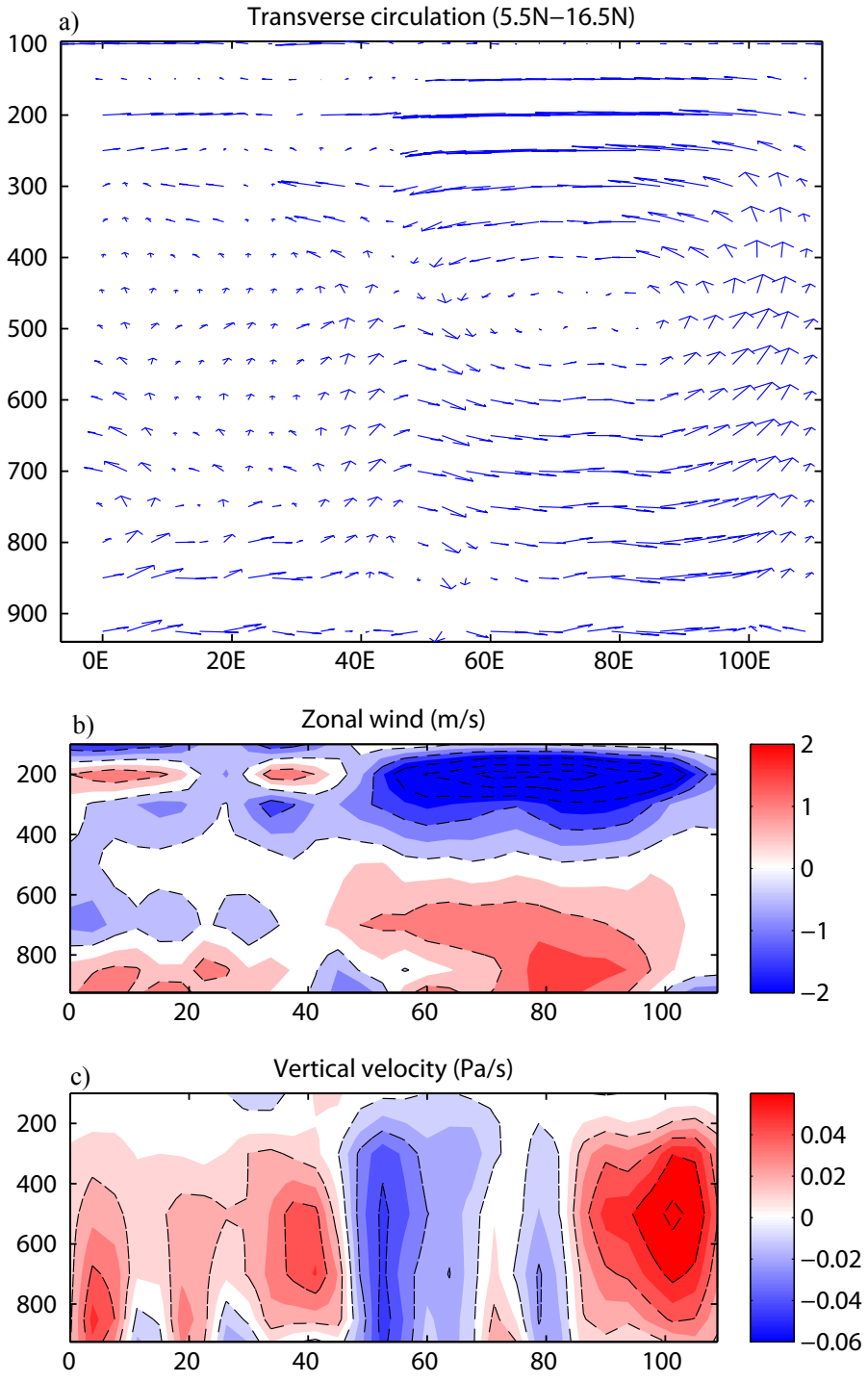

Figure 4.8: a) Transverse (zonal-vertical) circulation along 10°N from CTRL. Zonal divergent wind and omega are averaged between 5°N and 16°N from 0°E to 115°E. b) Cross section of zonal divergent wind. Units are ms^{-1}. c) Cross section of vertical velocity. The vertical velocity is taken the negative of the pressure vertical velocity in the model. Units are Pa s^{-1}.

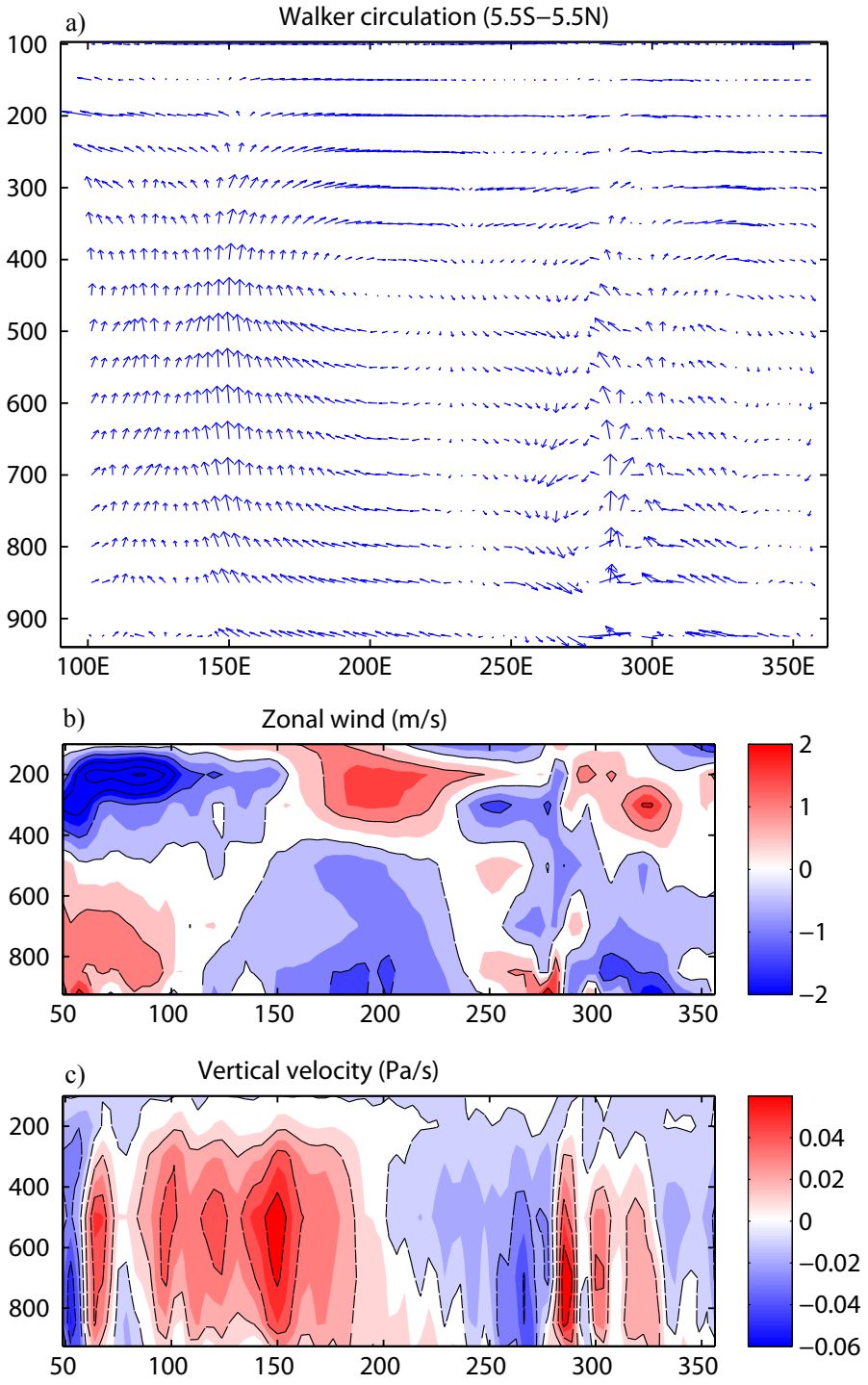

Figure 4.9: a) Walker circulation along the equator from CTRL. Zonal divergent wind and omega are averaged between 5°S and 5°N from 100°E to 360°E. b) Cross section of zonal divergent wind along the equator. Units are ms^{-1}. c) Cross section of vertical velocity along the equator. The vertical velocity is taken the negative of the pressure vertical velocity in the model. Units are Pa s^{-1}.

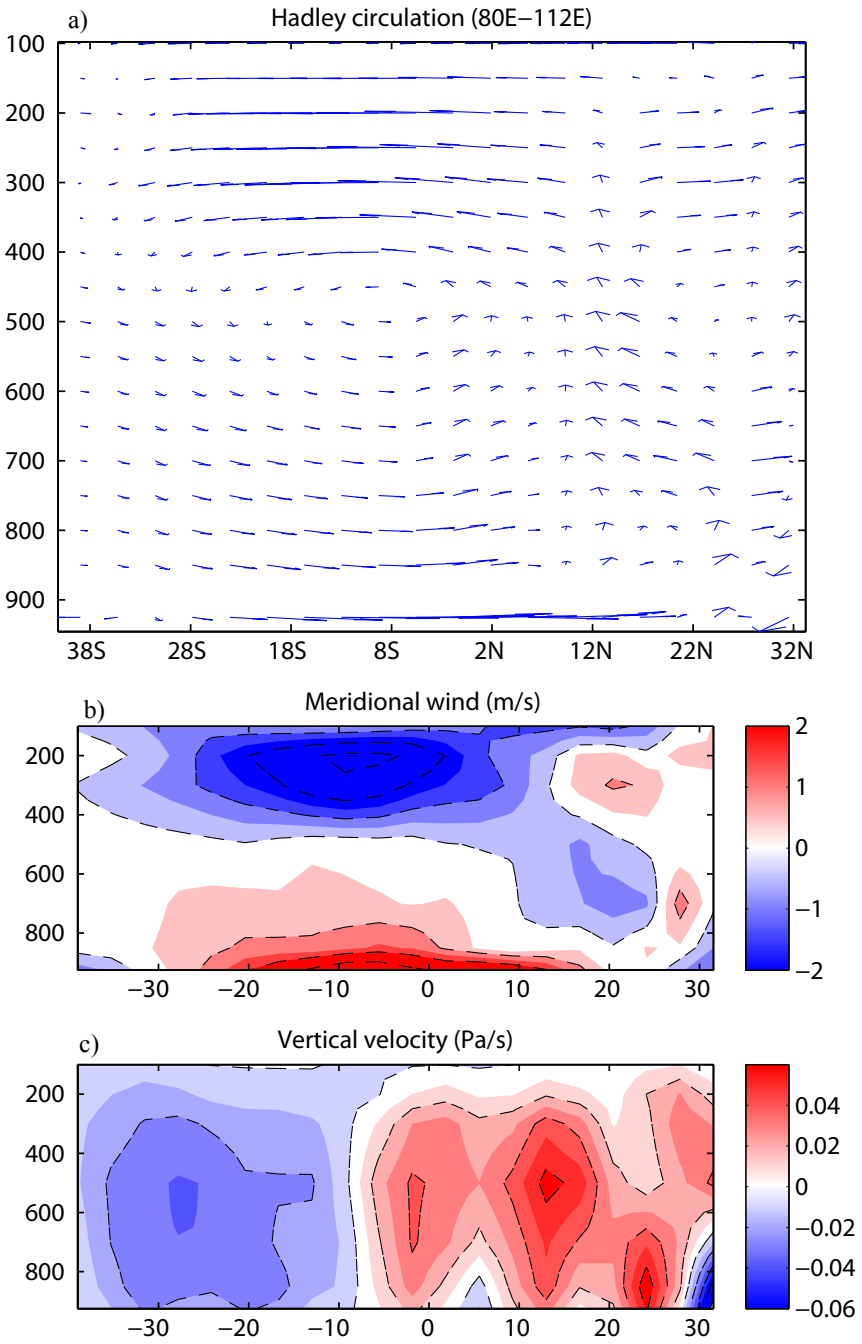

Figure 4.10: a) Local Hadley circulation over the Eastern Indian Ocean from CTRL. Meridional divergent wind and omega are averaged between 80°E and 115°E from 38°S to 32°N. b) Cross section of meridional divergent wind averaged between 80°E and 115°E. Units are ms^{-1}. c) Cross section of vertical velocity for the same region as in b). The vertical velocity is taken the negative of the pressure vertical velocity in the model. Units are Pa s^{-1}. d) Local Hadley circulation over the Western Indian Ocean from CTRL. Meridional divergent wind and omega are averaged between 45°E and 75°E from 38°S to 32°N. e) As in b) but averaged between 45°E and 75°E. f) As in c) but averaged between 45°E and 75°E.

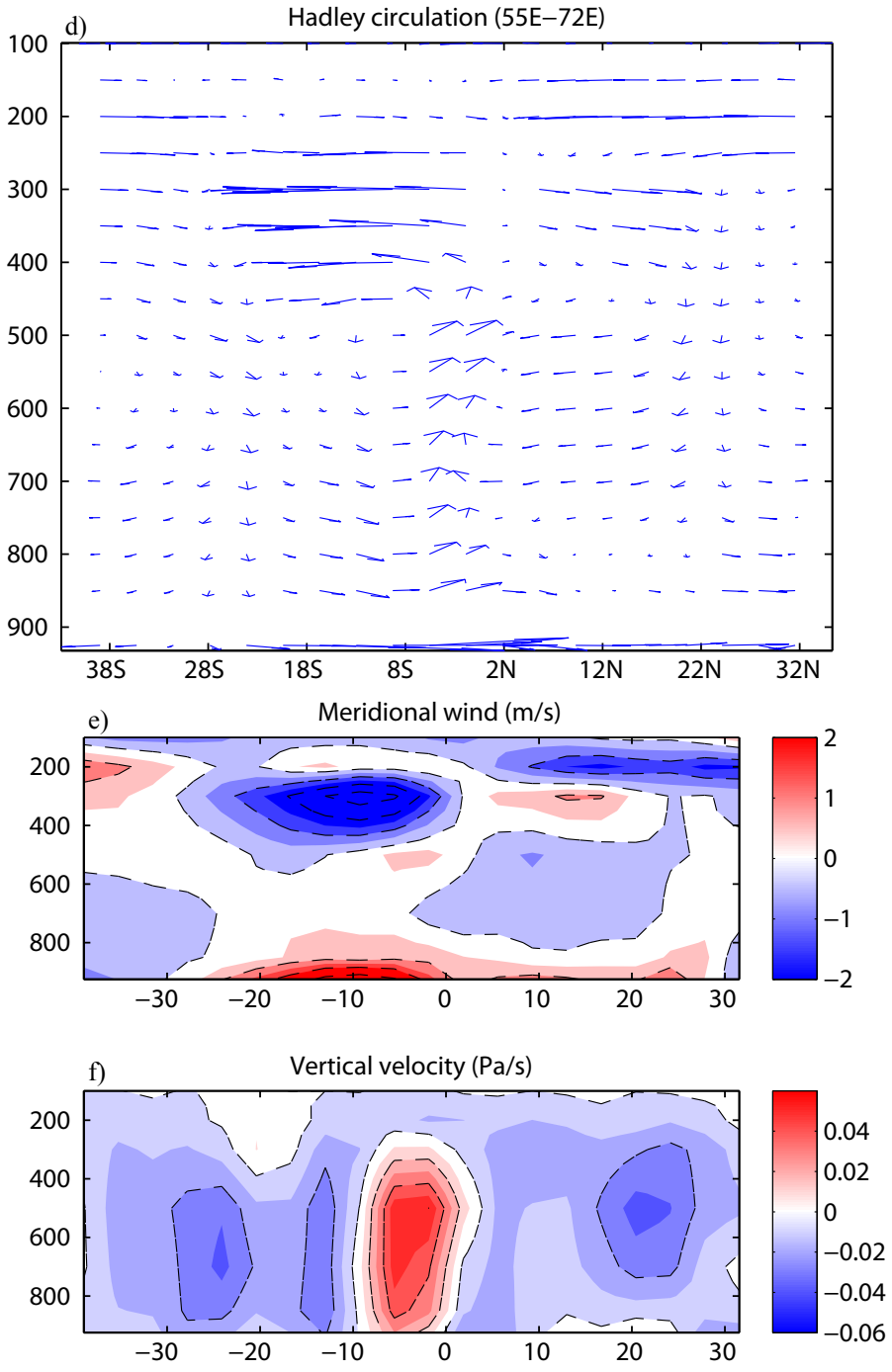

Figure 4.10 (continued)

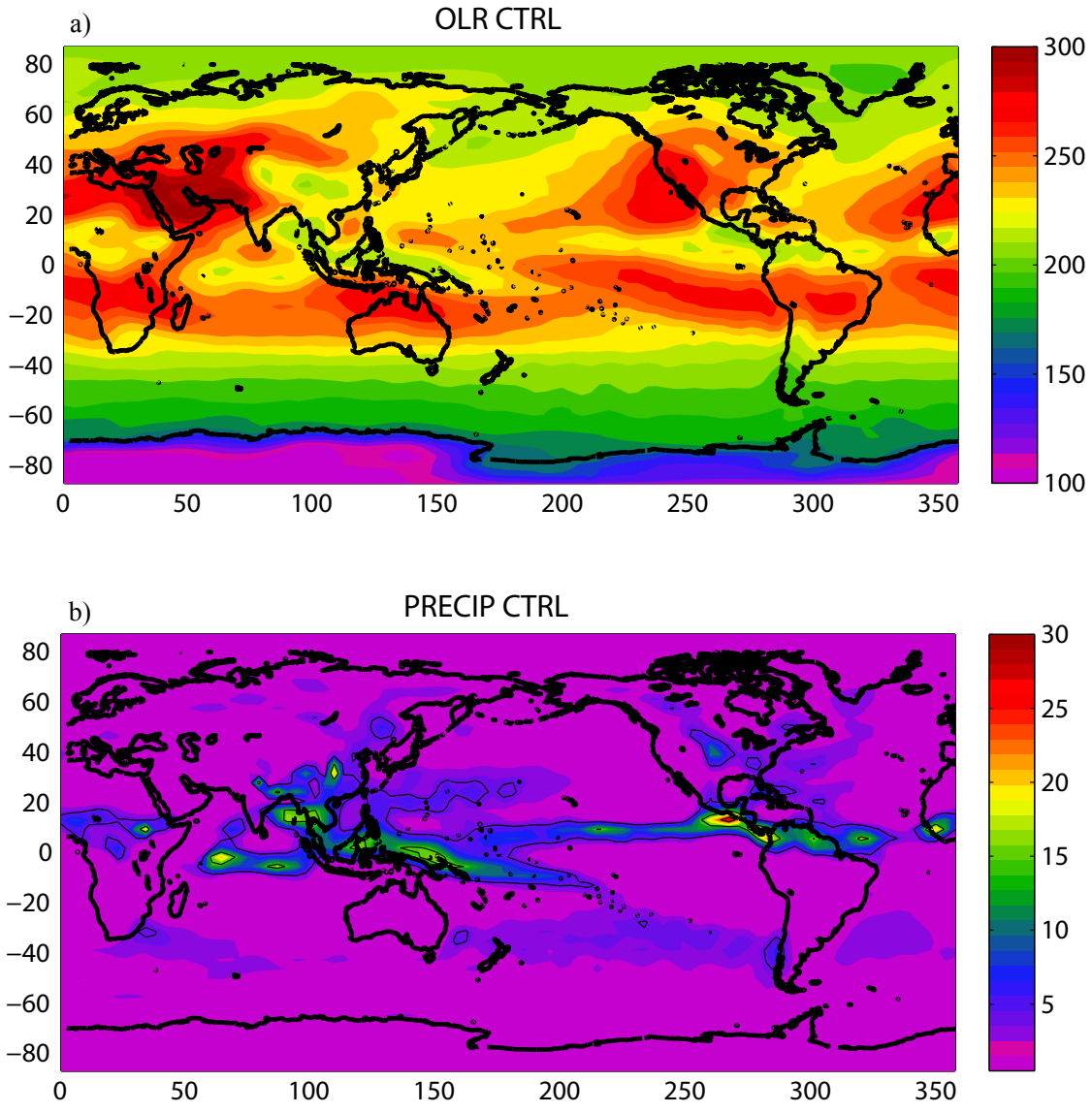

Figure 4.11: a) Mean summer OLR from CTRL run. Units are W m^{-2} b) Mean summer precipitation from CTRL run. Units are mm day^{-1}.

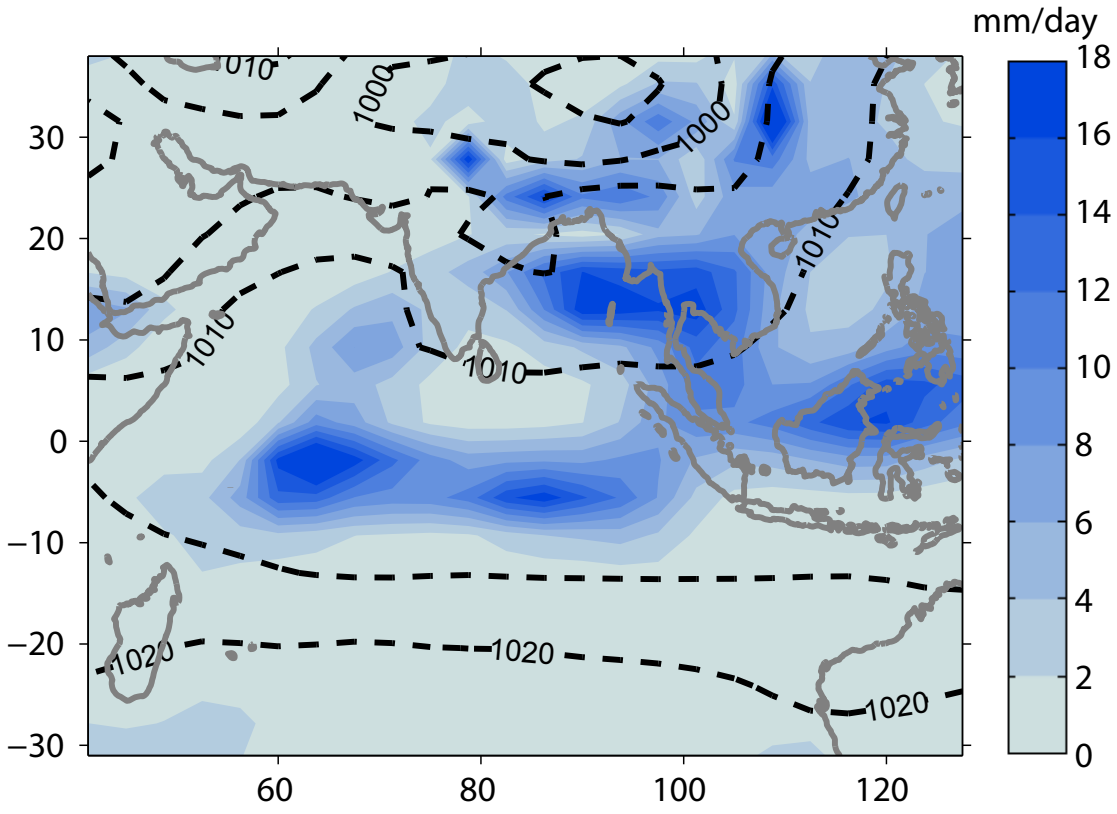

Figure 4.12: Regional map of precipitation and sea level pressure. Black contours denote sea level pressure. Contour intervals are 5 hPa. Colored contours indicate precipitation.

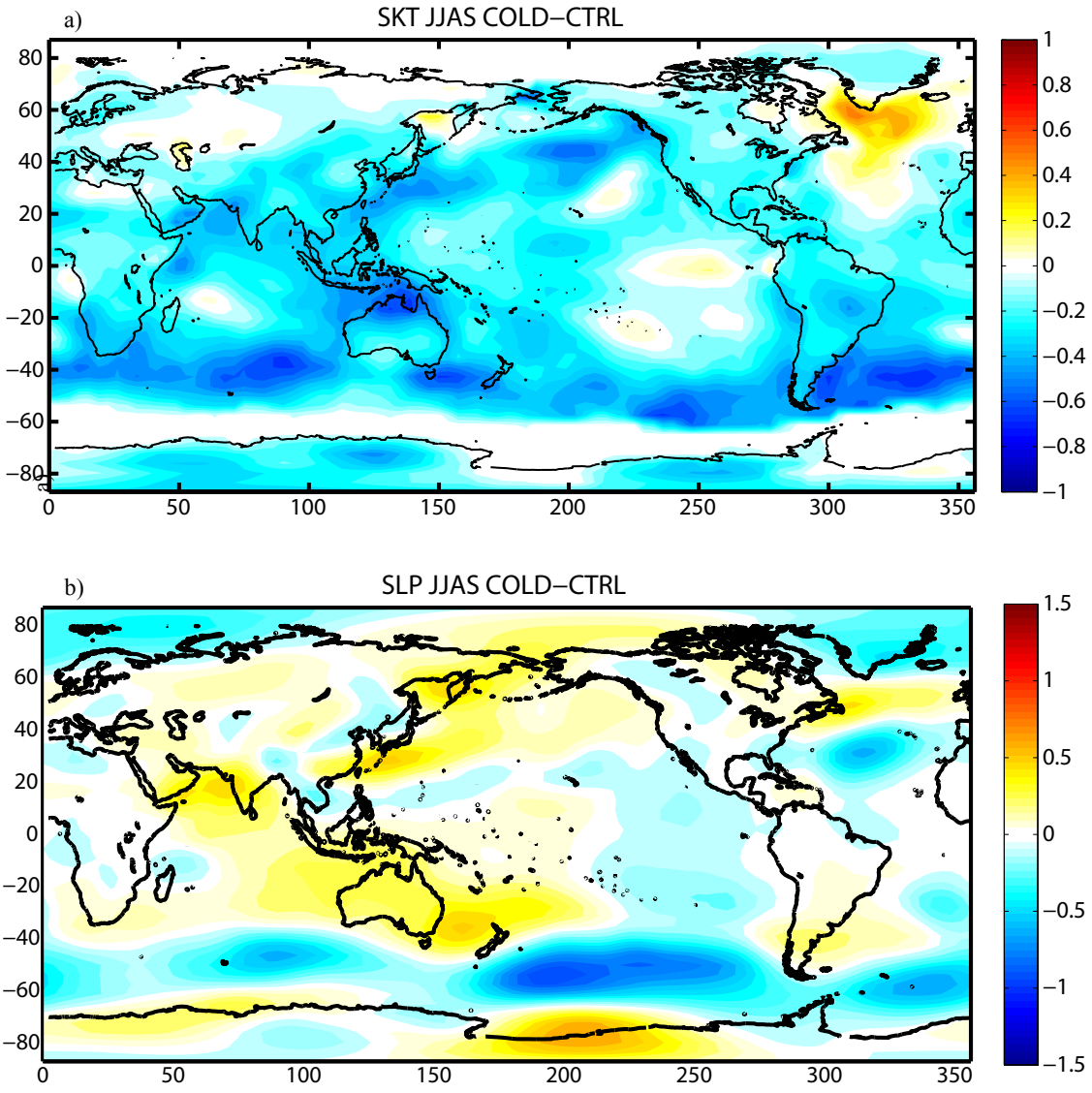

Figure 4.13: a) Differences in surface temperature between COLD and CTRL for the summer season. Units are °C. b) Differences in sea level pressure between COLD and CTRL. Units are hPa.

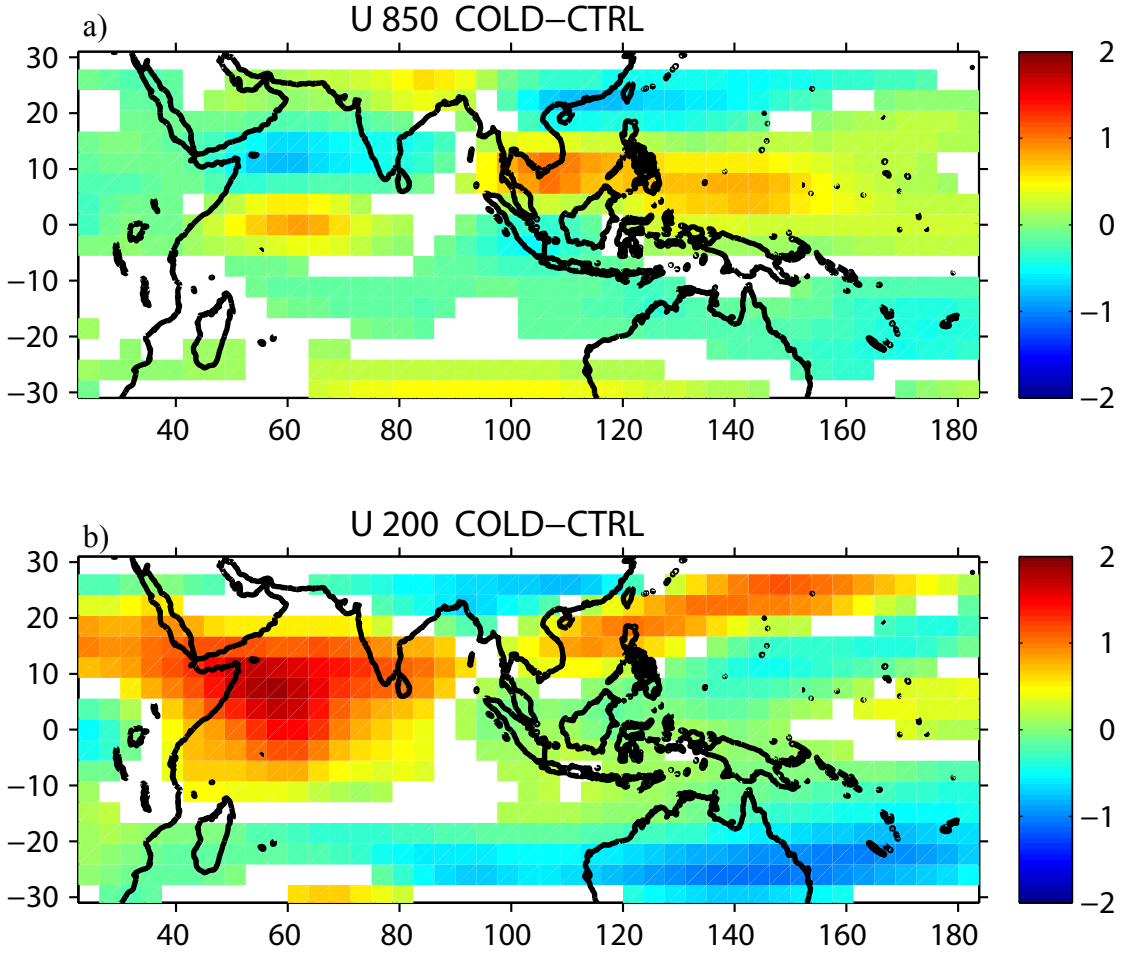

Figure 4.14: Differences in zonal wind between COLD and CTRL at: a) 850-hPa level; b) 200-hPa level. Units are ms^{-1}.

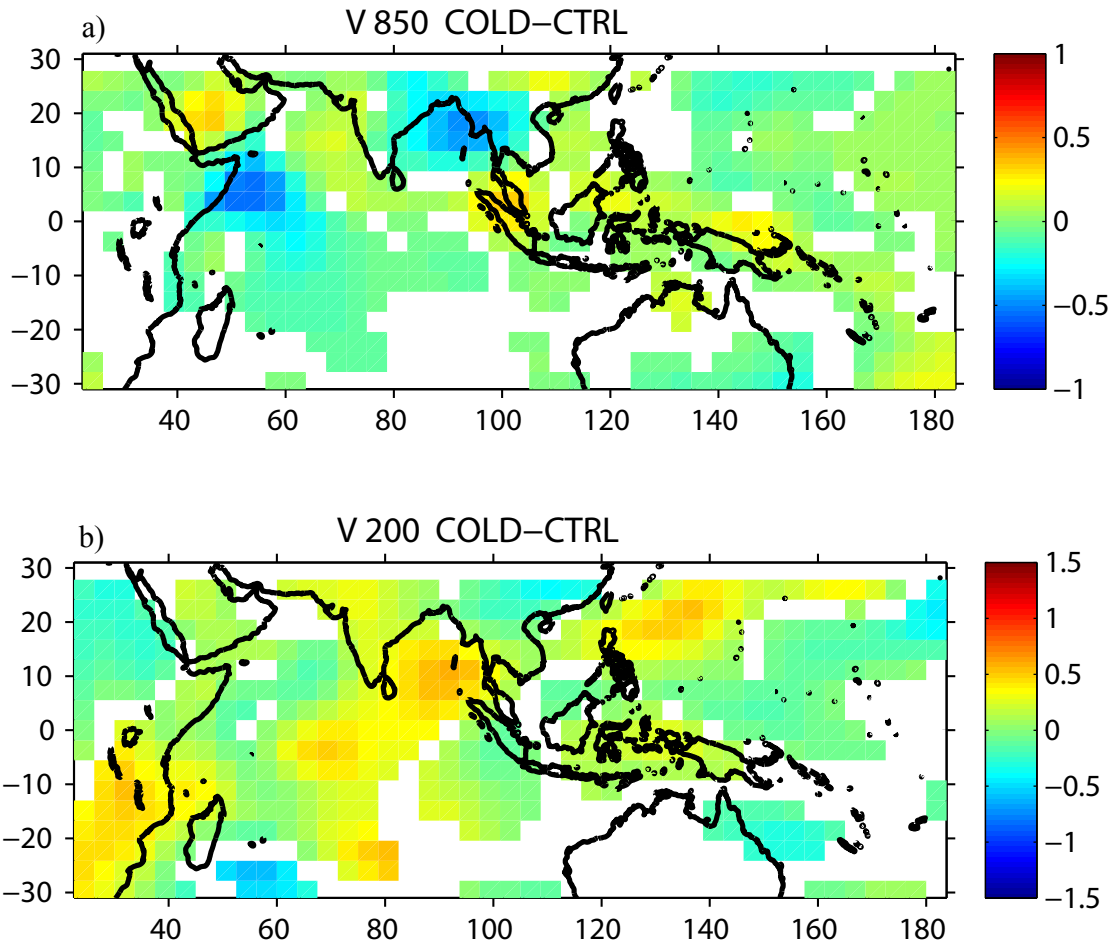

Figure 4.15: Differences in meridional wind between COLD and CTRL at: a) 850-hPa level; b) 200-hPa level. Units are ms^{-1}.

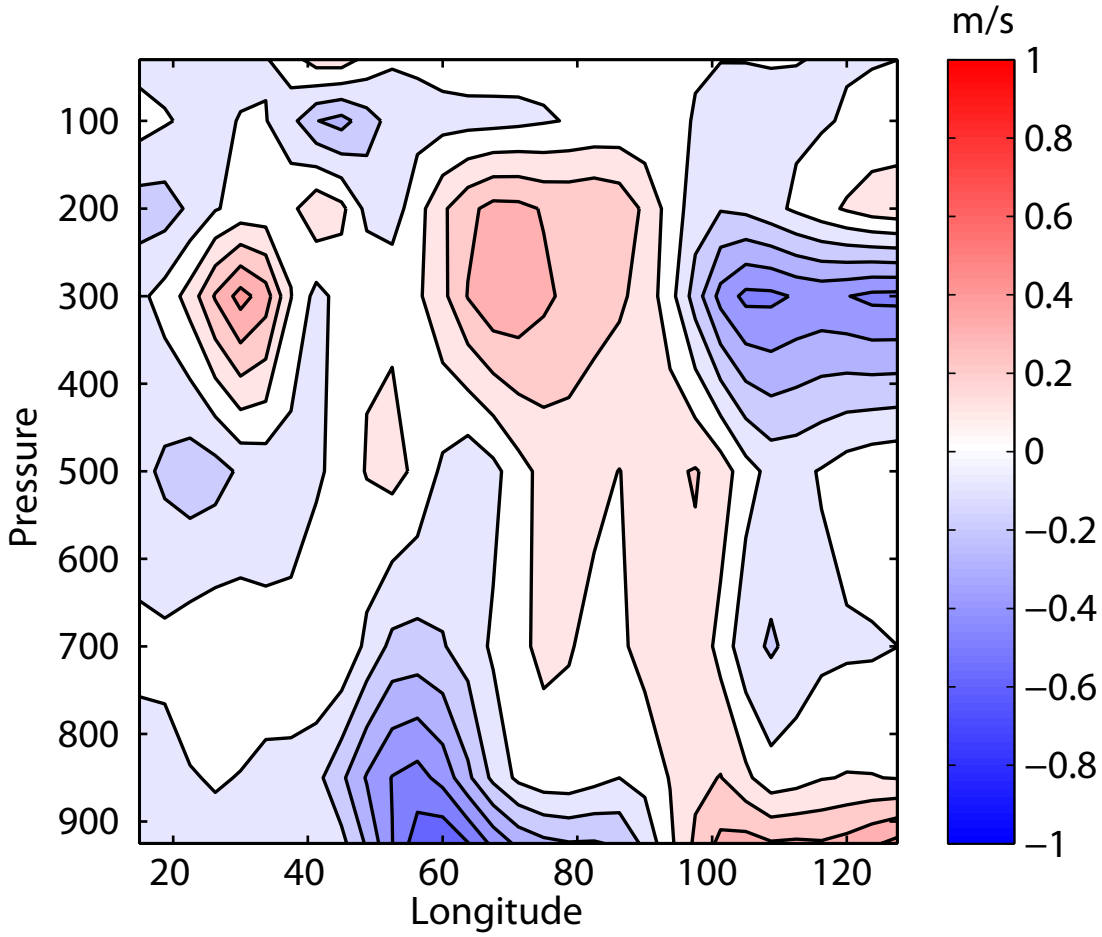

Figure 4.16: Seasonal mean cross equatorial meridional wind differences between COLD and CTRL. Differences are averaged between 5°S and 5°N. Units are ms^{-1}.

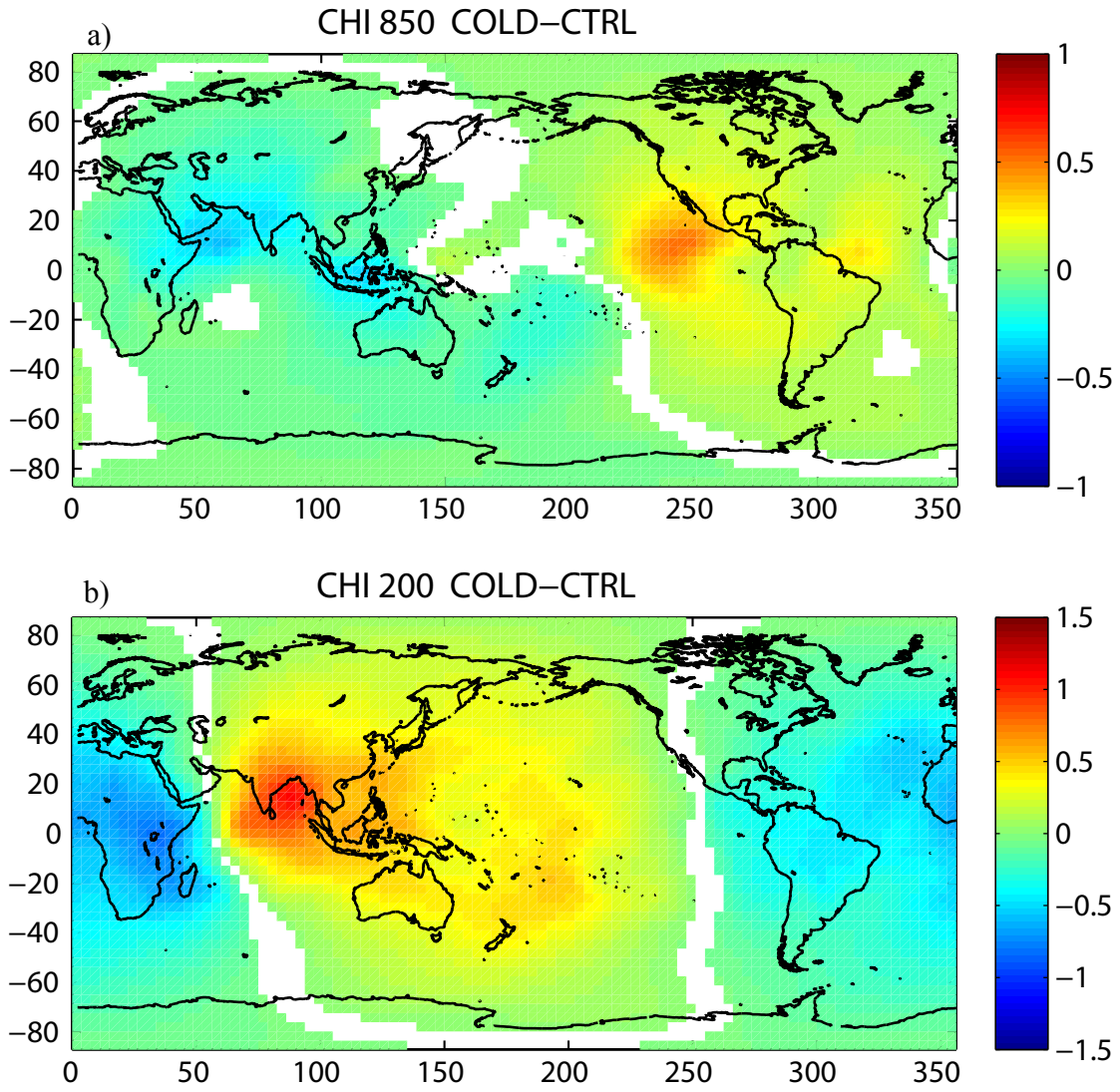

Figure 4.17: Differences in velocity potential between COLD and CTRL at: a) 850-hPa level; b) 200-hPa level. Units are $10^6 \mathrm{m}^2\mathrm{s}^{-1}$.

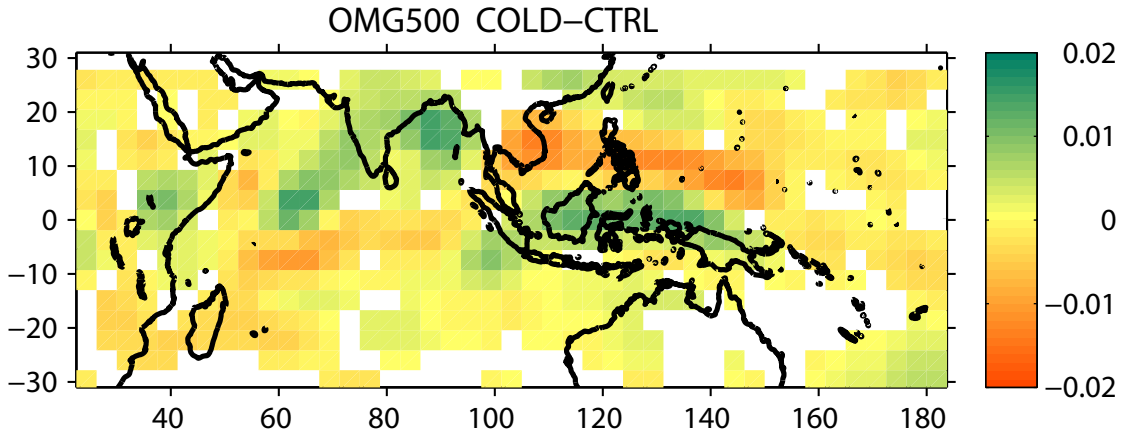

Figure 4.18: Differences in omega between COLD and CTRL at 500-hPa level. Units are Pa s^{-1}.

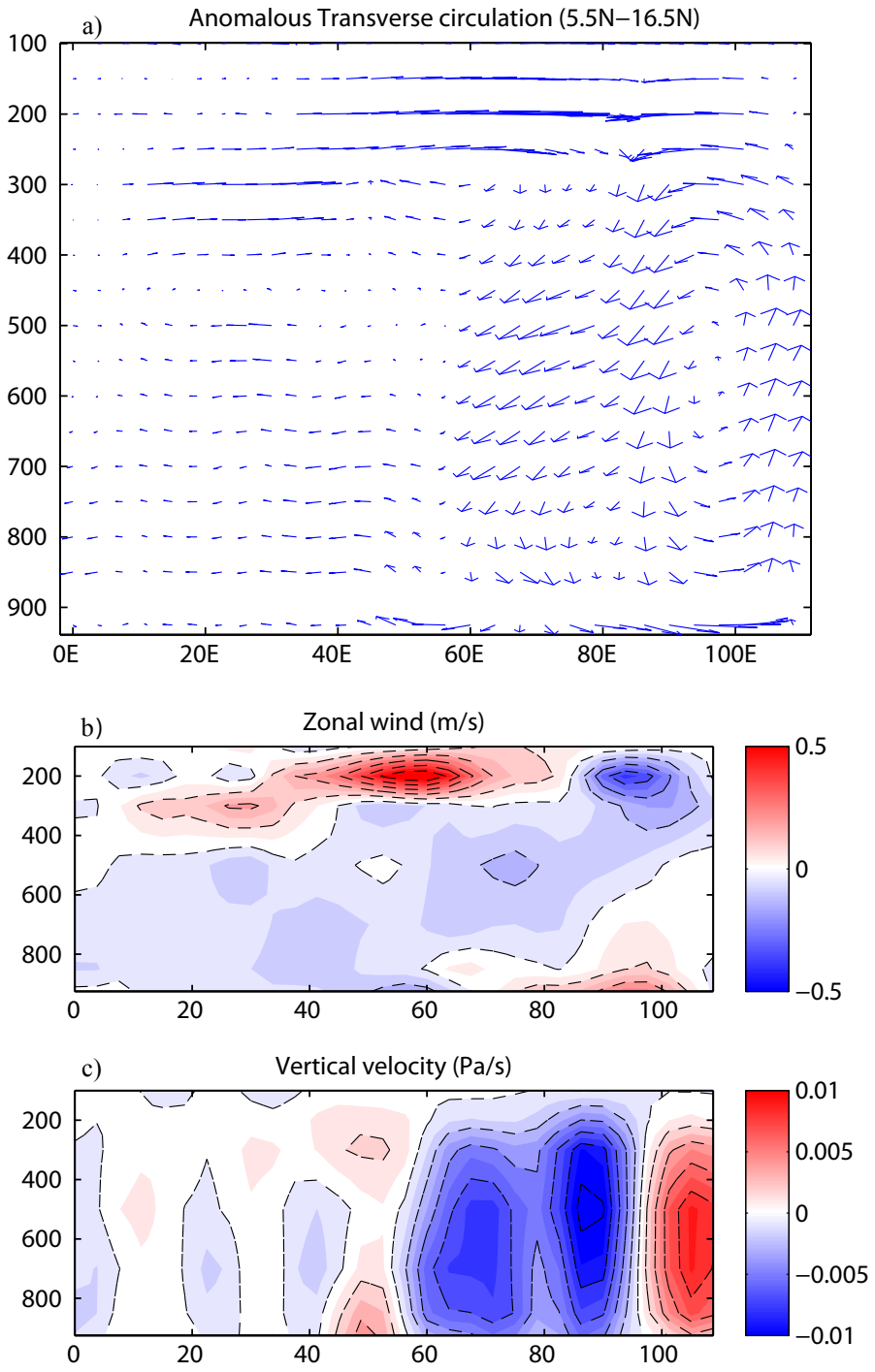

Figure 4.19: a) Anomalous transverse circulation (COLD - CTRL). Zonal divergent wind and omega differences are averaged between 5°N and 16°N from 0°E to 115°E. b) Cross section of zonal divergent wind differences. Units are ms^{-1}. c) Cross section of vertical velocity differences. The vertical velocity is taken the negative of the pressure vertical velocity. Units are Pa s^{-1}.

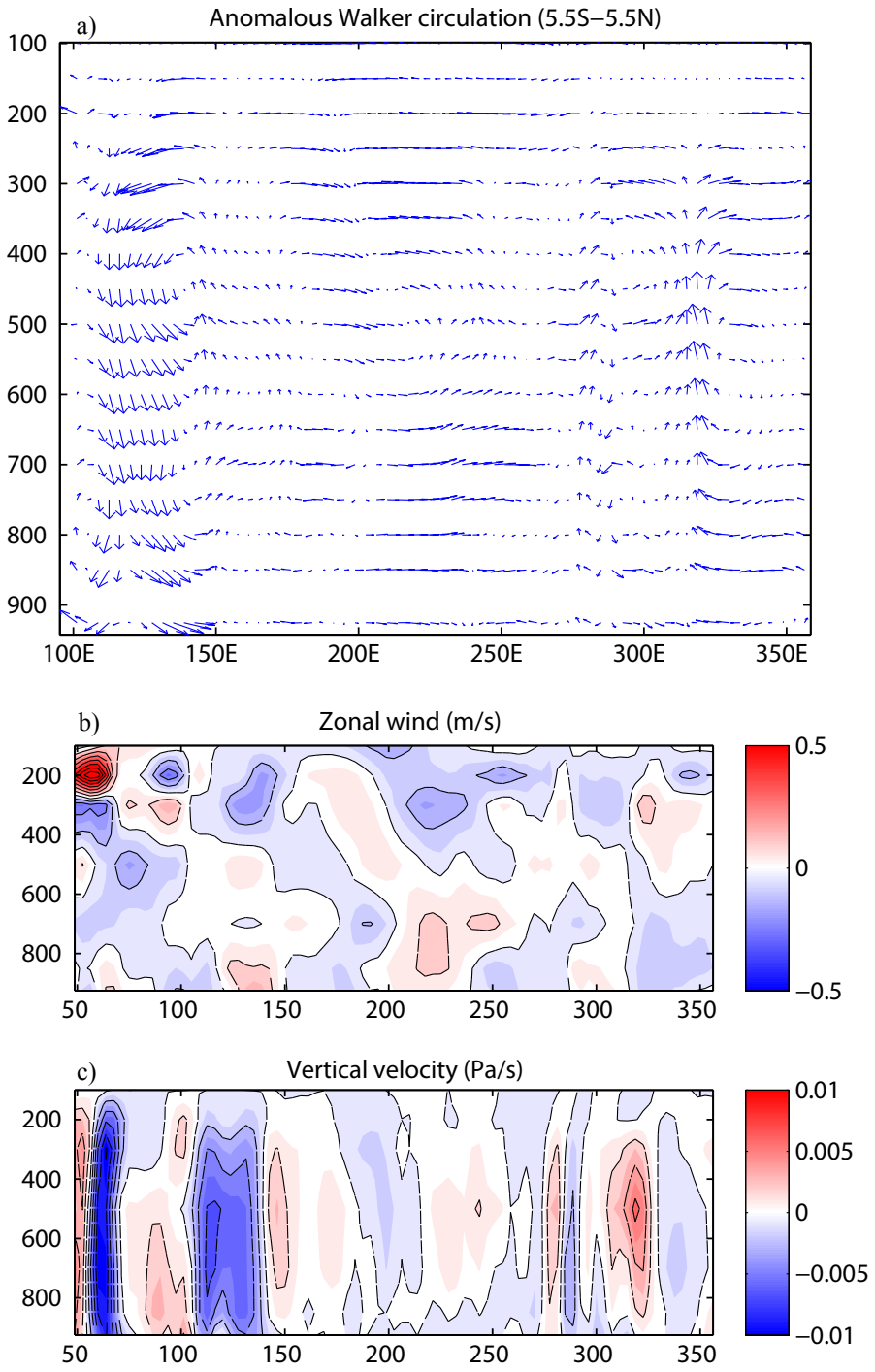

Figure 4.20: a) Anomalous Walker circulation (COLD - CTRL). Zonal divergent wind and omega anomalies are averaged between 5°S and 5°N from 100°E to 360°E. b) Cross section of zonal divergent wind differences along the equator. Units are ms^{-1}. c) Cross section of vertical velocity differences along the equator. Units are Pa s^{-1}.

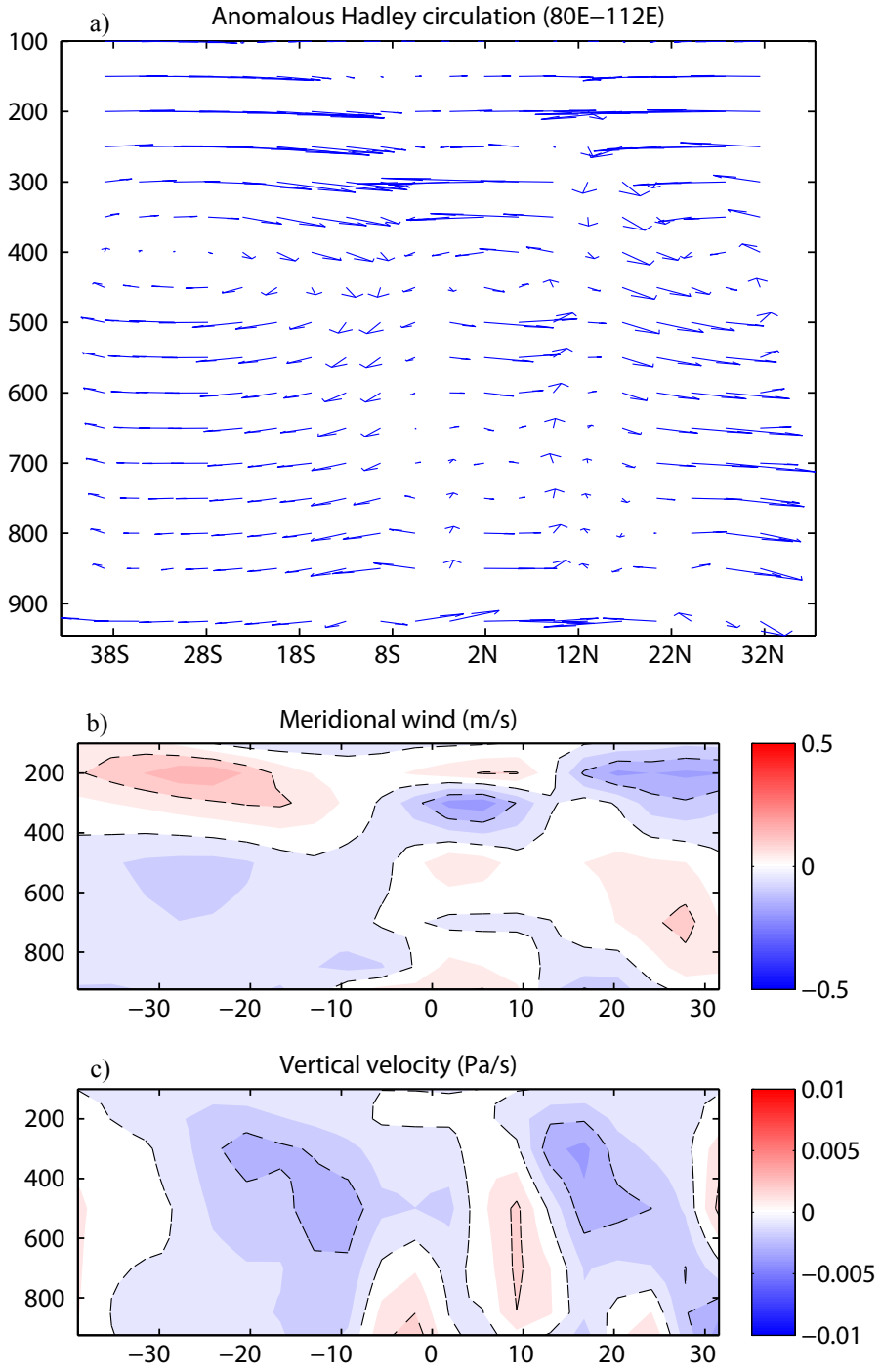

Figure 4.21: a) Anomalous local Hadley circulation over the eastern Indian Ocean (COLD - CTRL). b) Cross section of meridional divergent wind differences. Units are ms^{-1}. c) Cross section of vertical velocity differences. Units are Pa s^{-1}.

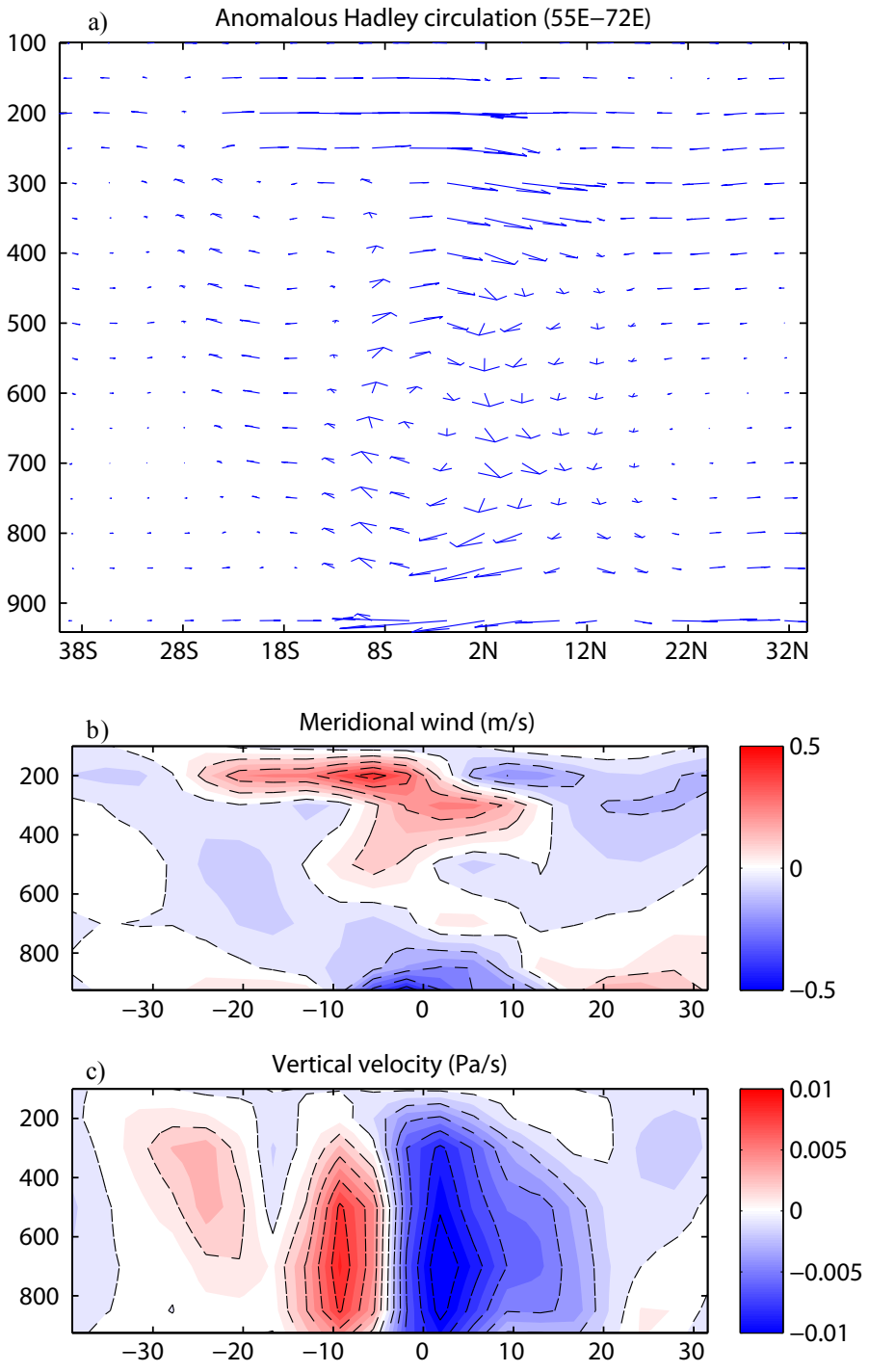

Figure 4.22: a) Anomalous local Hadley circulation over the western Indian Ocean (COLD - CTRL). b) Cross section of meridional divergent wind differences. Units are ms^{-1}. c) Cross section of vertical velocity differences. Units are Pa s^{-1}.

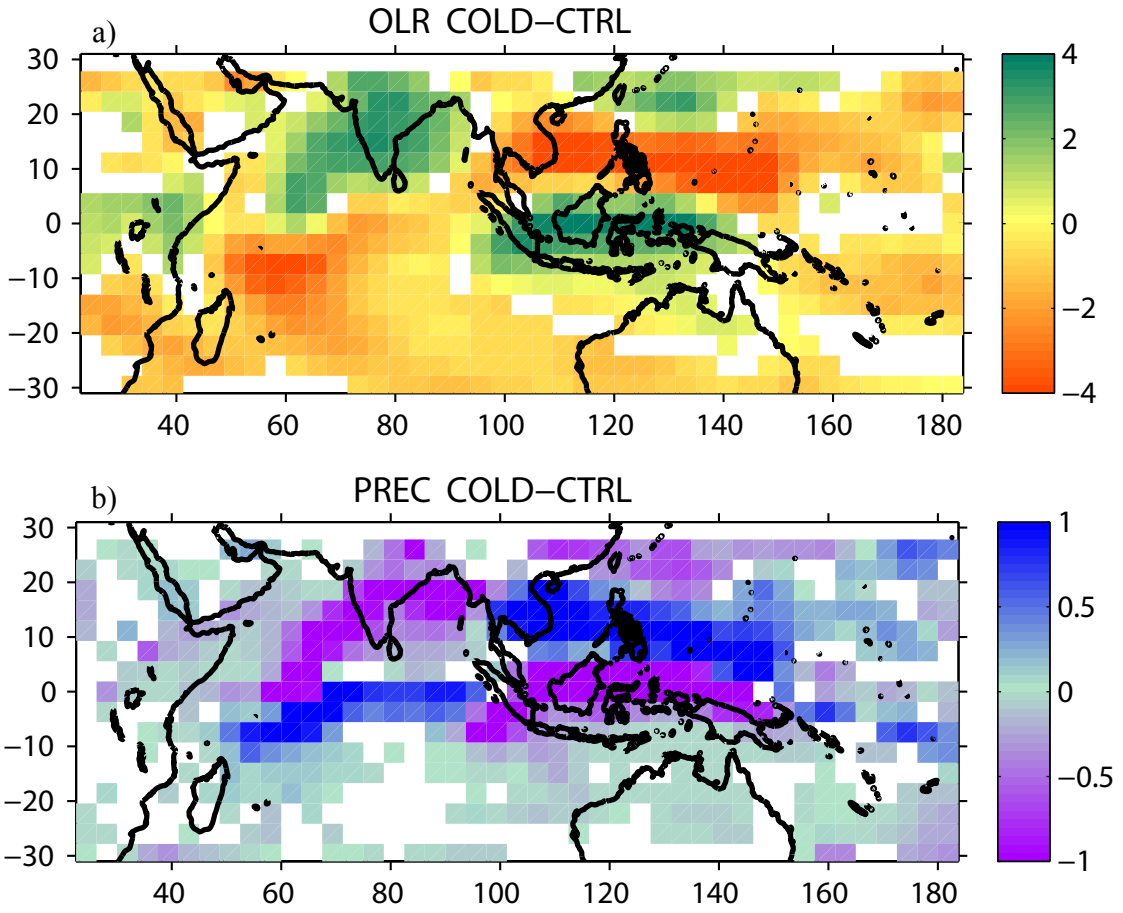

Figure 4.23: a) Differences in OLR between COLD and CTRL. b) As in a) but for precipitation.

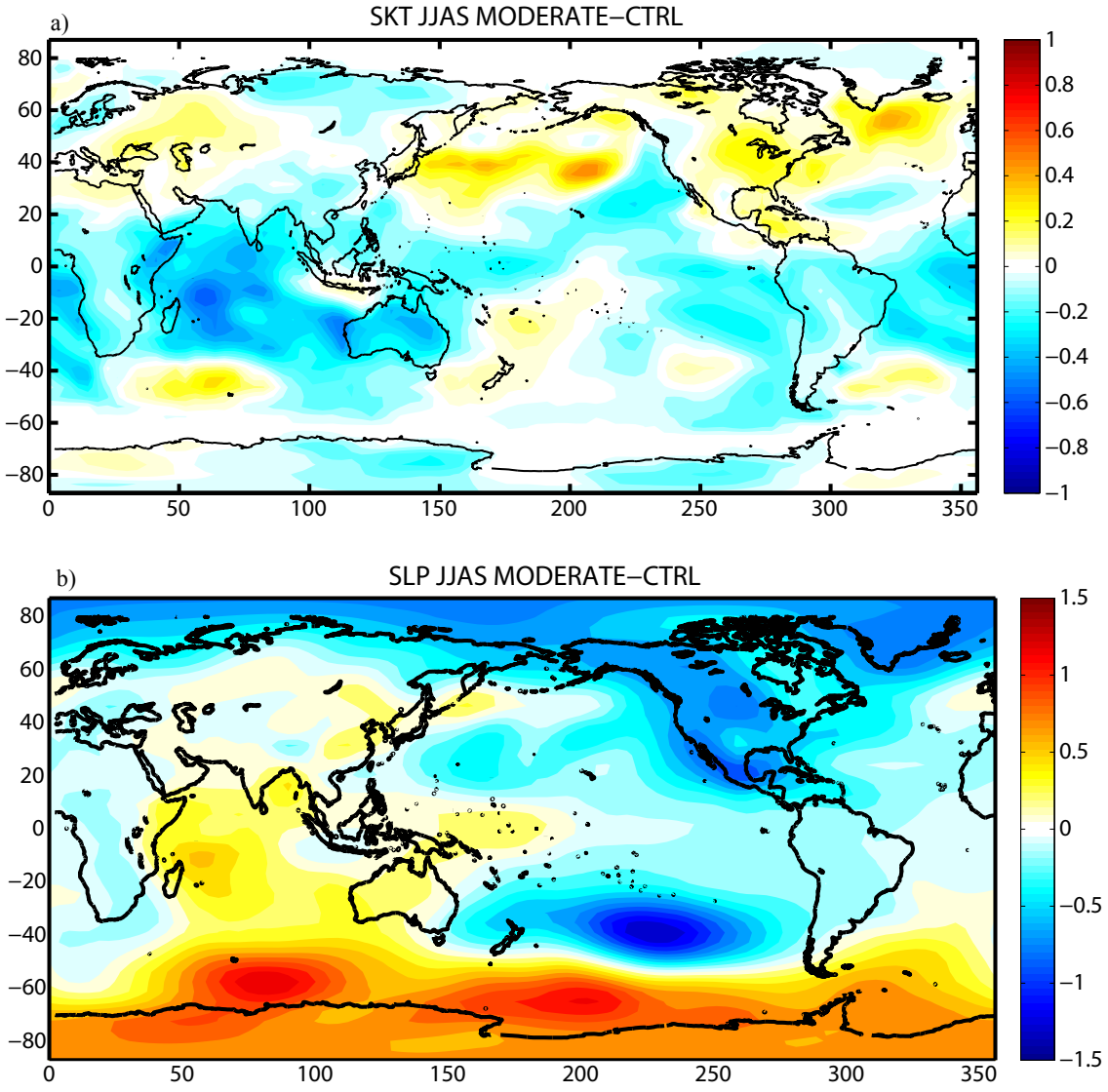

Figure 4.24: a) Differences in surface temperature between MODERATE and CTRL for the summer season. Units are °C. b) As in a) but for sea level pressure. Units are hPa.

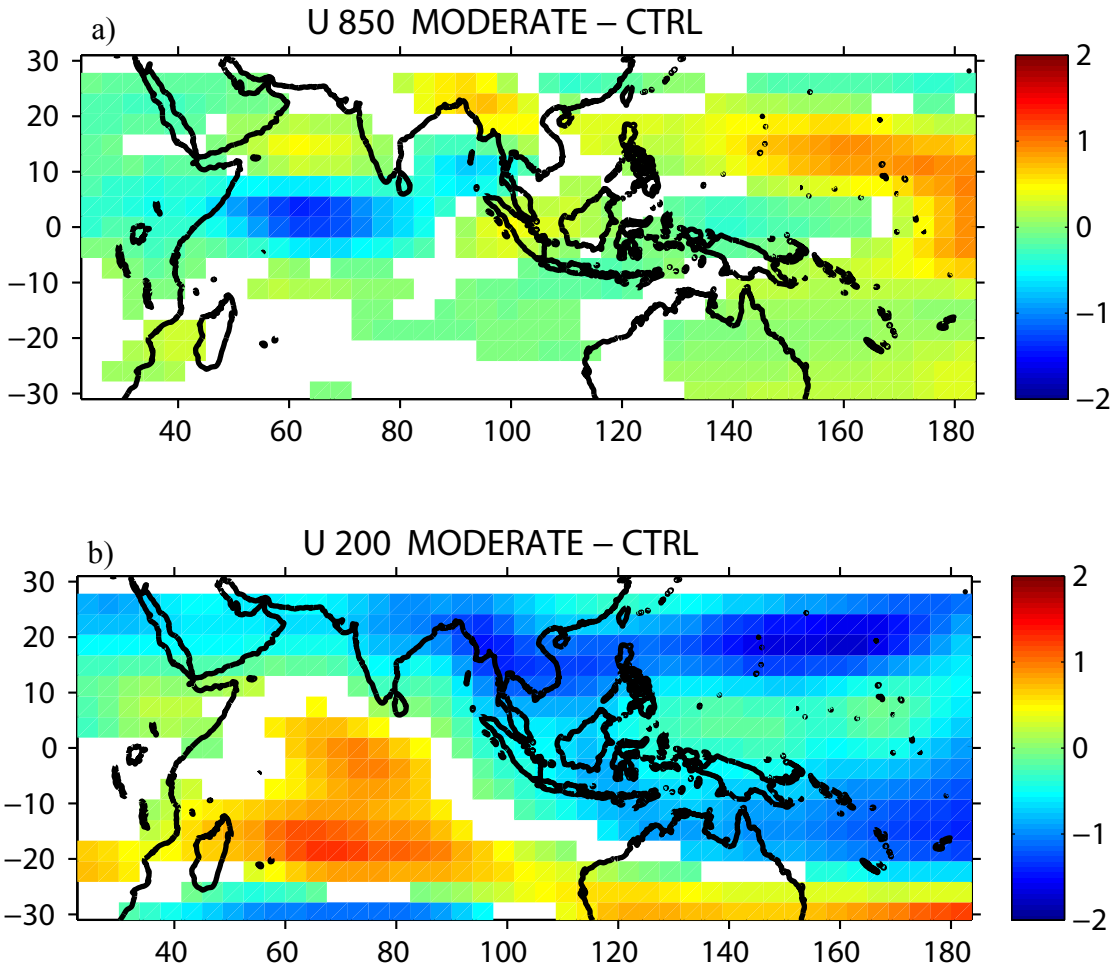

Figure 4.25: Differences in zonal wind between MODERATE and CTRL at: a) 850-hPa level; b) 200-hPa level. Units are ms^{-1}.

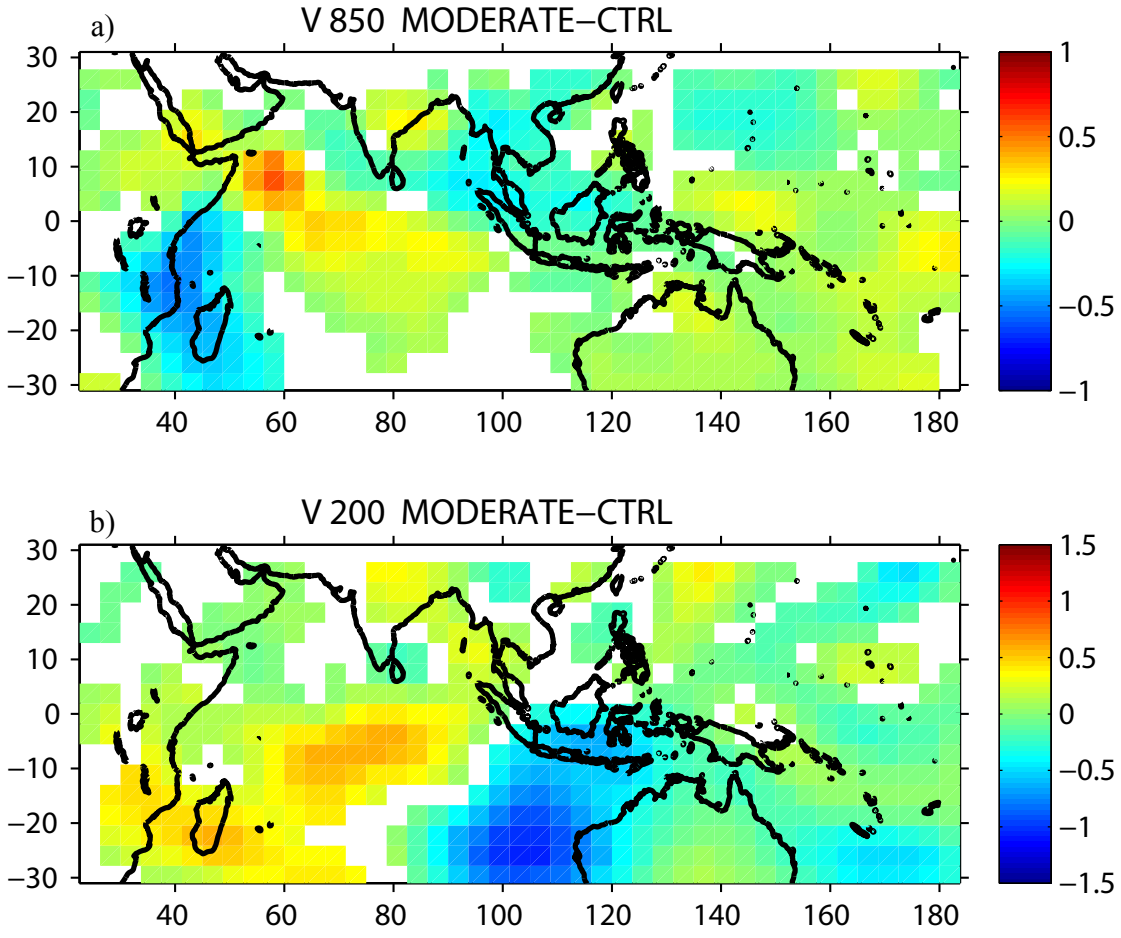

Figure 4.26: Differences in meridional wind between MODERATE and CTRL at: a) 850-hPa level; b) 200-hPa level. Units are ms^{-1}.

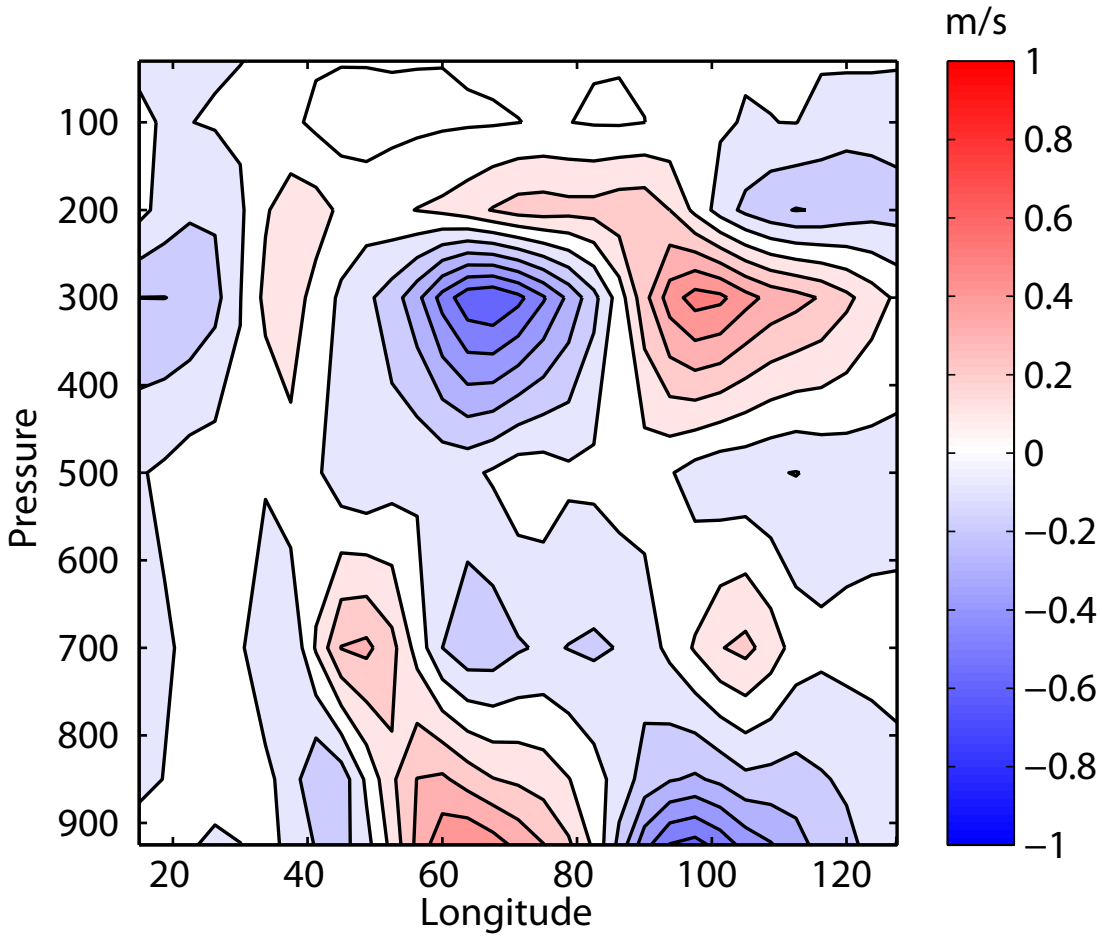

Figure 4.27: Seasonal mean cross equatorial meridional wind differences between MODERATE and CTRL. Meridional wind differences are averaged between 5°S and 5°N. Units are ms^{-1}.

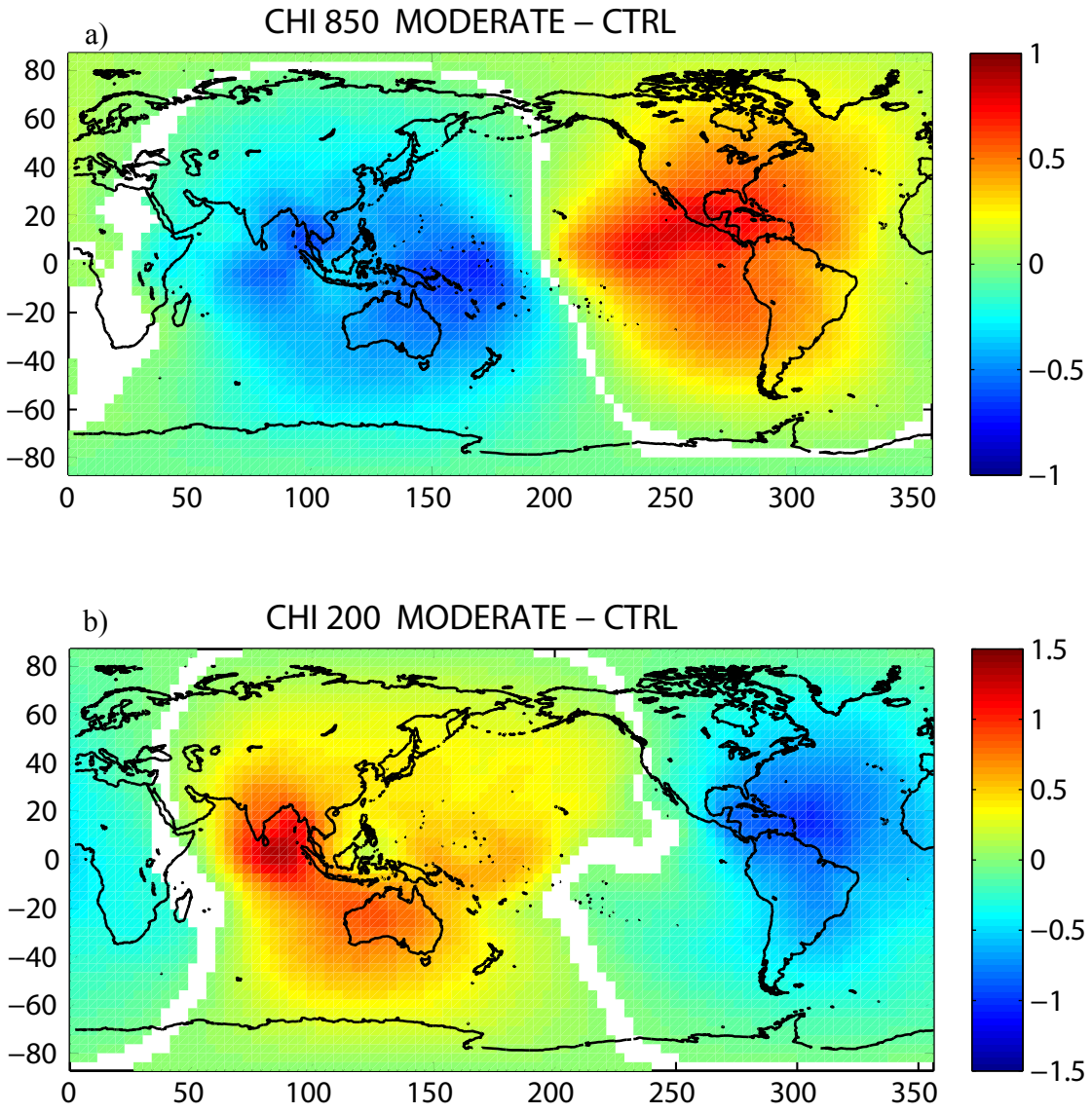

Figure 4.28: Differences in velocity potential between MODERATE and CTRL at: a) 850-hPa level; b) 200-hPa level.

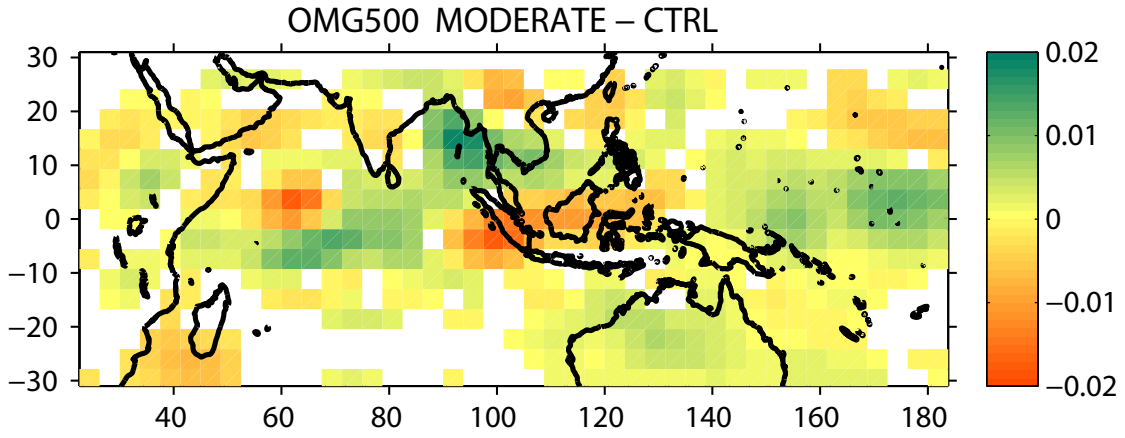

Figure 4.29: Differences in omega between MODERATE and CTRL at 500-hPa level.

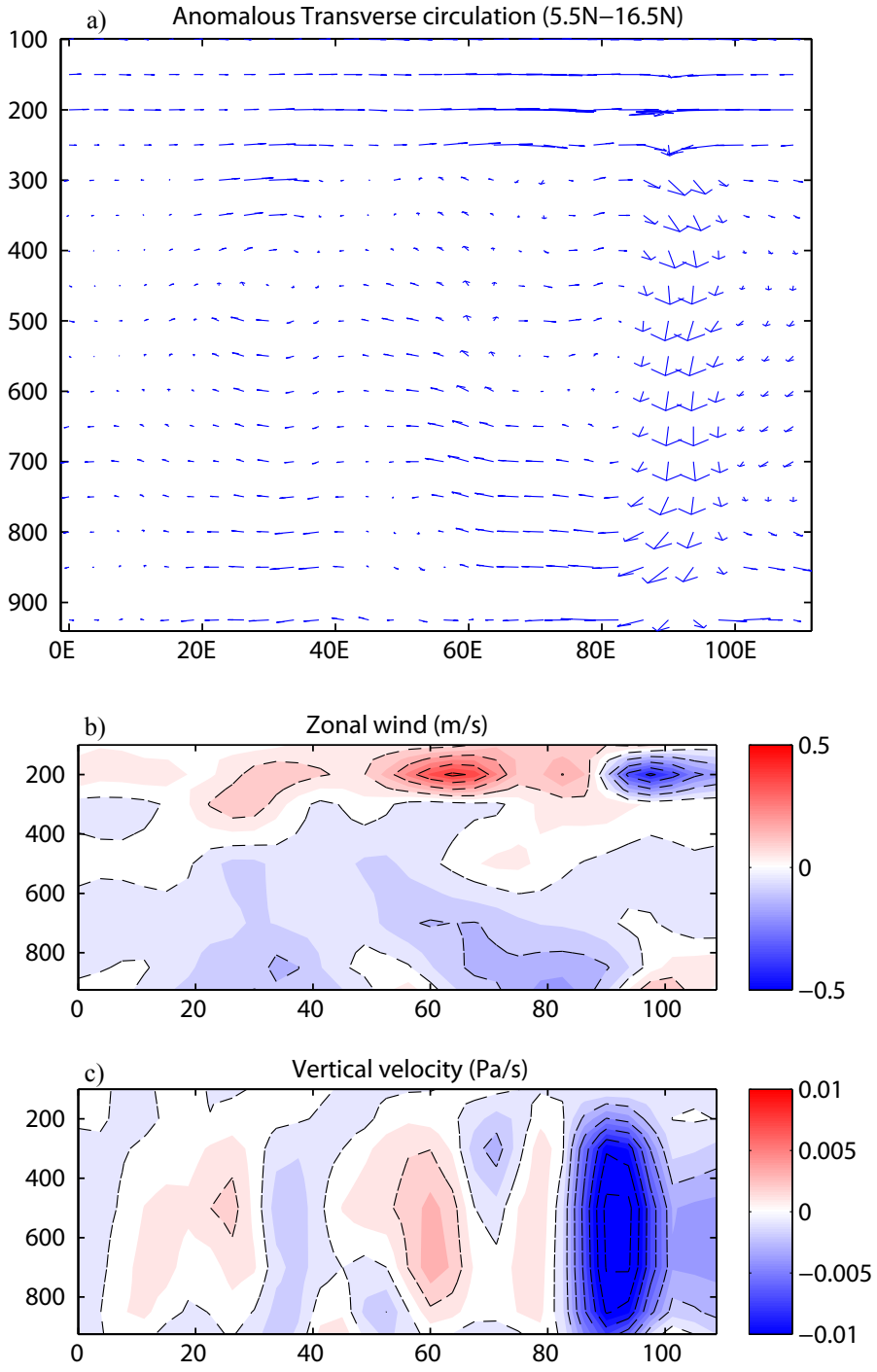

Figure 4.30: a) Anomalous transverse circulation (MODERATE-CTRL). b) Cross section of zonal divergent wind differences. Units are ms^{-1}. c) Cross section of vertical velocity differences. Units are Pa s^{-1}.

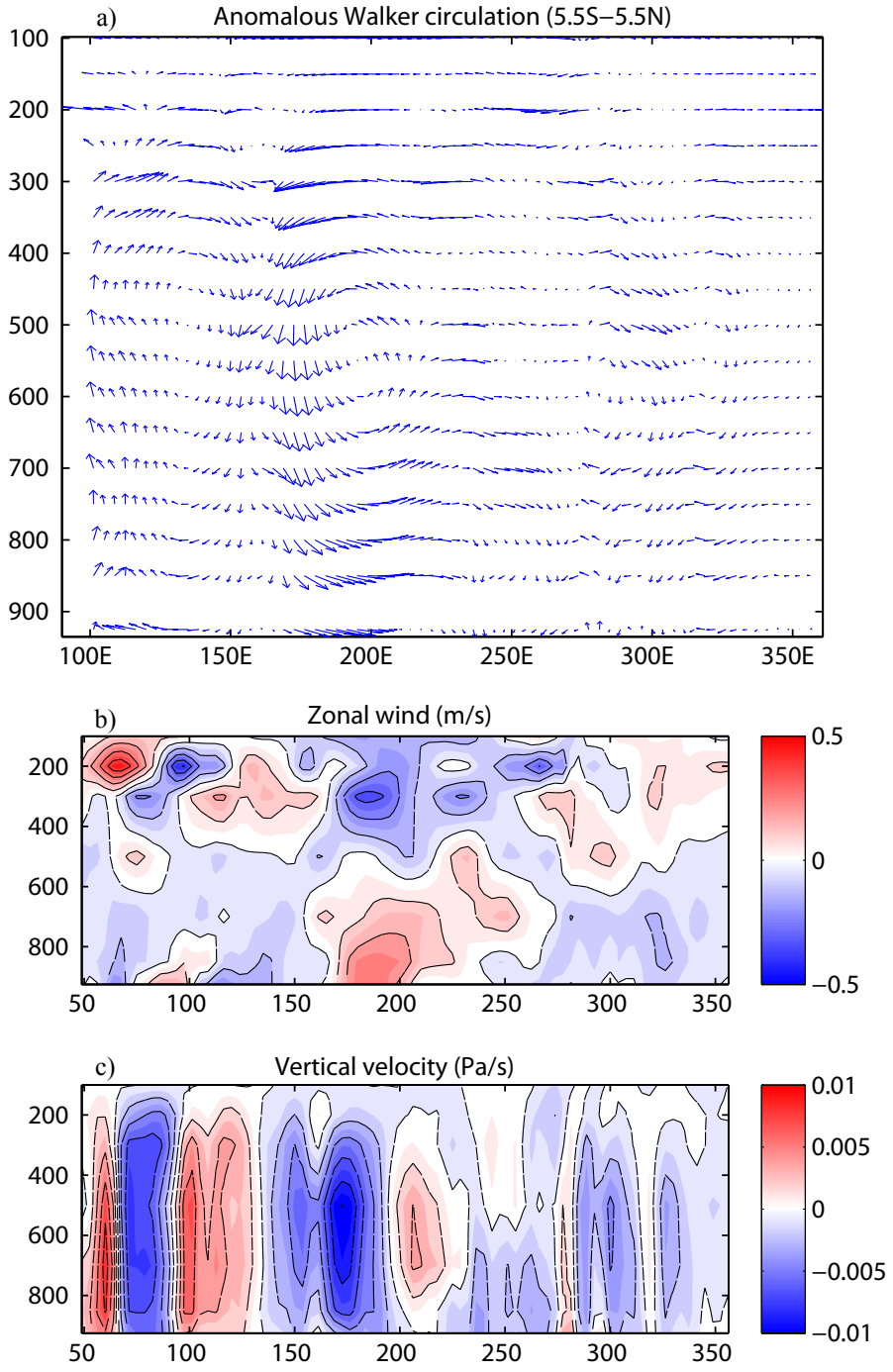

Figure 4.31: a) Anomalous Walker circulation (MODERATE-CTRL). b) Cross section of zonal divergent wind differences along the equator. Units are ms^{-1}. c) Cross section of vertical velocity differences along the equator. Units are Pa s^{-1}.

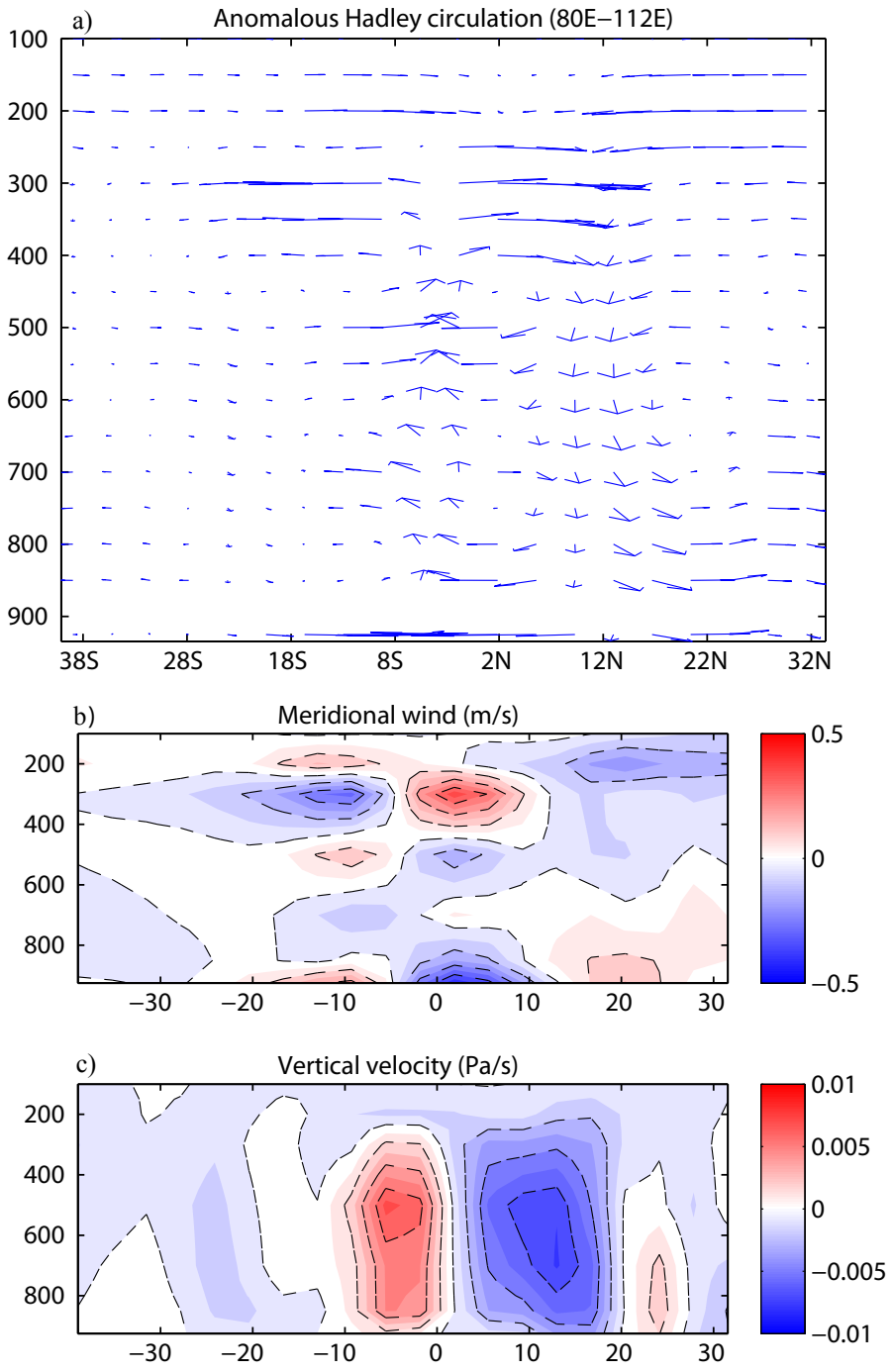

Figure 4.32: a) Anomalous local Hadley circulation over the eastern Indian Ocean (MODERATE-CTRL). b) Cross section of meridional divergent wind anomalies. Units are ms^{-1}. c) Cross section of vertical velocity anomalies. Units are $\mathrm{Pa\ s}^{-1}$.

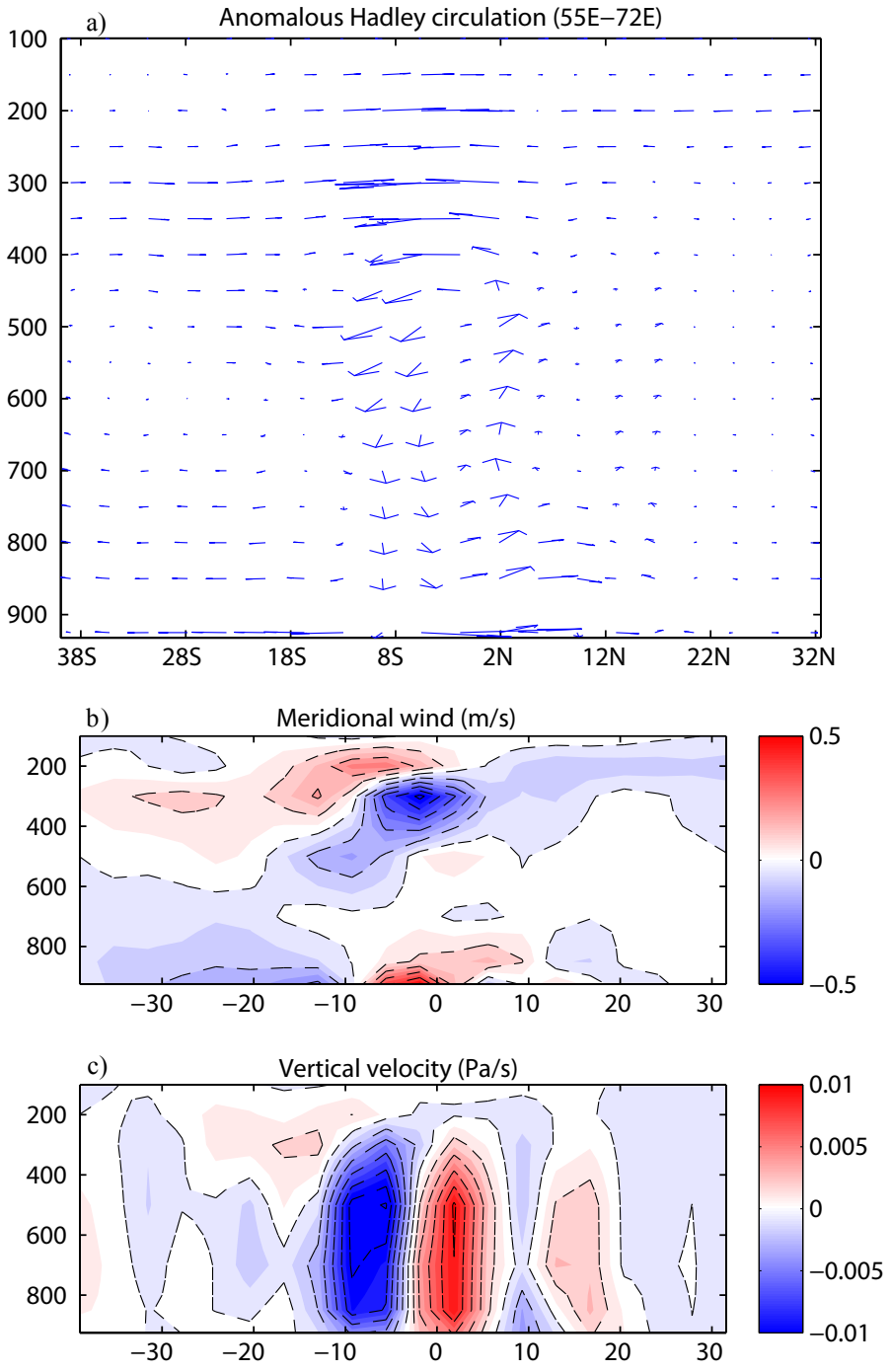

Figure 4.33: a) Anomalous local Hadley circulation over the western Indian Ocean (MODERATE-CTRL). b) Cross section of meridional divergent wind anomalies. Units are ms^{-1}. c) Cross section of vertical velocity anomalies. Units are Pa s^{-1}.

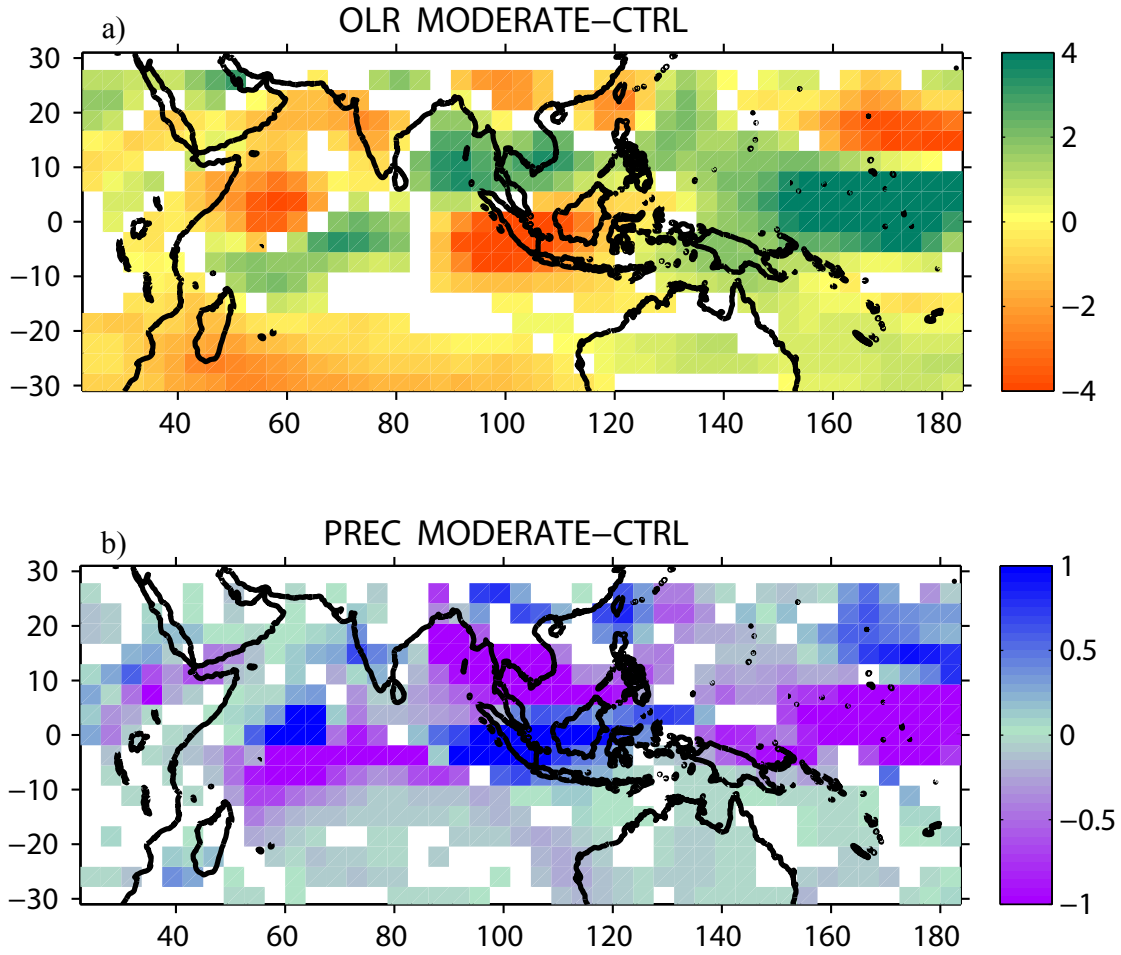

Figure 4.34: a) Differences in OLR between MODERATE and CTRL. b) As in a) but for precipitation.

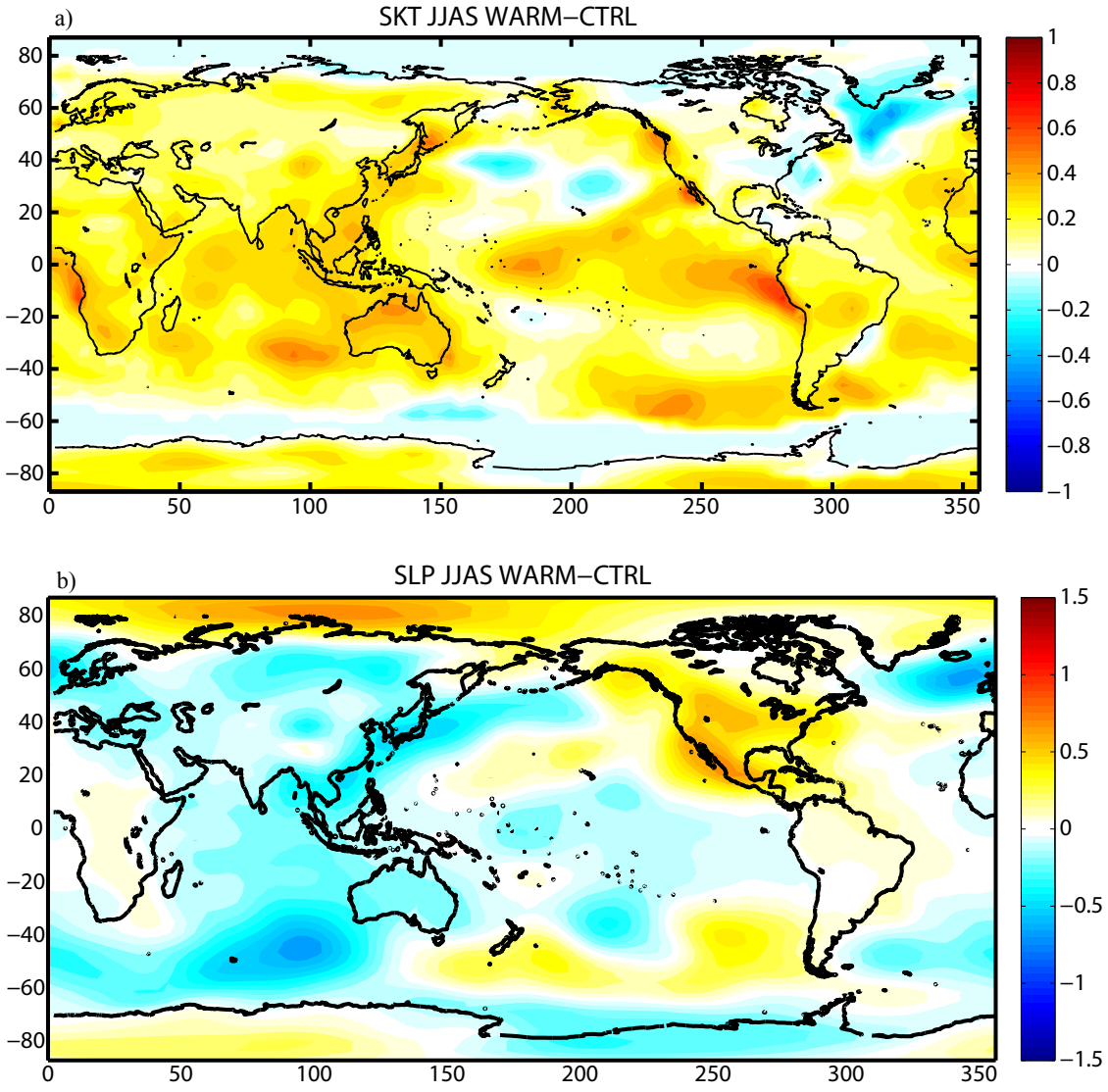

Figure 4.35: a) Differences in surface temperature between WARM and CTRL for the summer season. Units are °C. b) As in a) but for sea level pressure. Units are hPa.

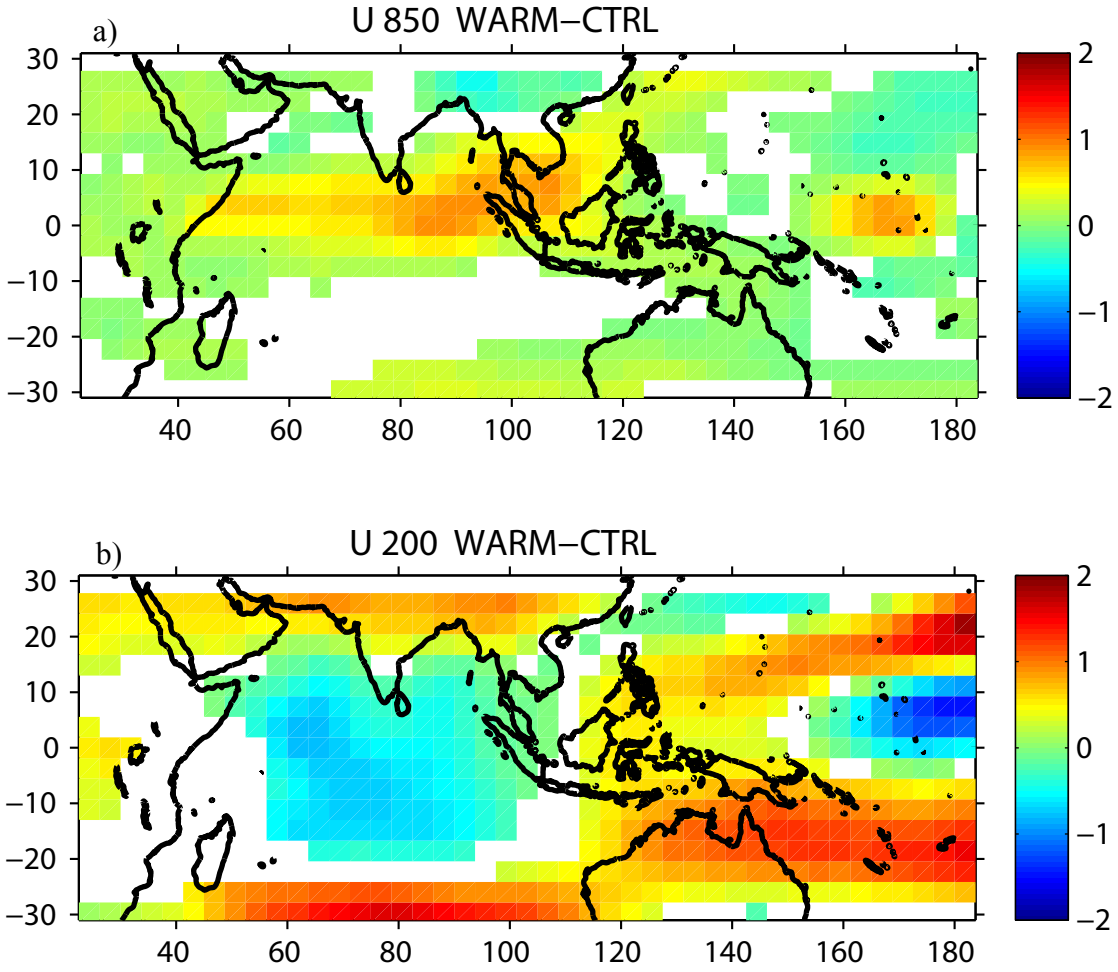

Figure 4.36: Differences in zonal wind between WARM and CTRL at a) 850-hPa level; b) 200-hPa level. Units are ms^{-1}.

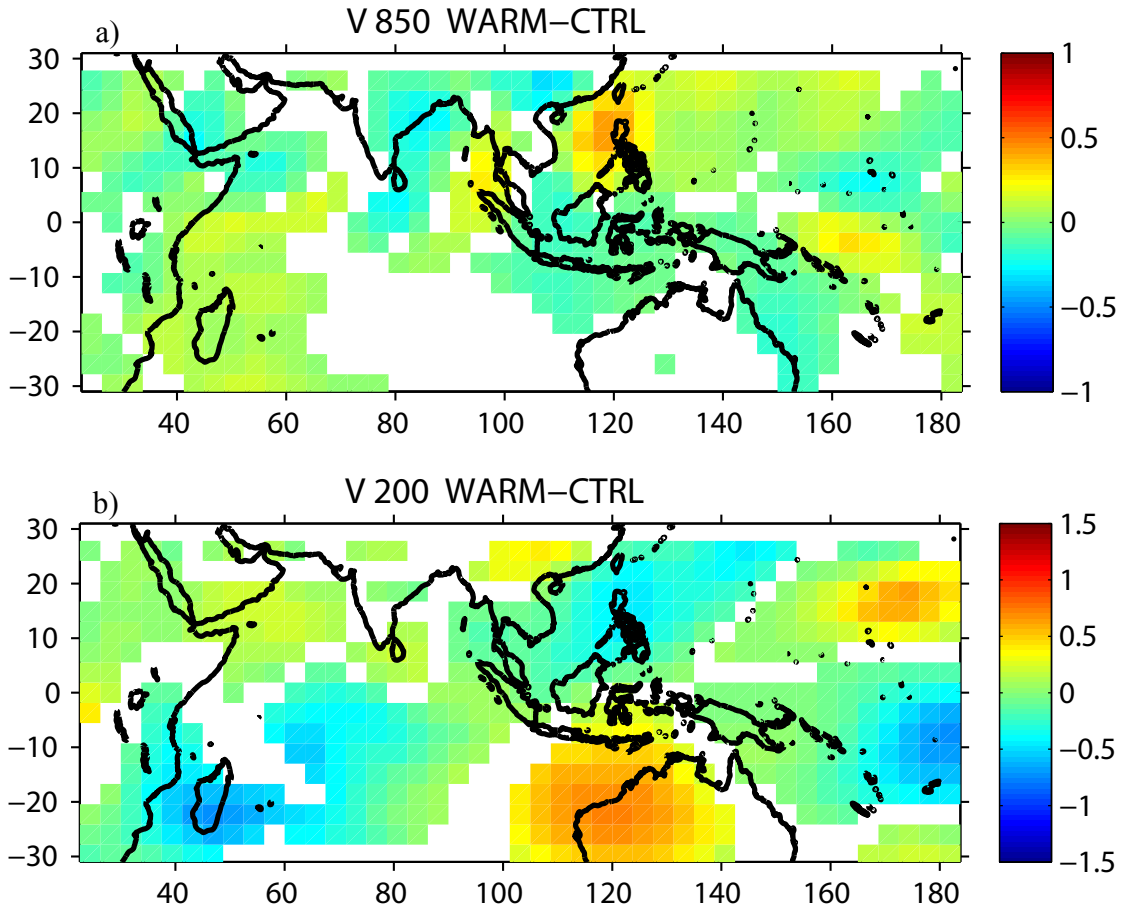

Figure 4.37: Differences in meridional wind between WARM and CTRL at a) 850-hPa level; b) 200-hPa level. Units are ms^{-1}.

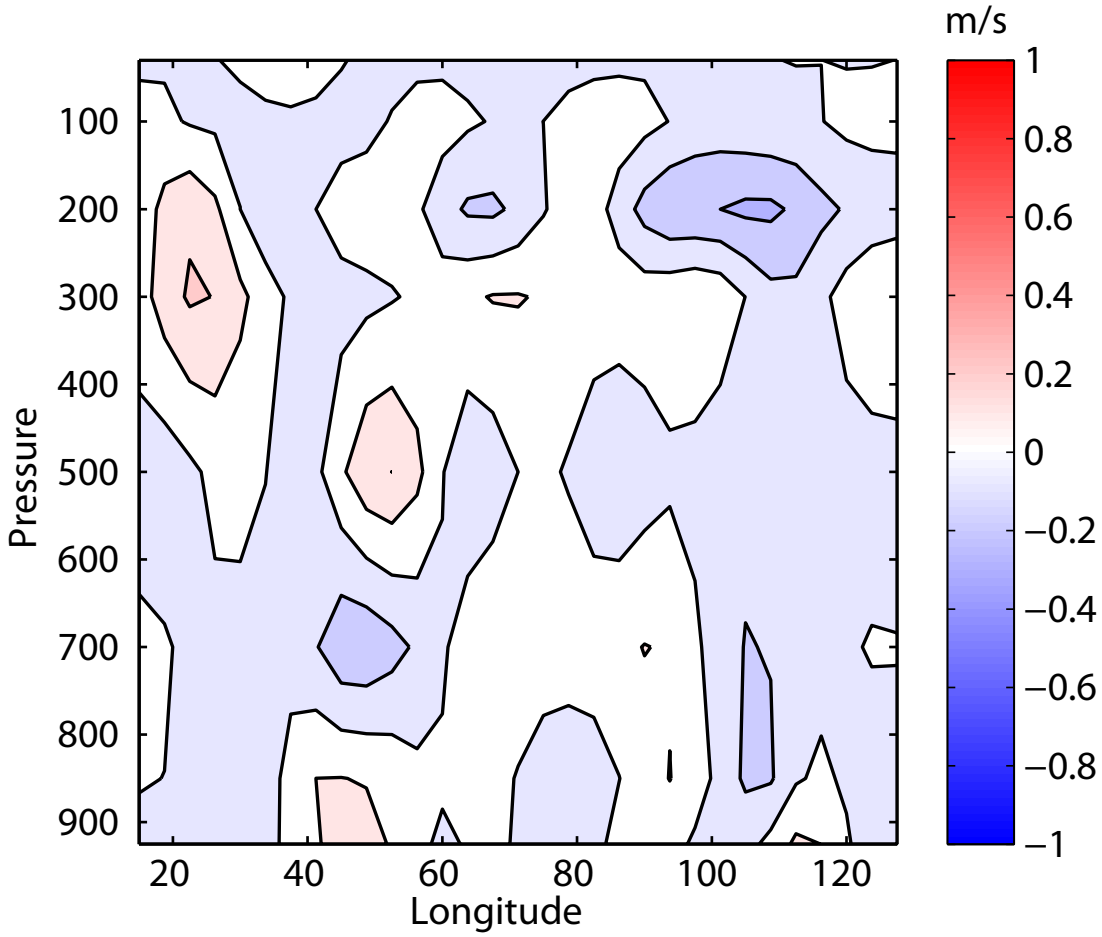

Figure 4.38: Seasonal mean cross equatorial meridional wind differences between WARM and CTRL. Meridional wind differences are averaged between 5°S and 5°N.

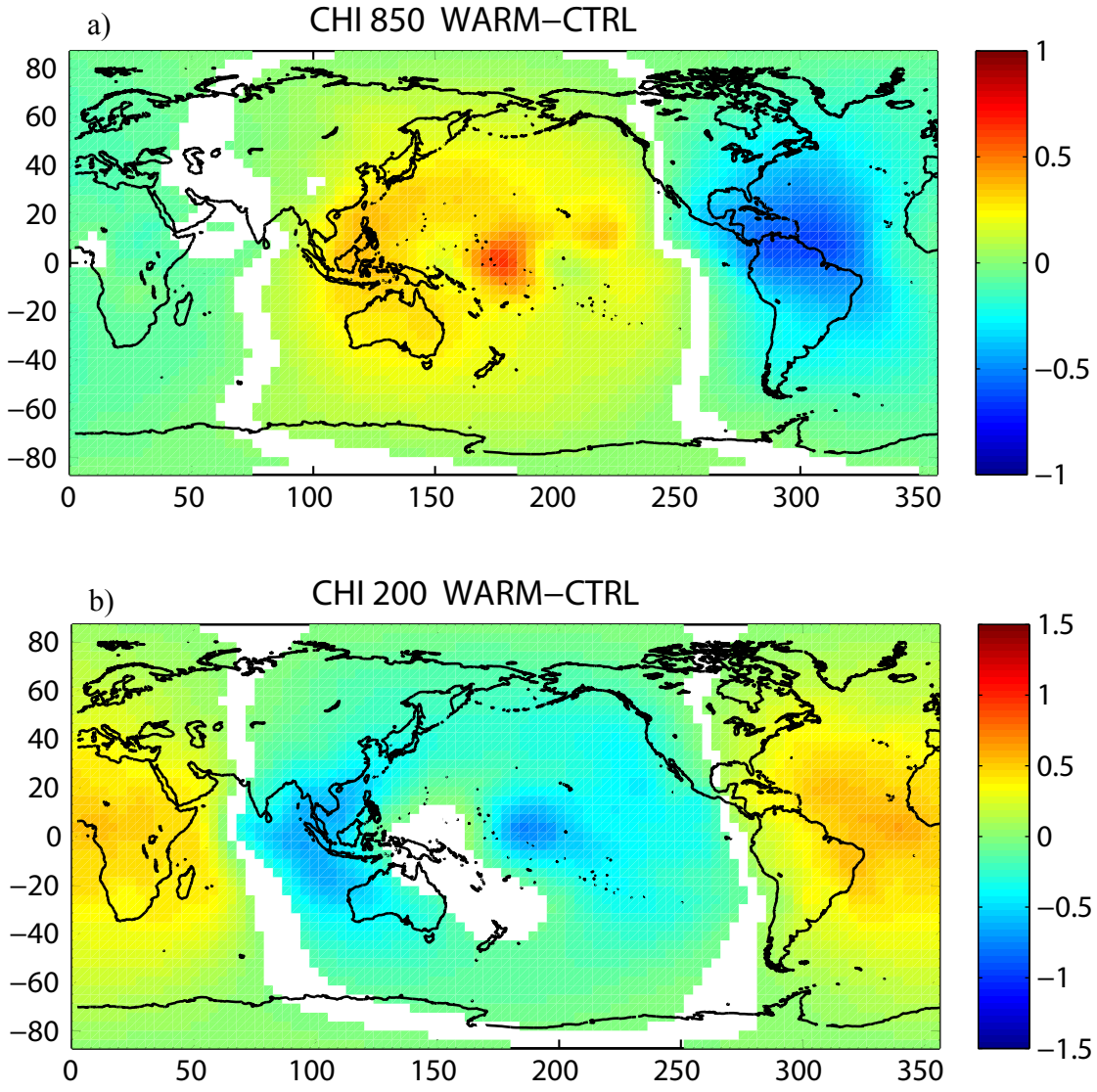

Figure 4.39: Differences in velocity potential between WARM and CTRL at a) 850-hPa level; b) 200-hPa level.

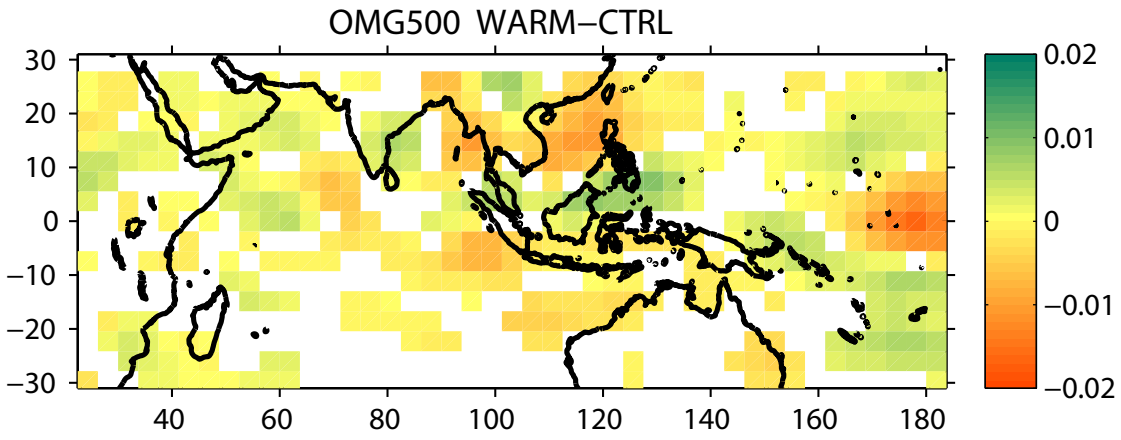

Figure 4.40: Differences in omega between WARM and CTRL at 500-hPa level.

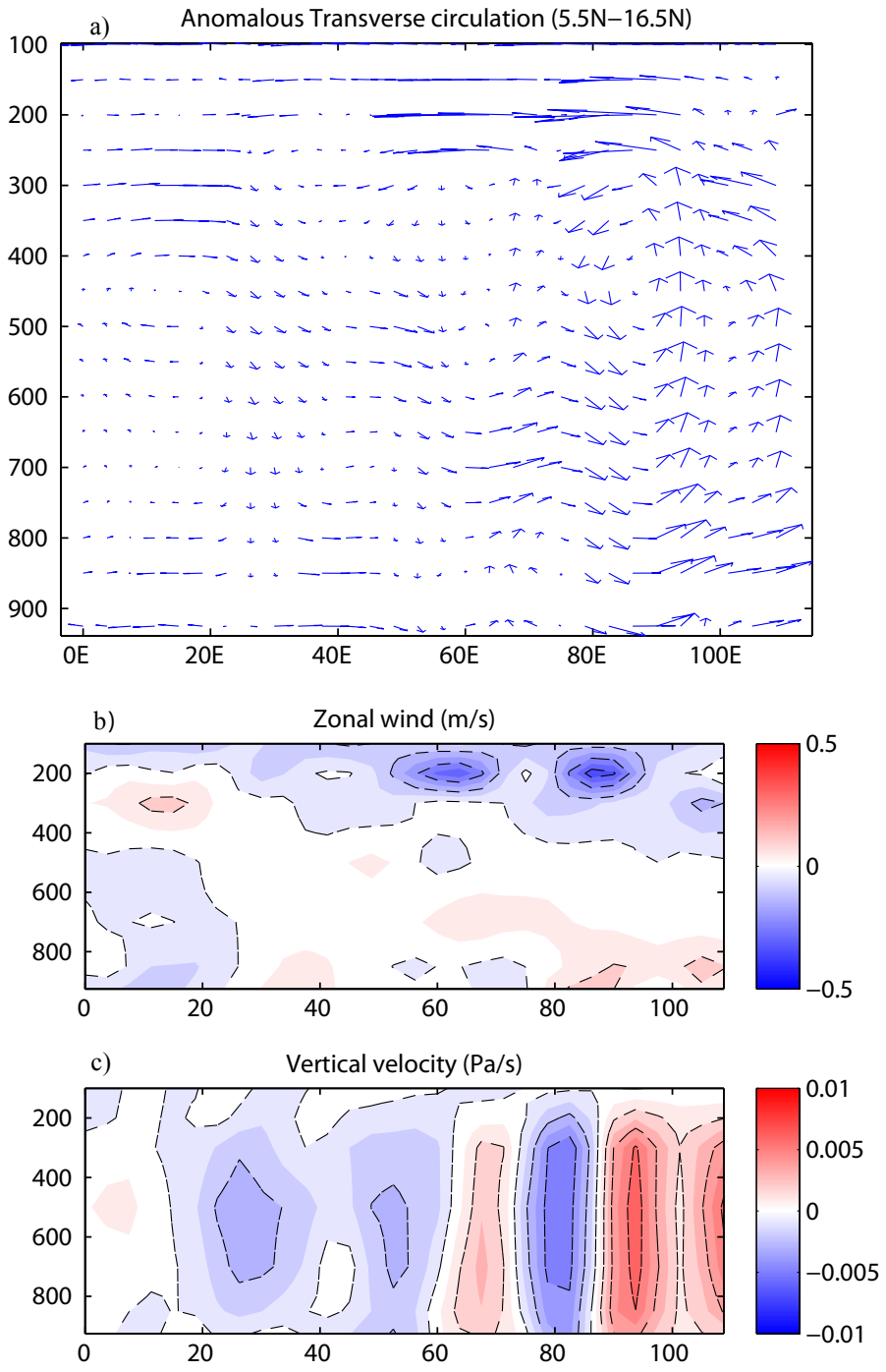

Figure 4.41: a) Anomalous transverse circulation (WARM-CTRL). b) Cross section of zonal divergent wind differences along the equator. Units are ms^{-1}. c) Cross section of vertical velocity differences along the equator. Units are Pa s^{-1}.

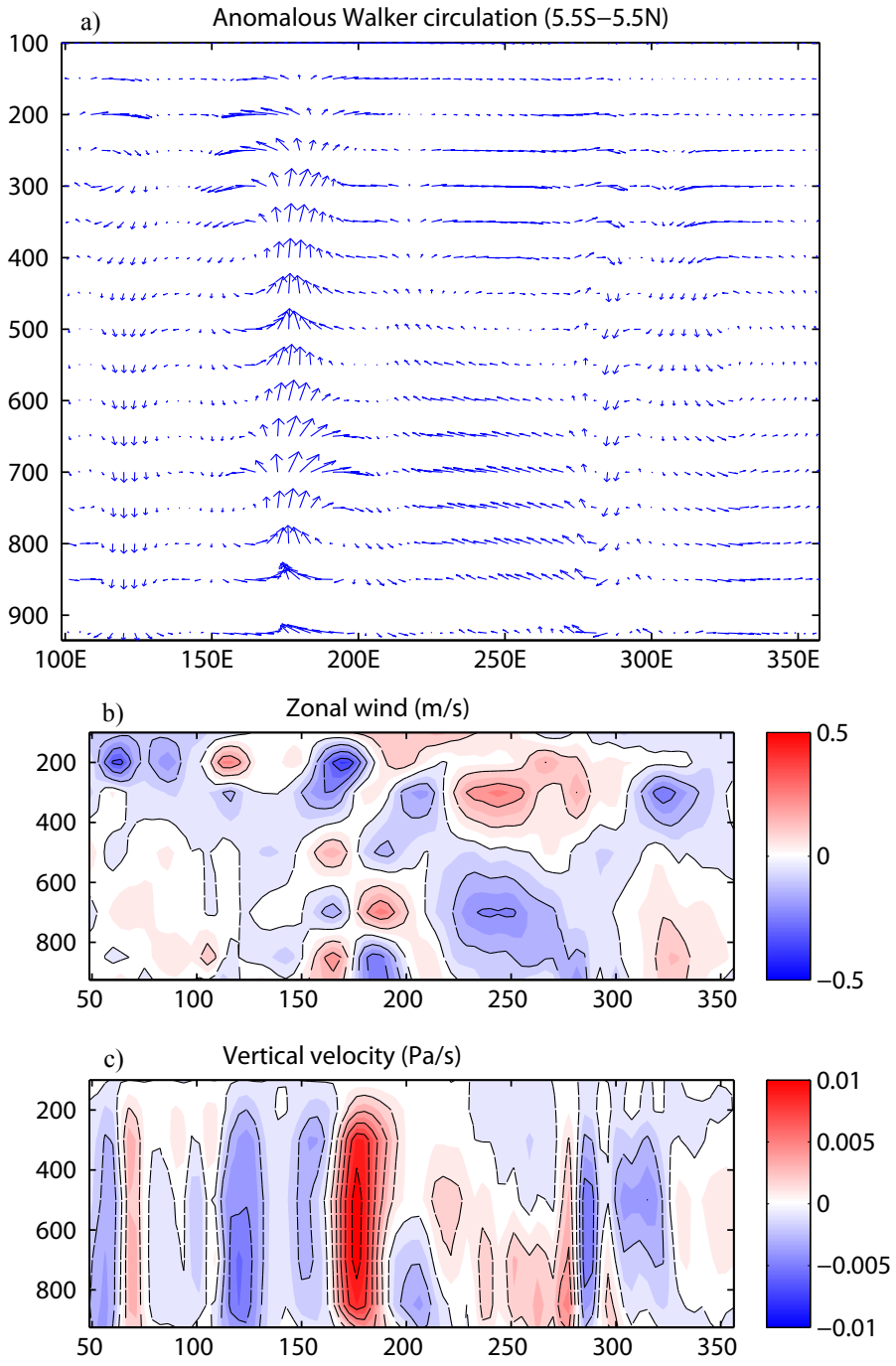

Figure 4.42: a) Anomalous Walker circulation (WARM-CTRL). b) Cross section of zonal divergent wind differences along the equator. Units are ms^{-1}. c) Cross section of vertical velocity differences along the equator. Units are Pa s^{-1}.

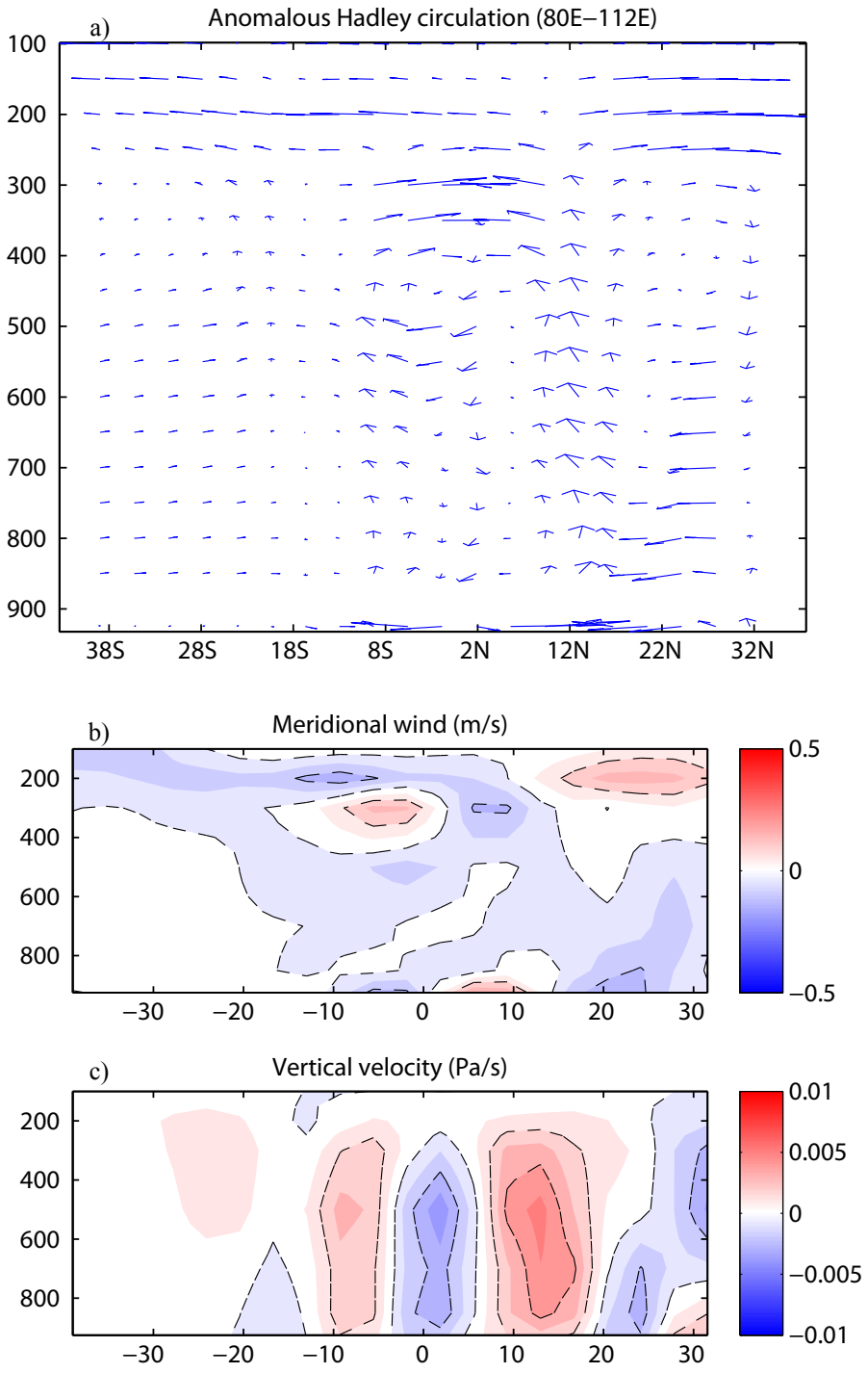

Figure 4.43: a) Anomalous local Hadley circulation over the eastern Indian Ocean (WARM-CTRL). b) Cross section of meridional divergent wind anomalies. Units are ms^{-1}. c) Cross section of vertical velocity anomalies. Units are Pa s^{-1}.

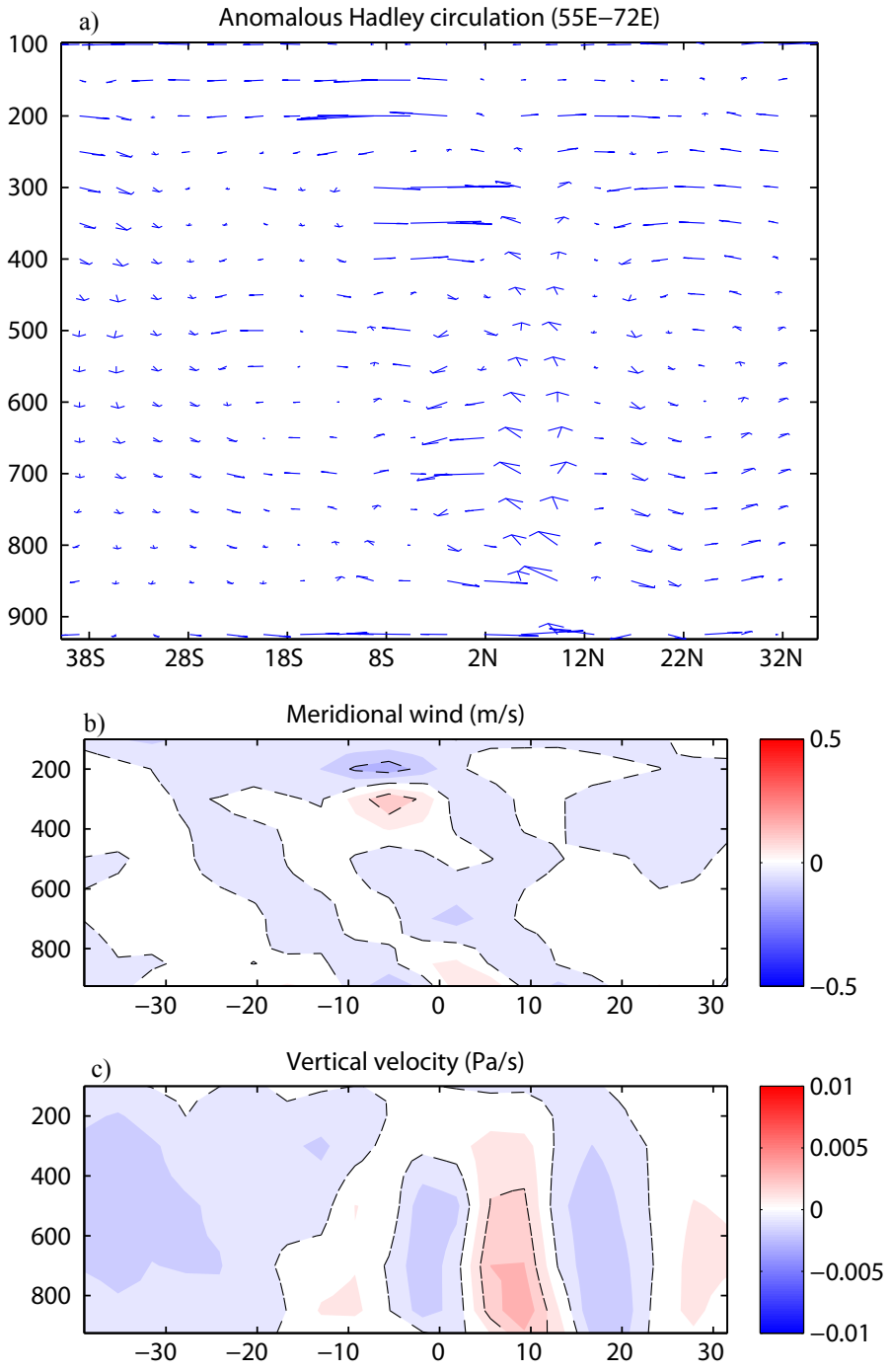

Figure 4.44: a) Anomalous local Hadley circulation over the western Indian Ocean (WARM-CTRL). b) Cross section of meridional divergent wind anomalies. Units are ms^{-1}. c) Cross section of vertical velocity anomalies. Units are Pa s^{-1}.

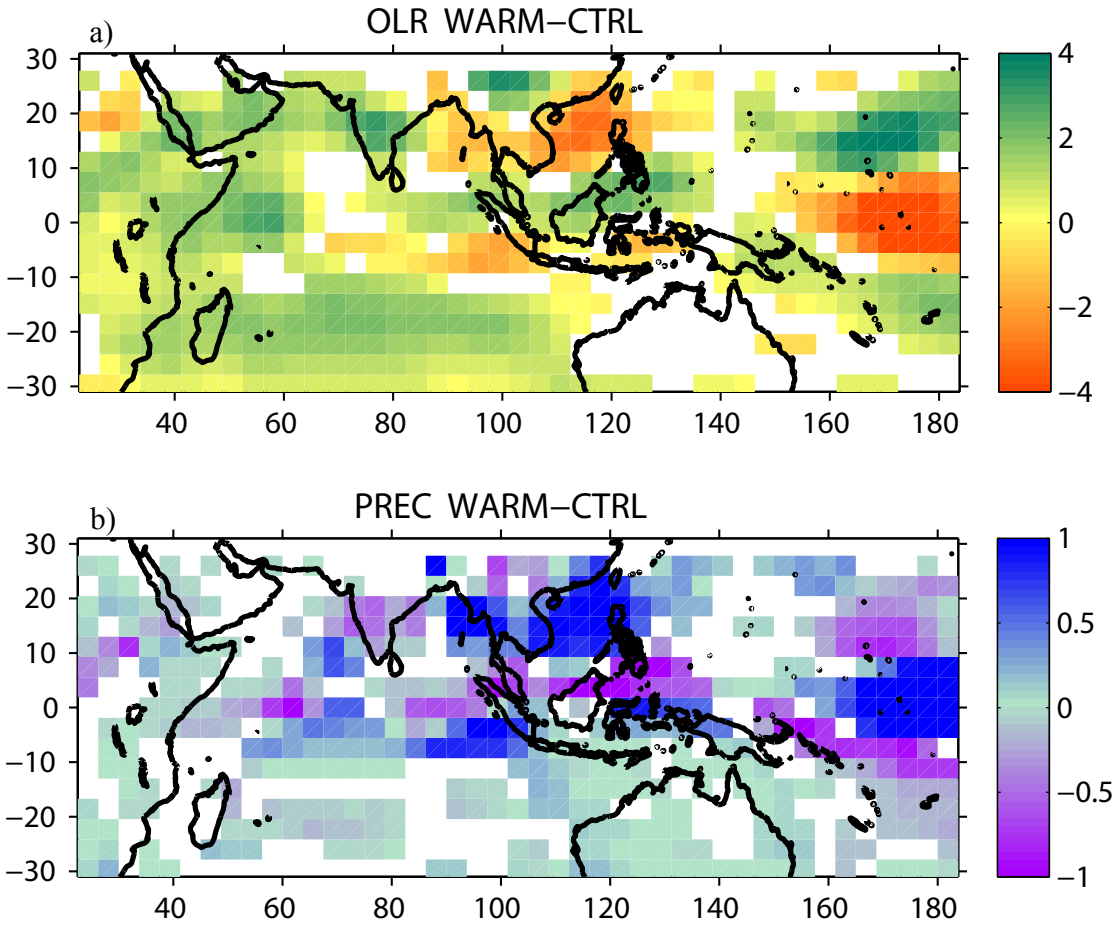

Figure 4.45: a) Differences in OLR between WARM and CTRL. b) As in a) but for precipitation.

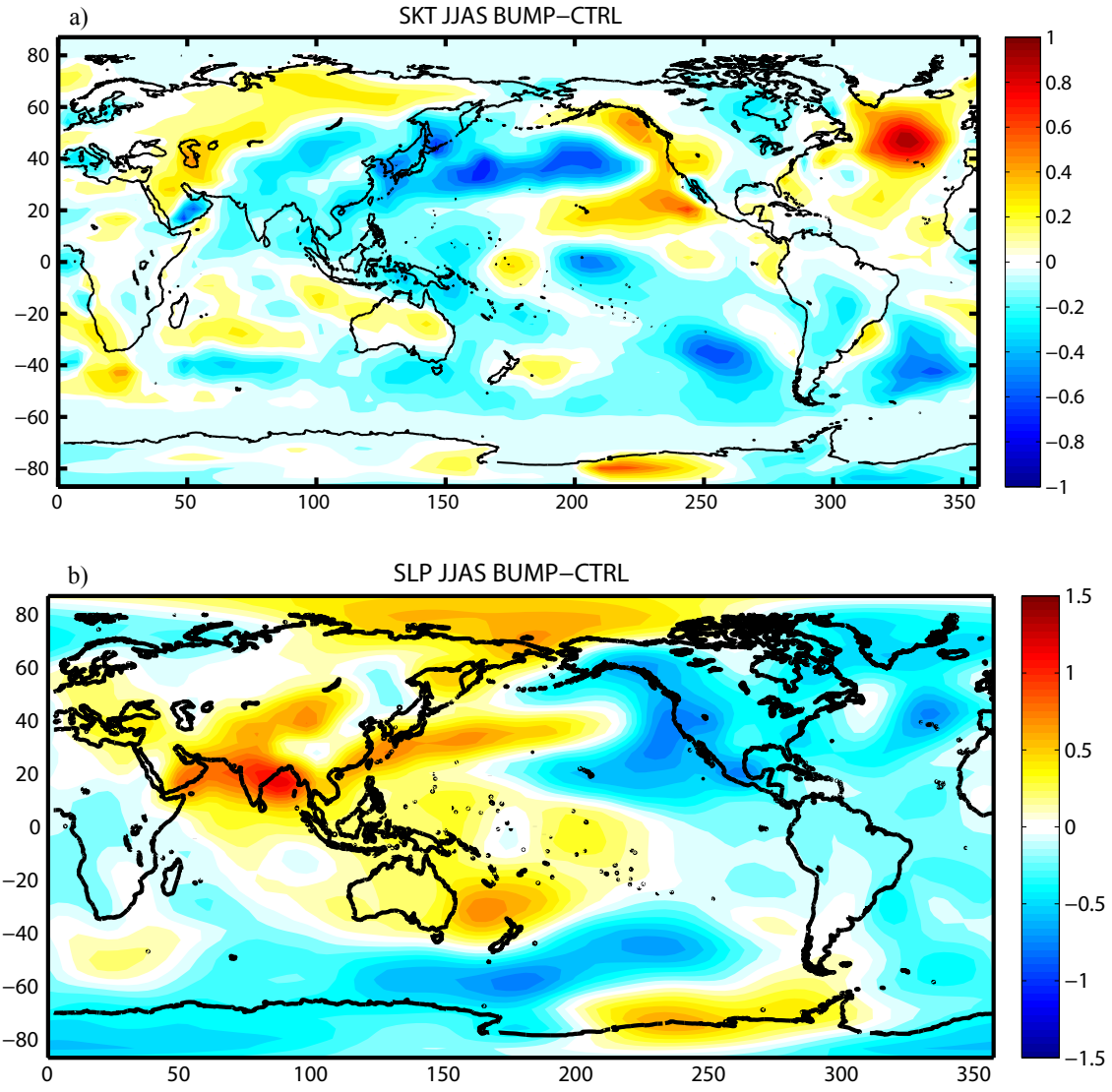

Figure 4.46: a) Differences in surface temperature between BUMP and CTRL for the summer season. Units are °C. b) As is a) but for sea level pressure. Units are hPa.

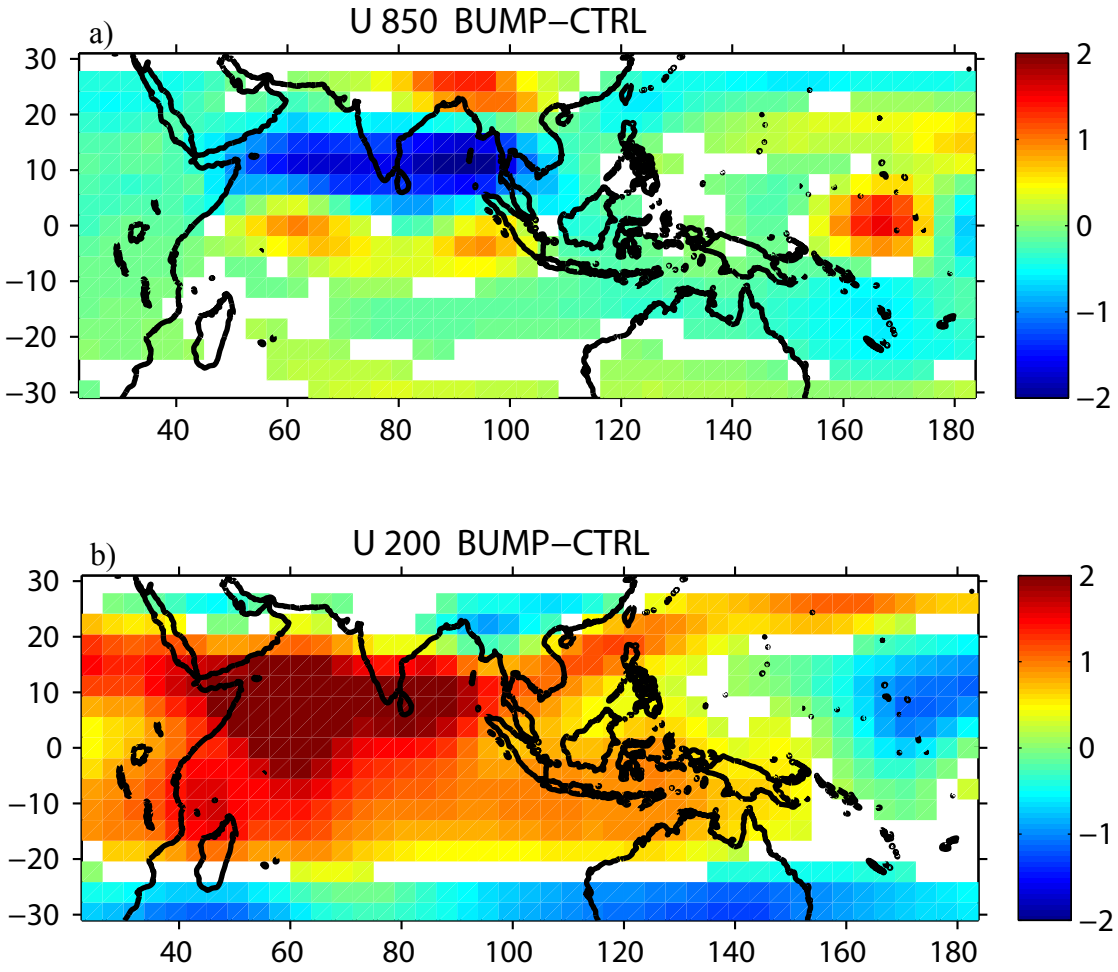

Figure 4.47: Differences in zonal wind between BUMP and CTRL at a) 850-hPa level; b) 200-hPa level. Units are ms^{-1}.

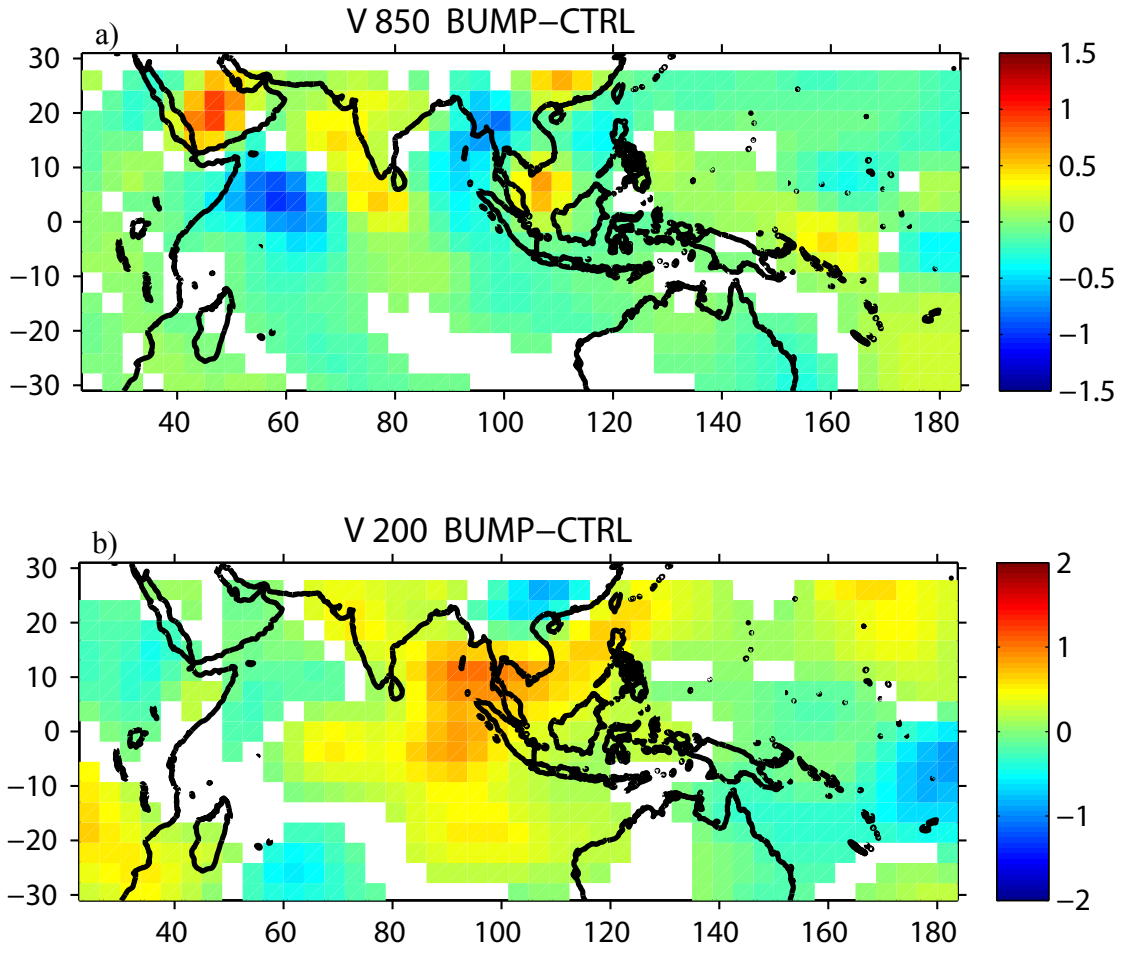

Figure 4.48: Differences in meridional wind between BUMP and CTRL at a) 850-hPa level; b) 200-hPa level. Units are m^{-1}.

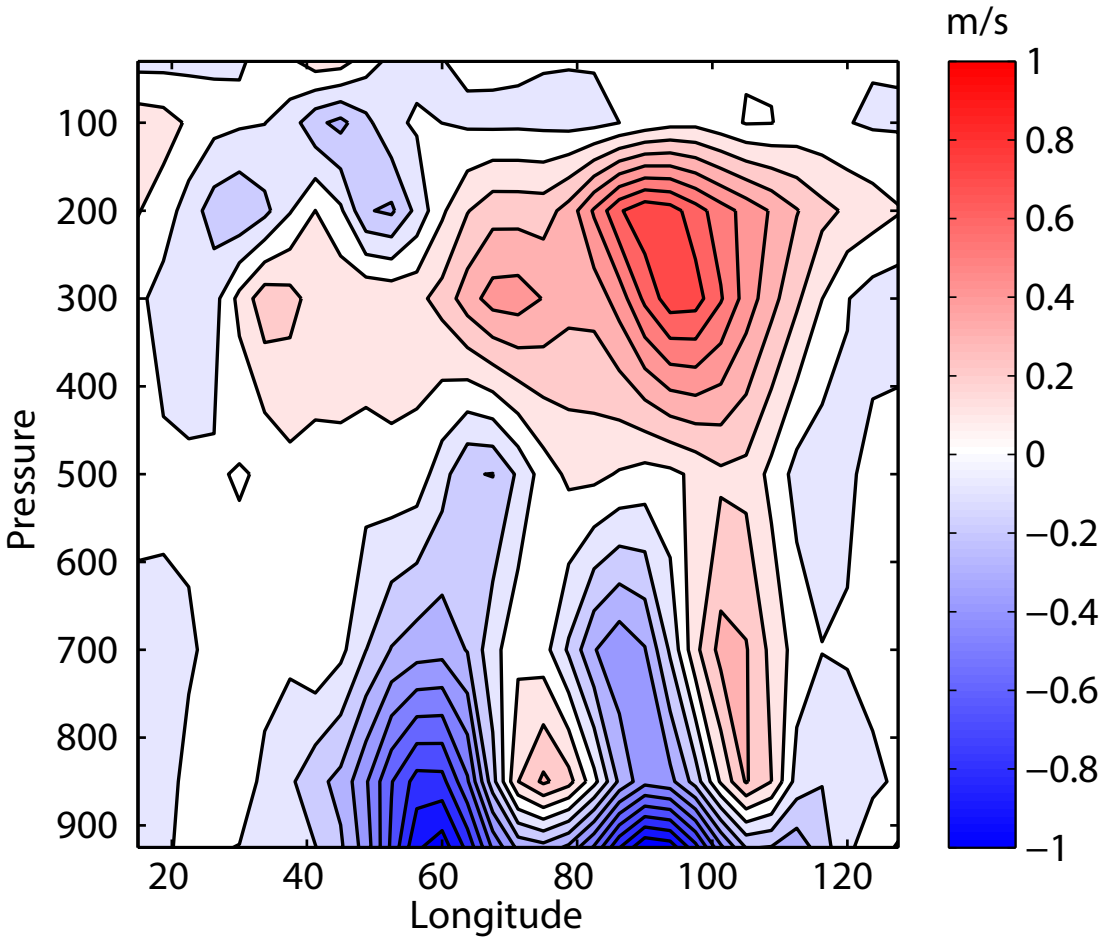

Figure 4.49: Seasonal mean cross equatorial meridional wind differences between BUMP and CTRL. Meridional wind differences are averaged between 5°S and 5°N. Units are ms^{-1}.

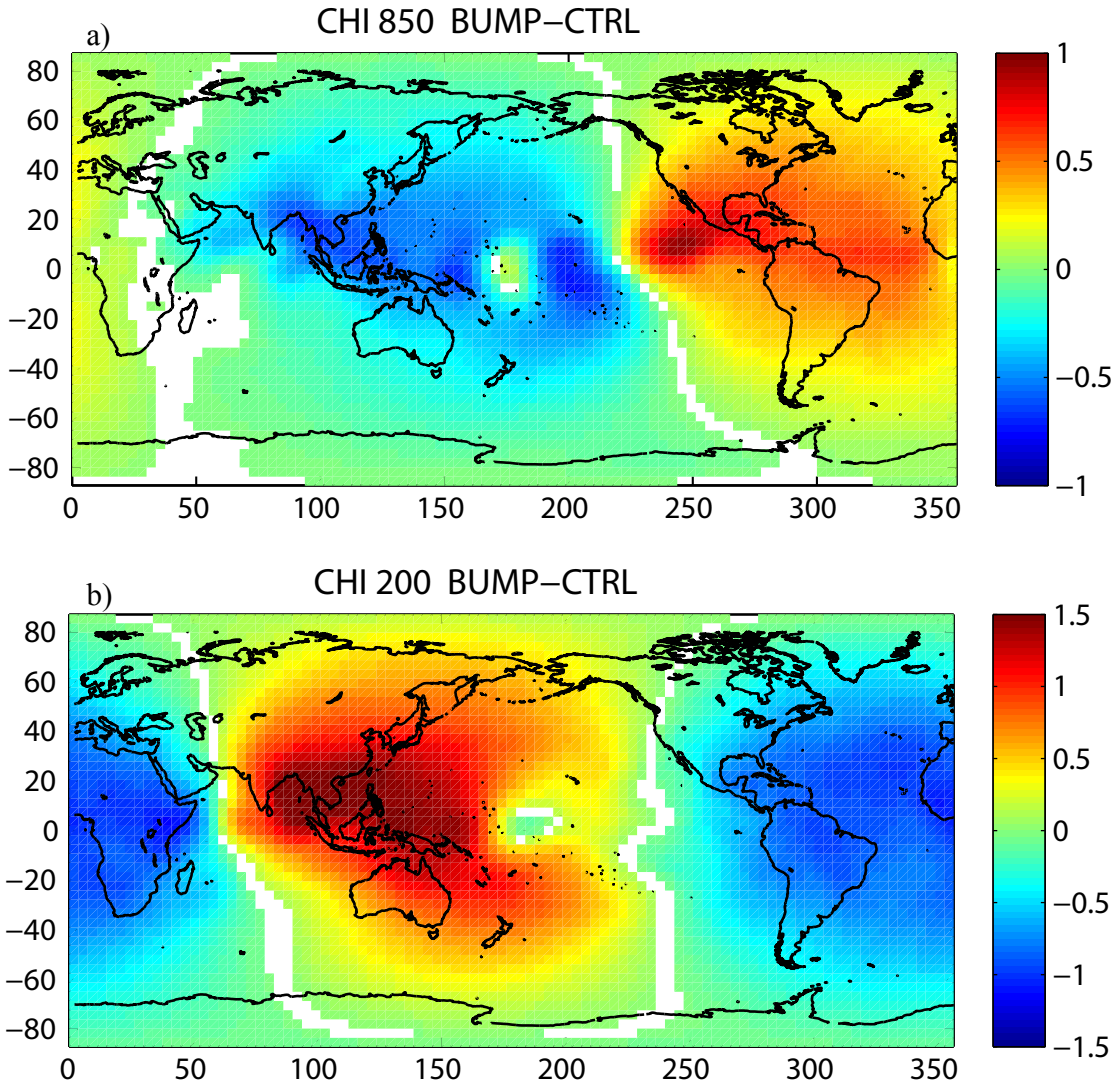

Figure 4.50: Differences in velocity potential between BUMP and CTRL at a) 850-hPa level; b) 200-hPa level.

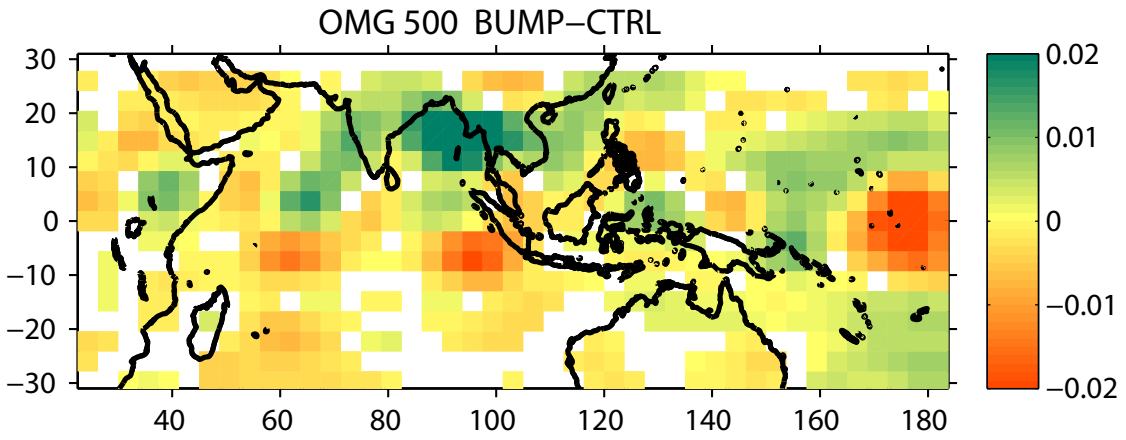

Figure 4.51: Differences in omega between BUMP and CTRL at 500-hPa level.

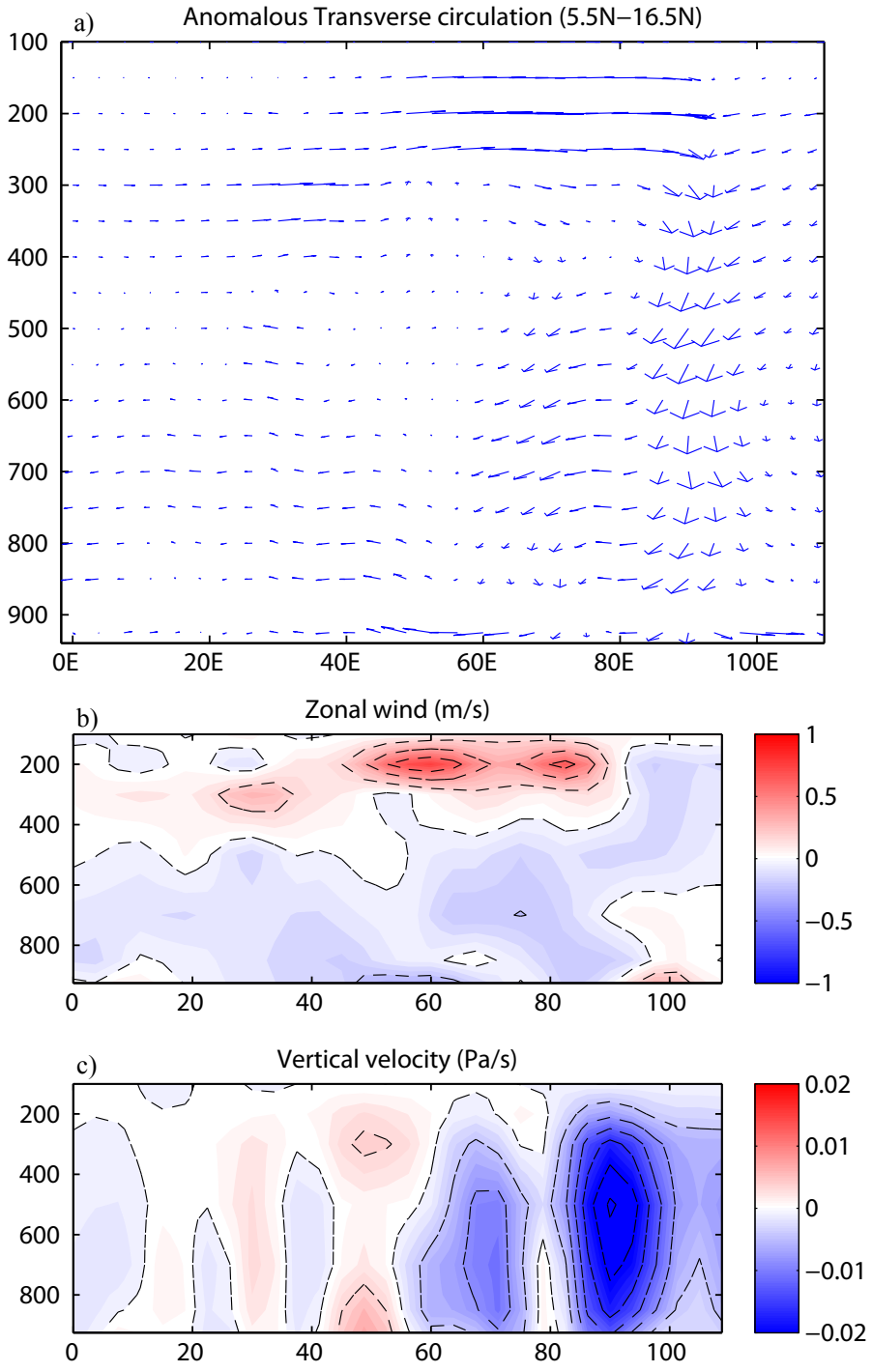

Figure 4.52: a) Anomalous transverse circulation (BUMP-CTRL). b) Cross section of zonal divergent wind anomalies. Units are ms^{-1}. c) Cross section of vertical velocity anomalies. Units are Pa s^{-1}.

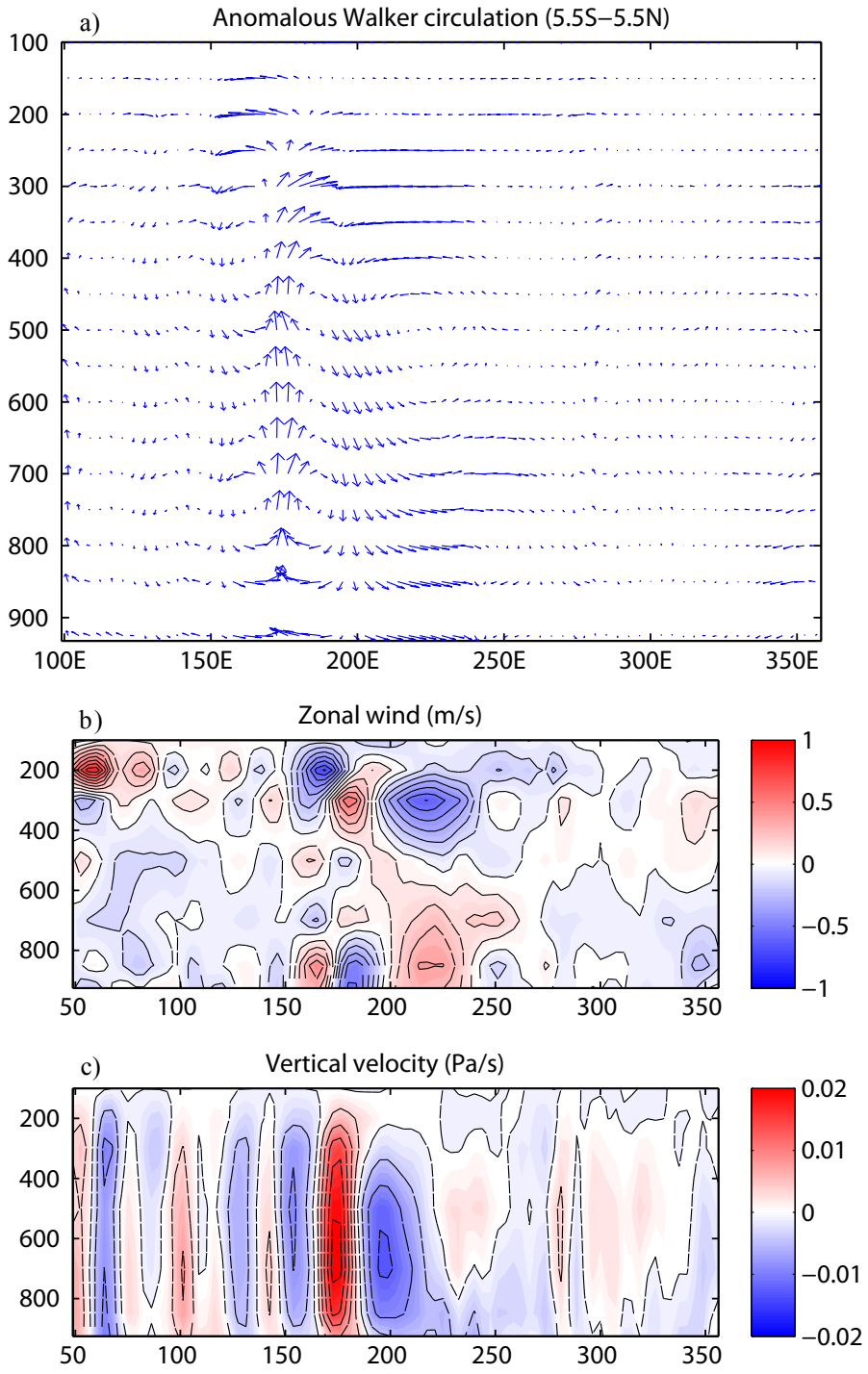

Figure 4.53: a) Anomalous Walker circulation (BUMP-CTRL). b) Cross section of zonal divergent wind differences along the equator. Units are ms^{-1}. c) Cross section of vertical velocity differences along the equator. Units are Pa s^{-1}.

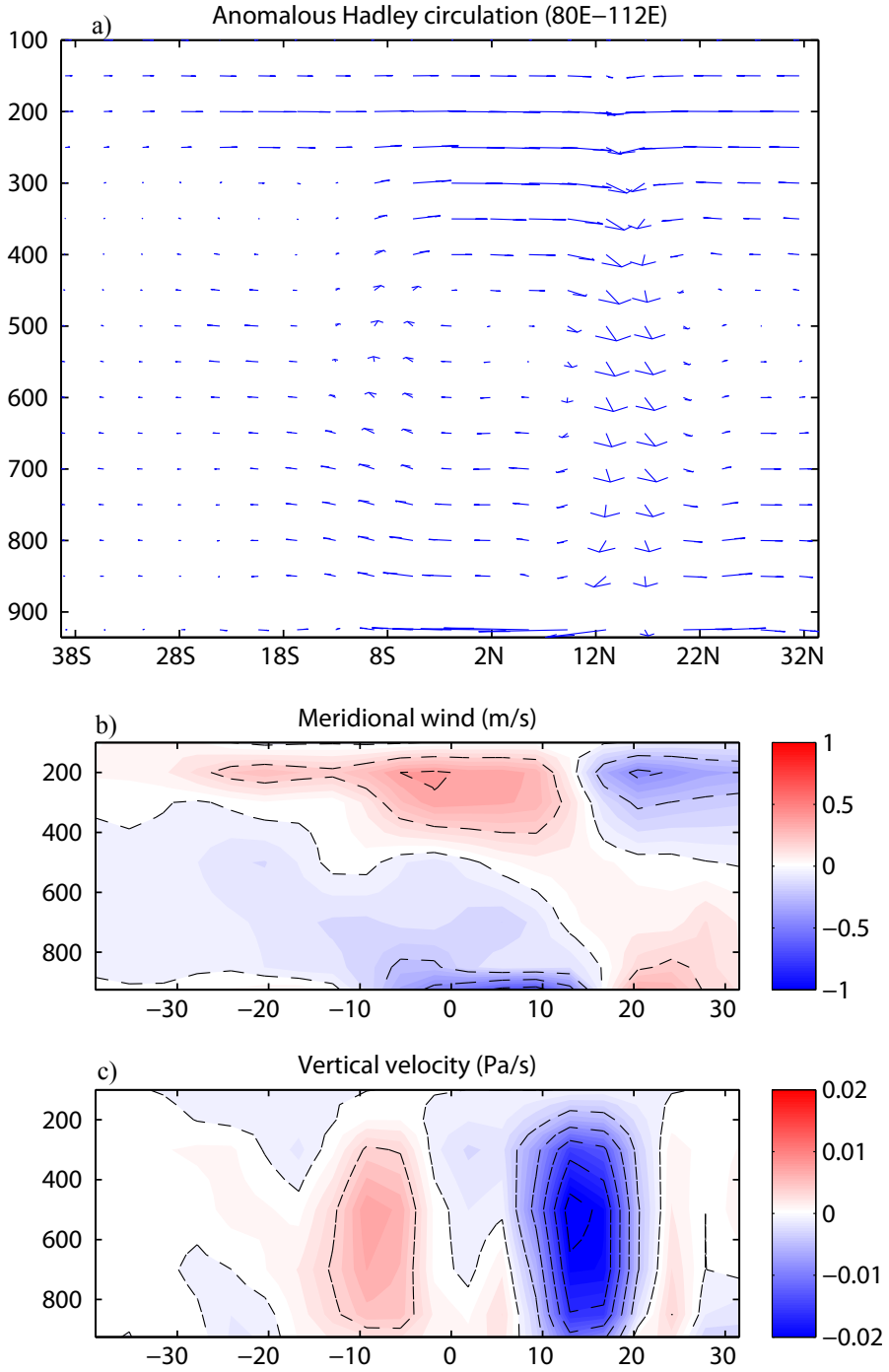

Figure 4.54: a) Anomalous local Hadley circulation over the eastern Indian Ocean (BUMP-CTRL). b) Cross section of meridional divergent wind anomalies. Units are ms^{-1}. c) Cross section of vertical velocity anomalies. Units are Pa s^{-1}.

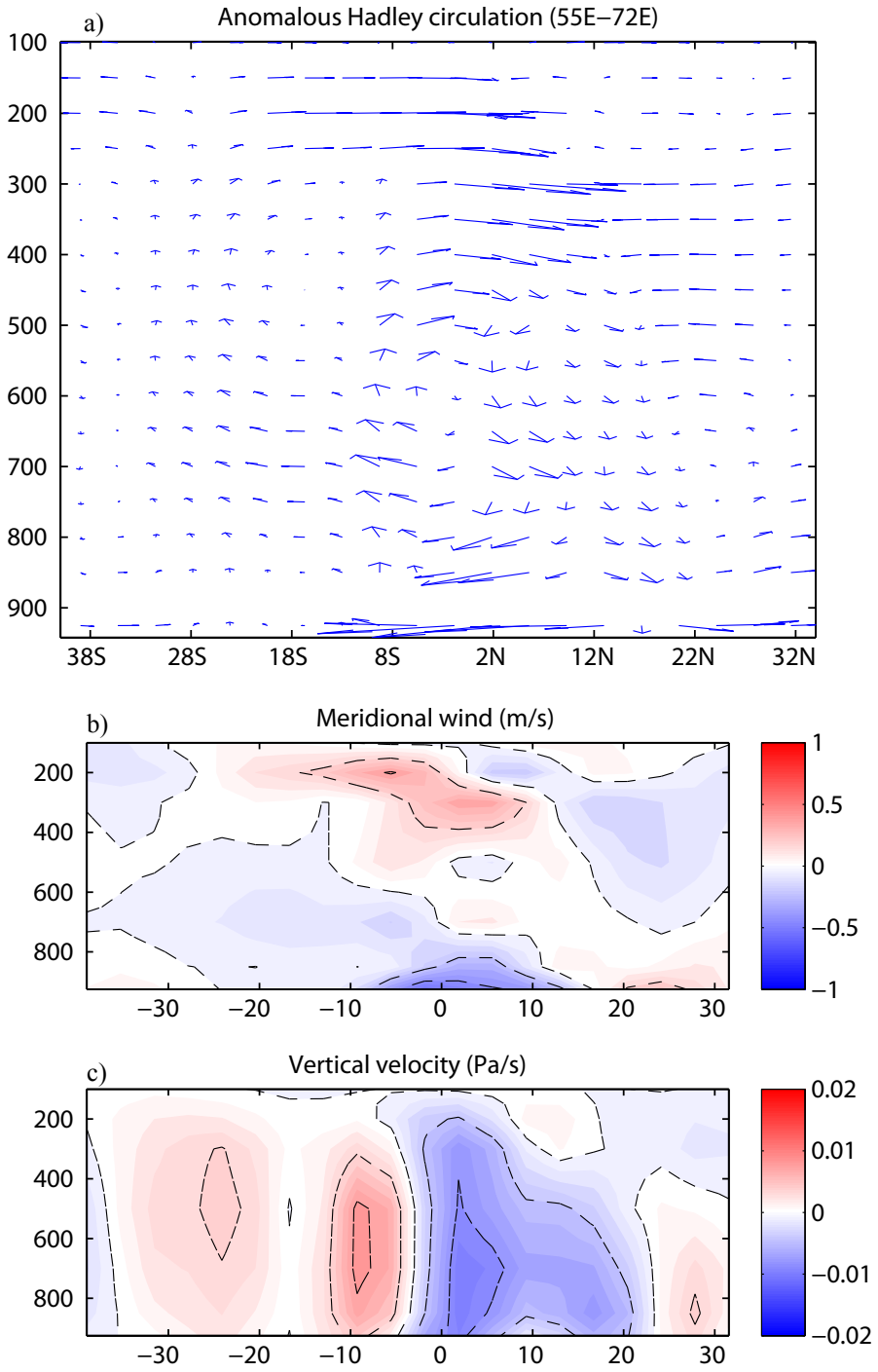

Figure 4.55: a) Anomalous local Hadley circulation over the eastern Indian Ocean (BUMP-CTRL). b) Cross section of meridional divergent wind anomalies. Units are ms^{-1}. c) Cross section of vertical velocity anomalies. Units are Pa s^{-1}.

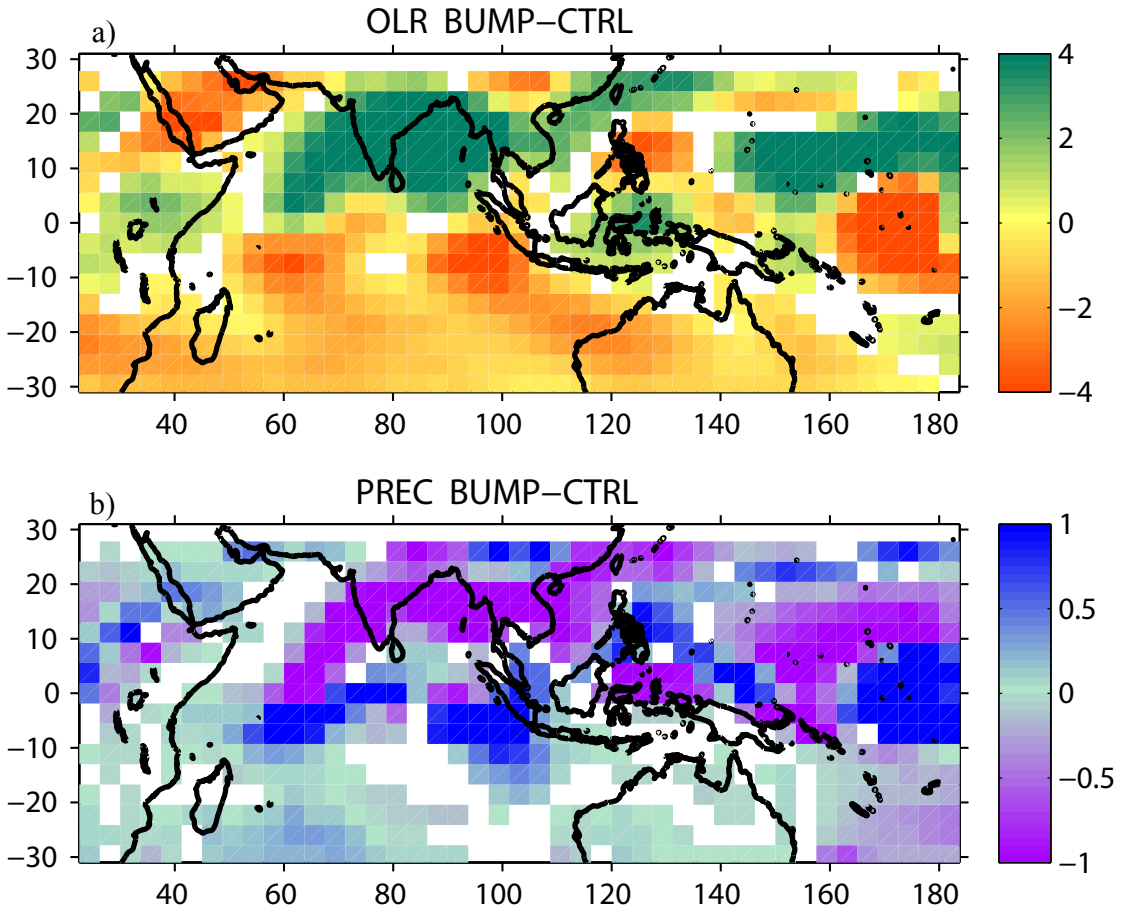

Figure 4.56: a) Differences in OLR between BUMP and CTRL. b) As in a) but for precipitation.

CHAPTER V

MOISTURE TRANSPORT AND PRECIPITATION VARIABILITY IN THE SOUTH ASIAN MONSOON

SST changes from era to era are not uniform and there is a strong regionality in these changes. Moreover, monsoon precipitation does not follow the changes in SST exactly. The influence of SST changes on the monsoon system is complicated, as it impacts the circulation while, through Clausius Clapeyron effect produces non-linear moisture phase changes and differential convective heating. The juxtaposition of these two effects is necessary to understand how SSTs variability modulates the monsoon system. In Chapter 4 we investigated the impact of SST changes on the large-scale monsoon circulation. In this chapter we carry out a moisture transport analysis to relate the large-scale circulation changes with the structure of precipitation.

5.1 Moisture transport

Vertical integrated moisture transport (VIMT) is an important component of the seasonal-mean atmospheric water balance equation. Since the atmospheric moisture transport is controlled mostly by the low level monsoonal circulation, and the pattern of SST is of prime importance in determining the low-level flow, a comparison of the VIMT was performed for all the experiments discussed in Chapter 3.

The atmospheric moisture budget equation can be expressed as

$$\frac{\partial W}{\partial t} = -\nabla Q + E - P$$

where W is the precipitable water, E is the rate of evaporation and P represents evaporation. Q is the vertically integrated moisture flux.

Following Fasullo and Webster (2002), the vertically integrated moisture transport Q (hereafter VIMT) is defined as

$$VIMT = \frac{1}{g} \int_{surface}^{300mb} q \cdot U \, (\partial p)$$

where q is specific humidity and U is the horizontal wind vector. According to Fasullo and Webster (2002), the magnitude of the specific humidity is very small above 300-hPa when compared to the surface values and therefore moisture transport above this level is not considered in the calculation of VIMT.

To illustrate differences in moisture transport between different sectors in the Indian Ocean, the Pacific Ocean and monsoonal regions of active convection, VIMT was integrated across key boundaries similar to those described by Fasullo and Webster (2002). These boundaries are located between the northern hemisphere and the southern hemisphere, the western Pacific Ocean and the western and eastern Indian Ocean, near equatorial and south Asian regions of deep convection. Calculations of VIMT are presented as a mean value for the summer months JJAS. The Asian monsoon domain covers south Asia, southeast Asia, west-central Pacific, the southern Indian Ocean and the northern Indian Ocean. In the VIMT diagram shown in Figure 5.1 for the CTRL, the integrated VIMT is positive to the east across a north-south boundary and positive to the north across an east-west boundary.

The VIMT for the CTRL, COLD, MODERATE, WARM and BUMP are shown in Figures 5.1-5, respectively. The largest westerly zonal VIMT occurs over the central-eastern northern Indian Ocean, India, Bay of Bengal and southeast Asia. Easterly VIMT flow takes place in the southern Indian Ocean and the central Pacific Ocean. Large interhemispheric VIMT flow is found in the western Indian Ocean, South China Sea and Indonesian region. The interhemispheric flow in these two distinct sectors constitutes a cross-equatorial exchange of moisture that couples regions of strong divergence in the southern hemisphere with regions of strong convergence in the

northern hemisphere (Fasullo and Webster 2002). During summer, regions of strong convergence are associated with the major centers of monsoonal convection in the Bay of Bengal and the area surrounding the Philippines (Wang and Fan 1999). These regions are characterized by low values of OLR ($\sim$200 Wm^{-2}) and by large values of precipitation exceeding evaporation. Over the western Indian Ocean, the Somali jet is responsible for the transport of moisture from the southern Indian Ocean into the northern Indian Ocean and the Arabian Sea. This transport is controlled by the strong meridional heating contrast. The meridional southerly component alone carries $\sim$218 x 10^6kg s^{-1}. Moisture that reaches the Arabian Sea is transported westward into India and Bay of Bengal ($\sim$89 x 10^6kg s^{-1}). Over the western Pacific Ocean, moisture is supplied by the divergent subtropical regions over the southern Indian Ocean, northwest of Australia, and over the southern Pacific Ocean. Southerly VIMT from the southern oceans, easterly VIMT from the Pacific and westerly VIMT from the South Asian monsoon region carry a great amount of moisture ($\sim$372 x 10^6kg s^{-1}) toward the convergent regions near the South China Sea and the Philippines. Southerly VIMT flow into the Bay of Bengal is also reasonable ($\sim$36 x 10^6kg s^{-1}) but not as large as expected. Southerly VIMT is exported from the Bay of Bengal and from southeast Asia into northern Asia.

As noted in Chapter 3, the model has problems reproducing the strength of the Somali jet and the westerlies that blow from the ocean into the Indian peninsula. For this reason, values of VIMT coming into the Arabian Sea and into India are lower than expected. For the purpose of this work, we are going to consider only comparative differences in moisture transport between each one of the experiments and CTRL to study the response of the South Asian monsoon to large scale SST variability and the possible impacts in monsoonal rainfall variability.

5.1.1 Differences in moisture transport associated with large scale sea surface temperature variability

Figure 5.2 shows the boundary integrated differences of VIMT (10^6kg s^{-1}) between the COLD experiment (Table 3.1: 1925 - 35) and CTRL for the summer season. Large bold numbers for boundary integrated VIMT indicate differences that are significant at a 95% level. The bold letters in the center of the squares represent the net convergence of the VIMT in an area. Large differences exist in the zonal VIMT transports between the equator and 12°N and in the meridional transports across the equator. Differences in VIMT into the Arabian Sea include a decline in the Somali jet flux (-22 x 10^6kg s^{-1}) and anomalous easterly VIMT across 40°E (-12 x 10^6kg s^{-1}). The impact of these changes is consistent with a reduction in the amount of water vapor that is transported from the southern Indian Ocean. Consistent with this decrease, westerly zonal VIMT into India (-7 x 10^6kg s^{-1}) and south of India and Bay of Bengal (-19 x 10^6kg s^{-1}) is also reduced. Moreover, southerly moisture transport along 12°N into Bay of Bengal is also diminished by -22 x 10^6kg s^{-1}. Overall, the moisture transport convergence anomalies suggest that there is a reduction in moisture convergence over India, Bay of Bengal and the northern eastern Indian Ocean. In fact, convergence of moisture south of India and the Bay of Bengal (0° – 12°N, 70°E – 102°E) is 15 x 10^6kg s^{-1}weaker in the COLD experiment than in CTRL. These results are consistent with the findings described in Chapter 4, which revealed a decrease in precipitation over Bay of Bengal and the Indian Peninsula (Figure 4.23b), and a weakening of Hadley circulation over the eastern Indian ocean (Figure 4.21).

Figure 5.2 shows, in addition, an anomalous southerly VIMT across Indonesia (14 x 10^6kg s^{-1}), implying an increase in the magnitude of the interhemispheric flow relative to CTRL. Westerly VIMT across 102°E into Indonesia region increases (22 x 10^6kg s^{-1}), and easterly VIMT flow coming from the western Pacific Ocean decreases (19 x 10^6kg s^{-1}). Overall, there is an increase in the net moisture flux

convergence in the North Indonesian domain and divergence over southern Indonesia. These distributions are consistent with the dipole in precipitation anomalies in the 120°-150°E region across the equator (Figure 4.23). In Southeast Asia there is an increase in moisture convergence over the Indonesian region of about +18 x 10^6kg s^{-1} relative to the CTRL case. However, there is decreased moisture convergence over the Philippines region of about 5 x 10^6kg s^{-1} weaker than in CTRL. These findings are also consistent with Figure 4.23b, showing an increase in precipitation at about 10°N and a decrease in precipitation around 20°N relative to CTRL.

In summary, the SST pattern during the 1925 - 35 is consistent with a weaker monsoon with slightly below average precipitation (Figure. 4.23). The changes in the SST distribution have changed the circulation patterns relative to CTRL with accompanying changes in patterns of evaporation and precipitation.

The boundary integrated VIMT differences between the MODERATE experiment and CTRL (1950 - 1960: Table 3.1) are shown in Figure 5.3. Of particular relevance are the changes in the fluxes in the monsoon regions along the equator and 12°N and across 70°E and 102°E. Interhemispheric flow over the western Indian Ocean increases by 5 x 10^6kg s^{-1} relative to the CTRL into the Arabian Sea region. Westerly flow north of the equator across 40°E decreases and results in a reduction of the flux across 70°E by -17 x 10^6kg s^{-1}. This decrease is consistent with a large reduction in moisture flux from tropical east Africa. Moreover, westerly VIMT into south of India and Bay of Bengal (-17 x 10^6kg s^{-1}) and southerly VIMT into Bay of Bengal (-7 x 10^6kg s^{-1}) are also reduced. This anomalous moisture transport pattern over South Asia produces a reduction in moisture convergence south of India and over the Bay of Bengal. The anomalous moisture divergence over this region (0° - 25°N, 70°E – 102°E) is of 11 x 10^6kg s^{-1} relative to the CTRL case. A comparison of monsoon precipitation difference fields (Figure 4.34) between the MODERATE experiment and CTRL shows a reduction in precipitation rate over Bay of Bengal and central

equatorial Indian Ocean.

Over southeast Asia, anomalous zonal VIMT flow from the eastern Indian Ocean into the Indonesian region is easterly, indicating a reduction of -7 x 10^6kg s^{-1}. In addition, anomalous VIMT flow is northerly across Indonesia (-9 x 10^6kg s^{-1}) and northerly across Philippines (-7 x 10^6kg s^{-1}). This anomalous pattern of moisture flux contributes to a decrease in moisture flux convergence in the Indonesian region. Over the Philippines region, moisture flux convergence remains stable.

Figure 5.4 shows differences in boundary integrated VIMT between the WARM experiment (Table 3.1: 1990 - 2000) and CTRL. There is a slight increase in the cross-equatorial flux transport into the Arabian Sea (3 x 10^6kg s^{-1}) and a decrease of integrated VIMT between the central and equatorial South Indian Ocean at 70°E (12 x 10^6kg s^{-1}). There is also a reduction in the northward integrated VIMT into the north Arabian Sea. Finally, there is a 20 x 10^6kg s^{-1} increase across 70°E in the equatorial Indian Ocean. The anomalous moisture flux pattern associated with this experiment suggests a weakening of the moisture flux convergence in the Arabian Sea region and a possible reduction in the westerly moisture flux into the Indian peninsula and Bay Bengal. A decline in the westerly moisture flux could be associated with a southward shift in the low level westerly jet over the Arabian Sea (e.g. Joseph and Simmon 2005), which ultimately reduces the amount of water vapor that reaches the Indian peninsula and the Bay of Bengal due to moisture flux convergence. Overall, the changes in flux convergence and divergence are small commensurate with relative small changes in precipitation patterns over the western Indian ocean and the monsoon regions (Figure 4.45).

In Southeast Asia, there is an anomalous westerly transport of 30 x 10^6kg s^{-1} at 102°E into the Indonesian region. Interhemispheric flow into this region decreases, displaying a northerly flow (-7 x 10^6kg s^{-1}). Meridional flow across the Philippines

increases in 22 x 10^6kg s^{-1}. However, moisture convergence differences in the Indonesian region relative to CTRL are not significant. On the other hand, convergence of moisture increases considerably over the Philippine region ($\sim$18 x 10^6kg s^{-1}) in agreement with an increase in precipitation rate relative to CTRL (see Figure 4.45).

Figure 5.5 shows the JJAS boundary integrated VIMT differences between the BUMP experiment and CTRL (1938 - 1942: Table 3.1). The most notable difference with the CTRL is the large decrease in cross-equatorial integrated VIMT with reductions of 29 and 16 x 10^6kg s^{-1} in the western and central Indian Ocean. Also, there is a very large decrease in moisture convergence in the Bay of Bengal of 33 units. This reduction corresponds to a large reduction in precipitation (Figure 4.56). Over the western Indian Ocean, anomalous VIMT is easterly along the 40°E meridian (-7,-9, and -11 x 10^6kg s^{-1}). Southerly moisture flow across 12°N increases (11 x 10^6kg s^{-1}) and westerly flow into India decreases (-18 x 10^6kg s^{-1}). Westerly flow from the western Indian Ocean into south of Indian and eastern Indian Ocean also decreases (-45 x 10^6kg s^{-1}). Meridional VIMT differences between 70°E and 102°E are negative across the equator (-16 x 10^6kg s^{-1}) and across 12°N (-18 x 10^6kg s^{-1}), implying that the amount of moisture that is transported into these regions is reduced. Accordingly, the moisture flux convergence is reduced relative to CTRL providing a total of -52 x 10^6kg s^{-1} difference into the Bay of Bengal and eastern Indian Ocean.

In Southeast Asia, largest differences in VIMT are observed across 102°E (-24 x 10^6kg s^{-1}) and 12°N (-18 x 10^6kg s^{-1}). The anomalous moisture flux pattern is consistent with a reduction in moisture convergence near the Philippines ($\sim$ 14 x 10^6kg s^{-1}) relative to CTRL. Changes in moisture convergence in the Indonesian region are small ($\sim$1 x 10^6kg s^{-1}).

5.2 Summary

VIMT analysis is very useful in providing an integrated view of the impact of SST variations on circulation and the hydrological cycle and hence moisture availability over major centers of convection (India, Bay of Bengal and Philippines) during the summer season. The SST distribution affects VIMT through an alteration of the low-level flow. Largest differences in vertically integrated moisture flux, that are important for the rainfall monsoon variability, are observed in the interhemispheric component and in the zonal component across the northern Indian Ocean. Since meridional moisture flux convergence is crucial in the maintenance of the south Asian monsoon (Murakami et al. 1999), a stronger SLP gradient in the western Indian Ocean would be associated with stronger meridional moisture fluxes and with a possible increment in moisture convergence, which would lead to the production of precipitation. In the MODERATE experiment, the SLP gradient is stronger than in CTRL and interhemispheric VIMT flow is also stronger. However, for this case, the zonal flow across the northern Indian Ocean is reduced and the transport of moisture from the western Indian Ocean to the eastern Indian Ocean is also reduced, limiting convergence of moisture flux over this region. In the COLD and BUMP experiments, a reduction in the SLP gradient over the western Indian Ocean is accompanied by a reduction in the interhemispheric VIMT flow, which impacts strongly the convergence of moisture flux over the Indian peninsula. Finally, in the WARM experiment, the SLP gradient is similar to the CTRL and differences in the interhemispheric VIMT flow are less dramatic than in the other experiments. Moreover, zonal flow in the northern Indian Ocean is stronger than in CTRL, and zonal VIMT flux increases. In this case, convergence of moisture flux is favored over portions of the Bay of Bengal and Southeast Asia.

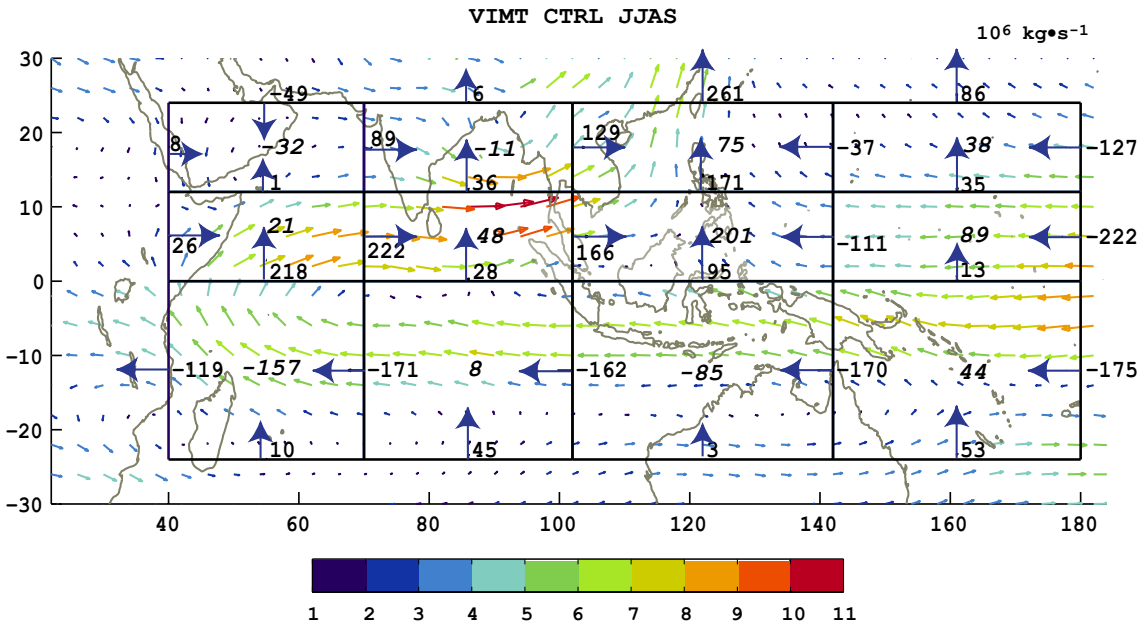

Figure 5.1: Vectors represent mean VIMT from CTRL for the summer season in units of km $m^{-1}s^{-1}$. Numbers and arrows indicate integrated VIMT across boundaries in units of km s^{-1}. Bold numbers in the center of the squares represent the net convergence of the VIMT in an area.

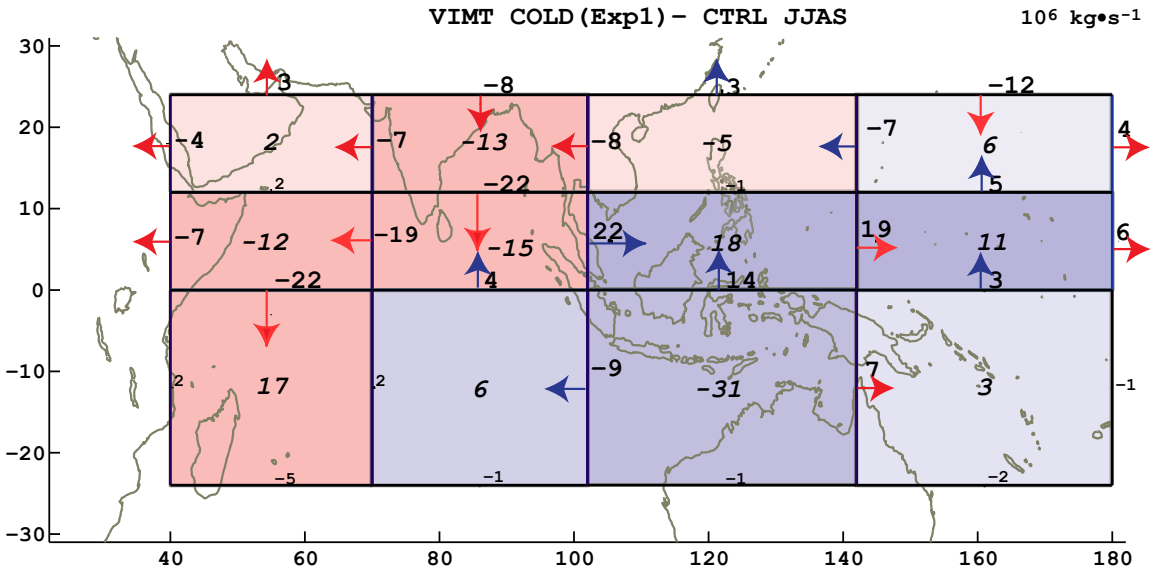

Figure 5.2: Integrated boundary VIMT differences between the COLD and CTRL. Blue arrows indicate positive VIMT anomalies relative to the CTRL and red arrows indicate negative VIMT anomalies relative to the CTRL. Large bold numbers for boundary integrated VIMT indicate differences that are significant at a 95%. level. Numbers in the center of the squares represent the differences in net convergence relative to the CTRL case. Blue (red) shading indicates positive (negative) VIMT net convergence over a region relative to the CTRL.

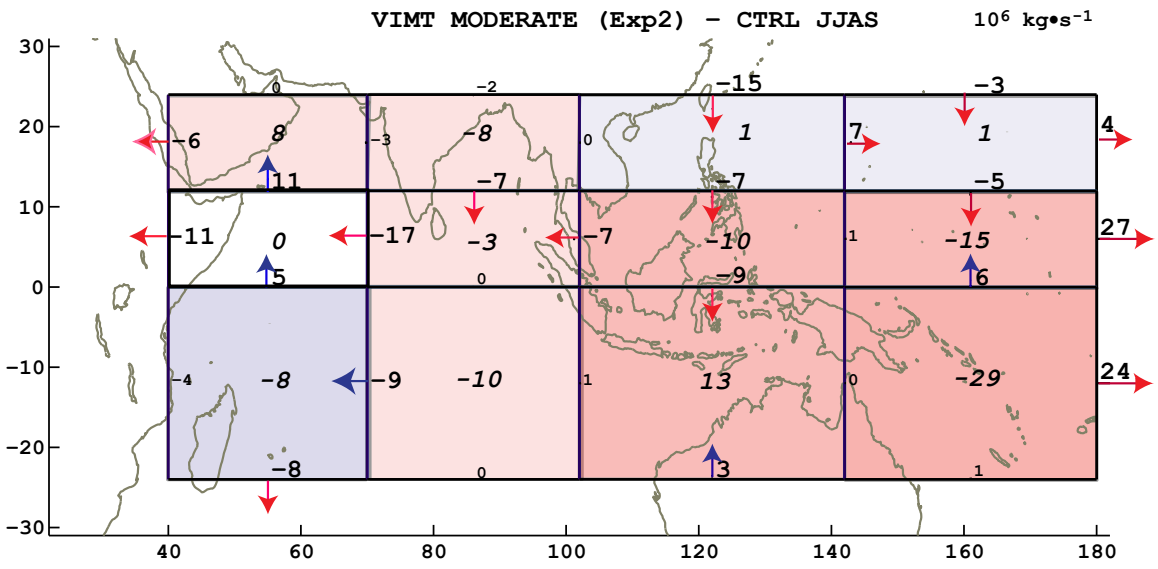

Figure 5.3: Integrated boundary VIMT differences between the MODERATE and CTRL. Blue arrows indicate positive VIMT anomalies relative to the CTRL and red arrows indicate negative VIMT anomalies relative to the CTRL. Large bold numbers for boundary integrated VIMT indicate differences that are significant at a 95%. level. Numbers in the center of the squares represent the differences in net convergence relative to the CTRL case. Blue (red) shading indicates positive (negative) VIMT net convergence over a region relative to the CTRL.

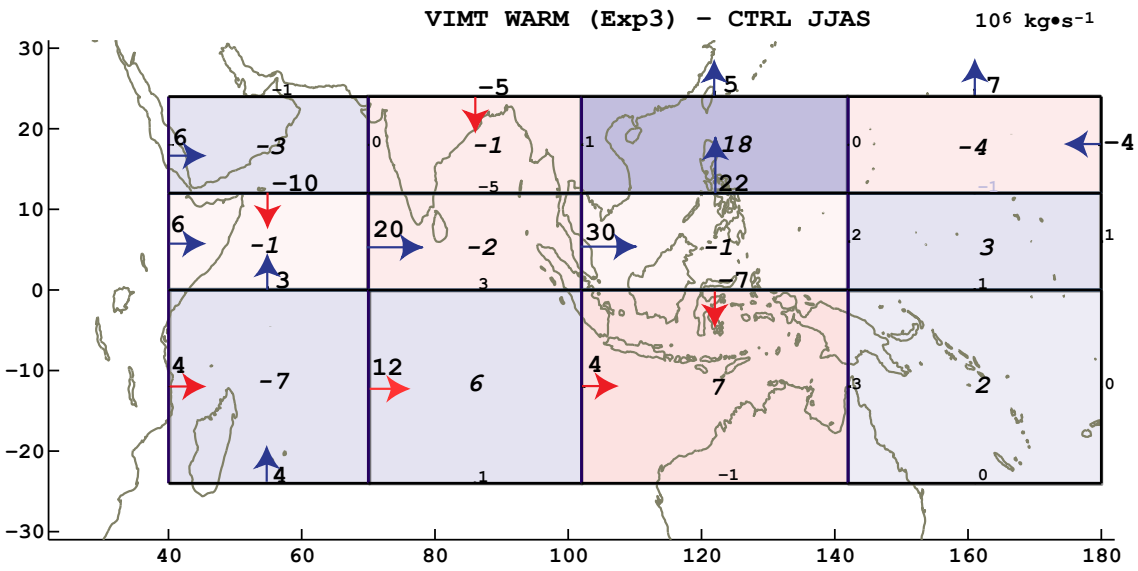

Figure 5.4: Integrated boundary VIMT differences between the WARM and CTRL. Blue arrows indicate positive VIMT anomalies relative to the CTRL and red arrows indicate negative VIMT anomalies relative to the CTRL. Large bold numbers for boundary integrated VIMT indicate differences that are significant at a 95%. level. Numbers in the center of the squares represent the differences in net convergence relative to the CTRL case. Blue (red) shading indicates positive (negative) VIMT net convergence over a region relative to the CTRL.

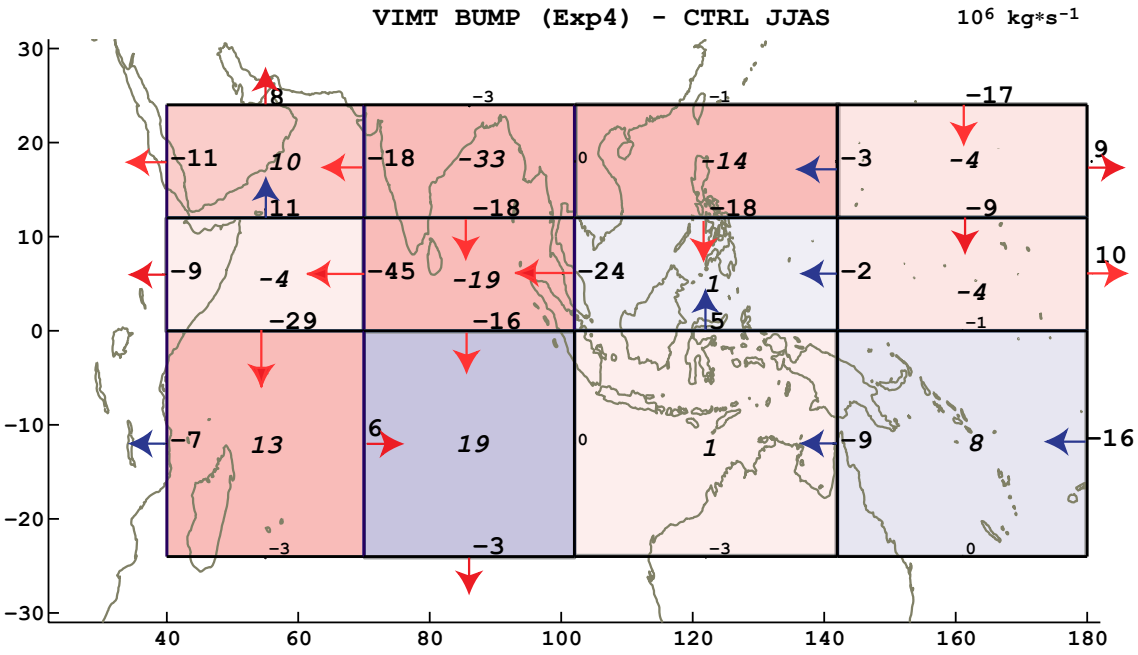

Figure 5.5: Integrated boundary VIMT differences between the BUMP and CTRL. Blue arrows indicate positive VIMT anomalies relative to the CTRL and red arrows indicate negative VIMT anomalies relative to the CTRL. Large bold numbers for boundary integrated VIMT indicate differences that are significant at a 95%. level. Numbers in the center of the squares represent the differences in net convergence relative to the CTRL case. Blue (red) shading indicates positive (negative) VIMT net convergence over a region relative to the CTRL.

CHAPTER VI

AFRICAN EASTERLY WAVES AND THE AFRICAN MONSOON

In previous sections we have studied the interdecadal variability of the monsoon noting the importance of the SST distribution on the monsoon's evolving nature. Here we look at the most rapid variability of a monsoon circulation associated with instability waves. In the following paragraphs we explore the nature of the monsoon instabilities. This study is a prelude to a systematic study of high frequency monsoon instabilities in the different monsoon systems of the planet.

African easterly waves (AEWs) are an important component of the weather and climate of North Africa, the African monsoon and the tropical Atlantic Ocean. Observations during the Global Atlantic Research Program (GARP) Atlantic Tropical Experiment (GATE; Kuettner 1974) revealed westward propagating synoptic-scale disturbances with mean periods of about 3.5 days, wavelengths of 2000 – 4000 km and a phase speed of about $6 - 8$ ms^{-1} (Carlson 1969b; Burpee 1972; Reed et al. 1977). GATE was the first major experiment of GARP that took place in the summer of 1974 and whose goal was to understand the tropical atmosphere and its role in the global circulation (Kuettner 1974). The experimental area of this project covered the tropical Atlantic Ocean from Africa to South America.

Westward propagating waves with periods between 6 – 9 days have also been detected with wavelengths of about 6000 km and a phase speed of about 6 ms^{-1} (e.g. Viltard et al. 1997; Diedhiou et al. 1998). These waves propagate across the tropical North Atlantic and can reach as far as the Caribbean (Riehl 1954) and even the West Pacific (Wallace 1970). AEWs are particularly important in the Atlantic

Ocean as they are associated with the formation of tropical cyclones (e.g. Frank 1970, Thorncroft and Hodges 2001). Frank (1970) showed that African waves account for the genesis of about half of the tropical cyclones in the North Atlantic.

Carlson (1969a,b) was the first to perform a detailed synoptic analysis of African easterly waves. Using radiosonde data collected between 20°E and 20°W, the study pointed out that some waves formed within the data network, but most of them propagated into the analysis region from further to the east. Later, Burpee (1972, 1974) used spectral and composite techniques to describe the basic structure of the waves and investigate the physical causes that could lead to the formation of the disturbances.

A more recent campaing, the international African Monsoon Multidisciplanary analysis (AMMA), was staged during the summer of 2006 over northern Africa. AMMA's primoridal goal is to improve the knowledge of the West African Monsoon and its variability with an emphasis on daily to interannual time scales (Redelsperger et al. 2006). AMMA's downstream extension, the NASA-AMMA program (NAMMA; Zipser et al. 2009), was implemented over the eastern Atlantic in August- September to examine the interaction between AEWs, the saharan air layer (SAL) and tropical cyclogenesis. A number of studies have described different dynamical aspects of the AEWs observed during the NAMMA/AMMA period (e.g. Cifelli et al. 2010, Zawislak et al. 2010, Ross et al. 2009)

In the following sections of this chapter, we describe the large-scale mean characteristics of the African monsoon climate during the boreal summer and review relevant studies concerned with the origin and dynamics of AEWs.

6.1 North African climate circulation

The main circulation features over Africa during the boreal summer are: the Tropical Easterly jet (TEJ), the African Easterly jet (AEJ), the Intertropical Convergence

Zone (ITCZ), the tropical rainbelt, and the Saharan thermal low. The TEJ lies in the upper troposphere at about 100 - 200hPa and is located on the southern side of the major Asian monsoonal heating. It is the southern flank of the upper-tropospheric anticylone centered over Tibet. This jet reaches core speeds greater than 35 ms^{-1}, extends through 20° of latitude and extends longitudinally from South Asia across equatorial Africa into the North Atlantic Ocean. The zone of surface convergence or ITCZ is located between 18°N and 20°N and it marks the transition in the zonal winds from the low-level easterly flow sweeping over the northwestern Sahara to the westerly flow of the low level monsoon (Nicholson 2009). This low-level easterly flow, known as the Harmattans, is confined between 20°N and 30°N (Figure 6.1b) and carries Saharan dust westward into the Atlantic Ocean (e.g. Carlson 1979). The Saharan low is an area of high temperatures and low surface pressures that migrates with the sun. During the summer this low pressure area is located over the Sahara and also lies between the Harmattans and the south-western monsoon flow. Strong subsidence persists above the heat low. The rainbelt is a region of high amounts of rainfall over West Africa, located south of the surface ITCZ. Figure 6.1a shows its mean location at about 10°N. This area of deep convection (OLR values less than 240 Wm^{-2}) is bounded by the TEJ and the AEJ defined below. Finally, the AEJ lies in the middle troposphere at about 700 - 600hPa. The jet core is located near 15°N and reaches maximum easterly velocities between 11 and 12 ms^{-1} (Cook 1999). This jet is perhaps the most important feature for the development of summer rainfall and westward propagating disturbances over northern Africa (e.g. Burpee 1972) as we will explore subsequently. Figure 6.1b shows locations of the AEJ and the TEJ from the ERA-40 reanalysis. The low-level westerly flow, between 10°S and 10°N, and Harmattan flow at about 25°N are also evident in this diagram. Interactions between all the above features are essential in the development of wave disturbances over Northern Africa.

6.2 Origin and dynamics of the waves

6.2.1 Structure of the AEWs

A number of observational studies used the data from the GATE intensive observational program to study the general characteristics of the wave disturbances (e.g. Burpee 1975; Reed et al. 1977; Norquist et al. 1977; Albignat and Reed 1980). In general, the AEWs have their largest amplitude in the middle troposphere near the jet level (see Figure 6.2). At this level the wave is characterized by a southwest-northeast horizontal tilt south of the jet, consistent with barotropic growth (Figure 6.3). At the lower levels there are also two regions of development, one between 5° to 10°N and the other further north at about 20°N. The development center poleward of the AEJ possesses greater amplitude than the one in the south and is characterized by baroclinic energy conversion (Norquist et al. 1977). The two preferential tracks observed north and south of the jet converge into one track off the West African coast (Figure 6.4).

Burpee (1972, 1974) suggested that near the latitude of the AEJ the meridional wind slopes eastward up to the jet level and westward above this level as shown in Figure 6.5. North of the jet the meridional wind slopes toward the west with height and south of the jet the meridional wind slopes toward the east. These vertical tilts are opposite to the vertical shear of the zonal wind and are also consistent with baroclinic energy conversions. Reed et al. (1977) found vertical tilts similar to Burpee's near the jet latitude. However, in the region south of the jet they found that the wave axis was more vertical, suggesting that the baroclinicity is weaker in this region.

Several studies have considered the question of the origin of the waves, in terms of the physical mechanisms involved and the geographical region of formation. Whereas consensus generally exists about the mechanisms that explain the growth of AEWS, consensus over where the AEWs initially form has not been reached.

Carlson (1969a) suggested that AEWs could be initiated east of 30°E near the

Ethiopian Highlands. However, Burpee (1972, 1974) found no evidence of wave activity so far east. Albignat and Reed (1980), on the other hand, suggested that initial weak perturbations may originate as far east as the southern tip of the Red Sea. As pointed out by Albignat and Reed (1980), the lack of consensus could be attributed to the use of different periods of record in the analyses. Another reason is the overall scarcity of data in the candidate genesis regions.

Thorncroft and Hodges (2001) carried out an automatic tracking of vorticity centers in ECMWF analyses and found evidence of wave activity around 35°E (western side of the Ethiopian Highlands) near the jet level. In the lower troposphere they found a peak in genesis density poleward of 15°N, just downstream of the Hoggar mountains (Figure 6.6). These results suggest that orographic processes could play a role in the origin of AEWs. Numerical simulations of Mozer and Zehnder (1996) showed that the flow of dry air past the topography of north-central Africa leads to the production of disturbances that are consistent with observed African waves. However, in general, relatively little attention has been given to the possible influence of orography on the development of AEWs and it is still not clear if orography plays a role in the early stages of the waves. In the following chapters we explore the association between orography and AEWs. In addition, Tomas and Webster (1997) suggested that a cross-equatorial pressure gradient set up in different parts of the planet by SST distributions was instrumental to the location of the ITCZ. Toma and Webster (2010b,a) have suggested that instabilities of the ITCZ, so produced, provide a source of Pacific easterly waves. Finally, Nicholson and Webster (2007) suggest that a strong cross-equatorial pressure gradient in the West African region may also be of importance in the generation of AEWs.

According to the studies referred to above, the main region of growth for the AEWs at the jet level is located south of the AEJ latitude and west of 10°E. At the lower levels (850-hPa) the main region of growth is located north of the jet around

10°E. A region of growth is also observed right at the coast at both levels. AEWs generally decay downstream of the West African coast.

6.2.2 Dynamics of AEWs

Numerous studies have been concerned with the causes and dynamics of AEWs. Much of the theoretical work concerned with the generation of AEWs focuses on the hydrodynamic stability of the zonal flow. Burpee (1972) was the first to suggest that the AEJ satisfies the Charney and Stern (1962) instability criterion. This criterion states that the instability of an internal jet requires a sign reversal of the meridional isentropic potential vorticity gradient (IPV).

Burpee (1972) suggested that the unstable jet could support the growth of AEWs through both barotropic and baroclinic energy conversions. He also evaluated the relative contribution of the horizontal and vertical shear of the mean zonal wind in creating the instability and found that both are important sources of perturbation energy. The vertical shear, which is associated with transport of heat flux, was measured to be the larger of the two.

Some studies used simple numerical models to obtain a better understanding of the AEWs. Rennick (1976); Simmons (1977); Mass (1979) and Kwon (1989) carried out linear instability analysis of the AEJ. All of these studies found westward propagating disturbances dominated by barotropic energy conversions and with horizontal wavelengths within the observed range (between 2000 and 4000 km). Rennick (1976) also included a simple parameterization of latent heat release to consider the effect of moist processes and found that moisture had no significant impact on the wave properties. Mass (1979) and Kwon (1989), on the other hand, found that the inclusion of latent heating parameterizations improved the structure of the waves, resulting in model fields closer to the observations.

Schubert et al. (1991) investigated the potential vorticity characteristics of the

ITCZ using a simple zonally symmetric balanced model of the Hadley circulation. It was found that a reversed meridional potential vorticity gradient can be generated in the middle troposphere by concentrated convective heating alone.

Primitive equation modeling studies by Thorncroft and Hoskins (1994a,b) and Thorncroft (1995) studied the linear and nonlinear behavior of the easterly waves near an idealized AEJ. These studies suggested that the easterly wave is initially dominated by barotropic conversion but later grows through mainly baroclinic energy conversions. It was found that the inclusion of latent heating increases the baroclinic conversion and improves the synoptic structure of the waves.

Hsieh and Cook (2005, 2007) analyzed simulated AEWs in a regional model and found that the generation of AEWs is more closely associated with convective activity that occurs south of the jet than with the strength of the jet. Their wave energetic analysis show that baroclinic overturning is the dominant source for wave generation and that significant barotropic conversion occurs when there is concentrated convection activity.

An observational analysis by Kiladis et al. (2006) and a modeling study by Hall et al. (2006) pointed out the importance of the dynamical influence of convection in the maintenance of AEWs. Their results show a slight phase lead of adiabatic forcing ahead of vertical motion, suggesting that convection within the AEWs is initiated by dynamical forcing, which induces vertical motion at the low levels. They also argue that the barotropic-baroclinic instability alone cannot explain the initiation and intermittence of AEWs, and a finite-amplitude initial perturbation is required. Mekonnen et al. (2006) also studied the association of convection with AEWs and suggested that the convection triggered on the western side of the mountains over central and eastern Africa has a role in initiating AEWs (H and E in Figure. 6.6.).

Cifelli et al. (2010), used the data collected during the AMMA/NAMMA campaing to examine the mesoscale convective sytems (MCSs) characteristics associated

with an AEW over the continent, at the coast and over the ocean. The found that the MCSs characteristis were different between regions. These differences are due to a combination of life cycle effects and changes in relative phasing between the propagating system and the position of low-level convergence and thermodynamic instability associated with the wave. Zawislak and Zipser (2010) found that waves of low amplitude with disorganized wind structure may have strong vorticity centers and are associated with large persistent rainig areas. In contrast, waves that are of high amplitude and have well-defined low-level circulations may contain less rainfall (Zawislak and Zipser 2010).

6.2.3 Energetics of the waves

The energetics of AEWs has been studied by a number of authors (e.g. Burpee 1972, Norquist et al. 1977, Reed et al. 1988). The analysis of energetics is a very useful technique because it allows identifying the mechanisms responsible for the growth and maintenance of the waves. Barotropic processes are related to the conversion of zonal to eddy kinetic energy through the zonal and meridional wind shears. Baroclinic processes are related to the conversion of eddy available potential energy to eddy kinetic energy. We will discuss these energy conversions in greater detail in Chapter 9.

Norquist et al. (1977) carried out the first comprehensive study of the energetics of easterly waves using the composite fields of the GATE data from Reed et al. (1977). They found that baroclinic conversions are stronger than barotropic conversions over land. Over the ocean the situation is reversed and barotropic processes are more important than the baroclinic processes. Moreover, they suggested that barotropic conversions reach maximum values at the jet level near the jet latitude and processes related with baroclinic conversions appeared to be larger at the lower levels north of the jet latitude. Analysis by Reed et al. (1988) and Pytharoulis and Thorncroft

(1999) confirmed the structure of these patterns.

Diedhiou et al. (2002) estimated the energetics of 3 – 5 day and 6 – 9 day easterly waves using the NCEP-NCAR reanalysis. They suggested that the 3 – 5 day waves that form south of the AEJ are a consequence of barotropic instability of the jet and that the waves that form north of jet grow through both baroclinic and barotropic conversions. The 6 – 9 day easterly waves showed energy conversion patterns similar to the 3 – 5 day regime. However, over the ocean, the 6 – 9 day regime depicts a greater barotropic energy conversion.

In general, modeling studies with a prescribed basic state of the AEJ tend to find that barotropic conversions are the main energy source of AEWs (e.g. Mass 1979, Thorncroft and Hoskins 1994a, b). On the other hand, models with prescribed diabatic heating usually suggest that baroclinic processes dominate (e.g. Estoque and Lin 1977). However, Hsieh and Cook (2007) analyzed the results of a regional climate model and found that baroclinic overturning is the dominant energy source. This baroclinic overturning is associated with upward motion of warm air that results from latent heat release due to convection.

Recently, AEWs studies have concetrated on undertanding differences between developing and non developing AEWs. During the NAMMA campaing, two developing waves experienced clear barotropic energy conversions in conjunction with positive diabatic heating (Ross et al. 2009). Non-developing waves, on the other hand, exhibited negative barotropic energy conversions (Ross et al. 2009). Arnault and Roux (2009) quantified the energetics of a developing AEW using a set of equations adapted from Lorenz's (1955). Their results showed that the growth or development of an AEW results from barotropic and baroclinic energy conversions over West Africa. Additionally, they found that the growth of an AEW over the tropical eastern Atlantic is mostly due to barotropic energy conversions.

6.2.4 SST gradients and AEWs

Nicholson and Webster (2007) argued that the sea surface temperature (SST) gradient determines the presence or absence of a strong low level westerly equatorial jet located just north of the Equator. Moreover, they suggested that the development of the westerly jet, occurring when there is a strong background cross-equatorial pressure gradient, displaces the AEJ northward into the Sahel. The tropical rainbelt also migrates northward with the jet. This displacement produces wet conditions in the Sahel and dry conditions along the Guinea coast to the south. This new paradigm is founded on the inertial instability mechanism of Tomas and Webster (1997). This mechanism explains the location of near-equatorial convection in regions of strong cross-equatorial pressure gradient and states that this convection maximum is equatorward of the SST maximum and surface pressure minimum. Tomas and Webster attribute this to a strong cross-equatorial flow that advects absolute vorticity across the Equator leading to an inertially unstable state. As a result, a stabilizing secondary circulation, producing low-tropospheric cyclonic vorticity, is generated in a conditionally-unstable atmosphere where absolute vorticity balances the shear of the zonal wind (see also Tomas et al. 1999 and Toma and Webster 2010a). This mechanism explains the location of convection over West Africa and the generation of a low level westerly wind maximum that is essential in the local dynamics.

Nicholson and Webster (2007) confirm that the various conditions for inertial instability in the eastern Tropical Atlantic are satisfied in August during wet years but not in dry years, suggesting that inertial instability plays a role in producing the wetter conditions in the Sahel. They observed that the westerly wind maximum, which results from the instability induced by the strong cross-equatorial pressure gradient, accounts for the northward displacement of the AEJ and associated disturbances. This result confirms that the location of the jet is linked to changes in the SST distribution.

Given that the AEJ is one of the sources of AEWs over Africa, changes in the SST distribution are expected to impact the wave activity. Grist and Nicholson (2002) and Grist (2002) investigated the link between rainfall variability and wave activity and found that in years characterized by wet conditions over the Sahel, the AEWs tended to be stronger near the AEJ level. These findings suggest that the SST distribution over the Tropical Atlantic is linked to the structure of the AEWs. The SST is expected to impact AEWs through changes in the structure of the AEJ and through changes in the relation between convection and AEWs. This aspect of the dynamics of AEWs has not received attention in previous works and will be explored in the following chapters.

In this study we use a regional model to explore the role of orography and cross-equatorial pressure gradients induced by SST in the genesis and maintenance of AEWs. For this purpose, we conducted a control experiment and two idealized experiments where topography and SST distributions are selectively added and removed.

Chapter 6 describes the model and the experimental design, and compares the results from the control simulation with observations. Chapter 7 discusses the changes in AEWS variability associated with orography and SST gradient. Results from the two experimental simulations are compared with the control simulation focusing on differences in the structure of the jet and differences in the statistical features of the AEWs. Chapter 8 describes the instability mechanisms associated with wave growth and evaluates whether these mechanisms are present in the experimental simulations. Finally, we discuss how energy conversions are modified by orography and SST gradient.

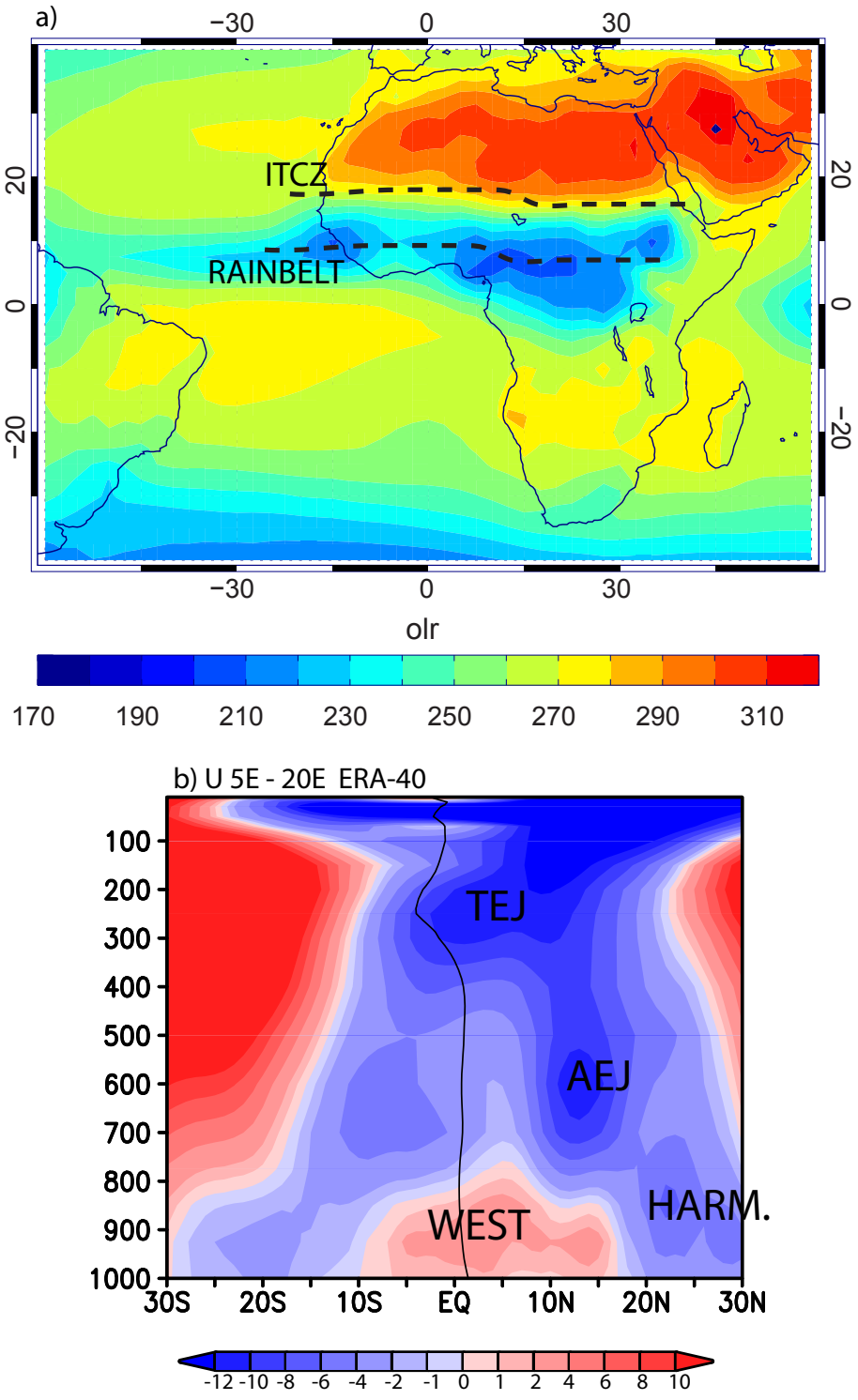

Figure 6.1: a) Mean OLR distribution for JJAS over Africa. Units are Wm^{-2}. b) Latitude-height cross section of zonal wind from the ERA-40 reanalysis averaged between 5°E and 20°E. Units are ms^{-1}. The main circulation features over Africa are indicated in these diagrams: ITCZ, rainbelt, TEJ, AEJ, Harmattans (HARM) and the low level westerly flow (WEST).

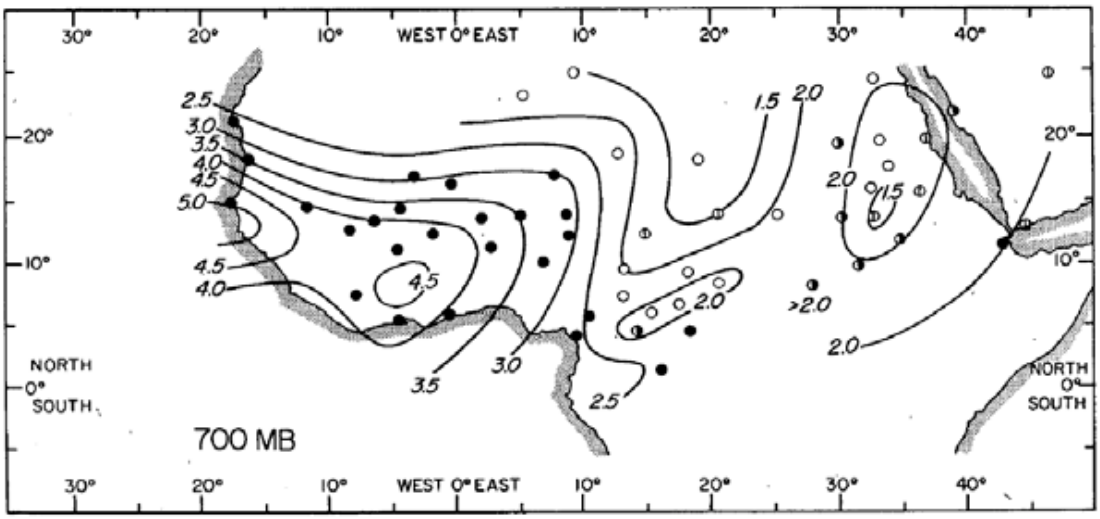

Figure 6.2: Amplitude of meridional wind oscillation in the 2 – 5 day band at 700-hPa based on the Phase III GATE dataset. Larger amplitudes are found south of 15°N in the region between 10°E and 0° . From Albignat and Reed (1980).

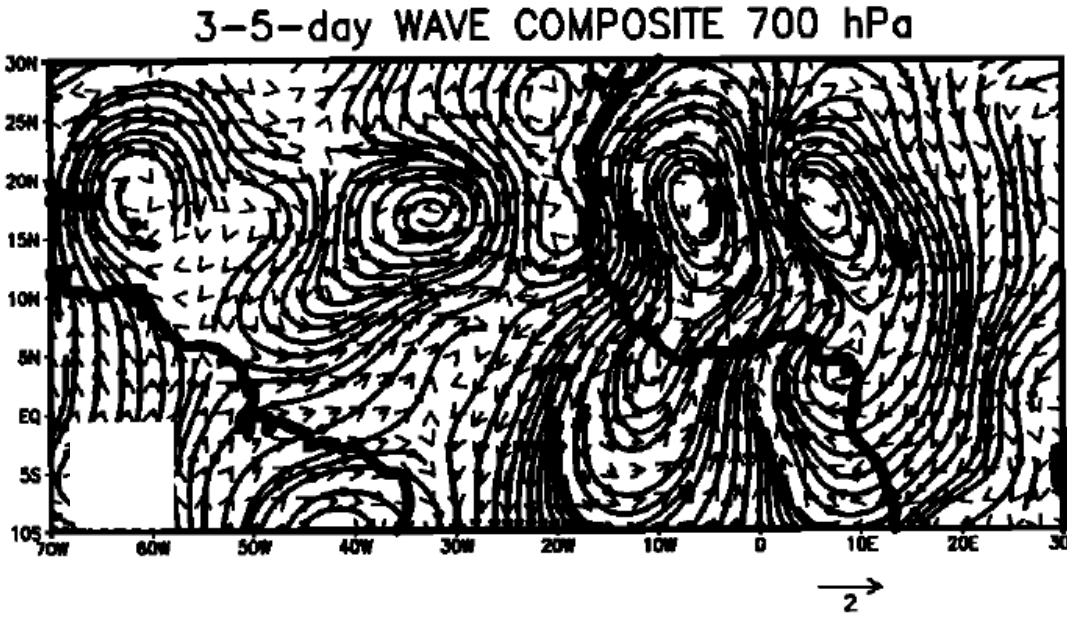

Figure 6.3: Composite streamlines and wind vectors at 700-hPa for the 3 – 5 day band based on the NCEP/NCAR dataset on the period 1979-1995. A southeast/northwest tilt is evident north of the AEJ and a southwest/northeast tilt is observed south of the AEJ. From Diedhiou et al. (1998)

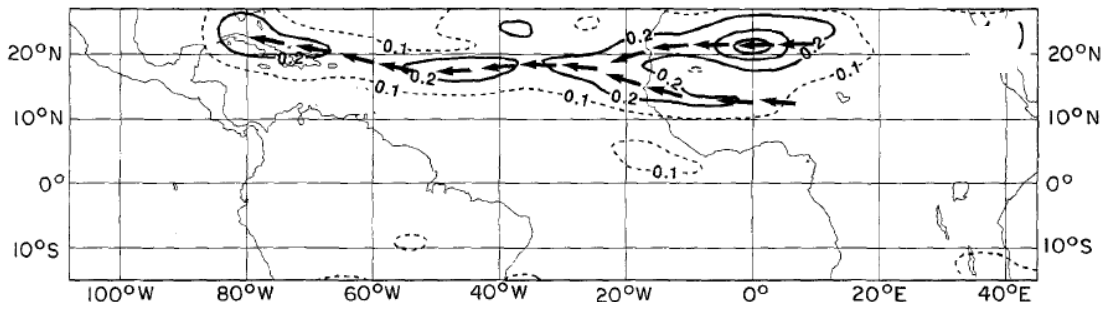

Figure 6.4: Variance of vorticity at 700-hPa in frequency bands corresponding to periods of 2.9 – 4.0 days. Broken arrows represent disturbance tracks. Distinct storm tracks can be seen emanating from the northerly and southerly regions of origin, merging into a single path at the coast. From Reed et al. (1988).

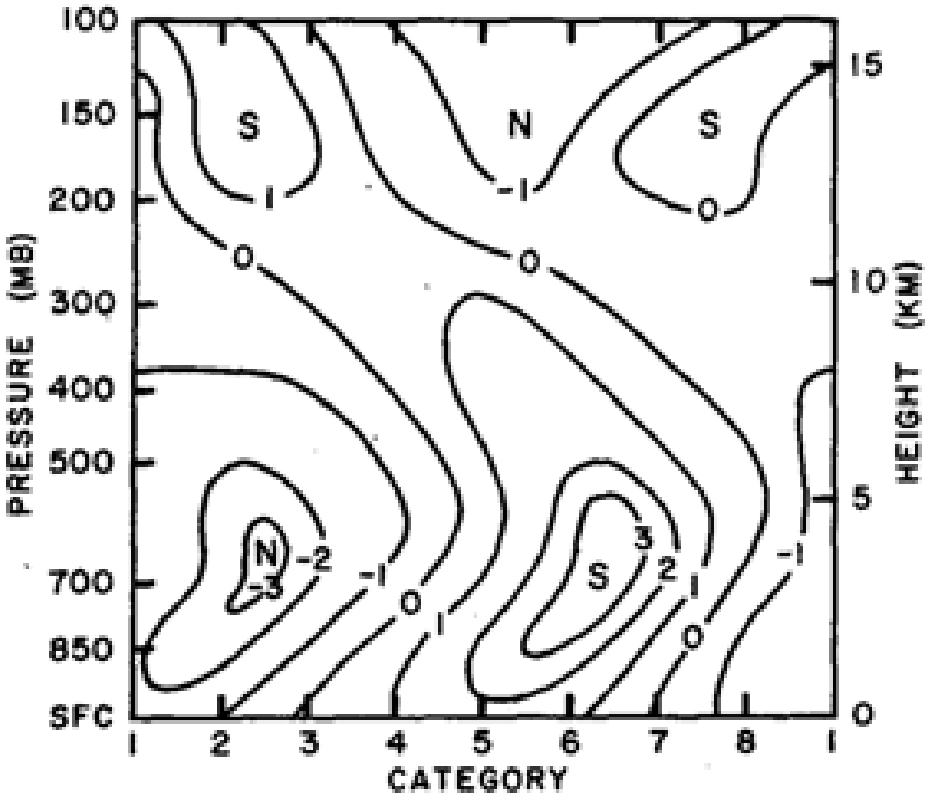

Figure 6.5: Composite diagram of meridional wind at Dakar (14°44'N, 17°30'W). In the diagram category 3 and 7 correspond to the trough and ridges axes of the wave, respectively. Meridional wind slopes eastward with height up to 600-650 hPa. Above 600-hPa it slopes westward. From Burpee (1974).

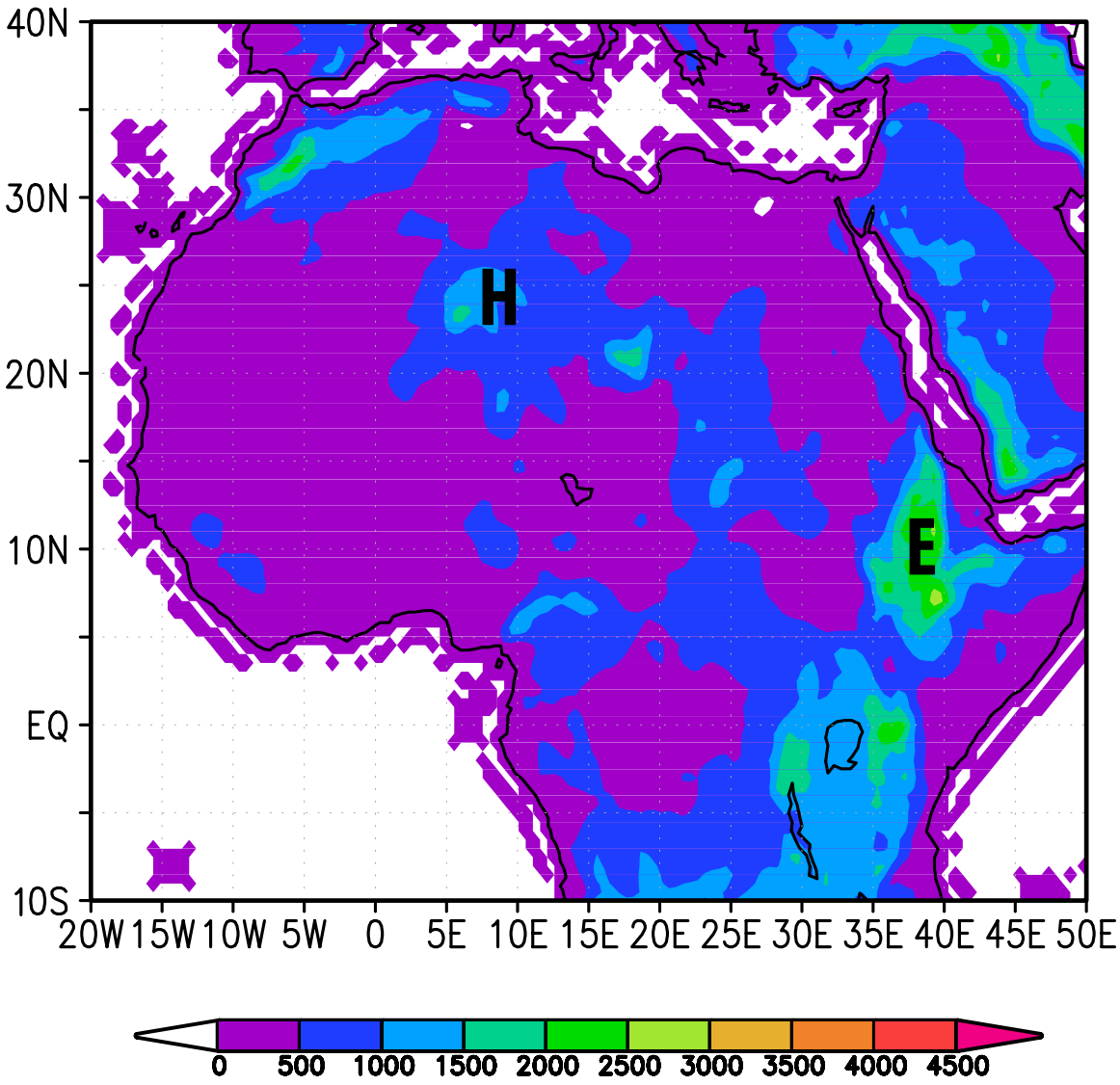

Figure 6.6: Topographic map of tropical Africa. Orographic features are designated by letters: E = Ethiopian highlands. H = Hoggar mountains.

CHAPTER VII

DATA AND METHODS

7.1 Model description

We utilize the Weather Research and Forecasting (WRF) regional model version 2.2 (Skamarock et al. 2005) to investigate the genesis, development and maintenance of African Easterly Waves (AEWs) over tropical Africa. Given the nature of the problem and the scale of the phenomenon to be studied, the ICTP general circulation model used in Part 1 is not appropriate. The WRF model is a fully compressible and nonhydrostatic model. It has a terrain-following σ hydrostatic-pressure vertical where $\sigma = (p_h - p_{ht})/\mu$, and $\mu = p_{hs} - p_{ht}$, p_h is the hydrostatic component of the pressure and p_{hs} and p_{ht} denote the values along the surface and top boundaries, respectively. A complete description of the vertical coordinate system can be found in Laprise (1992). The model uses an Arakawa C-grid staggering in the horizontal, meaning that normal velocities are staggered one half-grid length from the thermodynamic variables. The time integration scheme is the 3^{rd} order Runge-Kutta, with smaller time step for acoustic and gravity-wave modes (Wicker and Skamarock 2002). Additionally, the model uses 2^{nd} and 6^{th} order advection schemes in both horizontal and vertical directions.

The WRF model can be used to run both idealized simulations and real-data simulations. For real-data cases, initial conditions are pre-processed through a separate package that interpolates data from large-scale analysis or forecast analysis to the model grid and domain. For the lateral boundary conditions the model offers several options. Real data cases can use combinations of periodic, symmetric, open and time-dependent boundary conditions.

The WRF offers choices of numerous physics options that can be classified into the following categories: microphysics, cumulus parameterizations, surface physics, planetary boundary layer physics and atmospheric radiation physics. A brief description of the model configuration and physics used in the present study is provided in the following paragraph.

The WRF model for the control simulation was run over a domain extending from 65°W to 65°E and 40°S to 40°N, with a horizontal spatial resolution of 56 km. Figure 7.1 shows the model domain covering the African continent, the tropical eastern and central Atlantic Ocean and the western Indian Ocean. In the vertical, the model has 28 levels, with pressure p(top) at 50-hPa. The microphysics scheme is the WRF-Single-Moment 5, which allows supercooled water to exist, and a gradual melting of snow as it falls (Hong et al. 2004). The long wave radiation scheme is the Rapid Radiative Transfer Model (RRTM) based on Mlawer et al. (1997). The short wave radiation scheme is a simple downward integration of the solar flux based on Dudhia (1989). For the surface fluxes calculation the Monin-Obukhov scheme is used and land surface processes are parameterized using a 5-layer thermal diffusion scheme. The boundary layer scheme is the Yonsei University (YSU) scheme, which considers an explicit treatment of the entrainment layer at the planetary boundary layer top (Hong et al. 2006). For cumulus parameterization, the Betts-Miller-Janjic (Betts and Miller 1993; Janjic 1994) scheme is adopted.

7.2 Observational data

The ECMWF ERA-40 reanalysis data set (Uppala et al. 2005) is used as initial and lateral boundary conditions in all simulations. The horizontal resolution of the ERA-40 is 1° by 1° with 18 levels in the vertical. Lateral boundary conditions are updated every 6 hours at all levels. SST fields in the ERA-40 reanalysis are obtained from externally produced analysis from the Met Office (HADISST1; Rayner et al. 2003) and

NCEP (NOAA/NCEP 2D-Var dataset; Reynolds et al. 2002). The ERA-40 dataset is also used to evaluate the ability of the model to simulate AEWs.

The Global Precipitation Climatology Project (GPCP; Arkin and Meisner 1987; Adler et al. 2003) monthly rainfall dataset is used to evaluate the model performance. This product is the result of a merged analysis that incorporates precipitation estimates from surface rain gauge observations, satellite microwave data and satellite infrared data. Rainfall estimates are available from 1979 to the present, at a 2.5° by 2.5° horizontal resolution.

7.3 Experimental design

A series of experiments were designed to explore the mechanisms that trigger the formation and maintenance of AEWs. We are specifically interested in studying two specific possibilities: 1) the role of the mechanical effect of the African orography in the AEWs genesis whereby thermal and dynamic gradients are reversed invoking instabilities, and 2) the role of the cross-equatorial pressure gradients induced by SST in the genesis and maintenance of AEWs. For this reason we decided to conduct idealized modeling experiments where topography and SST distributions are selectively added and removed. Experiment 1 is the control case (CTRL) where full lateral boundary conditions are used to feed the model and SST is updated every 6 hours from ERA-40 reanalysis. With this experiment we expect to reproduce the main atmospheric features observed during the boreal summer over Africa, such as the African Easterly Jet (AEJ) and westward propagating disturbances. Mean states for several variables obtained from the control case will be compared with mean states obtained from observations. Figure 7.1 displays the model domain and the terrain height field used for this experiment. In Experiment 2, the orographic features are removed and replaced by a uniform elevation of 40 m overall land areas. Lateral boundary conditions along the southern, northern and western boundaries of the domain are the same as the

Table 7.1: Description of lateral boundary conditions, SST and topography used for each of the experiments

Experiment	Initial conditions and lateral boundary conditions	Sea surface temperature	Orography
Experiment 1	ERA–40 Reanalysis Updated every 6 h.	ERA–40 Reanalysis Updated every 6 h.	Full topography
Experiment 2	No flow along the eastern boundary Others ERA–40 Reanalysis, Updated every 6 h.	ERA–40 Reanalysis Updated every 6 h.	Flat topography
Experiment 3	ERA–40 Reanalysis Updated every 6 h.	Homogenized SST	Full topography

ones used for the control case. However, at the eastern boundary, a no-flow condition is imposed to avoid the extension of the low-level Asian monsoon flow into continental Africa due to the suppression of the Eastern African Mountains. For this reason, we consider a smaller domain in the longitudinal dimension, with lateral boundaries located at 60°W and 40°E. The latitudinal boundaries are identical to the control case. SST is updated every 6 hours from the ERA-40 reanalysis. Figure 7.2 shows the domain for this experiment. Finally, in Experiment 3 lateral boundary conditions and orography features are kept the same as in the control experiment but the SST is not updated from the ERA-40 reanalysis dataset. For this experiment, homogenized SST fields are imposed with a Gaussian function for each time step and are used to update the model every 6 hours. SST distribution was design in this way to ensure a reduction in the cross equatorial pressure gradient (CEPG) over the Eastern Atlantic Ocean. The model domain used in this simulation is shown in Figure 7.1. Table 7.1 provides a summary of the major differences between experiments.

The three experiments are initialized at 00Z on June 1^{st} 2001 and are run through September 30^{th} 2001 for a total of 121 days. The first 30 days of the simulations are discarded to allow for spin-up. All the simulations are run in "free mode", without updating the internal domain with observations. Except for the SST fields, the initial

and lateral boundary conditions, all dynamic and thermodynamic fields are calculated internally within the model.

Figure 7.3 shows a Hovmoller space-time diagram of unfiltered meridional wind averaged between 5°N and 15°N at 600-hPa over the African continent for July, August and September 2001 from the ERA-40 reanalysis. There is considerable activity of westward propagating disturbances generated by the model. Some of the disturbances originate over eastern Africa between 30°E and 40°E. Other waves appear to develop between 10°E and 20°E. Both sets of disturbances propagate westward across the African continent and continue into the Atlantic Ocean, with average wavelength of about 3000 km, phase speeds in the 5 – 7 ms^{-1} range and period between 2 – 5 days, values that are in the range of previously documented AEWs (e.g. Reed et al. 1977). The climate assessment report (Waple et al. 2002) states that during 2001 the Sahel experienced a near-average rainy season. Additionally, an equatorward shift of the AEJ south of 15°N across the Sahel and a near- average tropical easterly jet (TEJ) were evident. All these features make the year 2001 a suitable year for our simulations.

7.3.1 Filtering technique

For much of our analysis we band-pass filter the data from the simulations to leave out variability not associated with AEWs. For this purpose, we use the Fast Fourier Transform to extract variability between 2 and 6 days. The 2 - 6 day band was chosen to be consistent with previous studies (e.g. Reed et al. 1988; Albignat and Reed 1980; Reed et al. 1977).

Additionally, the discrete wavelet transformation method (e.g. Torrence and Compo 1998) was used to calculate the scale averaged global power spectrum of meridional wind for the three experiments. A Morlet wavelet function was used as the mother function.

7.4 Control simulation vs. observational data

First, we determine whether the WRF model with the configuration proposed for the control case, hereafter CTRL, is able to reproduce the main atmospheric features observed over Africa during the summer season. For this purpose, we compare the CTRL simulated mean fields with observations from ERA-40. Figure 7.4 displays the simulated surface wind field (wind at 10 m) from CTRL averaged from day 31 to 121 (July – August – September) and the ERA-40 surface wind field averaged over the same period. The thick black line represent the 10 m zero absolute vorticity isopleth. The model is able to reproduce the south easterly trade winds over the Atlantic Ocean crossing the equator and then turning to the east over West Africa. The general trajectory of the north easterly trades is also well represented. Moreover, the model captures fairly well the low-level circulation over the western Indian Ocean and along eastern Africa. The magnitude of the wind field is in general stronger in the model compared to the observations, and this is possibly due to the higher resolution of the WRF model (56 km) compared to ERA-40 (111 km).

Figure 7.5 shows the precipitation mean field from CTRL and from the GPCP dataset for the July-September period. Observations display a rainfall maximum located in a latitude band between 5°N and 15°N. Simulated rainfall distribution displays the same behavior, except that it depicts higher amplitudes over the ocean and in some regions over land. The location of the rainfall belt coincides with the regions where OLR values are smaller than 240 Wm^2 (see Figure 6.1a). The smoother observed patterns could result from difference in resolution between the GPCP dataset grid (2.5°) and the model grid (∼0.5°). Large values of precipitation along the eastern and western boundaries are due to boundary effects (e.g. Toma and Webster 2010b).

Pressure-latitude cross sections of zonal wind over land and over ocean are plotted in Figure 7.6. Over land, the average meridional section between 5°E and 20°E shows that the model reproduces the main features of the general circulation observed over

Africa during the boreal summer (Figure 7.6a and Figure. 7.6b). These features are:

- A mid tropospheric easterly jet (AEJ) at 650-hPa and 13°N, with peak strength of about 10 m s^{-1}.
- An upper level tropical easterly flow (TEJ) at about 200-hPa and equatorward of the AEJ.
- A low-level westerly flow confined in the lower levels, between 5°S and 15°N
- A low-level easterly flow north of the AEJ, known as the Harmattans
- A mid-latitude westerly jet to the north.

Although the model resembles the fundamental properties of the general circulation over Africa, there is a notable difference in the representation of the low-level westerly flow. The CTRL mean field shows a much deeper (up to 700-hPa) and stronger ($\sim$8 ms^{-1}) westerly flow compared to the ERA-40 ($\sim$4 ms^{-1}). This could explain the difference in the intensity of the AEJ in the CTRL simulation ($\sim$10 ms^{-1}) relative to the ERA-40 ($\sim$12 ms^{-1}).

Over the ocean the model also resembles the main observed features (Figure 7.6c and Figure 7.6d). The AEJ is still present at 650-hPa and 15°N. The TEJ and the low level westerly flow are also evident south of the AEJ. In summary, the model gives a clearly defined AEJ, which is well separated from the upper level and low-level easterlies.

Since one of our objectives is to study the role of the cross-equatorial pressure gradient (CEPG) induced by SST in the genesis and maintenance of AEWs, it is important to evaluate whether the model simulation displays a strong CEPG and the associated circulation patterns that are predicted by the inertial instability theory proposed in Tomas and Webster (1997); Tomas et al. (1999); Toma and Webster (2010a). The mean meridional circulation over the ocean, between 30°W and 20°W,

is plotted in Figure 7.7 for both the observations and the CTRL simulation. Figure 7.7 also shows the horizontal wind divergence and the zero absolute vorticity line. The two diagrams depict a very similar pattern. Both sections display a deep meridional circulation with southerly winds in the lower atmosphere ($\sim$6-8 ms^{-1}) and northerly winds in the upper troposphere ($\sim$8 ms^{-1}). A weaker shallow meridional circulation is also evident in both sections. However, the magnitude of the northerly flow is larger in the model simulation ($\sim$4 ms^{-1}) than in the observations ($\sim$1 ms^{-1}). This result is not surprising given that Zhang et al. (2008) reported that the shallow meridional circulations is very weak in ERA-40 over West Africa similar to those found by Tomas and Webster (1997); Toma and Webster (2010a). Moreover, the zero absolute vorticity contour is located some degrees north from the equator and bisect the divergence-convergence doublet in the lower atmosphere. Overall, the CTRL simulation depicts a divergent and meridional circulation that is consistent with inertial instability theory.

Figure 7.8 shows the latitudinal distribution of SST and surface pressure for the CTRL simulation averaged between 30°W and 20°W. An SST maximum is located north of the Equator and it does not coincide with the latitude of minimum surface pressure. A strong CEPG is also evident from this figure. According to Tomas and Webster (1997), convection is expected equatorward of the surface pressure minima.

Finally, we investigate if the model is able to portray westward propagating disturbances with wavelengths and phase speeds between the observed ranges for AEWs. Time-longitude diagrams of unfiltered meridional wind at 15°N for the CTRL simulation are shown in Figure 7.9 at 600-hPa and 850-hPa levels. The figure displays westward propagating disturbances at both levels. The wavelength of these disturbances is about 2700 km, with a phase speed of $6 - 7$ ms^{-1} and a period between $2 - 6$ days. In the mid troposphere, the westward propagating disturbances appear to originate somewhere between 30°E and 40°E, reach peak amplitudes between 10°W and 0° and decay over the ocean. In the lower troposphere, westward moving waves seem

to originate somewhere between 20°E and 40°E, debilitate between 10°E and 10°W and intensify near the African coast. Power spectra of 850 and 600-hPa meridional wind component along 15°N (Figure 7.10) for different longitudinal sections show, in fact, that the waves have a distinctive period of 2 – 6 days. Over East Africa, variance in the 2 – 6 day band is stronger at the jet level. Over West Africa, peaks in this band are stronger near the surface level. Along 30°E, there is also considerable variability associated with periods longer than 6 days.

In summary, the model simulation portrays the mean climatological features observed during the boreal summer over Africa, providing a reasonable representation of the AEJ structure and the AEWs. Moreover, the model resembles a meridional circulation that is consistent with the existence of a strong cross equatorial pressure gradient over the Eastern Atlantic. Based on the comparison between the CTRL simulation and the ERA-40 data, there is confidence that the WRF model is a valuable tool to investigate the role of orography and SST gradients in the genesis and maintenance of AEWs.

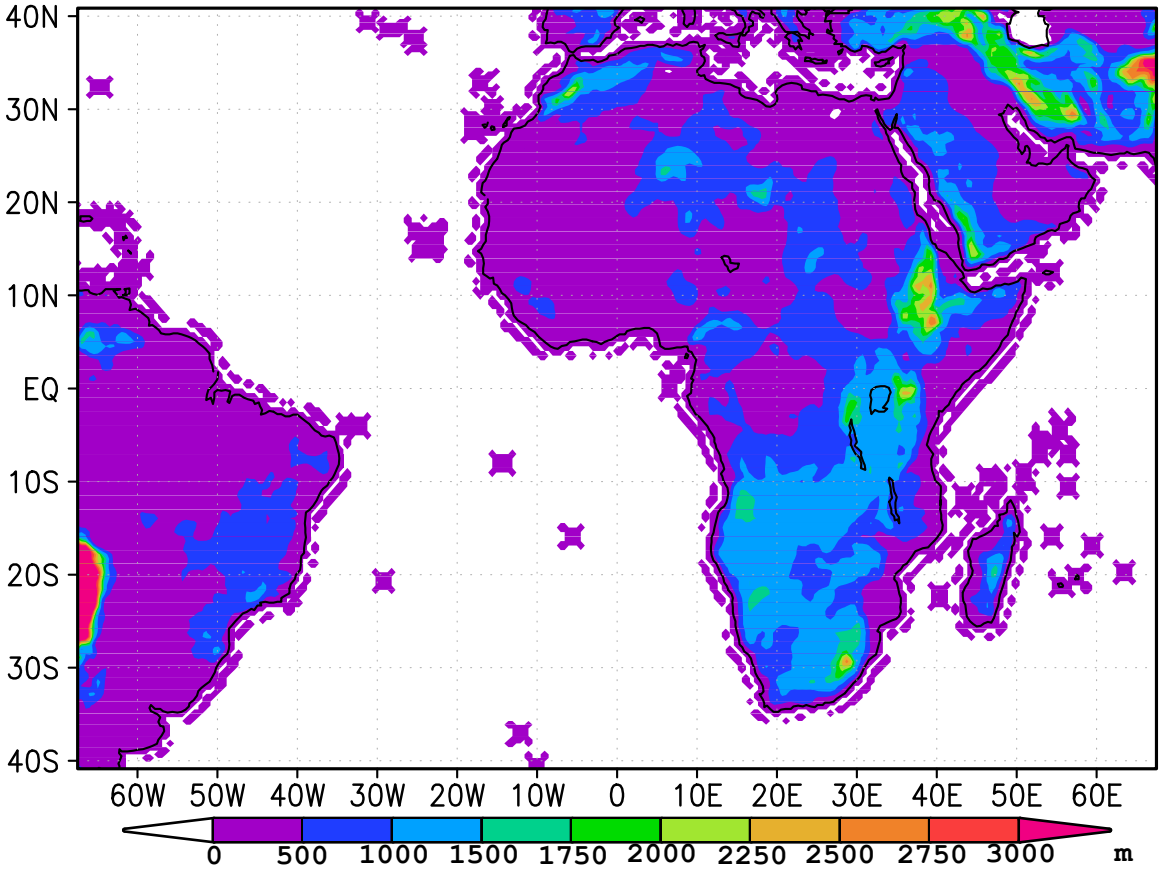

Figure 7.1: Physical domain and terrain height used in the control (CTRL) and Experiment 3 numerical simulations. Contour interval is 250 m.

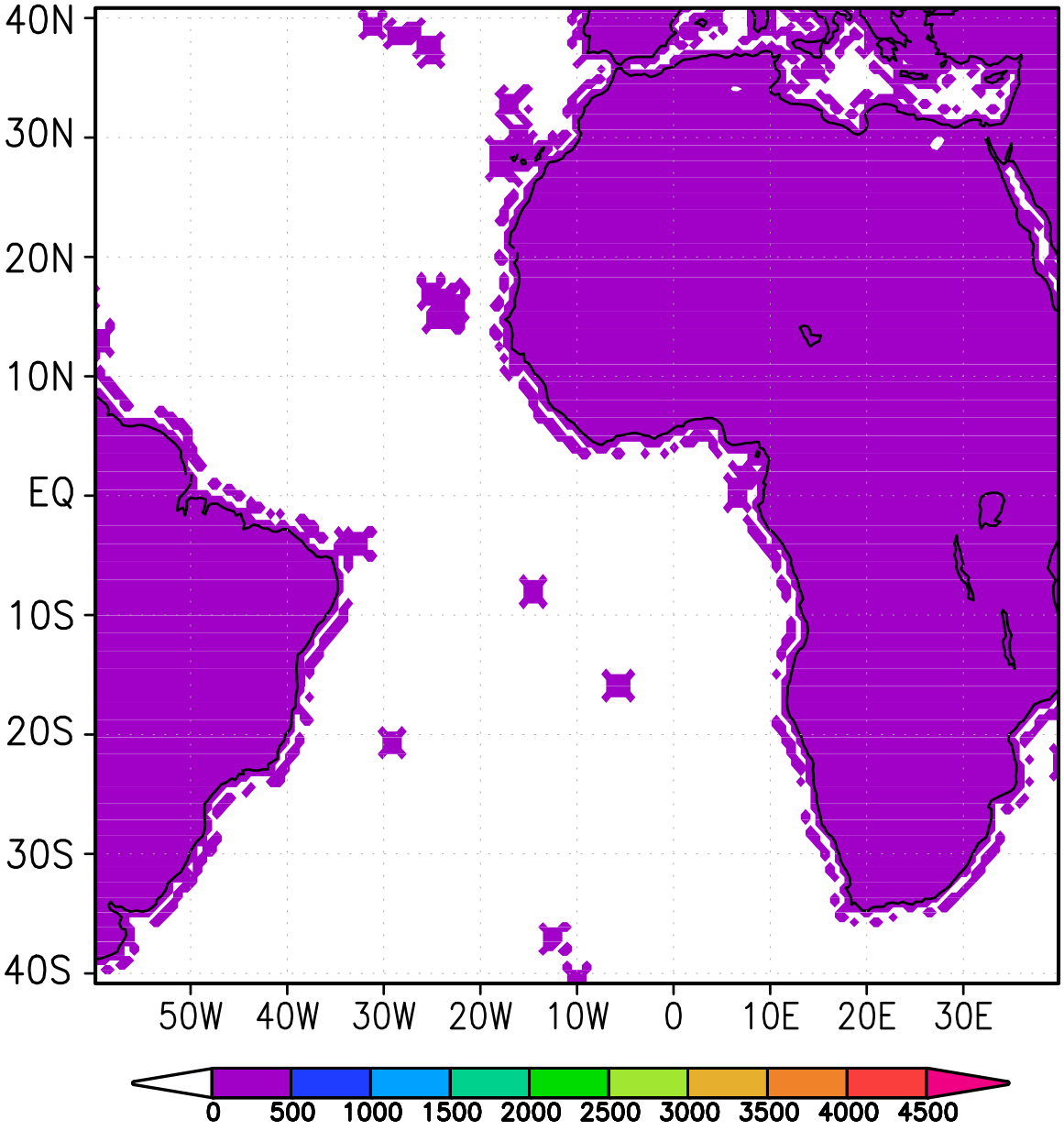

Figure 7.2: Physical domain and terrain height used in Experiment 2 (NO_ORO). Contour interval is 500 m.

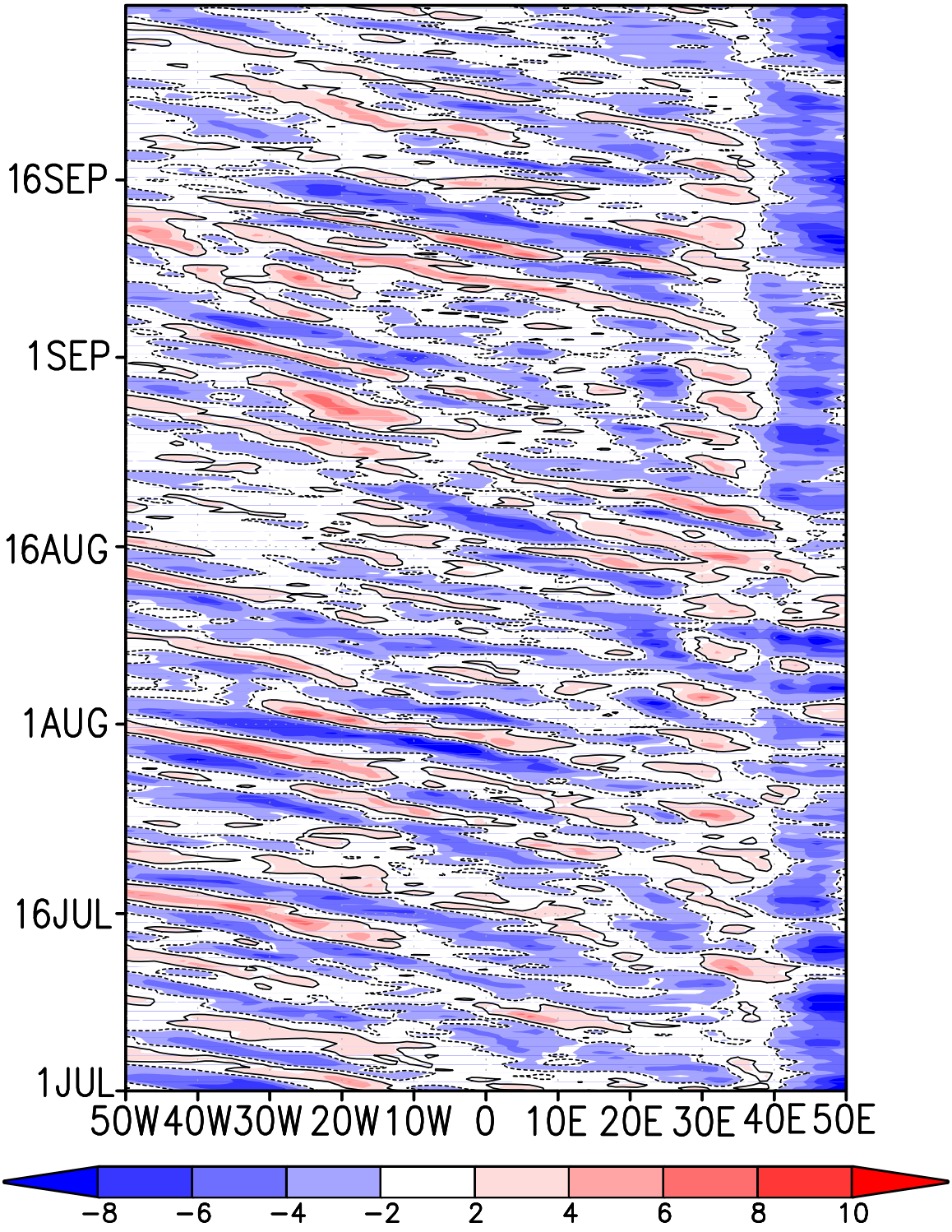

Figure 7.3: Space - time diagram of unfiltered meridional wind averaged between 5°N and 15°N, at 600-hPa for July, August, and September 2001 from ERA-40 reanalysis. Units are m s^{-1}.

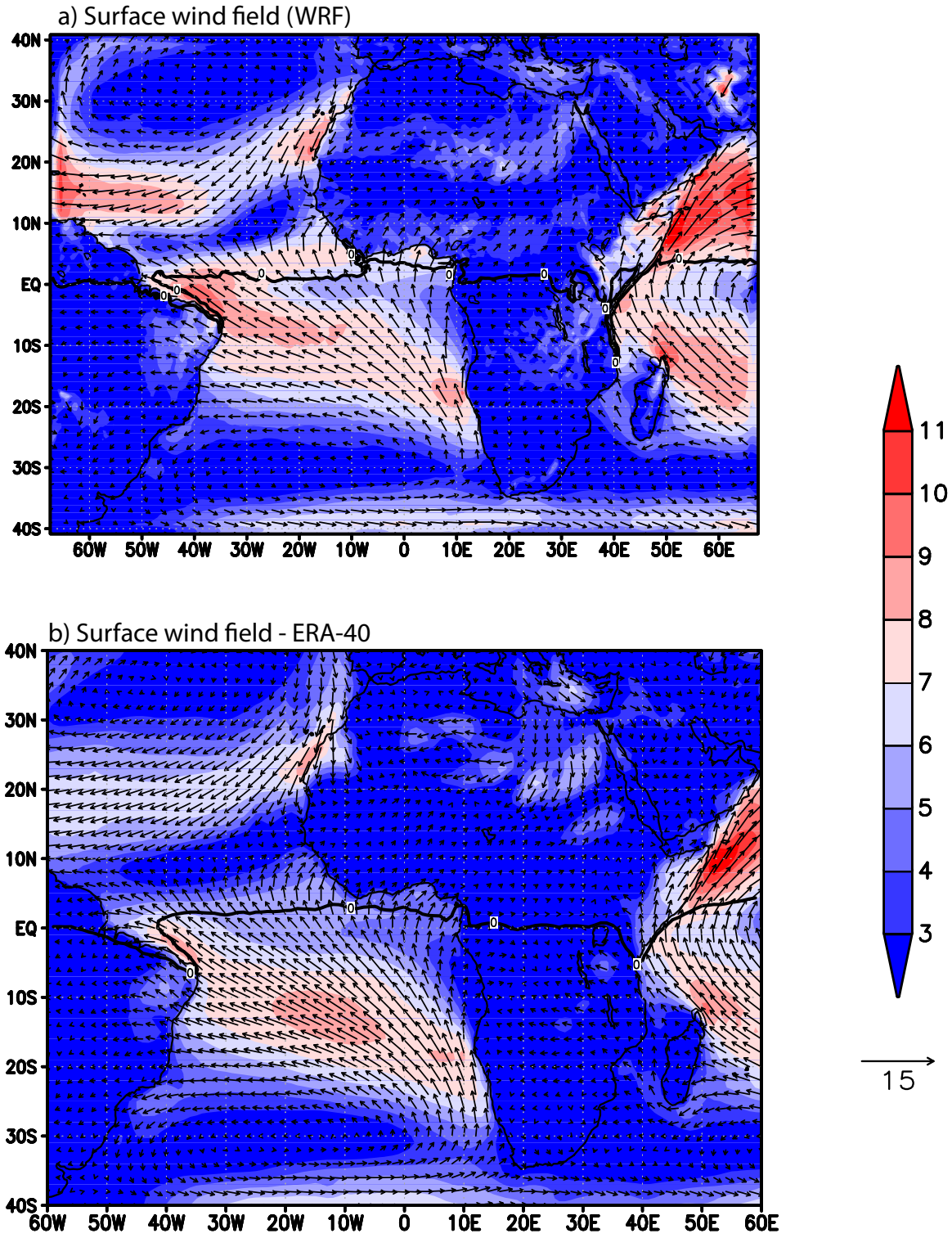

Figure 7.4: Mean distribution of the 10 m horizontal wind field from a) CTRL simulation (WRF). b) ERA-40 dataset. Units are m s^{-1} .The thick black line represent the mean absolute vorticity n=0 line at 10 m.

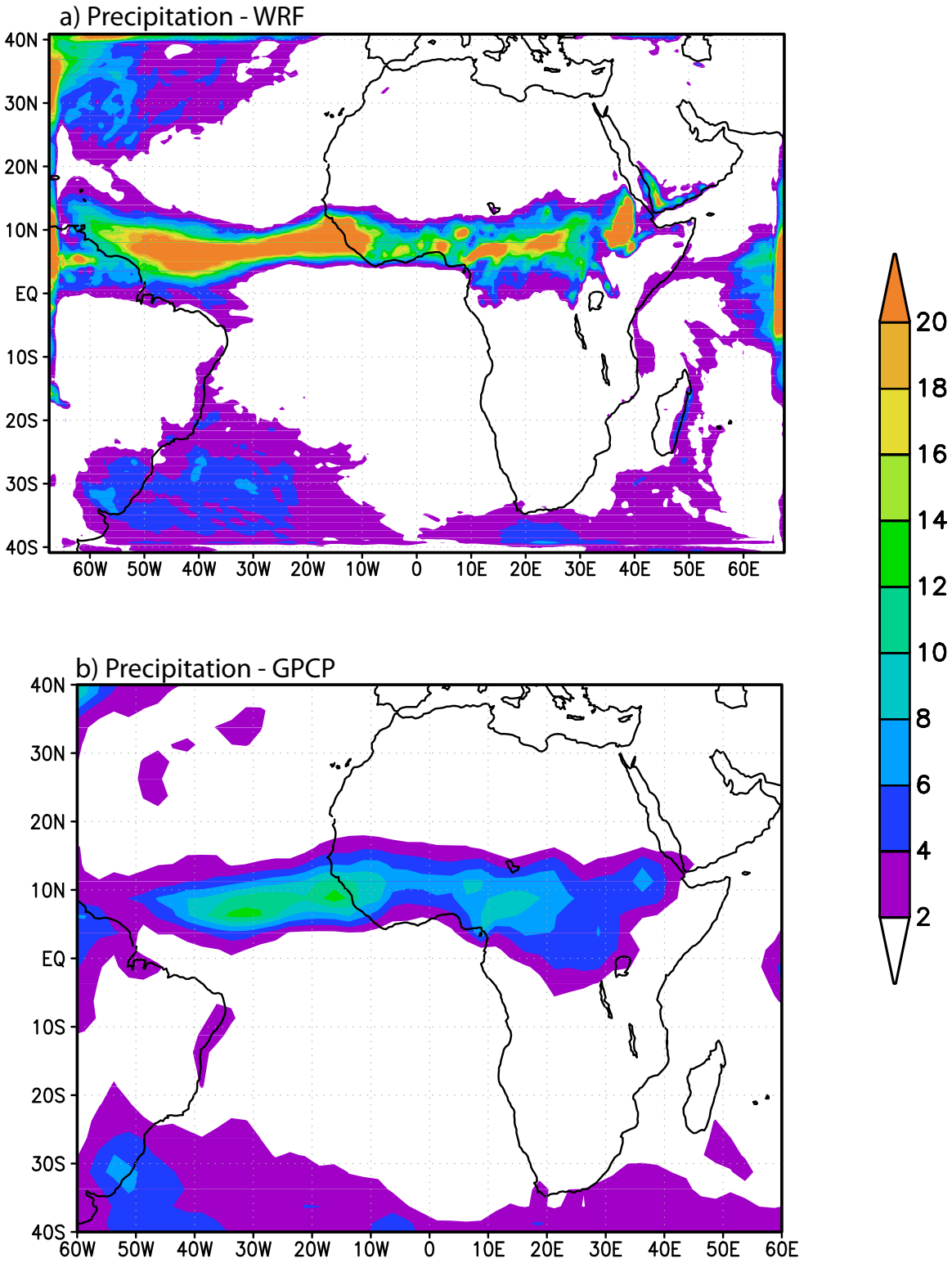

Figure 7.5: Mean distribution of precipitation rate for July- September 2001 from a) Control simulation (WRF) b) GPCP dataset. Units are mm day^{-1}.

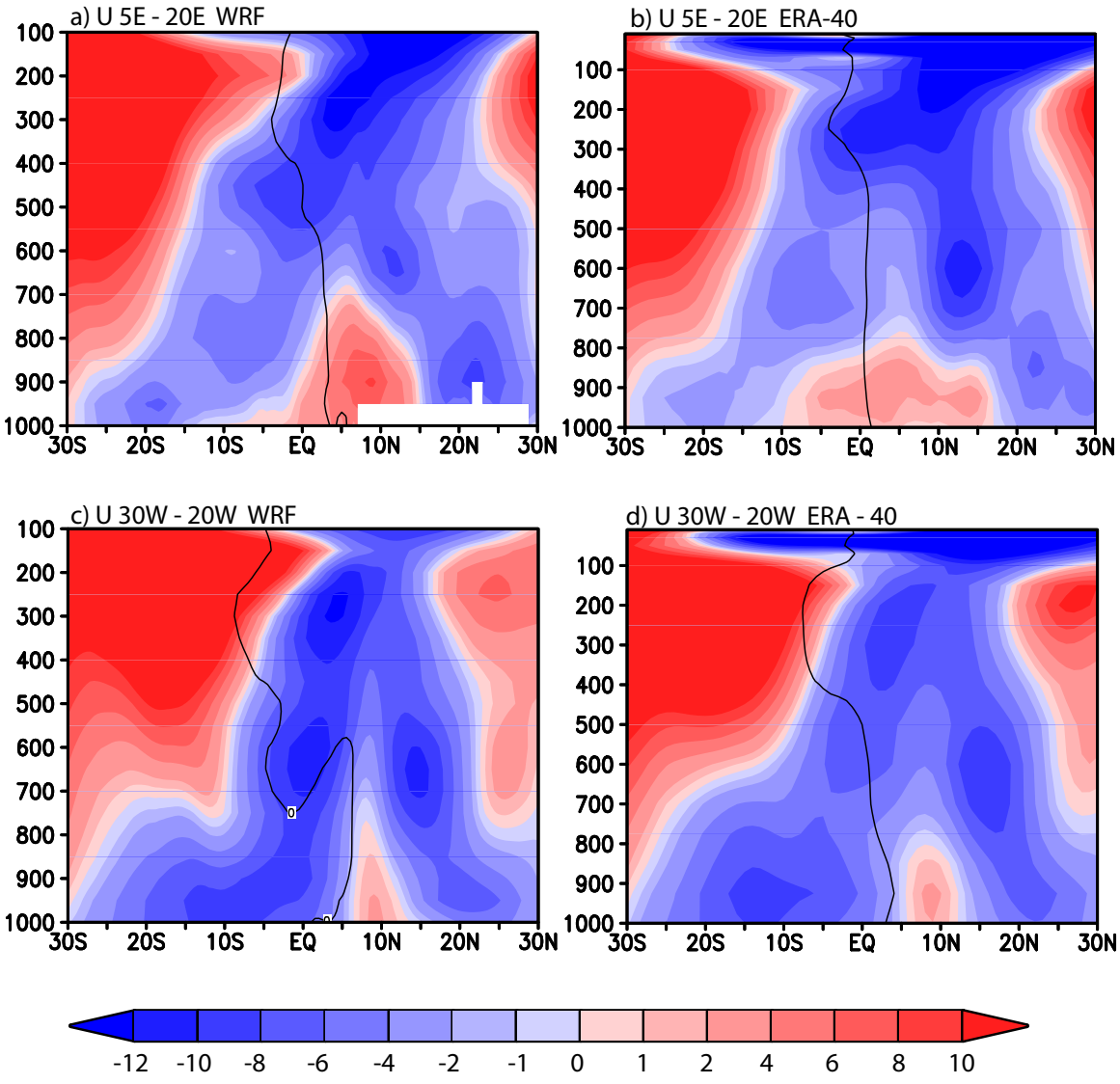

Figure 7.6: Meridional cross section of zonal wind from a) CTRL simulation (WRF), averaged between 5°E-20°E. b) As in a) but from ERA-40 dataset. c) CTRL simulation (WRF) averaged between 30°W and 20°W. d) As in c) but from ERA-40 dataset. Units are m s^{-1}. The thick black line represent the mean absolute vorticity n=0 line.

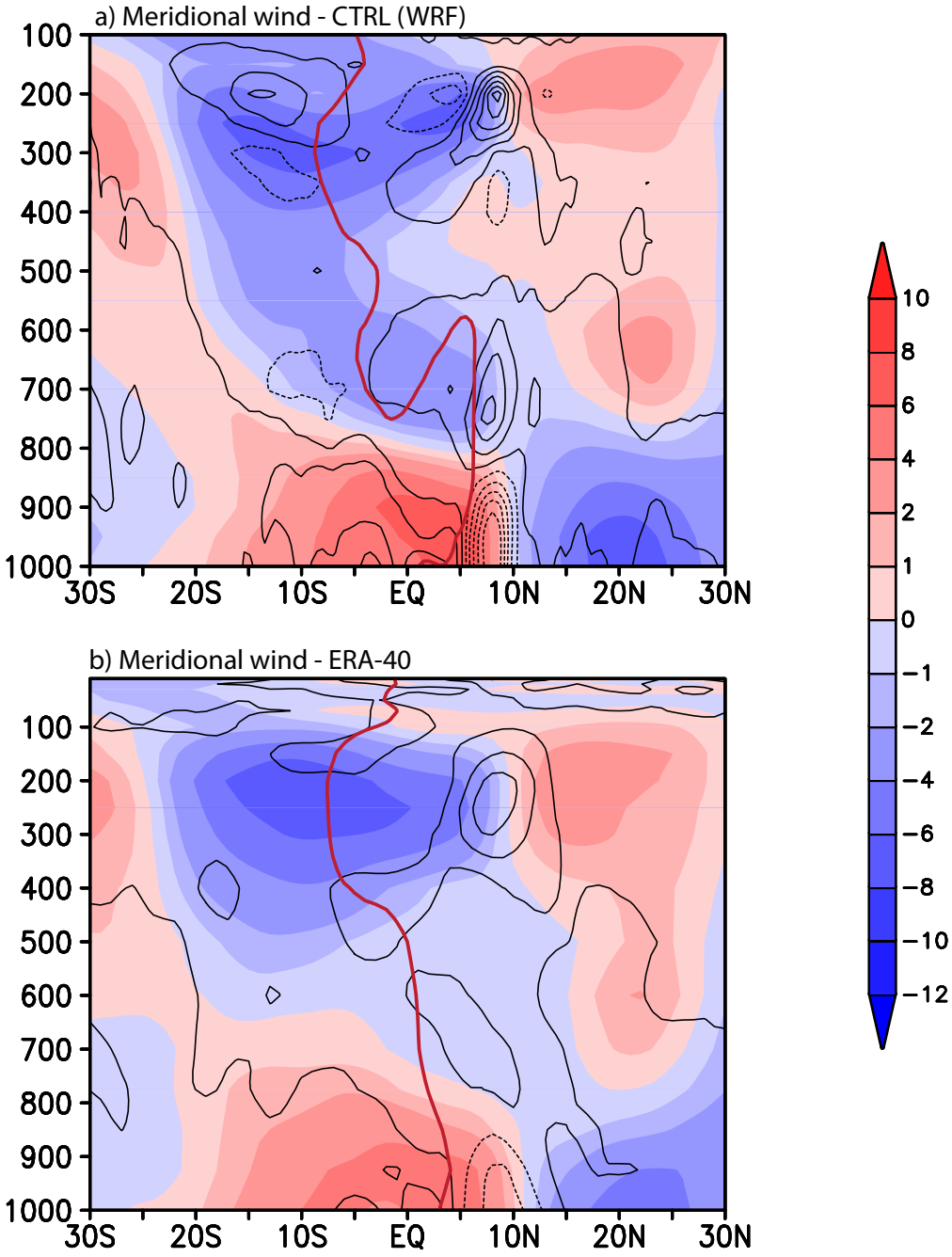

Figure 7.7: Pressure-latitude cross section of meridional wind averaged between 30°W-20°W from a) CTRL simulation (WRF); b) ERA-40 dataset. Units are m s^{-1}. Black contours represent the horizontal wind divergence (contour interval is $3*10^{-1}s^{-1}$). The thick red line represents the mean absolute vorticity n=0 line.

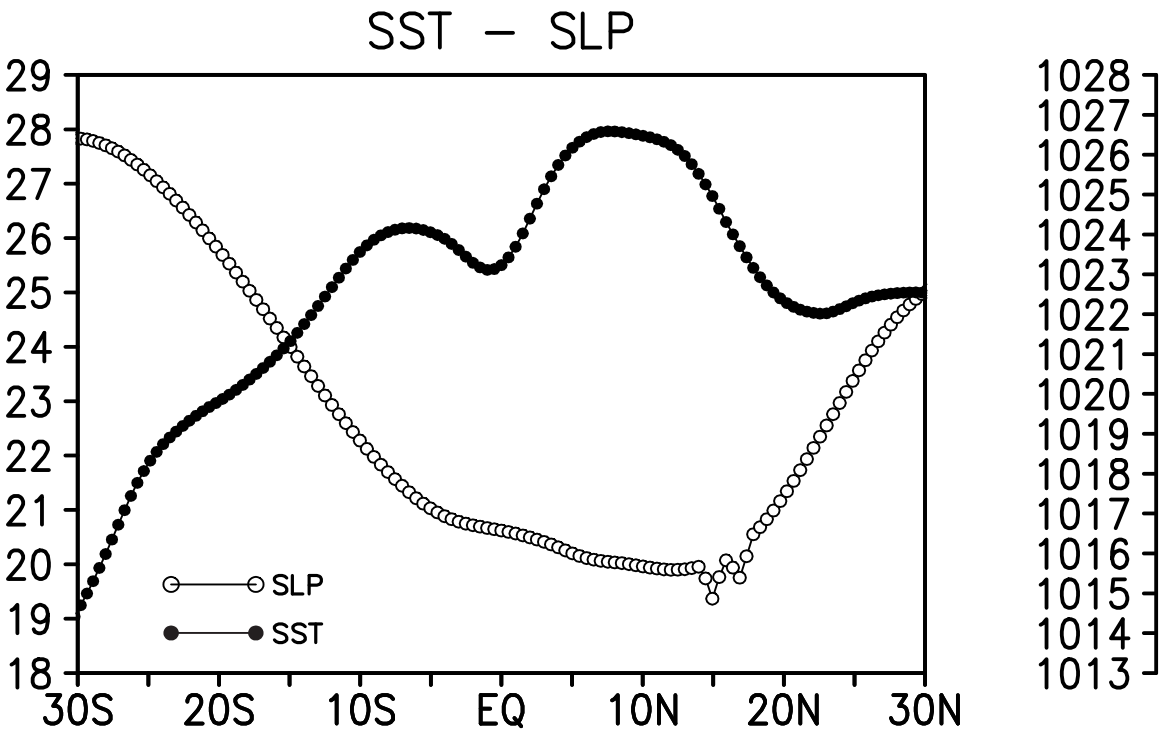

Figure 7.8: Distribution of sea surface temperature (SST) and sea level pressure (SLP) for the 30°W-20°W longitudinal band from CTRL simulation. Units of temperature are °C. Units of pressure are hPa.

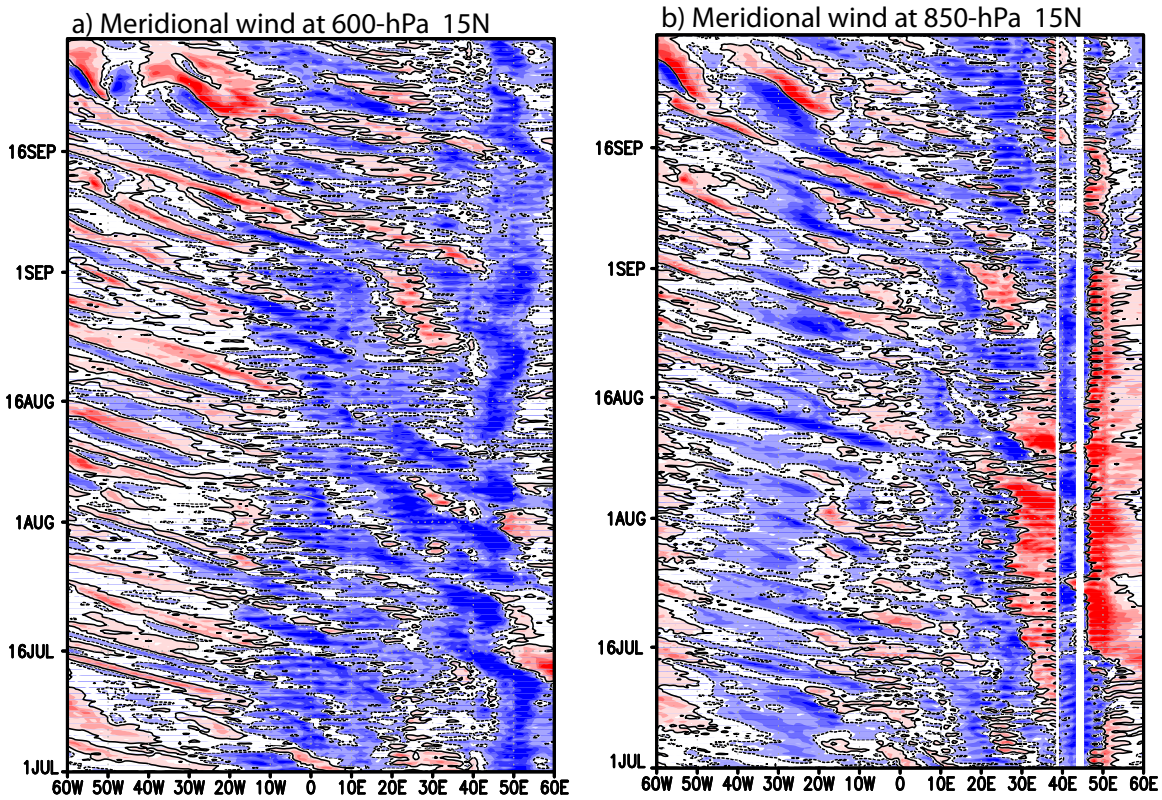

Figure 7.9: Time-longitude diagram of meridional wind from CTRL simulation at 15°N and a) 600-hPa; b) 850-hPa. Units are m s^{-1}.

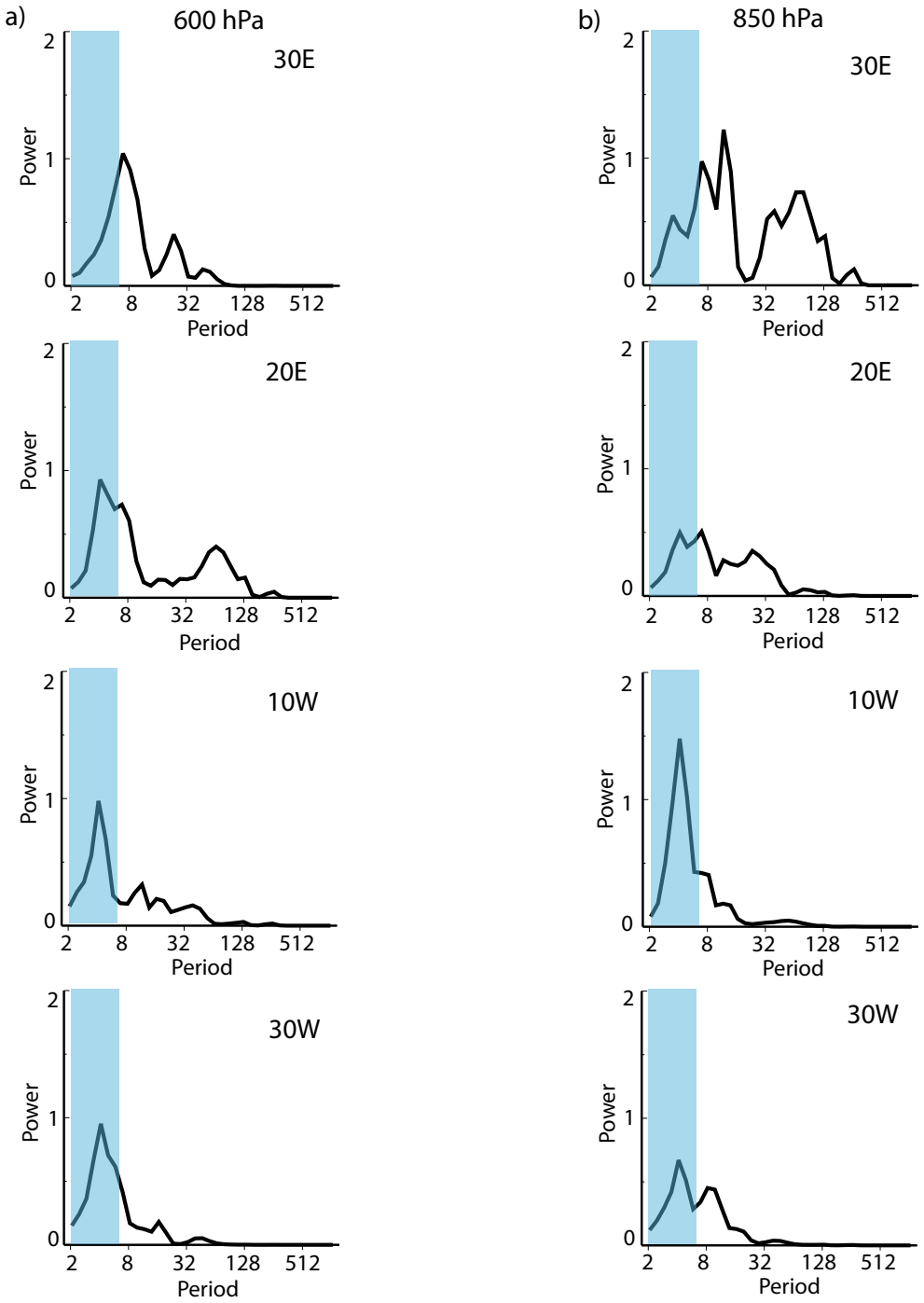

Figure 7.10: Global wavelet power spectra of meridional wind at longitudes 30°E, 20°E, 10°W, and 30°W at a) 600-hPa; b)850-hPa. Units are m^2s^{-2}.

CHAPTER VIII

CHANGES IN AFRICAN EASTERLY WAVE VARIABILITY ASSOCIATED WITH OROGRAPHY AND SST GRADIENTS

To investigate the role of orography and cross-equatorial SST gradients in African easterly wave genesis and maintenance, we carried out Experiment 2 and Experiment 3 (refer to Table 7.1). Here, we compare results obtained from these two experimental simulations with CTRL, focusing on: 1) differences in the structure of the AEJ, 2) structure and statistical features of westward propagating disturbances and 3) differences in surface temperature distribution.

8.1 Role of orography in African easterly wave structure

Figure 8.1 shows meridional cross-sections of zonal wind over land and over the ocean from Experiment 2 (hereafter NO_ORO) and from CTRL. Over land, Figures 8.1a and 8.1b indicate that the AEJ is much weaker in NO_ORO than in CTRL. An easterly flow, with an intensity on the order of 6 ms^{-1}, is evident at 650-hPa and near 13°N in Figure 8.1a but it does not have the same well defined core as in CTRL. The TEJ near 200-hPa and the Harmattans also appear to be weaker in NO_ORO than in CTRL. Over the ocean, Figure 8.1c shows no AEJ in the middle troposphere and a much deeper Harmattan flow. The monsoon flow is also reduced in strength compared to the CTRL (Figure 8.1d).

Figure 8.2 shows the mean zonal wind from NO_ORO and CTRL at 650-hPa and indicates distinct differences in the AEJ. Maximum easterly winds in NO_ORO are 8 m s^{-1}, while in CTRL they are near 12 ms^{-1}. This maximum, which takes

place on the West African coast, is located 3° south of the jet core in CTRL. Over West Africa the AEJ reach maximum easterly velocities between 6 and 7 ms^{-1} in the NO_ORO case, somewhat weaker than the 10 ms^{-1} in the CTRL case. These results confirm that orography is an important player in determining the structure of the AEJ, agreeing with previous findings by Wu et al. (2009). The structure and strength of the AEJ is a key factor in this study, because it has been hypothesized that genesis of AEWs is directly related to the jet (e.g. Burpee 1972).

The mean surface temperature from NO_ORO and CTRL is plotted in Figure 8.3. This figure reveals that the removal of orography also impacts the distribution of surface temperature. The region of highest temperatures covers a narrower latitudinal band in the NO_ORO case (∼10°) than in the CTRL case (∼20°) and temperatures over Central/East Africa reach higher values than normal south of 10°N. Thus, the distribution of meridional surface temperature gradients is expected to be different in the NO_ORO case, which translates in a modified structure of the AEJ.

The time-longitude evolution of unfiltered meridional wind at 600-hPa and 15°N (near the jet level and jet latitude) from NO_ORO and CTRL is plotted in Figure 8.4. The first aspect to note is the existence of westward propagating structures across Africa in NO_ORO, but with some differences in structure and strength compared to the CTRL case. In the NO_ORO case (Figure 8.4a), westward propagating disturbances appear to originate further west compared to CTRL, somewhere between 0° and 20°E. In general, the amplitude of the waves seems to be weaker in NO_ORO than in CTRL and they do not appear to intensify between 0° and 10°W.

Spectral analysis is a very useful technique for obtaining information on the main statistical properties of the westward propagating disturbances. In this study, we are going to use this type of analysis to determine the period of the waves observed in the time-longitude diagrams and to extract the imprint of AEWs on different atmospheric variables. Figure 8.5 shows the power spectra of the meridional wind component along

15°N, at 650 and 850-hPa for three different longitudinal sections from NO_ORO (in red) and CTRL (in black). Over East Africa (∼30°E), a large reduction in the 2 – 6 day variance is observed at 850-hPa. At the jet level the power spectrum from the CTRL shows a peak in the 6 – 10 day band. The power spectrum from NO_ORO displays a shift in the frequencies, showing a decrease in power in the 6 – 10 day band and a slight increase in the 3 – 6 day band. Along 20°E the reduction in the 2 – 6 day variance is not as dramatic as the reduction observed along 30°E. West of the prime meridian, a reduction in the 2– 6 day variance is evident at 850-hPa. At the jet level, variance in the 2 – 6 day band appears to recover over West Africa. These preliminary results suggest that the removal of orography affects the variability of AEWs over East Africa, mainly at the lower levels.

Previous studies (e.g. Burpee 1974; Reed et al. 1988; Pytharoulis and Thorncroft 1999; Thorncroft and Hodges 2001) have shown that AEWs propagate in two tracks over land. One is centered at roughly 20°N at the lower levels. The second locus is located equatorward of 15°N and is more active at the AEJ level. To investigate the influence of orography in African wave genesis and continued maintenance, the longitudinal evolution of the meridional wind variance in the 2 – 6 day band is displayed for the CTRL and for the NO_ORO cases in Figure 8.6 at different latitudes and levels. At the lower level (850-hPa), a reduction in variance is again evident over East Africa and over West Africa near the jet latitude. North of the jet, at about 20°N, decreased variance is also observed over West Africa. South of the jet (∼10°N), the evolution of variance in the 2 – 6 day band from NO_ORO is similar to that in CTRL over land. However, differences are observed over the eastern Atlantic Ocean. At the jet level (650-hPa), a reduction in variance in the 2 – 6 day band is not as evident as in the lower level near the jet latitude (at 15°N), however, south of the jet (at 10°N) a decrease in variance associated with AEWs is apparent between 10°W and 20°E. These diagrams indicate that the region with larger values of power in the

2 – 6 day band is located over West Africa between 10°W and 0°. Large values are also observed at the coast.

Figure 8.7 shows the spatial distribution of meridional wind variance in the 2 – 6 day band from CTRL and NO_ORO at 650 and 850-hPa. This diagram further confirms a decrease in variability associated with AEWs over East Africa and West Africa at the lower level. One prominent feature of the distribution of variance at 850-hPa is the area of large variance located at the coast (15°W, 12°N). Some possible causes that may explain the concentration of variability in this area will be explored in the next chapter. The spatial distribution of variance at the jet level is also consistent with the patterns described in Figure 8.6. There is a clear decrease in variability associated with AEWs west of 20°E, along the southern flank of the jet. Reduced variance is also evident north of 20°N over East Africa and West Africa. An increase in variance also occurs at the coast in a region located around 12°N and 15°W, which coincides with the region of maximum variance at the lower level.

8.2 Role of SST gradients in African easterly wave structure

Figure 8.8 shows the mean surface temperature distribution from Experiment 3, hereafter NO_CEPG (referring to the reduction of the cross-equatorial pressure gradient (CEPG) by the SST distribution), and CTRL. The SST distribution in the NO_CEPG case is homogeneous in the zonal direction and has a Gaussian shape with a maximum amplitude located along the equator. The distribution of surface temperature over land is the same as in the CTRL case. The shape of SST in NO_CEPG ensures a reduction in the CEPG over the ocean. Figure 8.8c displays the latitudinal variation of SST and surface pressure from NO_CEPG, averaged between 30°W and 20°W. As mentioned previously, the SST maximum is located at the Equator and coincides with the sea level pressure minimum. Moreover, the CEPG observed in Figure 7.8 for the CTRL case disappears.

Figure 8.9 compares the meridional cross section of zonal wind over land and over the ocean from the CTRL and the NO_CEPG cases. Over land, the NO_CEPG zonal winds display similar features to those of the CTRL: a westerly flow in the lower levels, an easterly jet in the mid-levels and a tropical easterly jet in the upper levels. The AEJ core is located approximately at 650-hPa and 11°N and its maximum intensity is stronger in CTRL ($\sim$10 ms^{-1}) than in the NO_CEPG case ($\sim$8 ms^{-1}). Over the ocean, Figure 8.9c shows an AEJ with a core located around 650-hPa and 12°N. Its maximum intensity is also stronger in CTRL ($\sim$12 ms^{-1}) than in the NO_CEPG ($\sim$10 ms^{-1}) case. Another prominent feature of Figure 8.9c is the weakening of the low level westerly flow. According to Tomas and Webster (1997), and Nicholson and Webster (2007), a decline in the westerly flow is consistent with a reduction in the CEPG and with a southward displacement of the zero absolute-vorticity contour.

The mean zonal wind from the NO_CEPG and the CTRL simulation is plotted in Figure 8.10 at 650-hPa. The NO_CEPG case depicts a well defined jet, confined between 7°N and 17°N. The jet maximum at the coast is located about 3° further south than the maximum in CTRL. The general shape and intensity of the jet is similar in both cases, however, its mean latitudinal location appears displaced to the south (about 3°) in the NO_CEPG case. This shift in location is consistent with a reduction in the cross-equatorial pressure gradient. Results described above confirm the notion that the structure of the AEJ is linked to changes in the SST gradient (Nicholson and Webster 2007).

Figure 8.11 displays the time-longitude evolution of unfiltered meridional wind at 600-hPa and 15°N (near the jet level and jet latitude) for NO_CEPG and CTRL. Westward propagating disturbances are evident in both cases. A comparison of these two diagrams does not show apparent differences between them. However, it we take the difference, a reduction in the amplitude of the waves is observed between 10°E and 10°W (see Figure 8.14).

Figure 8.12 shows the power spectra of the meridional wind along 15°N, at 650 and 850-hPa for four different longitudinal sections from NO_CEPG (in red) and CTRL (in black). At 30°E and 650-hPa the most prominent peak for the CTRL is at 8 days. Variance associated with this peak is reduced in NO_CEPG. At 30°E and 850-hPa, there is again a reduction in variance in the 2 – 8 day band, when compared to the CTRL. Along 20°E, a decrease in variability associated with AEWs is more evident at the jet level. West of the prime meridian, an examination of the power spectra at 10°W shows that there is a reduction in variance associated with AEWs, with the reduction being larger at the lower level. Over the ocean, a decline in variance in the 2 – 6 day band is again evident at 850-hPa. These results suggest that the removal of the CEPG affects the overall variability of AEWs. Larger changes are observed over West Africa and at the lower levels.

Figure 8.13 displays the longitudinal evolution of the meridional wind variance in the 2 – 6 day band for the CTRL and for the NO_CEPG at different latitudes and levels. At 850-hPa, the evolution of the 15°N variance shows a reduction in variability associated with AEWs in NO_CEPG over East Africa, around 30°E, and over West Africa, between 0° and 15°W. Some reduction is also observed over the ocean. Closer to the jet latitude for the NO_CEPG case (10°N), variance in the 2 – 6 day band decreases compared to the CTRL from 10°E to 20°W. North of the jet, the evolution of the 2 – 6 day variance in NO_CEPG is somewhat similar to the evolution observed in CTRL. At 650-hPa, there is a reduction in variance in the 2 – 6 day band at 15°N, mainly west of the prime meridian. At 10°N, a decrease in variance associated with AEWs is clear in NO_CEPG west of 10°E; however, a reduction near the coast (∼15°W) is not as evident as in the lower level. Variability in the 2 – 6 day band is also modified over the ocean.

Figure 8.14 provides a more general picture of the distribution of the 2 – 6 day band variability over Africa in NO_CEPG and CTRL. At the lower level, a comparison

of the two fields confirms a reduction in the variability associated with AEWs over West Africa and south of 20°N when the oceanic cross-equatorial pressure gradient is removed. The most noticeable difference between these two diagrams is the large reduction of variance that occurs at the coast, around 12°N and 15°W, and also over East Africa. At the jet level, the reduction in variance is more visible south of the jet in an area located west of 10°E.

In summary, the SST distribution also impacts the AEW variability and the structure of the AEJ. Results indicate that larger differences are expected over West Africa and at the lower levels. In the next chapter we explore some mechanisms that may explain the observed reduction in the AEWs.

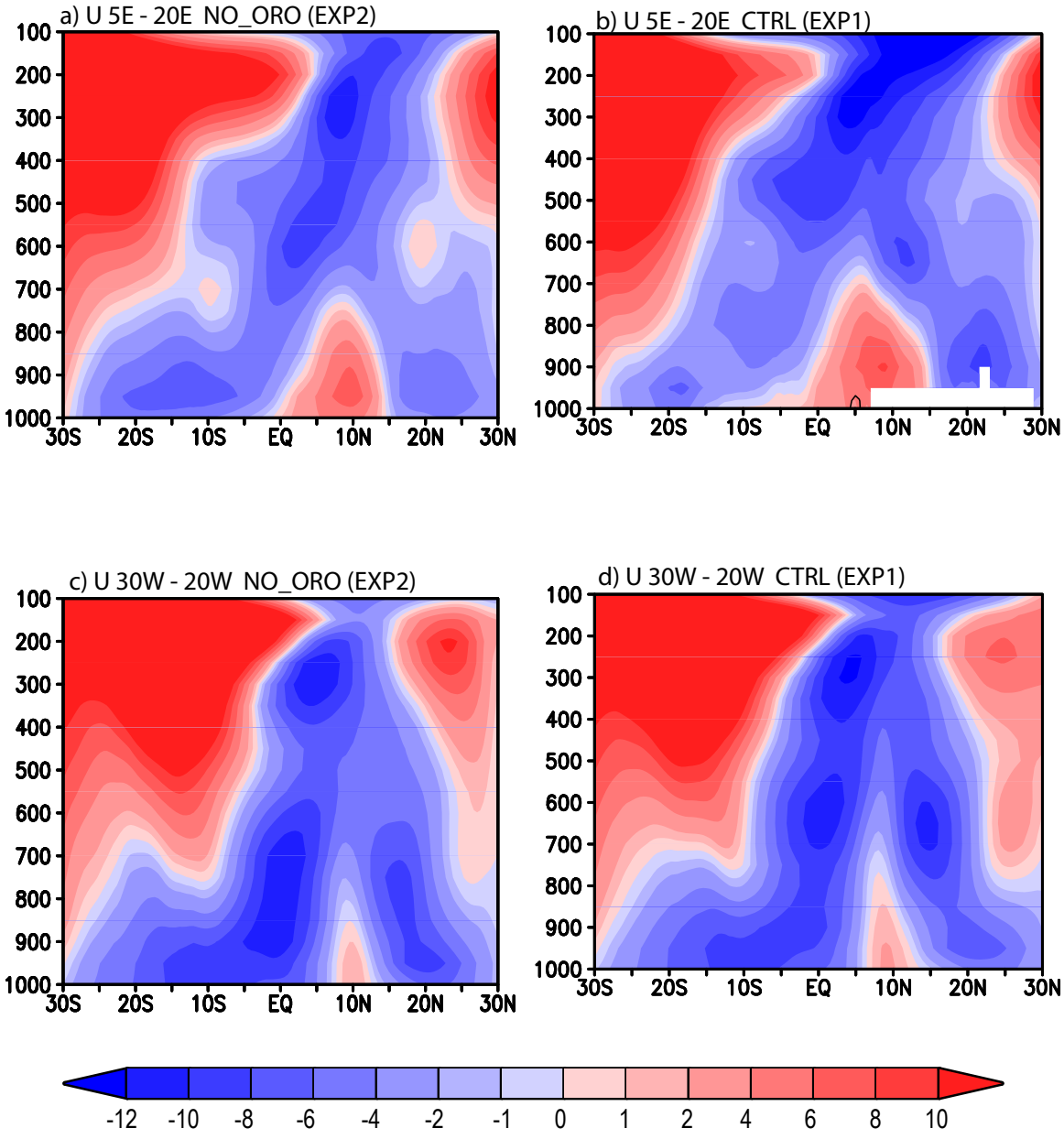

Figure 8.1: a) Meridional cross section of zonal wind from NO_ORO simulation averaged between 5°E-20°E. b) As in a) but from CTRL simulation. c) Meridional cross section of zonal wind from NO_ORO simulation averaged between 30°W and 20°W. d) As in d) but from CTRL simulation. Units are m s^{-1}. The thick black line represent the mean absolute vorticity n=0 line.

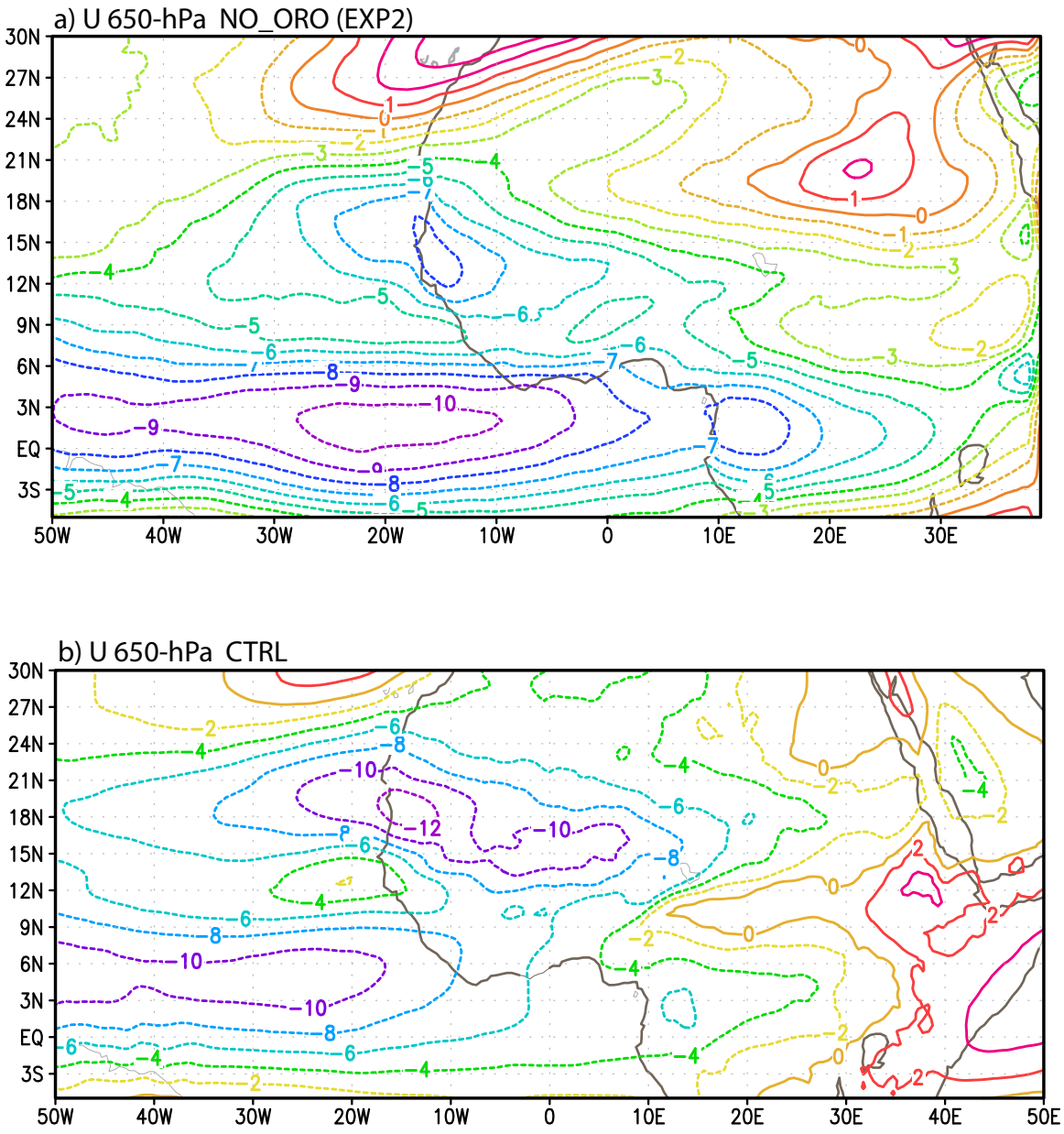

Figure 8.2: Mean zonal wind at 650-hPa from a) NO_ORO simulation; b) CTRL simulation. Units are m s^{-1}.

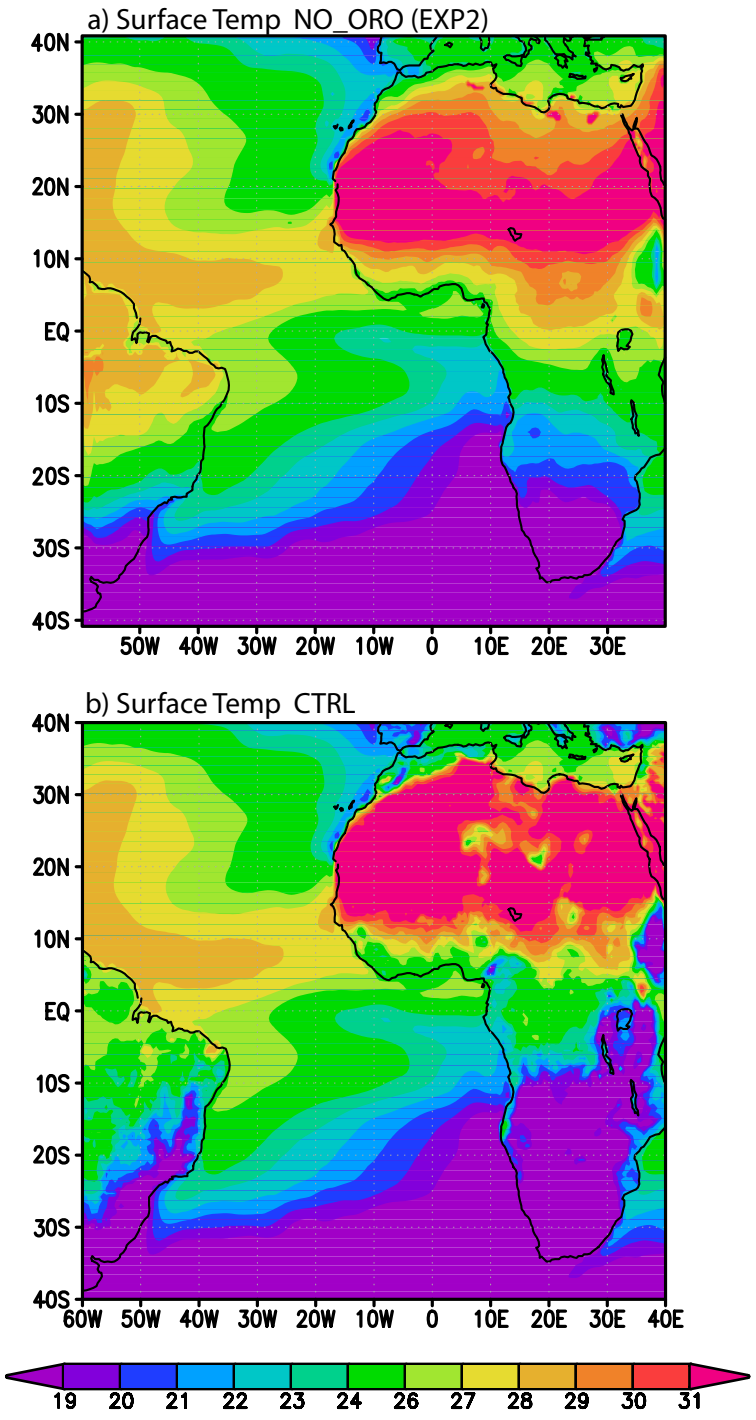

Figure 8.3: Mean surface temperature distribution from a) NO_ORO case; b)CTRL case. Units are °C.

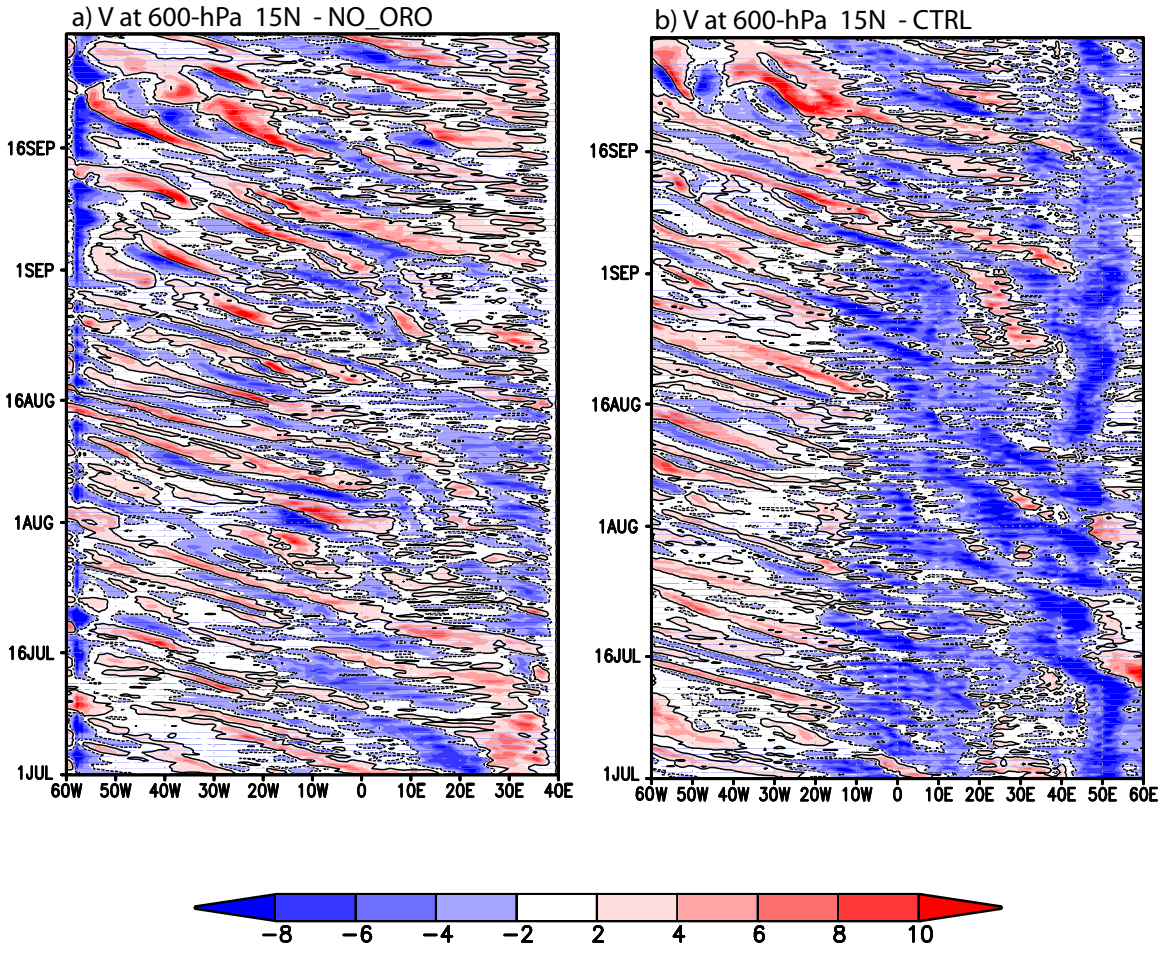

Figure 8.4: Time–longitude diagram of meridional wind at 15°N and 600-hPa from a) NO_ORO case; b) CTRL case. Units are m s^{-1}.

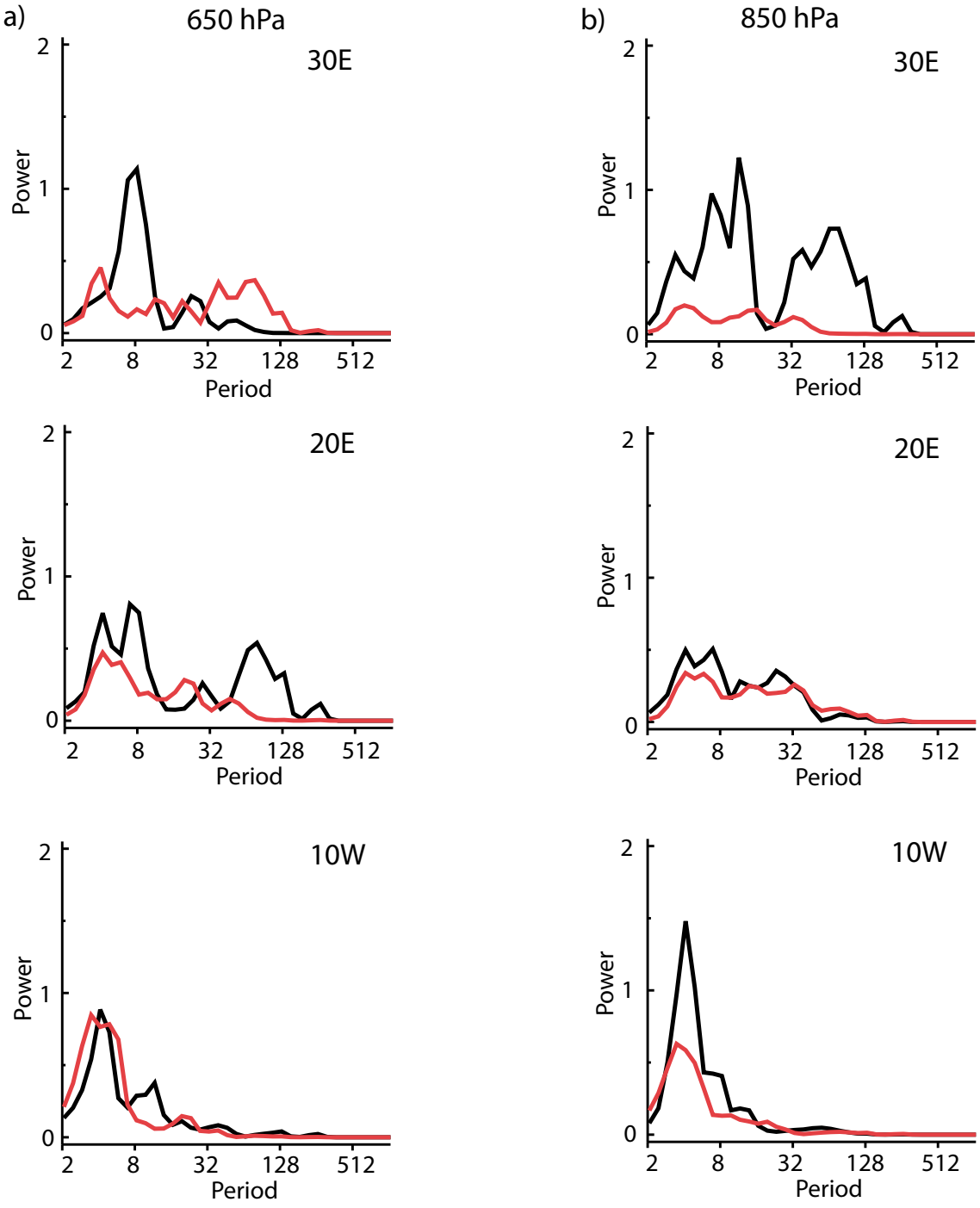

Figure 8.5: Global wavelet power spectra of meridional wind at longitudes 30°E, 20°E and 10°W at a) 650-hPa; b) 850-hPa. Units are m^2s^{-2}.

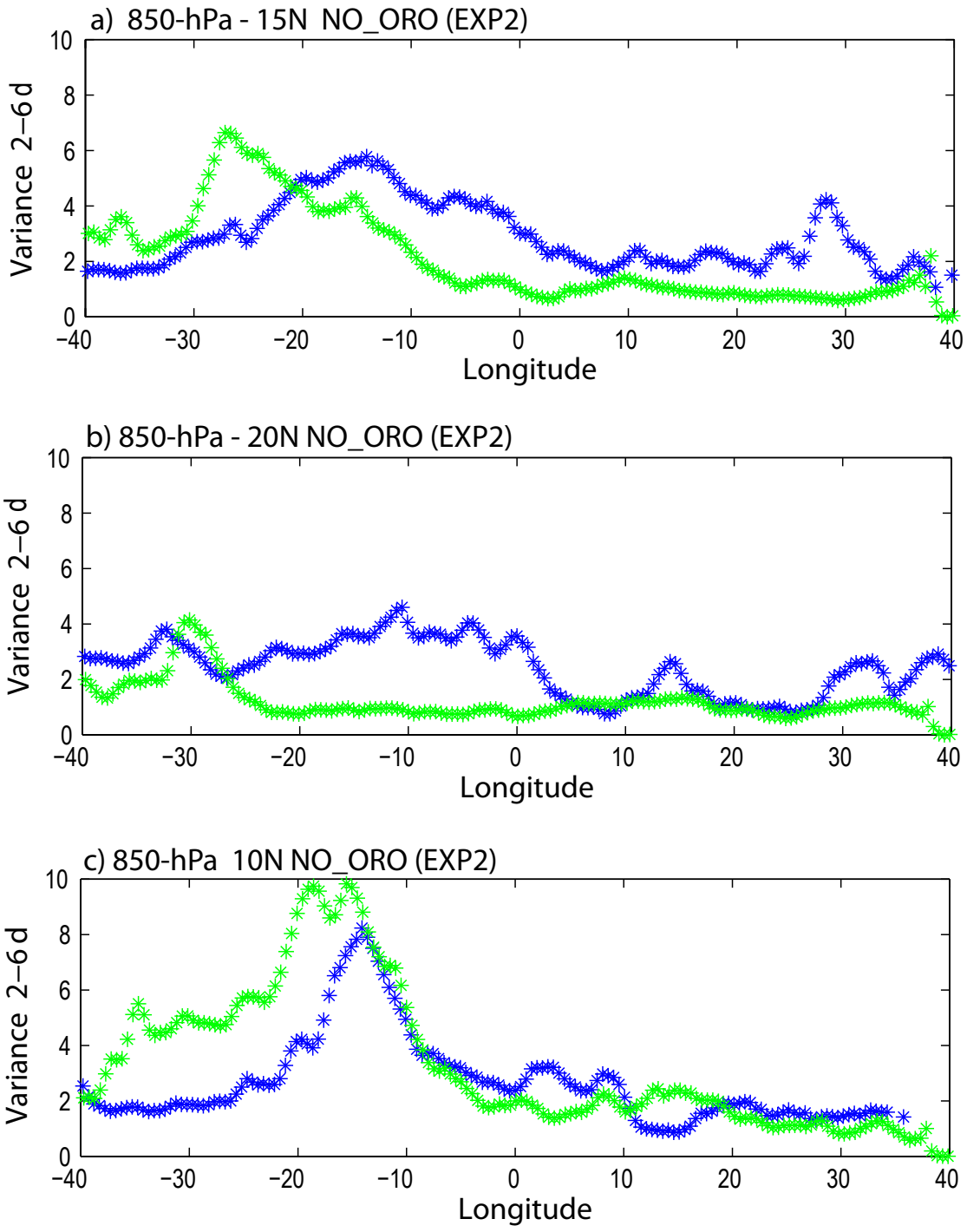

Figure 8.6: Longitudinal evolution of the meridional wind variance in the 2 – 6 day band at a) 15°N, 850-hPa. b) 20°N, 850-hPa. c) 10°N, 850-hPa. d) 15°N, 650-hPa and e) 10°N, 650-Pa. The blue line corresponds to the NO_ORO case. The green line indicates the CTRL case. Units are m^2s^{-2}.

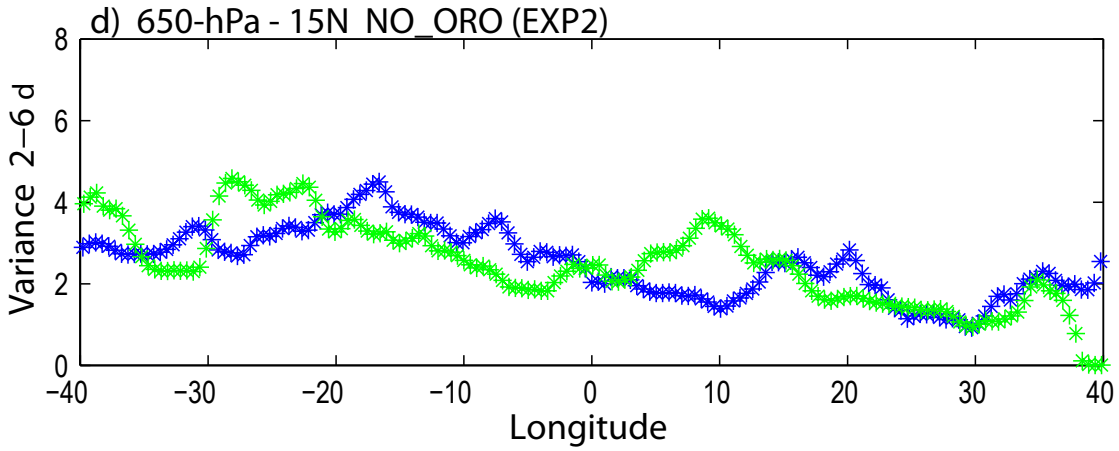

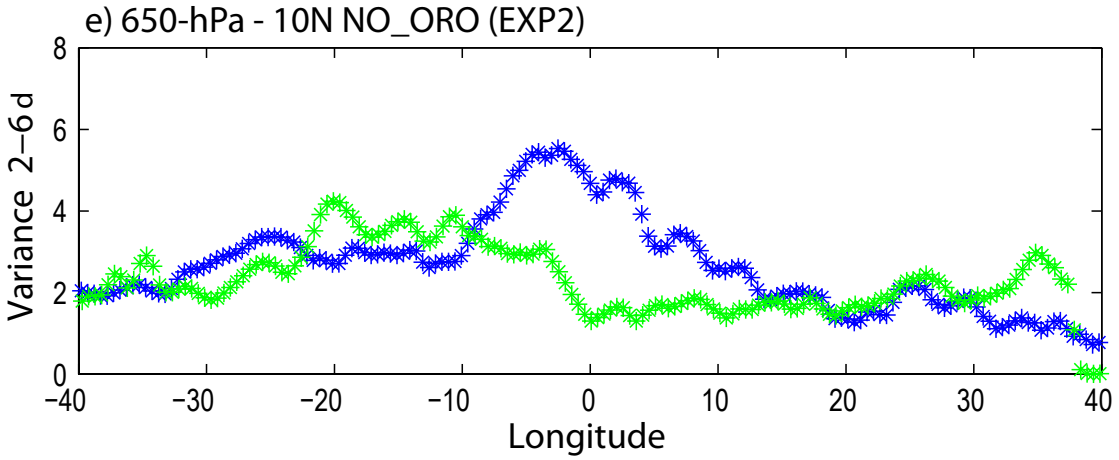

Figure 8.6 (continued)

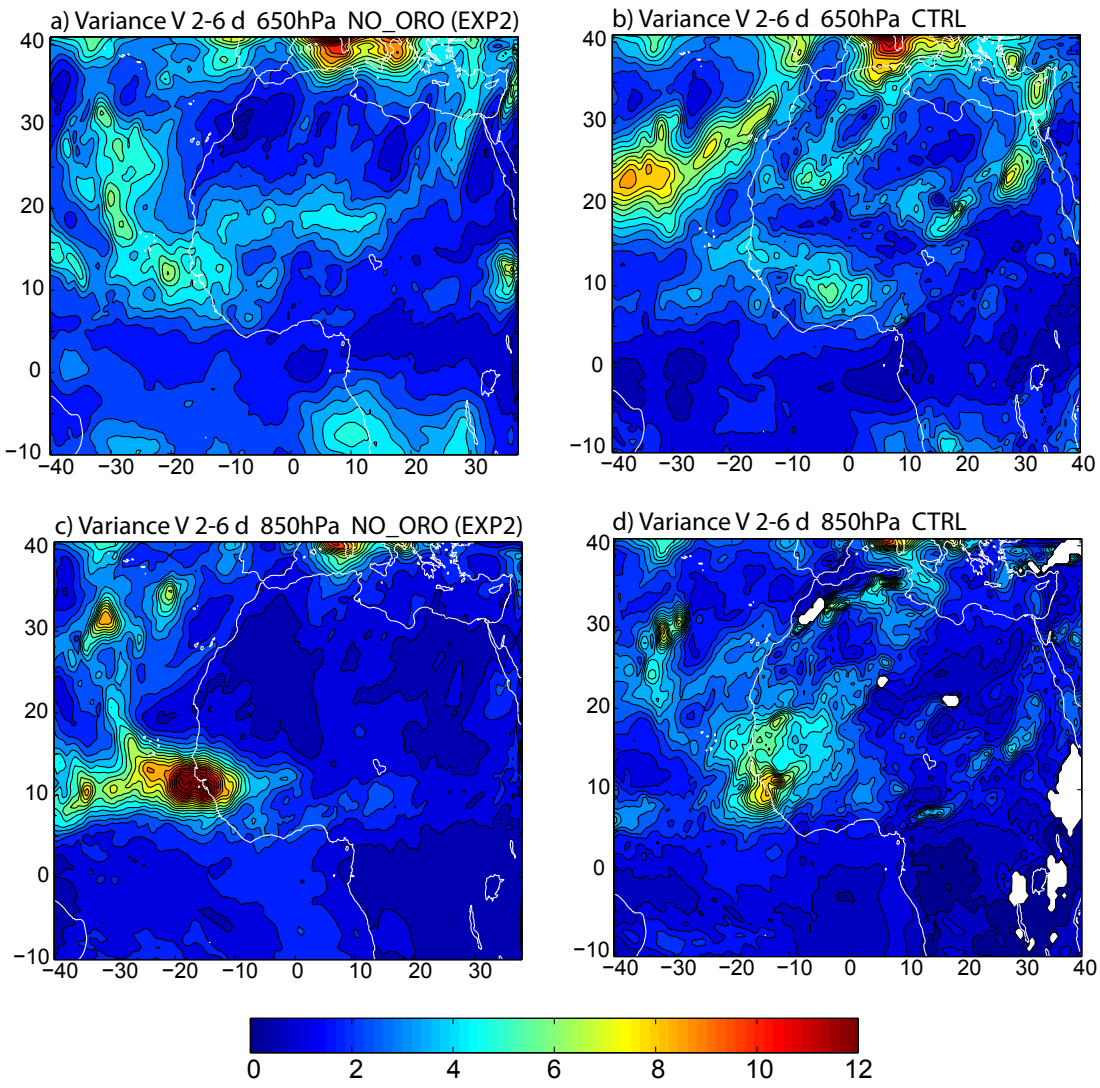

Figure 8.7: Spatial distribution of meridional wind variance in the 2 – 6 day band from a) NO_ORO at 650-hPa. b) CTRL at 650-hPa. c) NO_ORO at 850-hPa d) CTRL at 850-hPa. Units are m^2s^{-2}.

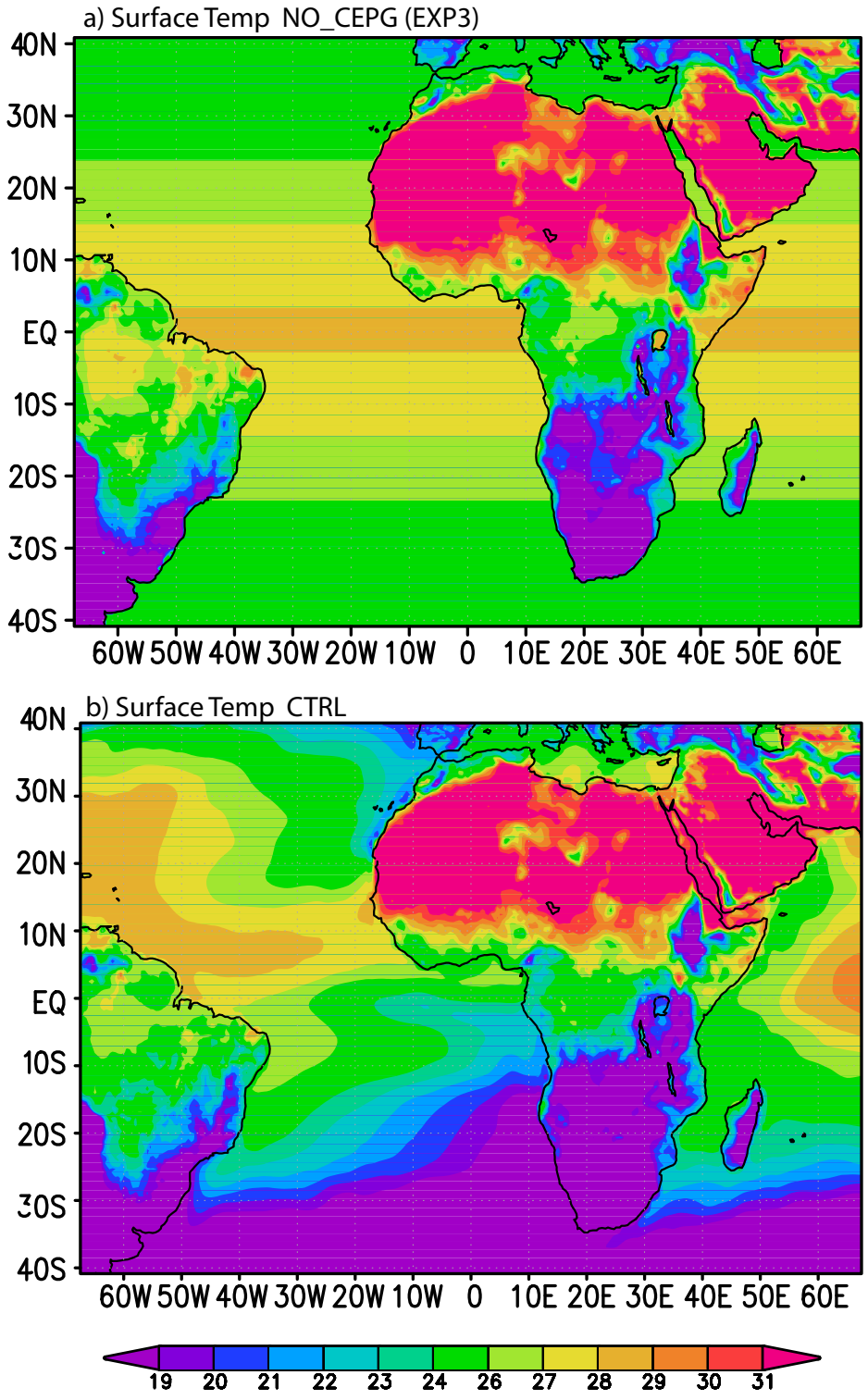

Figure 8.8: a) Mean surface temperature distribution from NO_CEPG. b) Mean surface temperature distribution from CTRL. Units are °C. c) Distribution of sea surface temperature (SST) and sea level pressure (SLP) for the 30°W-20°W longitudinal band from NO_CEPG simulation. Units of temperature are °C. Units of pressure are hPa.

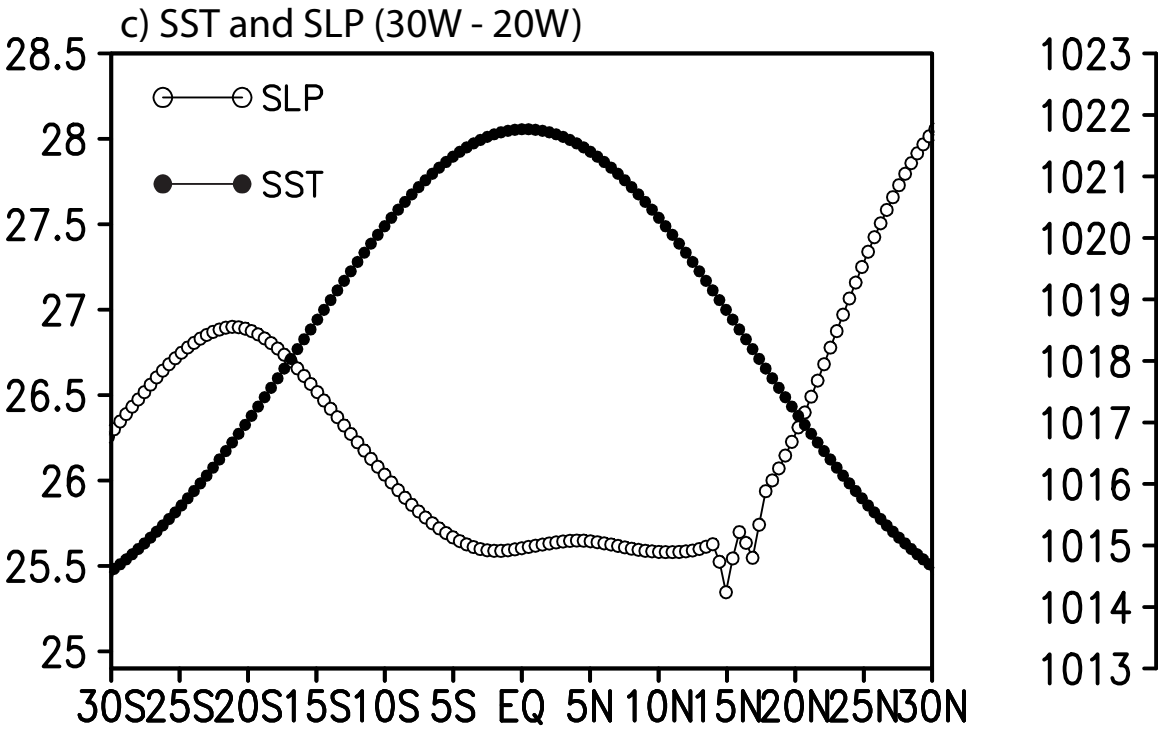

Figure 8.8 (continued)

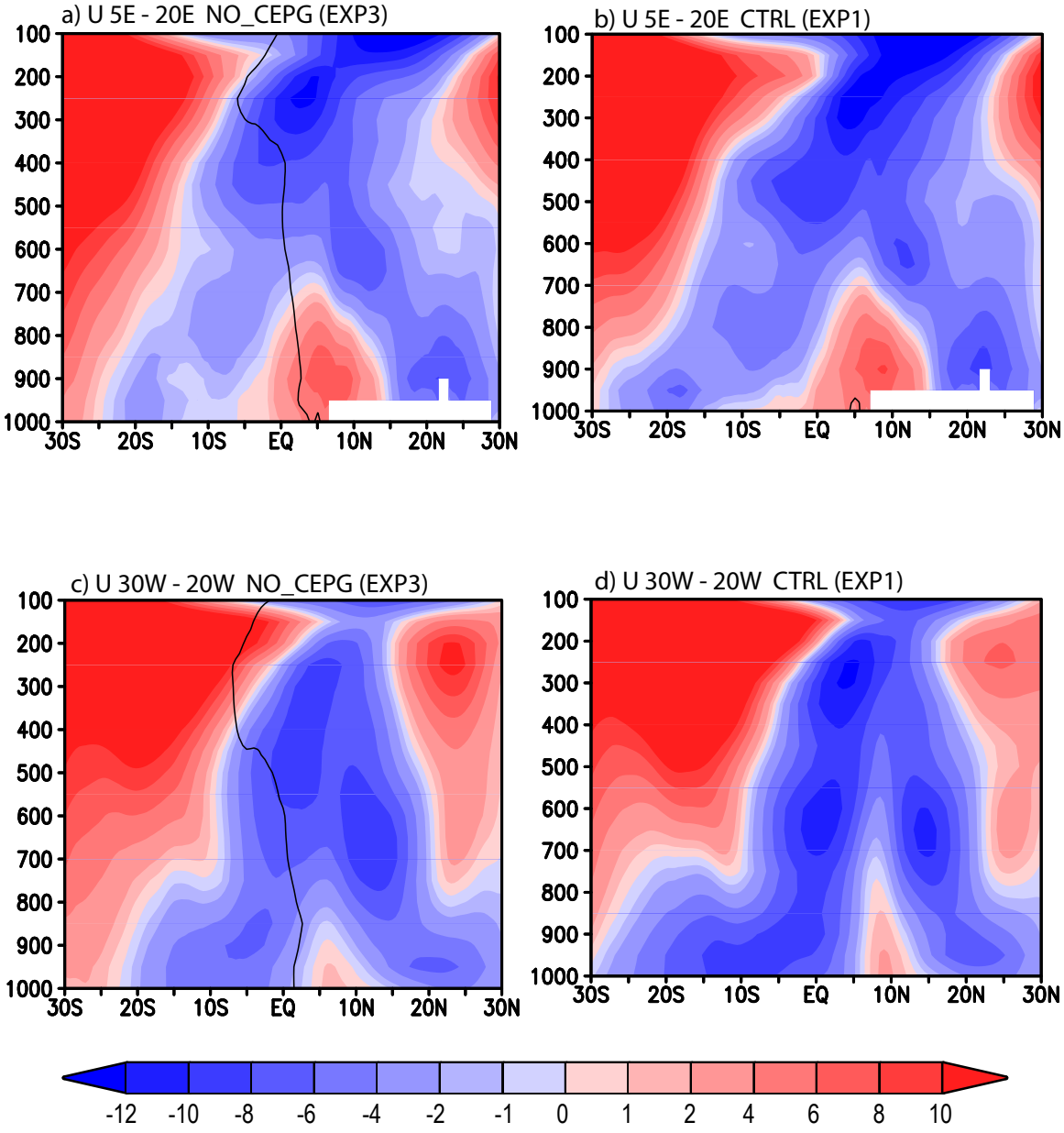

Figure 8.9: a) Meridional cross section of zonal wind from NO_CEPG simulation averaged between 5°E-20°E. b) As in a) but from CTRL simulation. c) Meridional cross section of zonal wind from NO_CEPG simulation averaged between 30°W and 20°W. d) As in c) but from CTRL simulation. Units are m s^{-1}. The thick black line represent the mean absolute vorticity n=0 line.

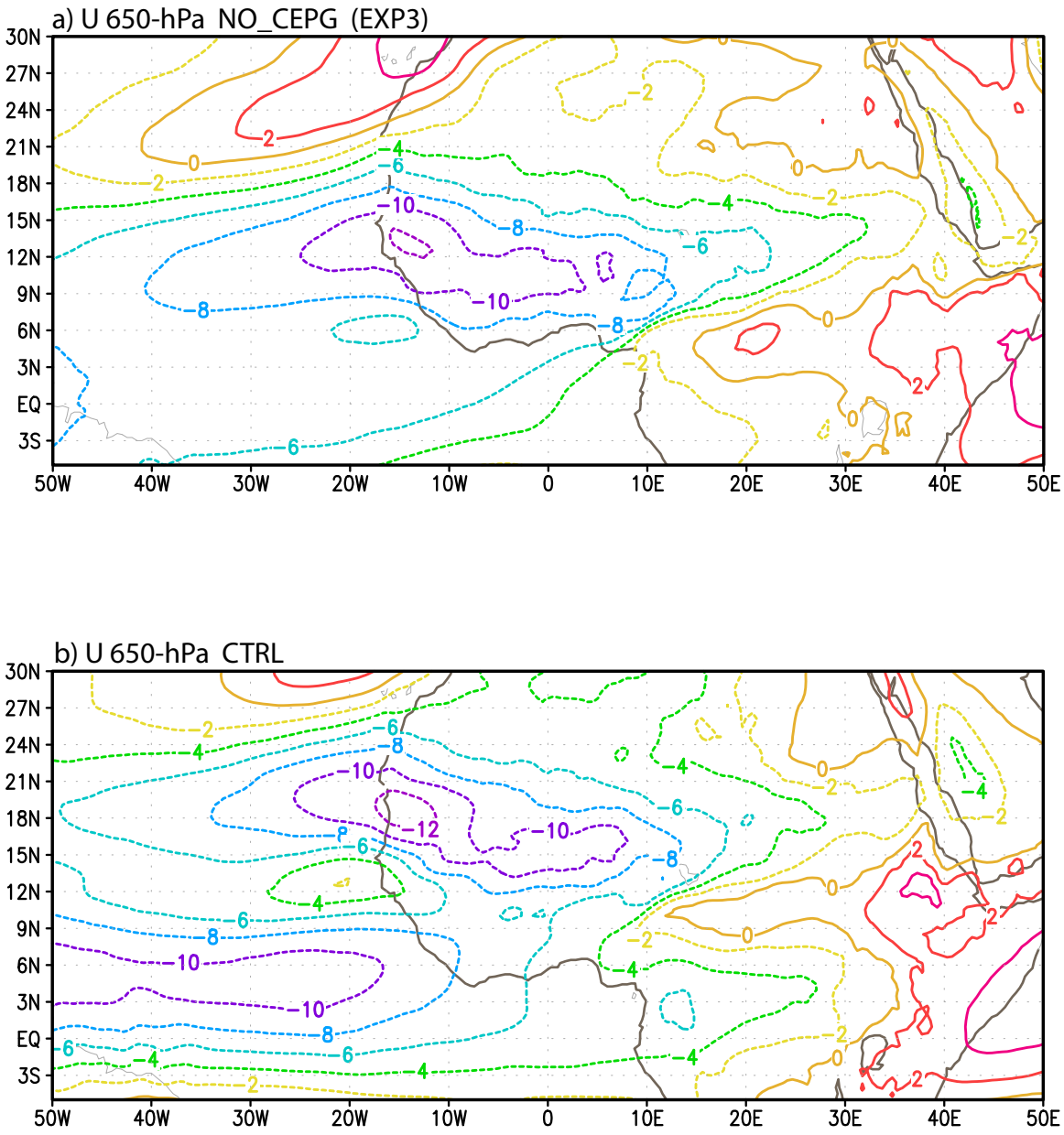

Figure 8.10: Mean zonal wind at 650-hPa from a) NO_CEPG simulation; b) CTRL simulation. Units are m s^{-1}.

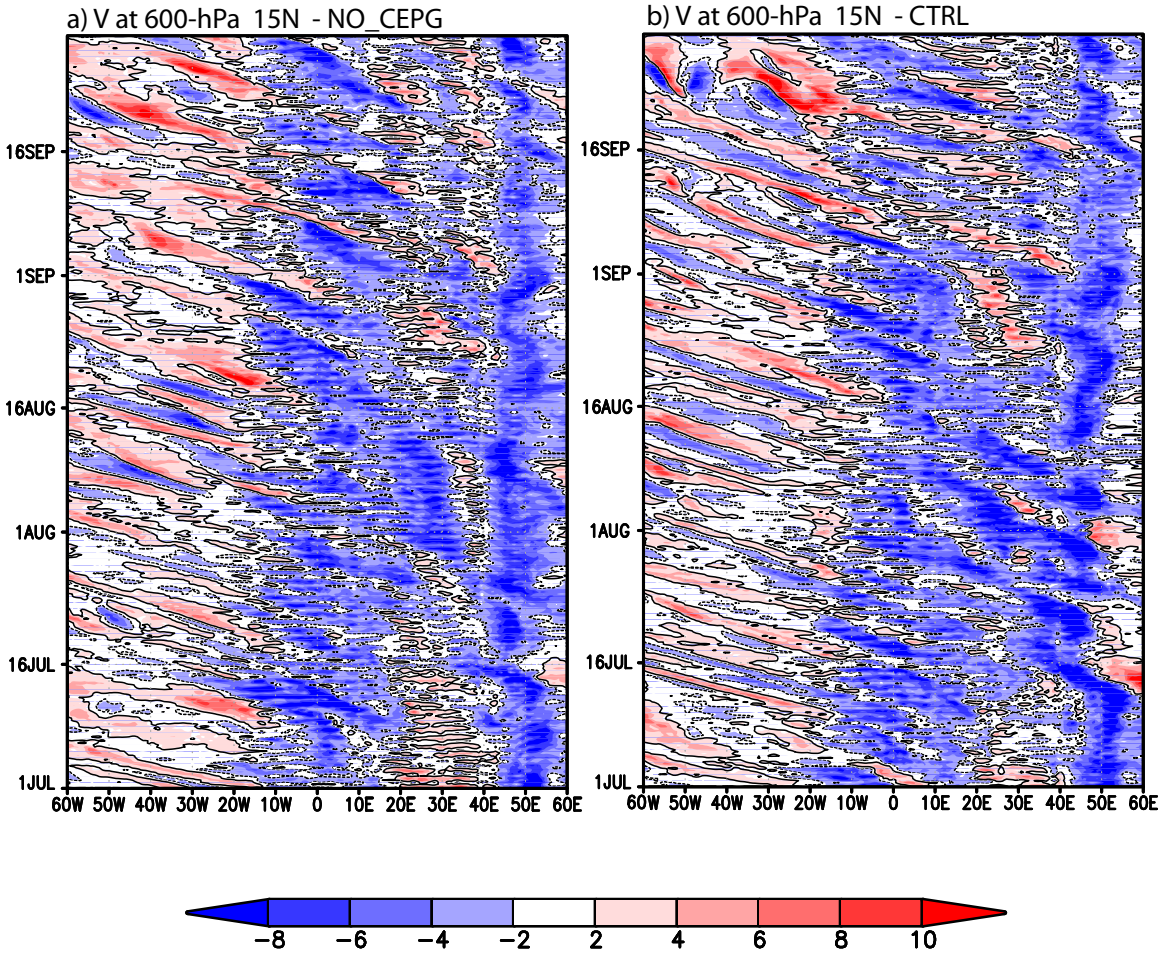

Figure 8.11: Time–longitude diagram of meridional wind at 15°N and 600-hPa from a) NO_CEPG case. b) CTRL case. Units are m s^{-1}.

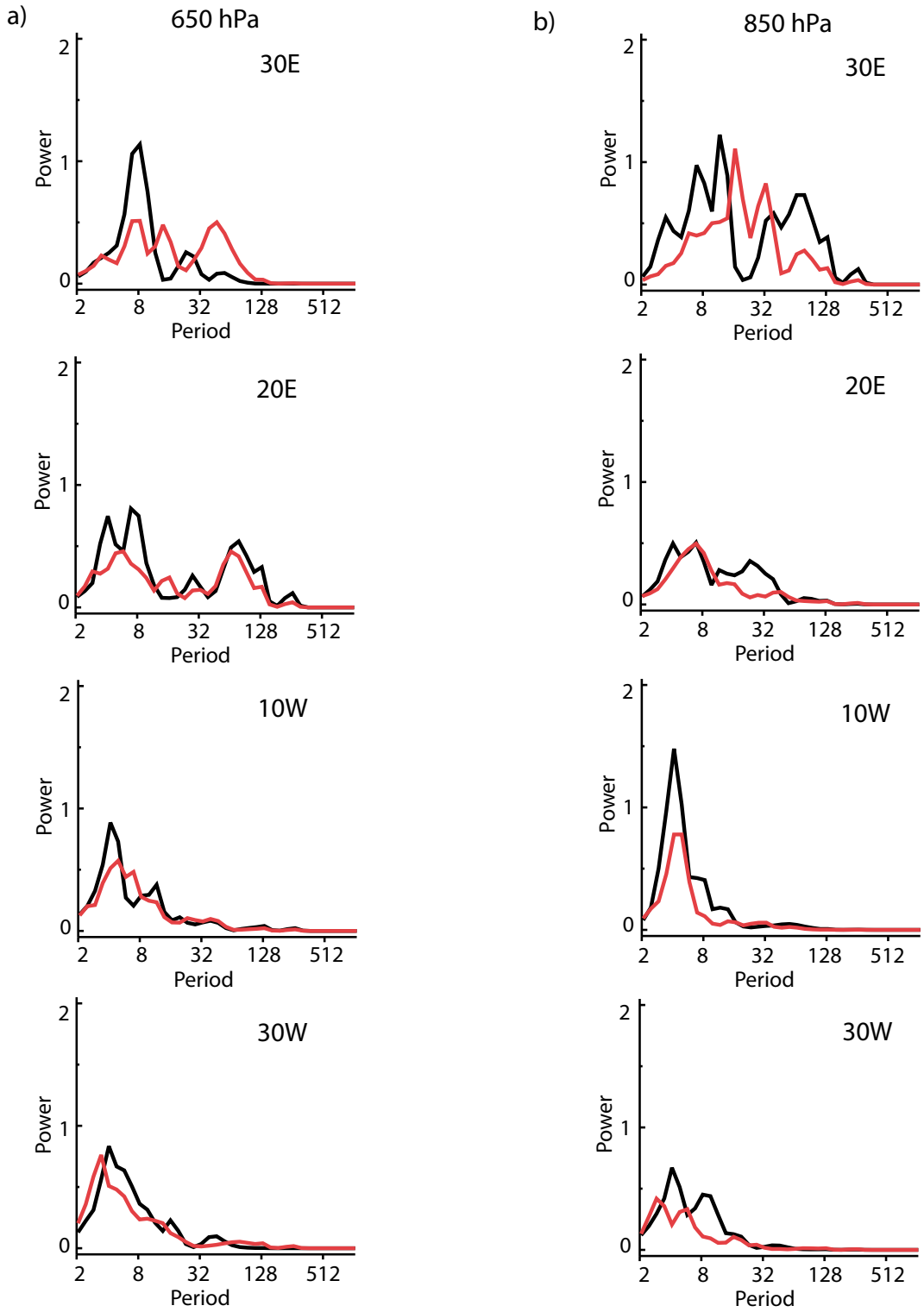

Figure 8.12: Global wavelet power spectra of meridional wind at longitudes 30°E, 20°E, 10°W from NO_CEPG at a) 650 hPa. b) 850 hPa. Units are m^2s^{-2}.

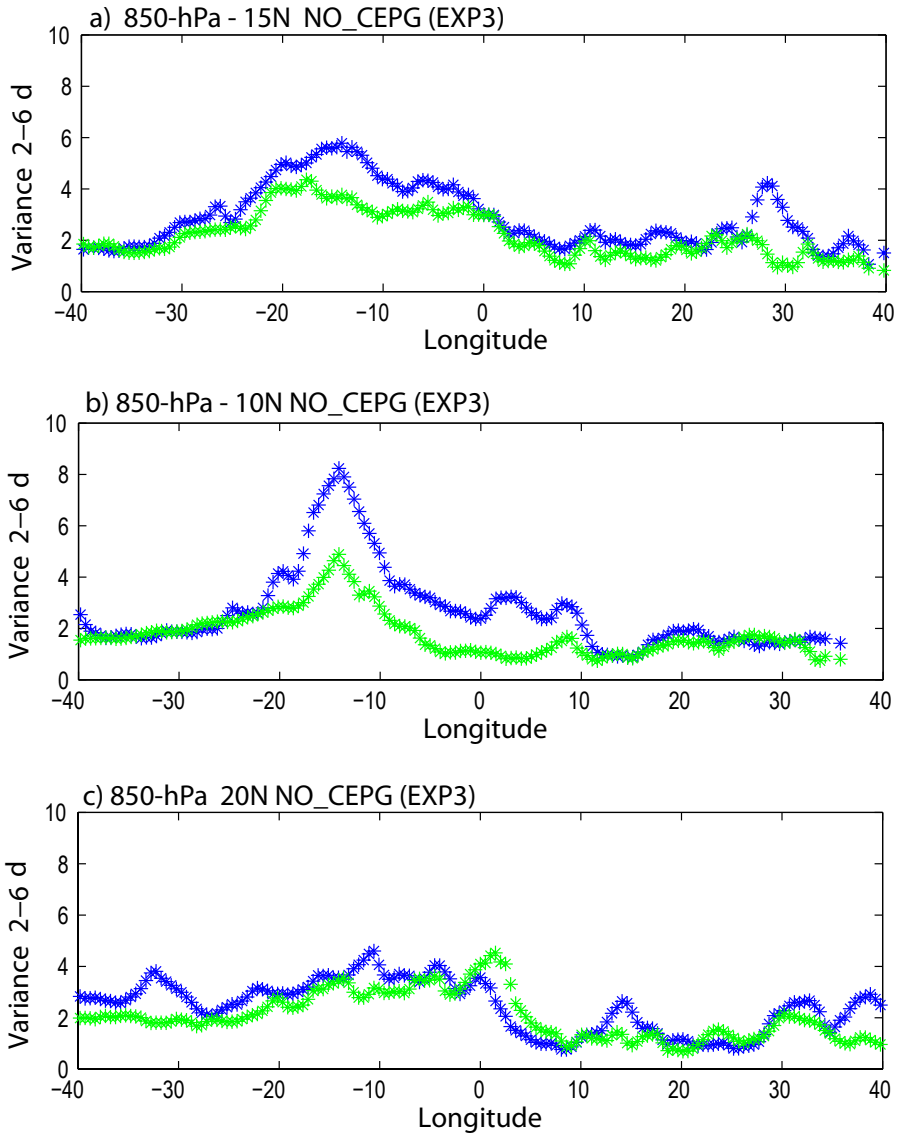

Figure 8.13: Longitudinal evolution of the meridional wind variance in the 2 – 6 day band at a) 15°N, 850-hPa. b) 20°N, 850-hPa. c) 10°N, 850-hPa. d) 15°N, 650-hPa and e) 10°N, 650-Pa. f) 20°N, 650-Pa. The blue line corresponds to the NO_CEPG case. The green line represents the CTRL case. Units are $m^2 s^{-2}$.

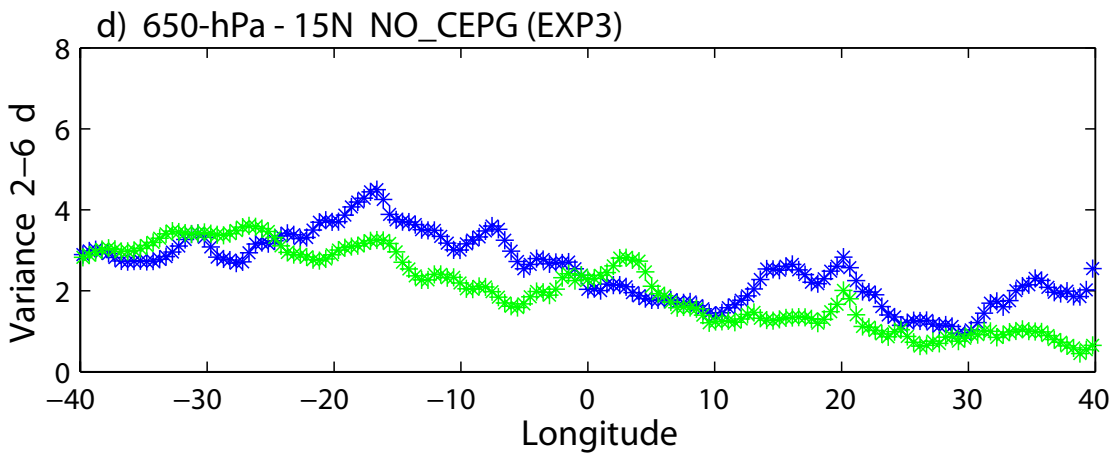

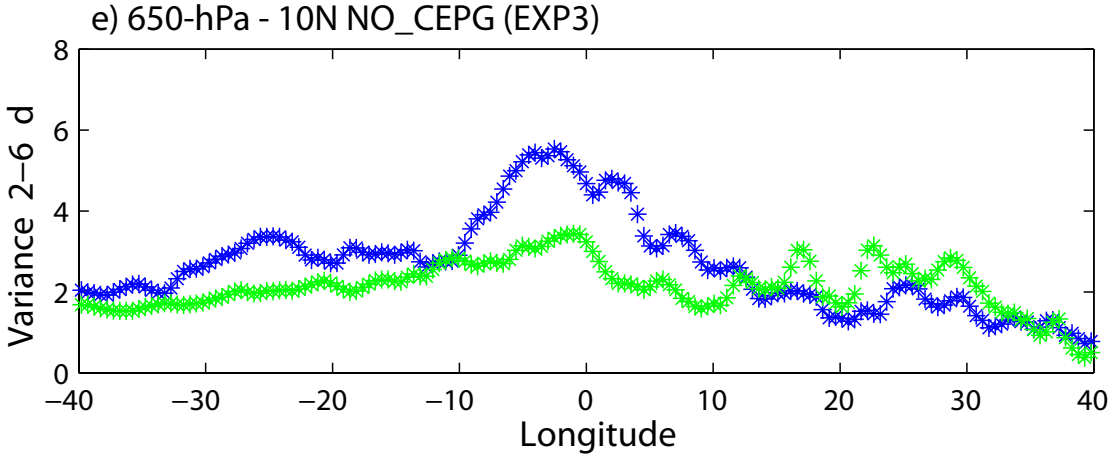

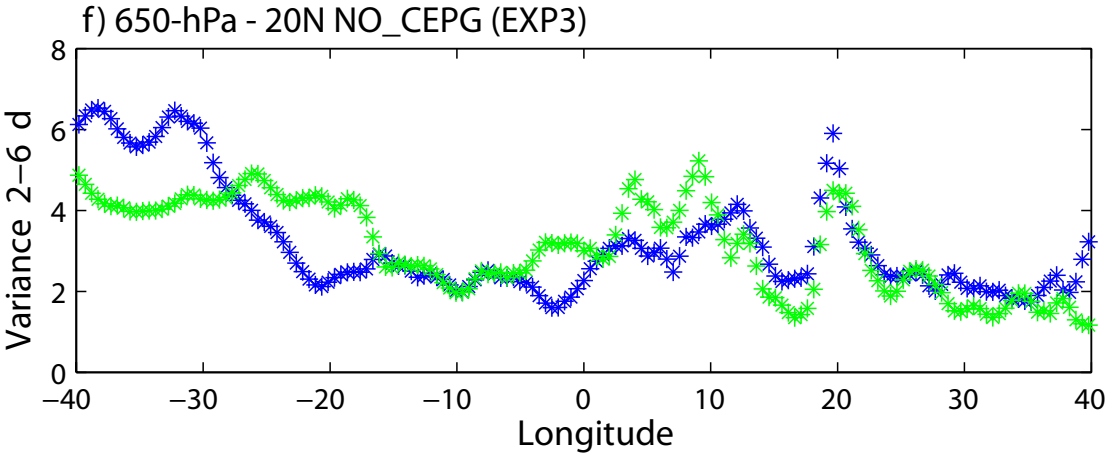

Figure 8.13 (continued)

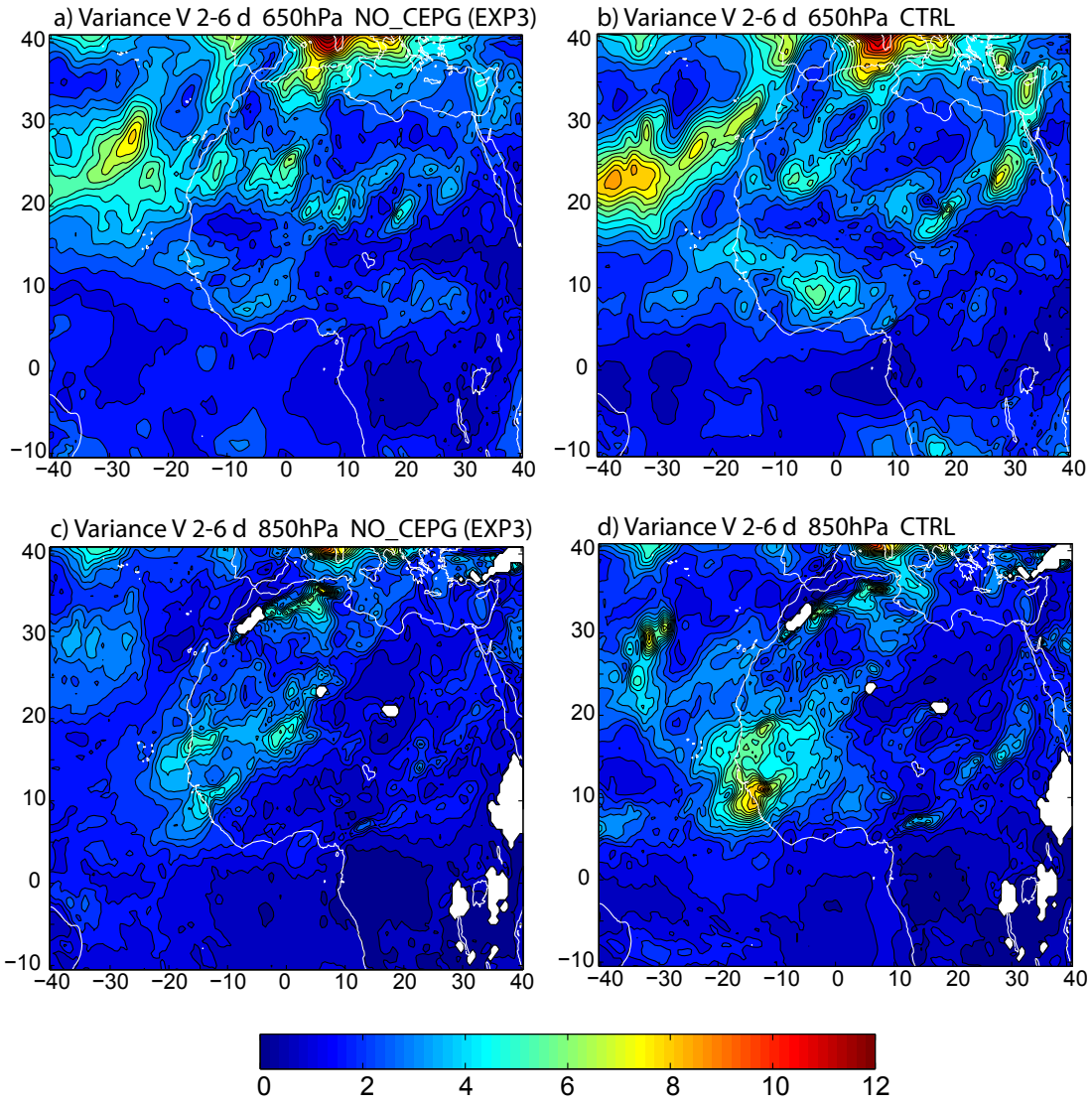

Figure 8.14: Spatial distribution of meridional wind variance in the 2 – 6 day band from a) NO_CEPG at 650-hPa. b) CTRL at 650-hPa. c) NO_CEPG at 850-hPa d) CTRL at 850-hPa. Units are m^2s^{-2}.

CHAPTER IX

AFRICAN EASTERLY WAVES GENESIS AND MAINTENANCE: ROLE OF OROGRAPHY AND CROSS-EQUATORIAL SST GRADIENTS

A number of studies have suggested that AEWs grow from an instability of the midtropospheric AEJ (e.g. Burpee 1972; Rennick 1976; Simmons 1977; Thorncroft and Hoskins 1994a,b) associated with the reversed temperature gradient induced by the East African orography. Burpee (1972) was the first to demonstrate that the AEJ satisfies the Charney and Stern (1962) instability criterion, and suggested that the jet could support waves evolving through both barotropic and baroclinic processes.

The Charney-Stern instability criterion states that for a flow to be unstable either 1) the quasi-geostrophic potential vorticity (PV) gradient must change sign along an isentropic surface, or 2) the quasi-geostrophic PV gradient must have the opposite sign to that of the surface temperature gradient. Additionally, for instability to be present, the Fjortoft condition requires that the mean zonal wind must be positively correlated with the quasi-geostrophic PV gradients and surface temperature gradients. According to Thorncroft and Hoskins (1994a), in the vicinity of the AEJ two possible strongest interactions of PV gradients exist. These are the interactions between the negative PV gradients in the jet core with 1) positive PV gradients on the equatorward flank of the jet and 2) the positive temperature gradients at the surface. The former is expected to be associated with barotropically unstable growth, and the latter to baroclinically unstable growth.

9.1 Mean PV and θ structure over Africa

Computations of potential vorticity were made for the monthly mean cross sections. As given in Hoskins et al. (1985),

$$PV = -g \cdot [f \cdot k + \nabla_p \times V] \cdot \nabla_p \theta$$

where PV is the potential vorticity on an isobaric surface, g is the acceleration due to gravity, ∇_p is the 3D gradient operator, V is the horizontal velocity vector, f is the Coriolis parameter, k is the vertical unit vector and θ is the potential temperature.

Figure 9.1 shows the mean CTRL meridional cross section of potential temperature, PV and zonal wind at 5°E for August. Maximum PV is at 9°N near the 315-K isentrope on the southern side of the AEJ, which is located near the 314-K isentrope between 10° and 15°N. An evaluation of PV gradients along isentropic surfaces, for example the 315-K surface, shows that they are characterized by negative values in the jet core and positive values south and north of the jet latitude. Thus, the Charney- Stern instability criterion 1) is satisfied. The region of negative meridional PV gradient in the midtroposphere goes from 10° to 15°N. In this region, Fjortoft necessary condition is also satisfied since the zonal flow is easterly. Figure 9.2 displays the mean horizontal distribution of potential temperature at 950-hPa for the July – September period. A positive meridional potential temperature gradient is evident at the surface, which together with the negative PV gradient associated with the jet, satisfies the Charney-Stern instability criterion 2).

As discussed in Schubert et al. (1991), the PV structure associated with the AEJ and the meridional PV gradients are important in determining the nature of the mixed barotropic-baroclinic instability that generates AEWs. To illustrate the mean distribution of PV and PV gradients further, we interpolated values of PV to the 315-K surface (Figure 9.3). This surface was chosen because it transects the AEJ. The jet-level PV gradients described in Figure 9.1 are clearly seen in this diagram.

Negative PV gradients occur in a region between 9°N and 16°N. South of 9°N, positive PV gradients extend from Eastern African to the Atlantic Ocean. Pytharoulis and Thorncroft (1999) pointed out that AEWs that form and propagate south of the jet would be expected to follow these positive gradients.

Next, we attempt to determine if instability mechanisms associated with wave growth are still present when orography is removed or when the CEPG is reduced. The PV cross-sections from the NO_ORO and the NO_CEPG cases are shown in Figure 9.4. For the NO_ORO case (Figure 9.4a), the PV maximum near 13°N is comparable in magnitude to that in the CTRL case, but it is located about 5° of latitude farther north and closer to the surface near the 310-K isentrope (∼700-hPa). Even though there is not a well defined jet in the NO_ORO simulation, reversals of meridional PV gradients are still evident in the middle troposphere. However, since the strength of the AEJ is weaker than in CTRL, a reduction in zonal mean kinetic and available potential energy is expected. Moreover, the area with negative PV gradients in the middle troposphere is reduced compared to that in the CTRL case, covering a region between 13°N and 15°N. For the NO_CEPG case (Figure 9.4b), the magnitude of the PV maxima at 9°N near the 315-K isentrope is smaller than in the CTRL case. PV gradient reversals are evident on the poleward side of the jet, in a region between 10° and 15°N. As in the CTRL case, PV gradients are positive south of the jet. In summary, the Charney-Stern and Fjortoft necessary conditions are satisfied in both cases.

Figure 9.5 shows the mean PV on the 315-K surface for the NO_ORO and NO_CEPG cases, and mean PV on the 310-K from NO_ORO. For the NO_ORO case, PV values on the 315-K surface increase from the Equator to about 13°N, where PV reaches a maximum of 0.2 PV units (PVU). Poleward of 13°N the PV values decrease, reaching a minimum at about 15°N. The distribution of PV values on the 310-K surface for the NO_ORO case shows an increase in PV values from the

Equator to about 12°N. Poleward of 12°N, PV values start to decrease, reaching a minimum at about 16°N. For the NO_CEPG case PV values on the 315-K surface reach maximum values between 0.2 and 0.3 PVU at about 9°N. PV values reach a minimum near 16°N.

Two aspects of the negative PV gradients are expected to have dynamical importance: its magnitude, which should relate to the growth rate of a disturbance (Molinari et al. 1997), and the extension of the area of negative PV gradients. To illustrate PV gradients differences between the simulations more clearly, Figure 9.6 isolates the regions where mean PV gradients are less than zero on the 315-K surface for all three cases. A substantial difference is observed between the NO_ORO and the CTRL in the vicinity of the AEJ. The area of negative PV gradients is noticeably reduced in the NO_ORO case, covering a region between 13°N and 15°N. Moreover, the magnitude of the reversals is smaller than in the CTRL case. On the 310-K surface (not shown), the region of negative PV gradients covers an area between 12°N and 16°N and the magnitude of the reversals is comparable to that on the 315-K surface. The distribution of PV and PV gradients for the NO_ORO case suggests that wave activity associated to PV reversals is reduced. For the NO_CEPG case, the distribution of negative PV gradients over land is comparable to that on the CTRL case. But, over the ocean, negative PV gradients seem to disappear, which could lead to a weakening of the waves when they move from Africa into the Eastern Atlantic.

As mentioned above, another possible interaction which could result in unstable growth occurs between the negative meridional PV gradients near the jet level and the meridional surface potential temperature gradients. This type of interaction is expected to be related with baroclinically unstable growth. In the CTRL case (Figure 9.2) strong potential temperature (θ) gradients exist over land. θ gradients do not extend into the Atlantic Ocean but follow the West African coast toward the north. An examination of Figure 9.2 and Figure 9.1 shows that high surface temperatures

and a deep well mixed layer between 17°N and 30°N, lead to a small dry static stability in the region north of he jet. As noted by Thorncroft (1995), the low static stability in the desert region increases the interaction between PV anomalies on the jet and the temperature anomalies at the ground. In the NO_ORO case (Figure 9.7a), surface θ decreases north of the jet, depicting a maximum value of 306-K over a large region north of 14°N. This pattern indicates that θ gradients are very small north of 14°N impacting the interaction between negative PV gradients in the middle troposphere and positive θ gradients at the surface in the regions north of the jet. In addition, θ gradients decrease over land south of 14°N and they reach maximum values right at the coast. For the NO_CEPG case (Figure 9.7b), the distribution of θ is comparable to that in the CTRL case, showing strong meridional surface θ gradients over land. Similarly, large θ gradients are found near the coast around 18°N.

9.2 Wave energetics inferred from filtered covariances

AEWs can be considered to be eddies or disturbances propagating on a zonal flow. These disturbances grow through instabilities of the mean flow, implying the development of energy transformations between the mean and transients. A better understanding of the growth and maintenance of the waves can be obtained by analyzing the energetics of the system since any instability must have certain energy sources for it to grow. In this section, we carry out a comparative analysis of the energetics of AEWs obtained from the three experiments to asses how energy conversions are controlled or modified by orography and SST gradients.

Lorenz (1955) derived the equations for investigating the growth of wave energy, partitioning the potential and kinetic energy equations into zonal and eddy forms. The form and notation of the energy equations used in the present work are taken from Norquist et al. (1977). The governing equations for eddy kinetic energy and

eddy available potential energy are:

$$\frac{\partial K_E}{\partial t} = C_E + C_K + BK_E + B\Phi_E - D_E$$

$$\frac{\partial A_E}{\partial t} = C_A + C_E + BA_E + G_E$$

where K_E is the eddy kinetic energy, A_E the eddy available potential energy, C_E the conversion of eddy available potential energy to eddy kinetic energy, C_K the conversion of zonal kinetic energy to eddy kinetic energy and C_A represents the conversion of zonal available potential energy to eddy available potential energy. The other terms represent boundary fluxes of energy (BK_E, $B\ \phi_E$, BA_E) , the generation of eddy available potential energy by heat sources and sinks (G_E) and frictional dissipation of eddy kinetic energy (D_E). Specifically, C_K represents the sum of barotropic energy conversions, C_E the baroclinic energy conversions and C_A conversions of energy due to eddy heat flux along the zonal mean temperature gradient.

The energetics of the AEWs has been studied by a number of authors (e.g. Norquist et al. 1977; Diedhiou et al. 2002; Hsieh and Cook 2007). In the present work it is of interest to examine the spatial distribution of the conversion terms that involve baroclinic and barotropic instabilities associated with the jet and with the surface temperature gradients. Therefore, we are going to consider only the conversions C_K, C_E and C_A. This approach was previously followed by Albignat and Reed (1980) and Reed et al. (1988). It is important to clarify that a strict analysis of the energetics of the waves is not intended.

The mathematical expressions for these conversions are as follows:

$$C_E = -\frac{1}{g}\int_{100}^{ps} \frac{R}{p}\overline{[\omega' T']}dp$$

$$C_K = -\frac{1}{g}\int_{100}^{ps} \overline{[u'v']\,\frac{\partial [u]}{\partial y}}dp - \frac{1}{g}\int_{100}^{ps} \overline{[v'^2]\,\frac{\partial [v]}{\partial y}}dp - \frac{1}{g}\int_{100}^{ps} \overline{[u'\omega']\,\frac{\partial [u]}{\partial y}}dp - \frac{1}{g}\int_{100}^{ps} \overline{[v'\omega']\,\frac{\partial [v]}{\partial p}}dp$$

$$C_A = -\frac{1}{g}\int_{100}^{ps} \frac{\overline{\partial[v'T']}}{\overline{\sigma}} \frac{\partial[T]}{\partial y} dp - \frac{1}{g}\int_{100}^{ps} \frac{\overline{[\omega'T']}}{\overline{\sigma}} \frac{\partial[T]^*}{\partial y} dp$$

where u is the zonal wind component, v is meridional wind, ω is omega, T is temperature, p is pressure, ps is the surface pressure, g is acceleration of gravity, R is the gas constant for dry air, σ is the mean static stability and y is the northward directed coordinate. In the above expressions $[(\ )]$ represents a zonal average of the quantity $(\ )$ and $\overline{[(\ )]}$ represents a meridional average of the zonal average. A prime indicates a deviation from zonal average and an asterisk the deviation of a zonal average from the area mean.

The spatial distribution of covariances for the leading terms of C_K, C_E and C_A are calculated for the CTRL, NO_ORO and NO_CEPG cases. Norquist et al. (1977) found that the remaining terms in the equations above are one or more orders of magnitude smaller than the leading term, therefore they are not considered in our analysis. Bandpass filtering in the 2 – 6 day band at different pressure levels was performed on the zonal and meridional wind, vertical velocity and temperature in order to calculate these covariances.

Before discussing the differences in covariances for the model simulations, the spatial distribution of mean eddy kinetic energy (EKE), calculated as $0.5\left(u'^2 + v'^2\right)$, is introduced here for the CTRL and for the NO_ORO and NO_CEPG cases at different pressure levels. Since the conversion terms contribute to the growth of eddy kinetic energy, this quantity gives an idea of the strength of the AEWs in the simulations. Figure 9.8 displays horizontal distribution of eddy kinetic energy associated to AEWs from the CTRL case at 950-hPa, 850-hPa and 650-hPa. At 650-hPa (the jet level), EKE attains large amplitudes at the southern flank of the jet. EKE starts to increase in magnitude from about 10°E and reaches a maximum of 9 m^2s^{-2} at the coast at about 10°N. The distribution of EKE suggests that AEWs that form south of the jet experience their main growth west from 10°E and then intensify when they reach

the coast. These results partly agree with Albignat and Reed (1980) findings, since they also found a second amplitude maximum near the Greenwich meridian. Large amplitudes of EKE also appear north of 20°N between 20°E and 30°E. The existence of these maxima is also documented in Albignat and Reed (1980), and appears to coincide with regions of cyclonic circulation and strong shear over north East Africa.

At 850-hPa (Figure 9.8b), the most prominent feature is the existence of two centers of maximum amplitude over West Africa. The maximum at the north (∼20°N) corresponds to the AEWs that form poleward of the AEJ (Pytharoulis and Thorncroft 1999) and the maximum at the south (∼10°N) correspond to the AEWs that form equatorward of the AEJ. At the lower level (Figure 9.8c) the maximum amplitude is located near the African coast on the northern side of the jet (∼20°N). At this level AEWs experience their main growth west from 5°E and reach energy amplitudes of 10 m^2s^{-2}. The formation of these waves is associated with the strong low-level θ gradients and the low static stability over the Saharan region.

Figure 9.9 shows the distribution of EKE associated to AEWs from the NO_ORO simulation. For the NO_ORO and the NO_CEPG cases only the diagrams at 950 and 650-hPa will be shown because they provide the salient features associated with the AEWs energetics. At 650-hPa (NO_ORO: Figure 9.9a), EKE starts to increase in magnitude further west than in the CTRL case, at about 0°, and reaches a maximum of 7 m^2s^{-2} just off the coast near 10°N. At 950-hPa (Figure 9.9b), EKE reaches a maximum value of 10 m^2s^{-2} near the coast at about 15°N. At this level the distribution of EKE for this case is quite different from the one observed for the CTRL case, showing a more elongated east-west shape and a maximum located 5° south from the maximum observed in the CTRL case. These results suggest that barotropic and/or baroclinic energy conversions near the jet level are reduced when orography features are removed. Moreover, the spatial distribution of the conversion terms is also modified. Note that the energy maximum observed at 950-hPa is consistent with

the maximum of variance shown in Figure 8.6. The analysis of the spatial distribution of the covariance terms may offer insights into how energy conversions are modified.

Figure 9.10a displays the distribution of EKE at 650-hPa from the NO_CEPG case. At this level, EKE reaches a maximum of 6 m^2s^{-2} off the coast on the equatorward side of the AEJ. Even though EKE attains values stronger than 2 m^2s^{-2} over West Africa, larger amplitudes start to develop further west than in the CTRL case. Energy values stronger than 3 m^2s^{-2} are reached at about 0° longitude. At the lower level (Figure 9.10b), the maximum amplitude is located over West Africa and near the coast at about 18°N, where EKE reach values of 9 m^2s^{-2}. The distribution of EKE for this case suggests that baroclinic and/or barotropic conversions of energy are not as effective as in the CTRL over West Africa near the jet level. Also, baroclinic energy conversions appear to be slightly impacted near the surface.

The spatial distributions of the $\overline{\omega' T'}$, $\overline{v' T'}$, $\overline{u' v'}$ covariances are now examined to understand better how the energy conversions are modified in our simulations. For the purpose of obtaining the most meaningful patterns, the $\overline{u' v'}$ covariance is depicted at 650-hPa, and the $\overline{\omega' T'}$, $\overline{v' T'}$ covariances are depicted at 950-hPa. Norquist et al. (1977) found that these energy conversions reached maximum values at these respective levels.

The $\overline{u' v'}$ covariance from CTRL (Figure. 9.11a) displays positive values south of the jet and negative values north of the jet (refer also to Figure 8.2b). Higher values are observed south of the jet, reaching 3 m^2s^{-2} over West Africa (at about 0°) and 5 m^2s^{-2} over the ocean. Albignat and Reed (1980) and Reed et al. (1988) found similar patterns of $\overline{u' v'}$ near the jet level. Since the AEJ is characterized by negative meridional gradients to the south of its axis and positive meridional gradients to the north, the observed configuration implies a conversion of zonal kinetic energy to EKE on both sides of the jet. This pattern suggests that barotropic energy conversions promote the growth of AEWs at the jet level. A minor covariance maximum is also

present around 30°E, indicating that barotropic conversions associated with the jet are also active over East Africa.

The $\overline{v'T'}$ covariance from CTRL (Figure 9.11b) shows negative values over West Africa and over the ocean between 7°N and 20°N. Maximum values are found near 13°N, 5°E, reaching 2 ms^{-1} K. The sign of the covariance in conjunction with the strong positive meridional gradient of temperature (see Figure 9.7a) implies a conversion of zonal available potential energy to eddy available potential energy. Hence, baroclinic energy conversions help maintain AEWs at the lower levels.

The $\overline{\omega'T'}$ covariance exhibits negative values over West Africa and near the coast. Maximum values are found around 17°N, 18°W. The sign of this covariance indicates conversion of eddy available potential energy to EKE north of the jet latitude. The region of large conversion extends eastward near 5°E. This pattern is very similar to the $\overline{v'T'}$ covariance pattern because, as Reed et al. (1977) pointed out, northerly (southerly) winds are associated with relative warm and dry ascending air (cold and moist descending air).

Next, we examine the distribution of covariances from the NO_ORO and NO_CEPG cases. Figure 9.12 shows the covariances for NO_ORO. The $\overline{u'v'}$ covariance (Figure 9.12a) displays positive values between 10°N and 15°N over West Africa and over the ocean. Maximum positive values occur near 12°N, 20°W (over the ocean), and reach 4 m^2s^{-2}. Over West Africa, the covariance reaches values of 1 m^2s^{-2}. Negative values are found north and south of this region. The sign of the covariance associated with the meridional gradient of zonal wind for this simulation implies a conversion of zonal kinetic energy to EKE. This diagram reveals that barotropic conversions associated with the jet, over land, are much weaker in NO_ORO than in CTRL, suggesting that orography constitutes an important factor in the maintenance of the AEWs over the continent.

Figure 9.12b displays the $\overline{v'T'}$ covariance from the NO_ORO case. The highest

negative values are found at about 15°N, 15°W, reaching a value of 3 ms^{-1} K. This pattern exhibits an elongated in the east–west shape, similar to that of EKE. Taking into account the surface distribution of temperature for this case, the sign of the covariance implies a conversion of zonal to eddy available potential energy. Although the magnitude of the covariance is similar to that in CTRL over West Africa, the pattern differs considerably from the one observed in Figure 9.11b.

The $\overline{\omega' T'}$ covariance (Figure 9.12c) exhibits a very different structure from that in CTRL with negative values over Africa that extend along a latitudinal band between 5°N and 15°N. Maximum values of about 10 Pa s^{-1} K are found right at the coast at 15°N. This pattern is also similar to that for the $\overline{v' T'}$ covariance. The sign of the covariance indicates conversion of eddy potential to eddy kinetic energy in this latitudinal band.

In summary, the removal of orography results in a weaker AEJ and in a different distribution of surface temperatures. A weakening of the strength of the jet is directly associated with a reduction in the zonal mean kinetic energy and the available potential energy, which is going to affect the magnitude of the barotropic conversions near the jet. In fact, the weaker jet in the NO_ORO case leads to weaker PV reversals impacting the interactions of negative and positive PV gradients that take place near the jet. At the jet level, the $\overline{u' v'}$ covariance over land is weaker in NO_ORO than in the CTRL case, indicating that the barotropic conversion C_k is reduced over land. West of 10°W the covariance associated with C_k starts to increase reaching maximum values off the coast of Africa. In this region, the jet reaches its maximum intensity, and the meridional gradient of zonal wind increases leading to stronger values of C_k over the ocean. An examination of the $\overline{u' v'}$ covariance and the EKE distribution at the jet level indicates that most of the wave activity observed at 650-hPa results from barotropic energy conversions. Furthermore, these barotropic conversions are weaker in the NO_ORO case than in CTRL. At the lower level, the patterns of $\overline{v' T'}$

and $\overline{\omega' T'}$ covariances are very different from the ones observed in the CTRL case due to changes in the surface temperature distribution. In the NO_ORO case the region of high surface temperatures is located between 10°N and 20°N, therefore, the region of high values of $\overline{v' T'}$ and $\overline{\omega' T'}$ covariances are displaced southward from 20°N, showing maximum values near 15°N, 18°W. The pattern of $\overline{v' T'}$ and $\overline{\omega' T'}$ covariances indicate that weak baroclinic energy conversions take place over land and that strong baroclinic conversions occur right at the coast where surface temperature gradients are stronger. The distribution of EKE at the lower level is in agreement with these patterns, displaying high values of energy at the coast. These results suggest that low level waves own their maintenance and development to baroclinic energy conversions. Moreover, the pattern of covariances associated with barotropic and baroclinic energy conversions is in strong agreement with the distribution of meridional wind variance in the 2 – 6 day band (Figure 8.7). The intensification of barotropic conversions at the jet level and baroclinic conversions at the lower level right at the coast, explain the maximum of variance observed in this region.

Figure 9.13 shows the covariances from the NO_CEPG case. The $\overline{u' v'}$ covariance (Figure 9.13a) exhibits positive values south of the jet along 8°N and weaker negative values north of the jet. Positive values reach 2.5 $m^2 s^{-2}$ over the ocean and at different regions over land, meaning that the horizontal momentum flux is weaker in NO_CEPG than in CTRL. Another important feature from this diagram is the lack of intensification of the momentum flux near the African coast. Considering the distribution of zonal wind, the sign of the covariance suggests a conversion of zonal kinetic energy to EKE. This pattern indicates that barotropic conversions associated with the jet decrease in the NO_CEPG case.

The $\overline{v' T'}$ covariance from NO_CEPG (Figure 9.13b) is negative over West Africa and right at the coast between 10°N and 20°N. Highest values ($\sim$ -1.5 ms^{-1} K) observed over West Africa at about 13°N, 5°W are slightly weaker than the values

observed in CTRL. Another difference between this pattern and the one shown in Figure 9.11b is that the values of this flux start increasing further east in the CTRL case.

The $\overline{\omega' T'}$ covariance at 950-hPa exhibits large values north of the jet, with a maximum (∼6 Pa s-1 K) at about 18°N, 18°W. Over West Africa the values tend to be weaker than in CTRL. The sign of the covariance indicates conversion of eddy potential to eddy kinetic energy in this region.

In summary, the removal of CEPG results in a displacement of the jet by about 3° to the south. A southward displacement of the jet implies a debilitation of the interaction between the negative PV gradients at the jet level and the θ gradients at the surface impacting the baroclinic conversions at the lower levels. An examination of the $\overline{v' T'}$ and $\overline{\omega' T'}$ covariances at 950-hPa confirms a decrease in the baroclinic energy conversions C_E and C_A when compared to the CTRL case. As a result, the distribution of EKE at the lower levels, which is mostly the result of baroclinic wave growth, shows slightly weaker values than in the CTRL. A reduction of the CEPG and the displacement of the jet also impacts the precipitation processes.

According to Grist and Nicholson (2001) a southward displacement of the jet is associated with ″dry″ conditions over West Africa. Since the C_E term is related to an upward movement of warm air due to convective processes, a decrease in the magnitude of the $\overline{\omega' T'}$ covariance could be related to a decrease of latent heat release. At the jet level, the pattern of $\overline{u' v'}$ covariance indicates that barotropic conversions are active south of the jet westward from 30°E. The magnitude of these conversions are weaker than in CTRL, which translates into a reduction of EKE and variability of meridional wind (Figure 8.14) in the 2 – 6 day band south of the jet at 650-hPa.

This work has shown the importance of orography in creating meridional surface temperature gradients and a defined AEJ that favor the growth and maintenance of AEWs through barotropic and baroclinic energy conversions. Moreover, it has been

shown that the magnitude of the CEPG over the Eastern Atlantic Ocean regulates the location of the AEJ, which is going to control the magnitude of the energy conversions that lead to the development of AEWs. A weak CEPG is expected to impact the connection that exists between the convection activity that takes place south of the jet and the maintenance of AEWs, although here this aspect is not treated and requires further investigation. Finally, we only studied the role of orography and CEPG in African easterly wave genesis and maintenance focusing on processes related to the dynamical stability of the jet and to the distribution of surface temperature gradients. Whereas the study here is not exhaustive, it has identified two major players (orography and SST gradient) in determining the character of AEW genesis and character.

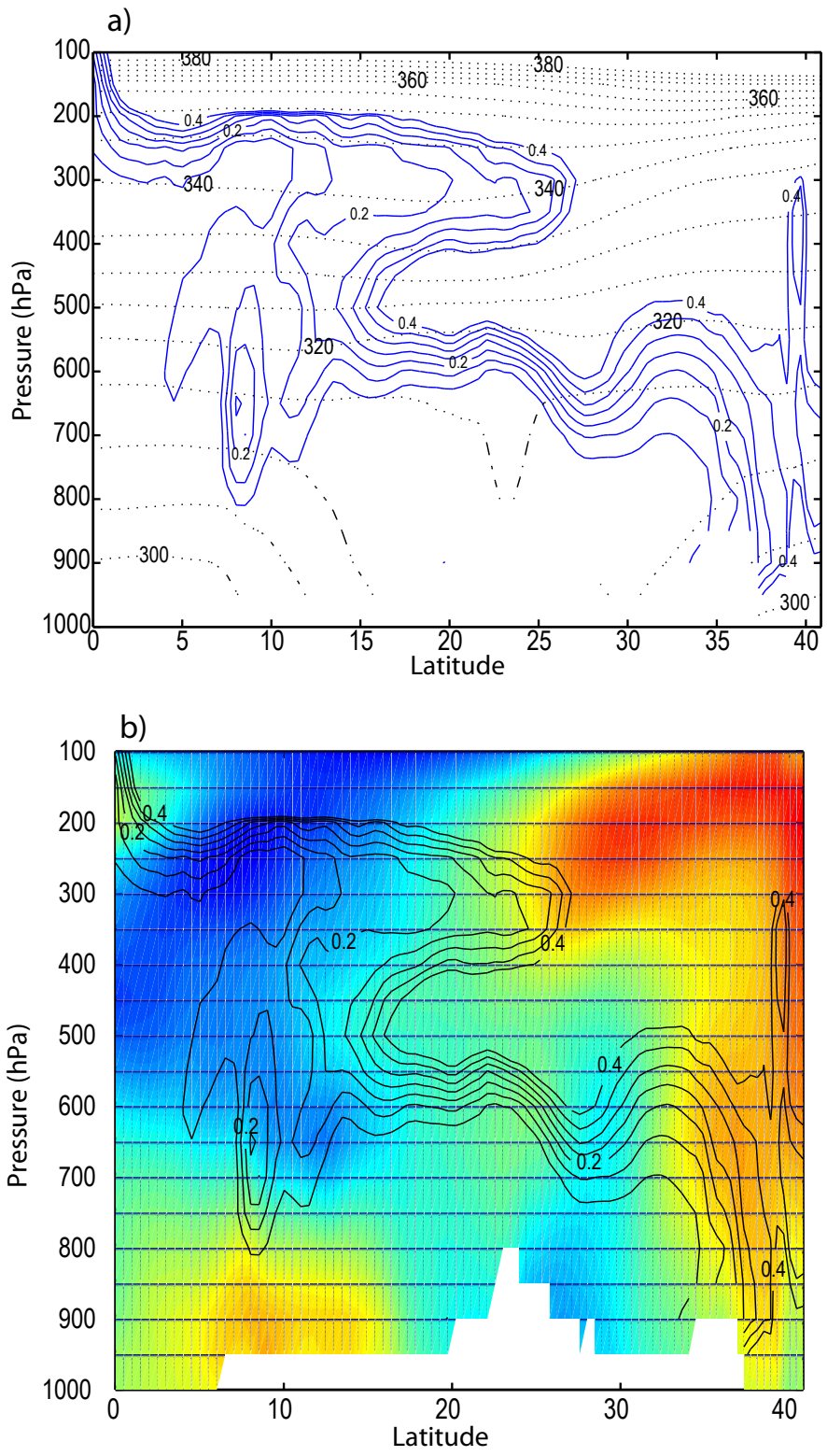

Figure 9.1: Meridional cross-section of potential temperature at 5°E and Ertel PV from CTRL. For the PV only values between 0.1 and 0.4 are plotted. Contour intervals are 5K, 0.05 PVU (1 PVU = 10^{-6} m^2Ks^{-1} kg^{-1})

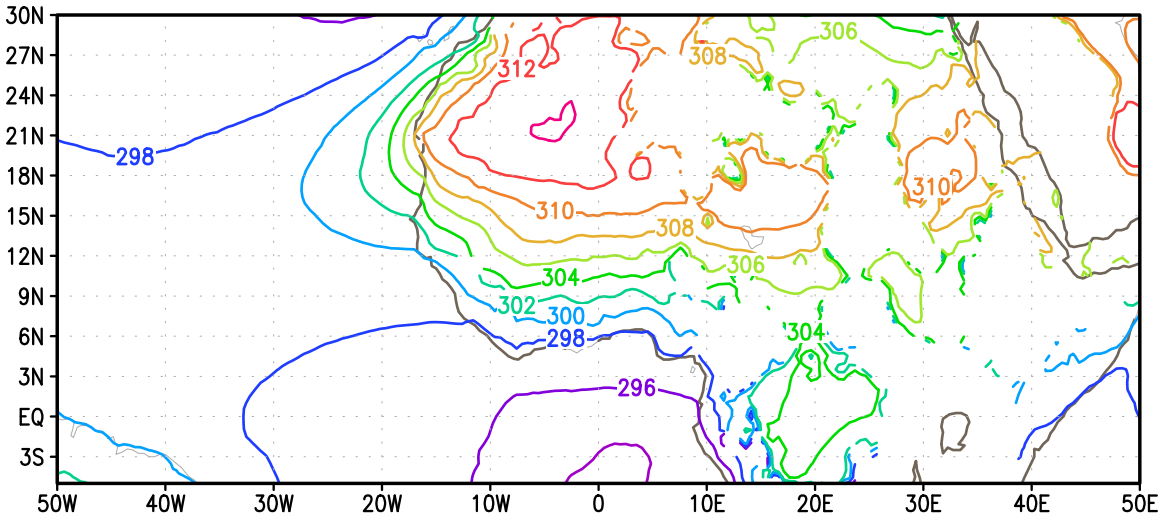

Figure 9.2: Mean horizontal distribution of potential temperature at 950-hPa from CTRL. Contour interval is 2 K.

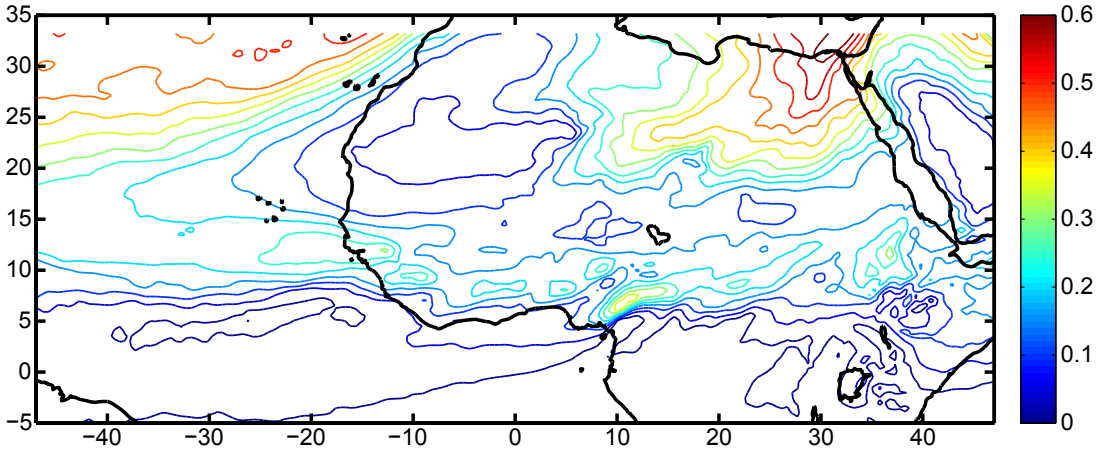

Figure 9.3: Mean horizontal section of PV at 315 K from CTRL. Contour interval is 0.5 PVU

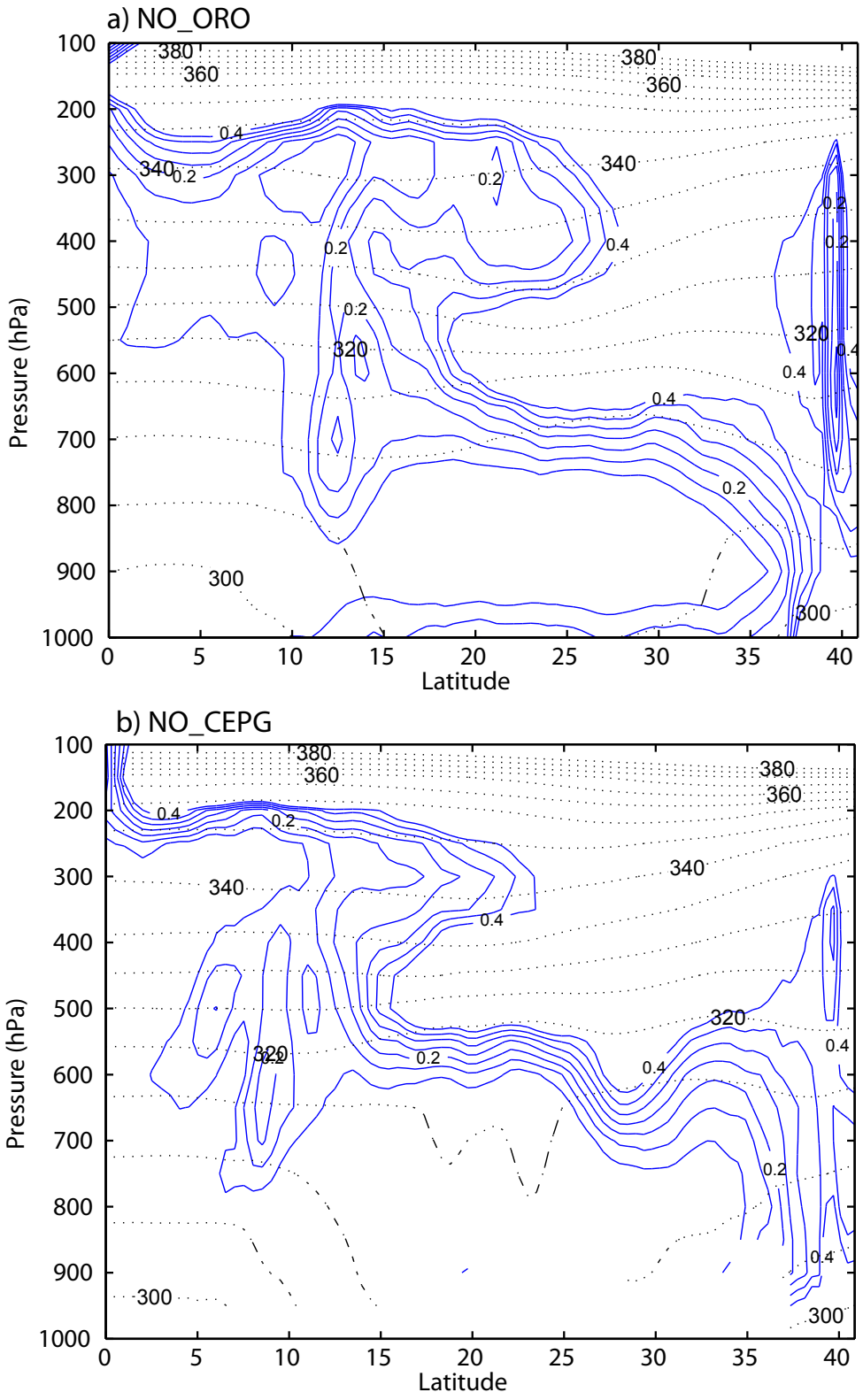

Figure 9.4: Meridional cross-section of potential temperature at 5°E and Ertel PV from a) NO_ORO. b) NO_CEPG. For the PV only values between 0.1 and 0.4 are plotted. Contour intervals are 5K, 0.05 PVU (1 PVU = 10^{-6}m^{2}Ks^{-1} kg^{-1}).

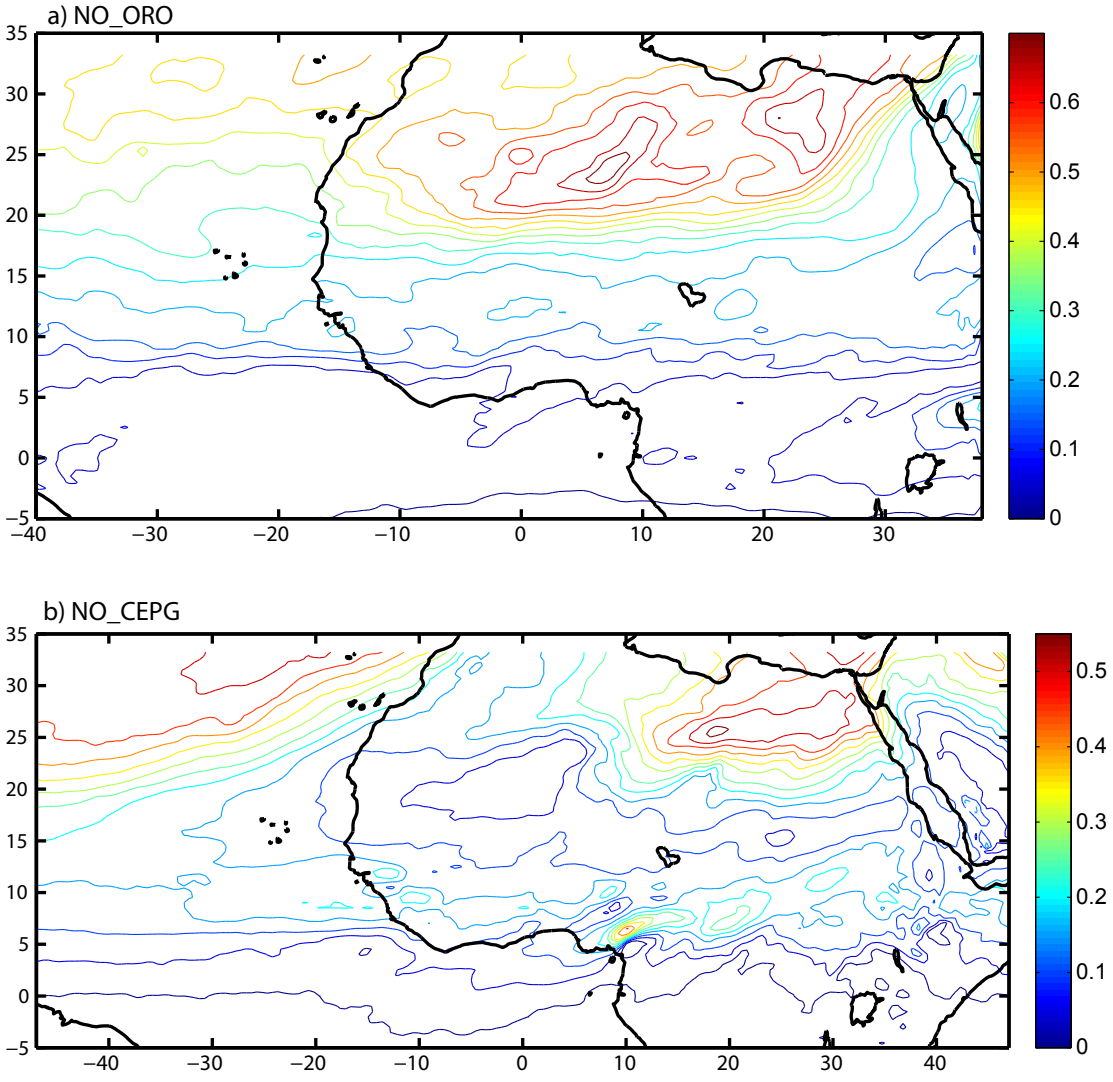

Figure 9.5: Mean horizontal section of PV at 315 K from a) NO_ORO. b) NO_CEPG. Contour interval is 0.5 PVU

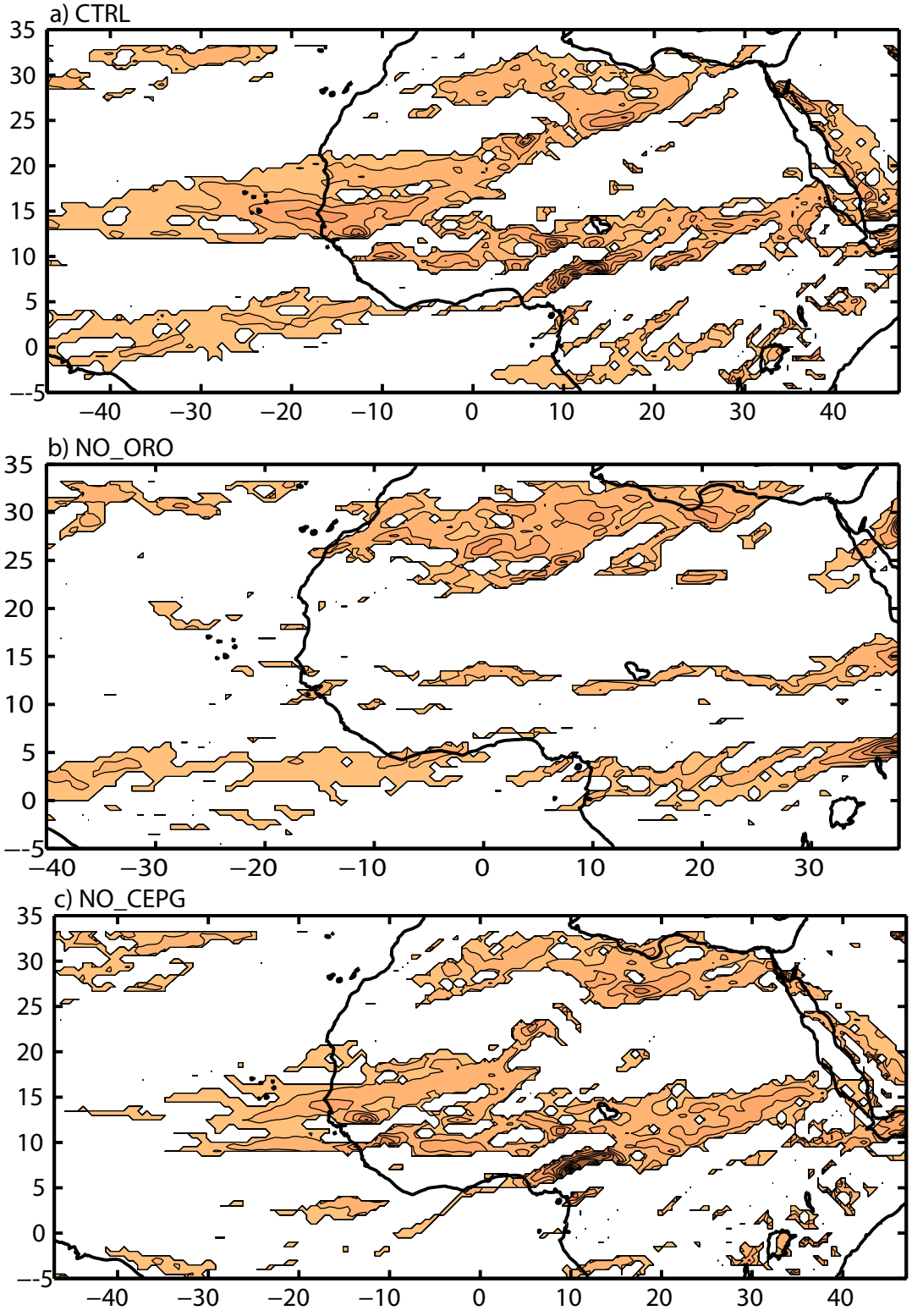

Figure 9.6: Regions of negative PV gradients at 315 K from a) CTRL. b) NO_ORO and c) NO_CEPG.

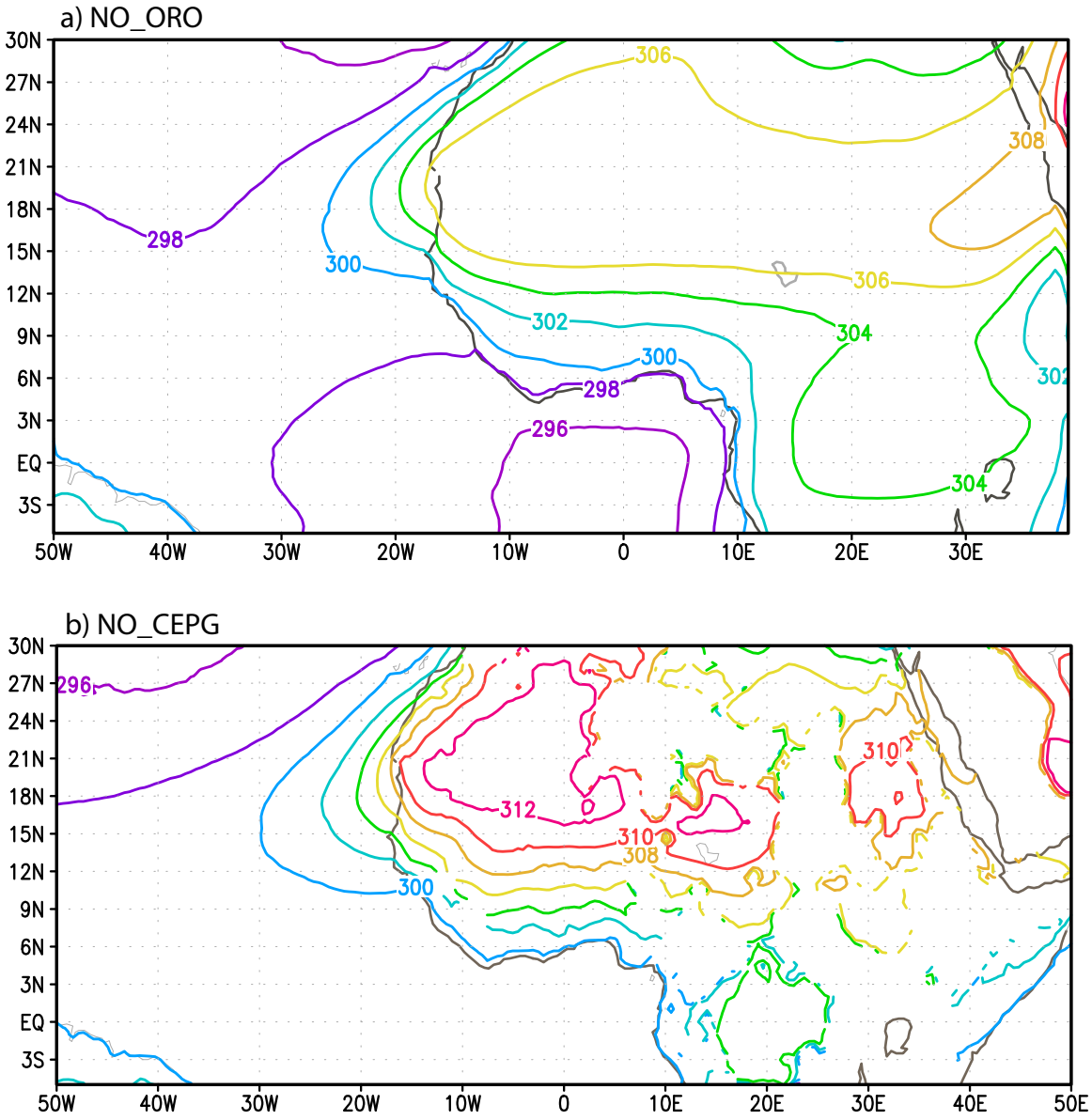

Figure 9.7: Mean horizontal distribution of potential temperature at 950-hPa from a) NO_ORO. b) NO_CEPG. Contour interval is 2 K.

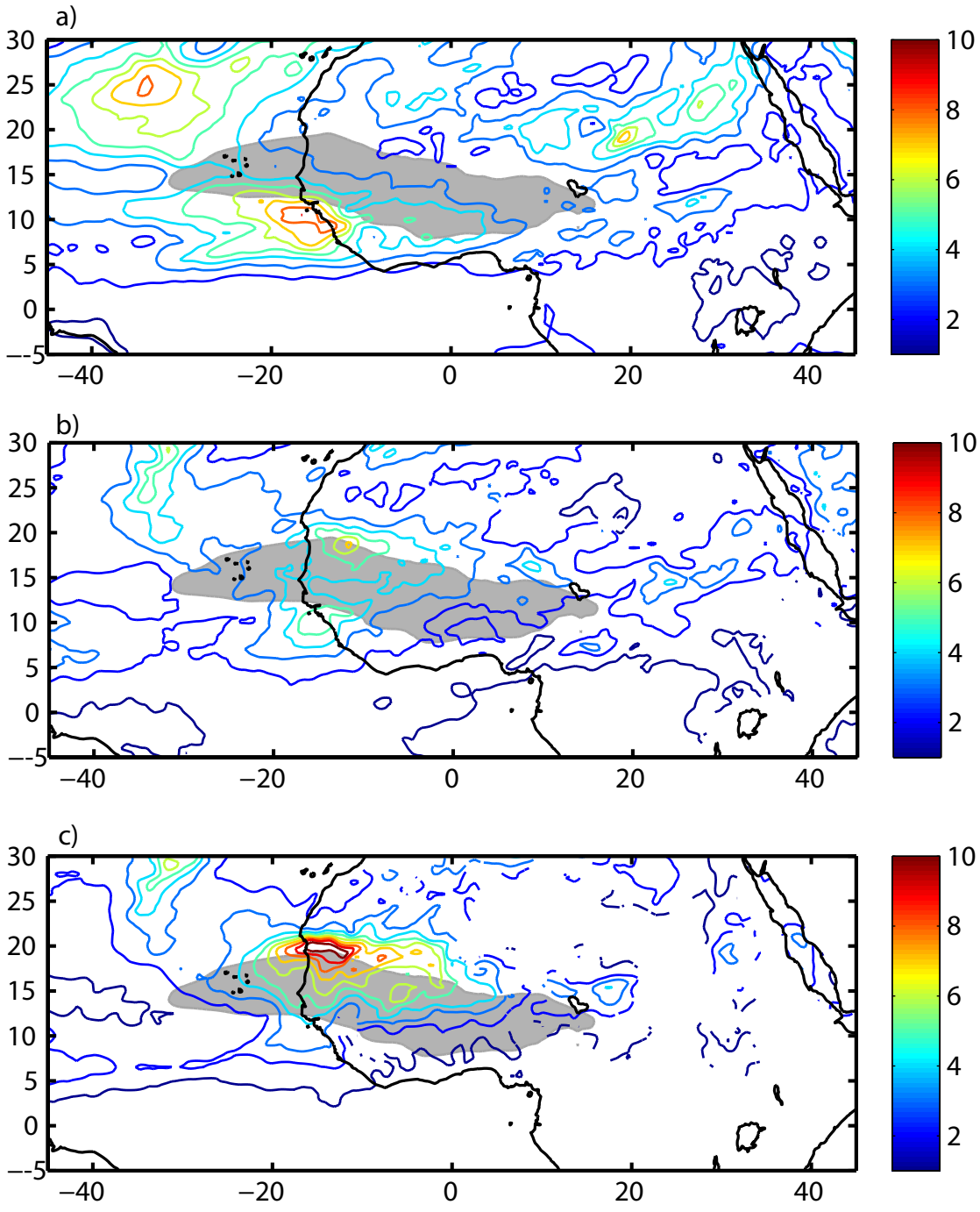

Figure 9.8: Mean EKE from CTRL at a) 650-hPa. b) 850-hPa c) 950-hPa. Contour interval is 1 m^2s^{-2}. The shaded region indicates the mean location of the AEJ.

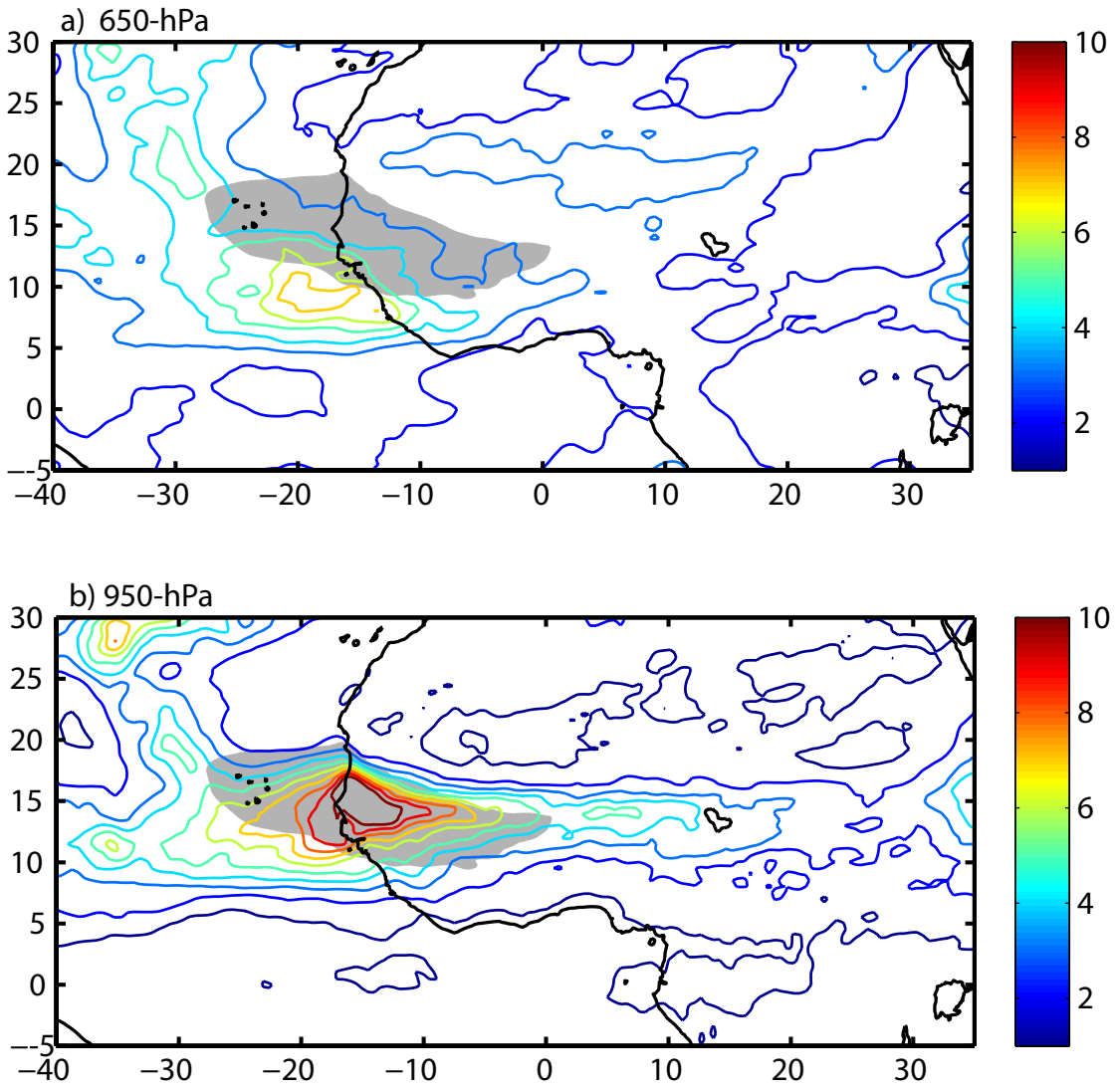

Figure 9.9: Mean EKE from NO_ORO at a) 650-hPa. b) 950-hPa. Contour interval is 1 m^2s^{-2}. The shaded region indicates the mean location of the AEJ.

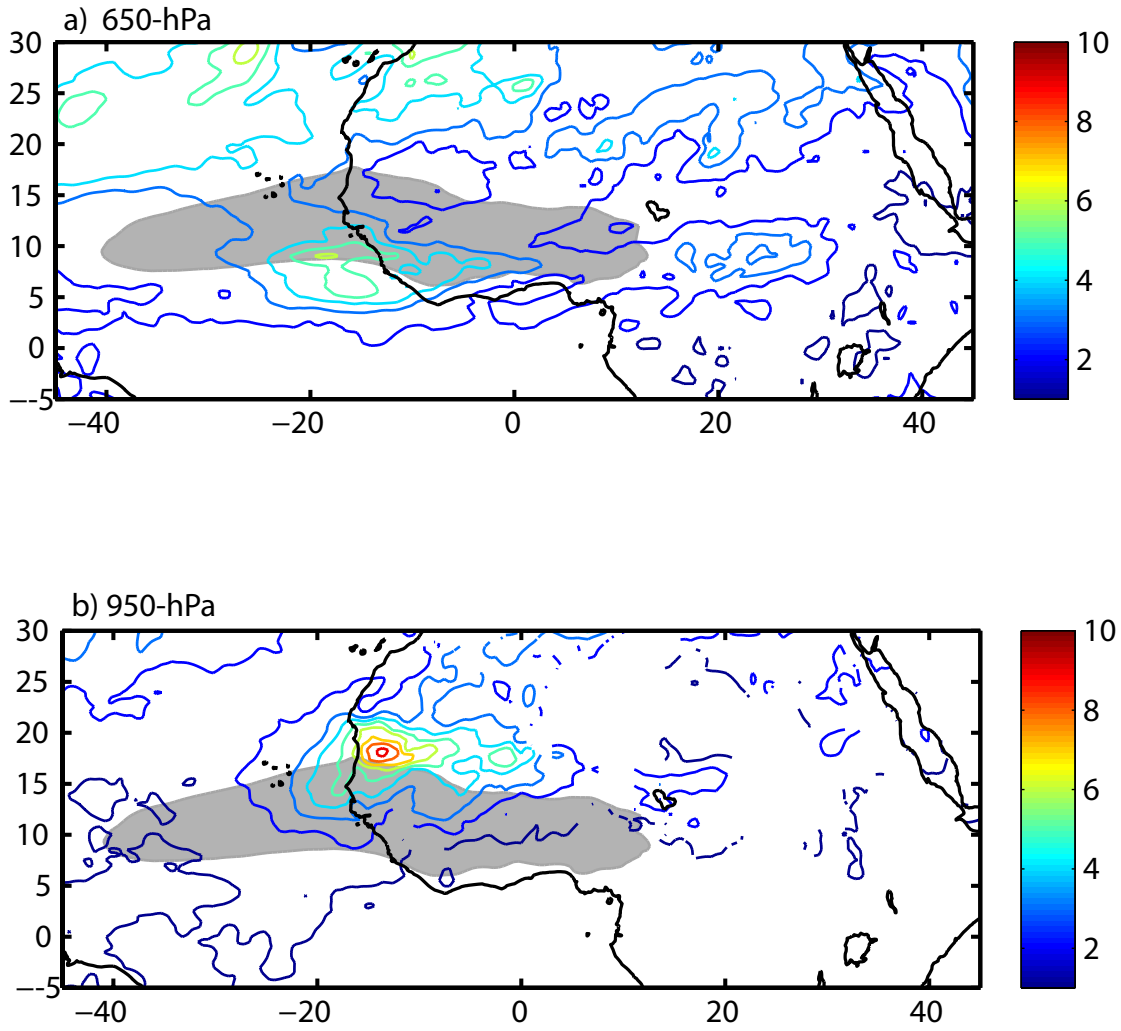

Figure 9.10: Mean EKE from NO_CEPG at a) 650-hPa. b) 950-hPa. Contour interval is 1 m^2s^{-2}. The shaded region indicates the mean location of the AEJ.

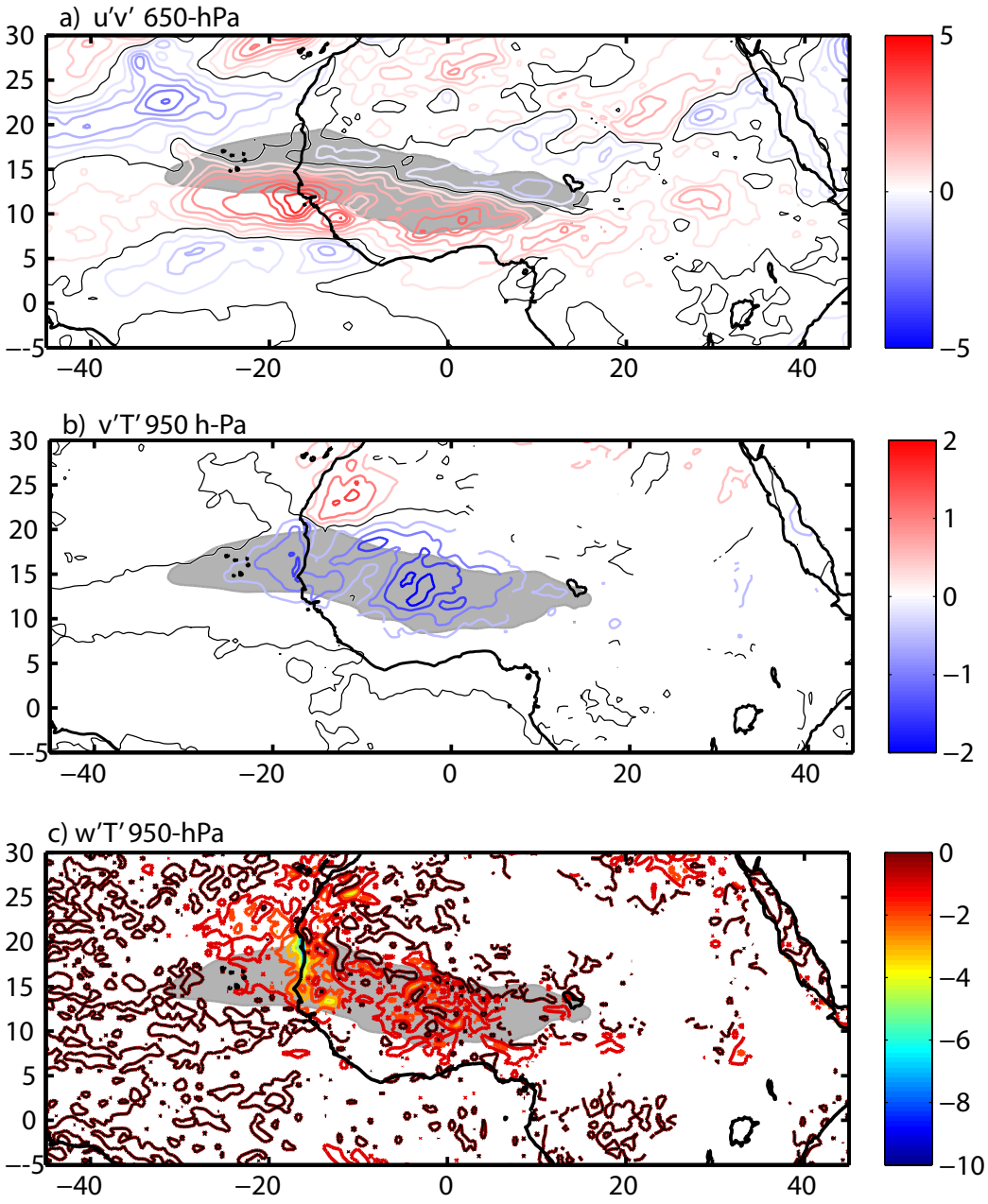

Figure 9.11: Covariances for the 2 – 6 day band from CTRL of a) zonal and meridional winds (m^2 s^{-2}) at 650-hPa; b) meridional wind and temperature (m^2 s^{-1} K) at 950-hPa; c) omega and temperature (10^{-2} Pa s^{-1} K) at 950-hPa. Contour intervals are 0.5, 0.5, 0.1, respectively. The shaded region indicates the mean location of the AEJ.

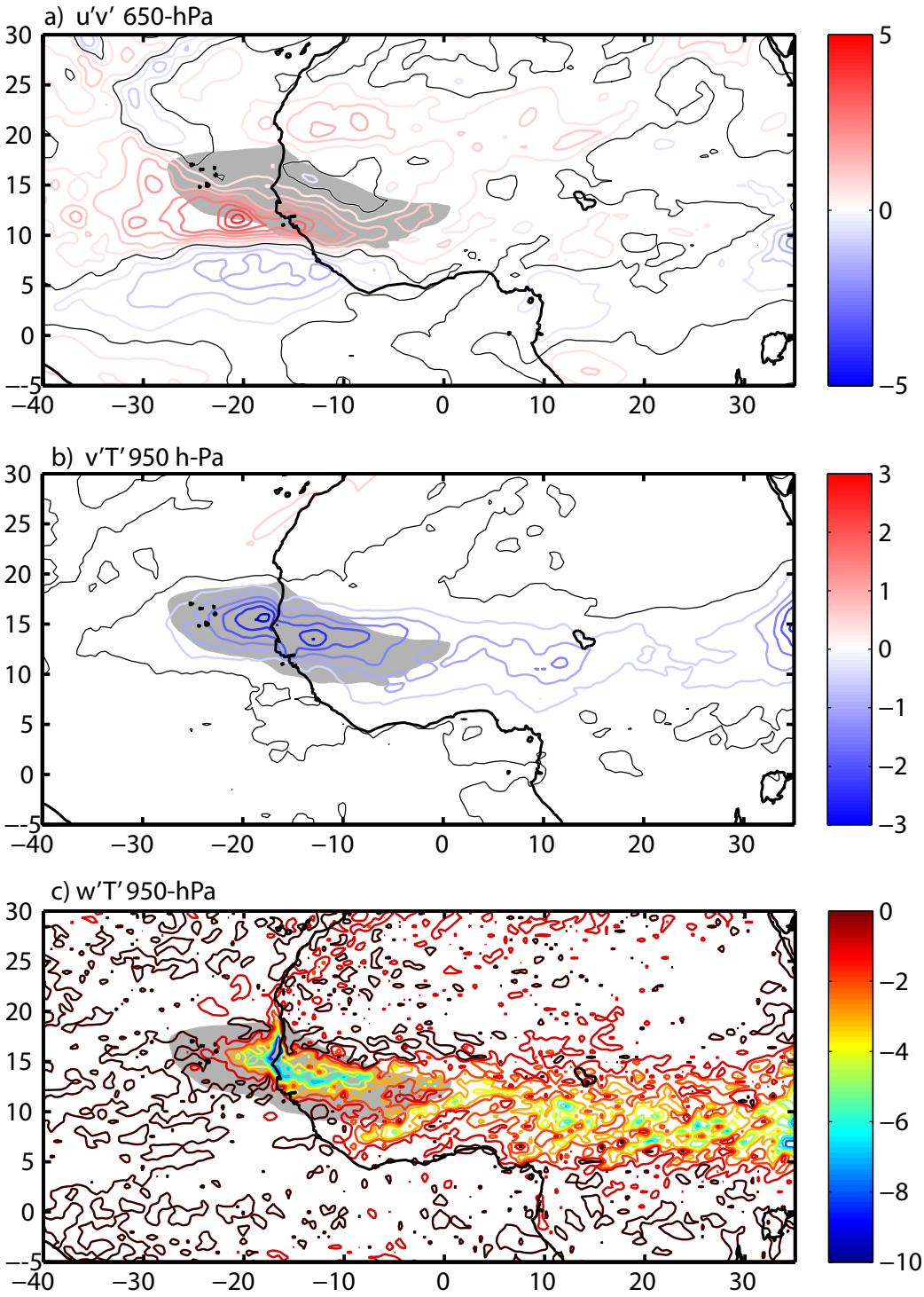

Figure 9.12: Covariances for the 2 – 6 day band from NO_ORO of a) zonal and meridional winds (m2 s^{-2}) at 650-hPa; b) meridional wind and temperature (m^2 s^{-1} K) at 950-hPa; c) omega and temperature (10^{-2} Pa s^{-1} K) at 950-hPa. Contour intervals are 0.5, 0.5, 0.1, respectively. The shaded region indicates the mean location of the AEJ.

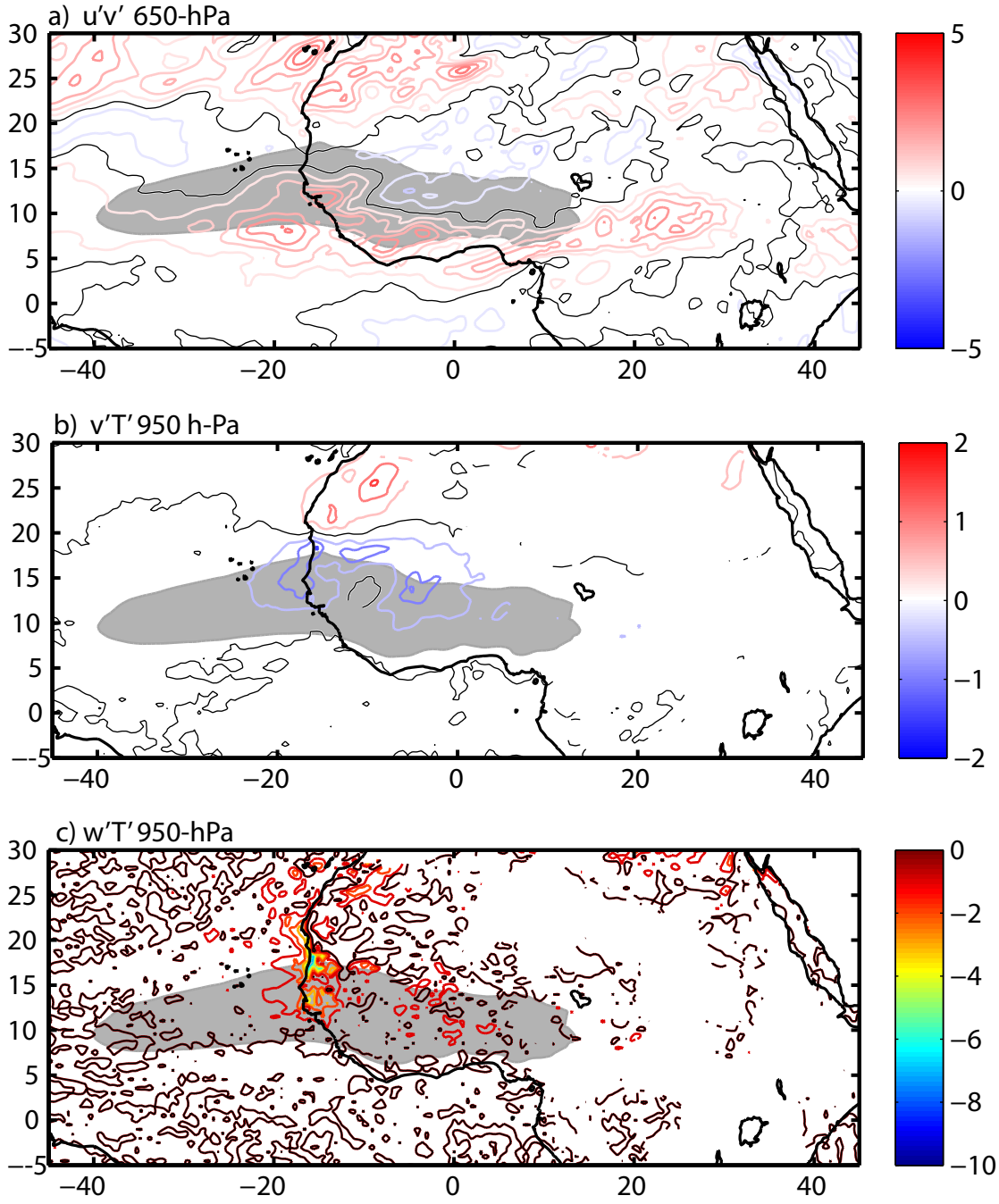

Figure 9.13: Covariances for the 2 – 6 day band from NO_CEPG of a) zonal and meridional winds (m^2 s^{-2}) at 650-hPa; b) meridional wind and temperature (m^2 s^{-1} K) at 950-hPa; c) omega and temperature (10^{-2} Pa s^{-1} K) at 950-hPa. Contour intervals are 0.5, 0.5, 0.1, respectively. The shaded region indicates the mean location of the AEJ.

CHAPTER X

CONCLUSION AND CONCLUDING REMARKS

Part I

The large features of the mean state of the summer monsoon were investigated in response to different configuration of SST during the last century. The ICTP AGCM was forced by monthly varying SST from the NOAA Extended Reconstructed SST dataset over the period 1930 - 2000. In addition to the Control (CTRL) experiment, four major ensemble experiments have been carried out with different SST forcing. The four periods COLD, MODERATE, WARM, and BUMP are the basis of the experiments and were chosen to allow the largest changes in boundary forcing to be isolated and to test if there is any influence on the monsoon precipitation. The BUMP experiment in particular, uses as boundary conditions that period where there may have been a large scale global oscillation in the SST. Analysis of the CTRL simulation reveals that the large-scale circulation associated with the Asian monsoon is reasonably well simulated.

In the COLD configuration, the SST distribution causes a large scale shift of divergence and convergence centers along the equator relative to the CTRL experiment. This shift is accompanied by a weakening of the zonal vertical shear over south Asia, a weakening of the meridional vertical shear over the eastern Indian Ocean and a weaker low level cross-equatorial flow. In addition, both the transverse circulation and the Walker Circulation suffer an eastward shift of their ascending branch, generating anomalous subsidence over the equatorial eastern Indian Ocean, Bay of Bengal and the Indian subcontinent and anomalous upward motion over southeast Asia. This anomalous circulation results in a reduction in convective activity and precipitation

over India and Bay of Bengal relative to the CTRL case and in enhanced precipitation over southeast Asia. Overall, the circulation patterns associated with the COLD SST distribution are consistent with a weakening of the monsoon.

In the MODERATE case, the SST distribution causes a larger impact on the large scale divergence and convergence pattern than in the COLD case and generates stronger anomalous divergence (convergence) over south Asia, southeast Asia and the western equatorial Pacific and anomalous convergence (divergence) over the eastern Pacific and the Americas in the lower troposphere (in the upper troposphere). This anomalous pattern is consistent with a weaker monsoon circulation. SLP gradients associated with the SST induce a stronger cross-equatorial flow and weaker low level westerlies than in the CTRL case. Moreover, decreased easterlies are found in the central equatorial Indian Ocean and the meridional vertical shear also decreases over the Bay of Bengal. For this case, the transverse circulation shows anomalous subsidence over Bay of Bengal and southeast Asia and weak anomalous upward motion over the Arabian Sea. The Walker Circulation exhibits anomalous subsidence over the west Pacific and increased upward motion over Indonesia. The local eastern Hadley circulation also exhibits anomalous subsidence over Bay of Bengal. This anomalous circulation results in decreased precipitation over Bay of Bengal, southeast Asia and the western equatorial Pacific and increased precipitation over Indonesia.

In the WARM configuration SSTs are almost universally warmer than in CTRL with the exception of the North Pacific. The SLP anomalous gradients favor an increase in low level westerlies over the northern-central Indian Ocean. In the upper troposphere increased easterlies are also observed over this same region. Furthermore, the cross-equatorial low level flow shows no substantial differences with the CTRL case. The velocity potential fields for this case display low level increased convergence and upper level increased divergence over the eastern Bay of Bengal and southeast

Asia, consistent with a stronger monsoon. In a coherent manner, the transverse circulation and the local eastern Hadley circulation exhibit anomalous upward motion over the southeast Asia and eastern Bay of Bengal and the transverse circulation exhibits anomalous downward motion over India. The Walker Circulation shows increased upward motion over the eastern portion of its ascending branch and diminished upward motion over Indonesia. This anomalous circulation derives in enhanced precipitation over southeast Asia and the eastern Bay of Bengal and decreased precipitation over India.

In the BUMP case, large SSTs anomalies are found in the northern Pacific and Atlantic Oceans. SSTs anomalies are slightly negative in the northern Indian Ocean and slightly positive in the southern Indian Ocean. The associated SLP distribution depicts strong positive SLP anomalies over south Asia and the northern Indian Ocean, resulting in a decreased cross-equatorial pressure gradient relative to the CTRL. The resulting wind fields show weaker low level westerlies and weaker upper level easterlies over south Asia. Moreover, meridional vertical shear also decreases over the eastern Indian Ocean. Velocity potential fields show decreased low level convergence and decreased upper level divergence over south Asia. For this case, the transverse circulation and the local eastern Hadley circulation exhibit anomalous subsidence over southeast Asia, Bay of Bengal and the Indian subcontinent. The ascending branch of the Walker Circulation over the western Pacific also weakens in this case. The weakening of the ascending branch over south Asia results in a consistent weakening of precipitation. Overall, this pattern is consistent with a weakening of the monsoon.

The results demonstrate that the response of the Asian monsoon to SST changes is somewhat complex and confirm the importance of SST distribution in regulating the strength of the Asian monsoon. SST gradients constitute a key factor for controlling the intensity of the monsoonal winds and the strength of the divergent circulations. The SST variability impacts the monsoon system through changes in the circulation

and through changes in the moisture distribution and availability. A moisture transport analysis was also carried out to relate the changes in the large-scale tropical circulation with the changes in precipitation.

The VIMT analysis shows that the SST distribution affects the moisture distribution through an alteration of the low level flow. Largest differences in the VIMT, that are important for the monsoon rainfall variability, are observed in the interhemispheric component and in the zonal components across the northern Indian Ocean. In the MODERATE experiment, stronger cross-equatorial SLP pressure gradients lead to stronger interhemispheric VIMT flow over the western Indian Ocean. However, for this case, the zonal flow across the northern Indian Ocean is reduced and the transport of moisture from the western Indian Ocean to the eastern Indian Ocean is also reduced, limiting convergence of moisture flux over this region. In the COLD and BUMP experiments, a reduction in the SLP gradient over the western Indian Ocean results in a reduction in the interhemispheric VIMT flow, strongly impacting the convergence of moisture flux over the Indian peninsula. Furthermore, zonal flows across the northern Indian Ocean are also highly reduced. Finally, in the WARM experiment, the SLP gradient is similar to the CTRL and differences in the interhemispheric VIMT flow are less dramatic than in the other experiments. Moreover, zonal flow in the northern Indian Ocean is stronger than in CTRL, and zonal VIMT flux increases. In this case, convergence of moisture flux is favored over portions of the Bay of Bengal and Southeast Asia.

These results suggest that the changes imposed by the SST distribution on the monsoon circulation could affect the convergence of moisture into the continental regions. In the WARM experiment, the reduction in convective processes over the Indian subcontinent could be associated with a modification of the divergent circulations which affect the ascending motion over this region and the associated flux of moisture. Our model simulation, however, does no show significant changes in the

moisture transport into India, perhaps due to the poor representation of the westerlies that blow from the ocean into the Indian peninsula. Further work with a regional model needs to be done to better understand the recent changes in moisture availability over India. Finally, it is important to highlight the advantage of our experimental design. The ICTP AGCM with its coarse resolution is a valuable tool to investigate large-scale climate variability.

Part II

In Part 2, we utilized the WRF regional model to investigate the role of orography and cross equatorial pressure gradients induced by SST in the genesis and maintenance of AEWs. For this purpose we conduct idealized modeling experiments where topography and SST distribution are selectively added and removed. Given the nature of the problem and the scale of the phenomenon to be studied, the ICTP AGCM used in Part 1 was not appropriate.

A comparison of the CTRL simulation with observations show that the model simulation portrays the mean climatological features observed during the boreal summer over Africa, providing a reasonable representation of the AEJ structure. Regarding the structure of AEWs, the model is able to portray westward propagating disturbances with wavelentghts and phase speeds between the observed ranges of AEWs and with a distinctive period of 2 – 6 days. Moreover, the model resembles a meridional circulation that is consistent with the existence of a strong cross-equatorial pressure gradient over the Eastern Atlantic.

We compare the structure of the AEJ, statistical features of AEWs and the structure of surface temperatures between the CTRL case and the two additional experimental simulations: NO_ORO (referring to the removal of orography) and NO_CEPG (referring to the reduction of the cross equatorial pressure gradient).

When orography is removed, the structure of the AEJ changes considerably showing a weaker jet with a maximum located 3° south of the jet core in CTRL. Other climatological features, that are the TEJ and the Harmattans, also appear to be weaker in NO_ORO. Moreover, westward propagating disturbances depict differences in structure and strength relative to the CTRL case. The removal of orography also impacts the distribution of surface temperature, favoring a reduction of the region of highest temperature relative to the CTRL.

Spectral analysis results show that the variability associated with AEWs (2 – 6 day band) is reduced over East Africa and West Africa at the lower level (850-hPa) and increases at the coast near 15°W, 12°N when orography is removed. Reduced variance is evident west of 20°E along the southern flank of the jet and north of 20°N over East Africa and West Africa at the jet level.

The SST maximum is located at the Equator and coincides with the sea level pressure minimum when the CEPG gradient is reduced. As a result the low level westerly flow is weaker than in CTRL and the contour of zero absolute-vorticity displaces southward in agreement with the inertial instability mechanism (e.g. Tomas and Webster 1997). In the NO_CEPG the general shape and intensity of the AEJ is similar to that in CTRL, however its mean latitudinal location displaces to the south, consistent with a reduction in the CEPG. These results confirm the idea that the structure of the AEJ is linked to changes in the SST gradient (Nicholson and Webster 2007). Furthermore, the distribution of surface temperature over land is the same as in the CTRL case.

An examination of the statistical features of the AEWs for the NO_CEPG case shows that the SST distribution also impacts the AEW variability. At the lower level, a large reduction of variance in the 2 – 6 day band is found at the coast and also over East Africa. At the jet level, the reduction in variance is more evident south of the jet and west of 10°E.

A comparative analysis of the dynamical instability of the AEJ and of the energetics of AEWs between the three experiments was done in order to explore changes in AEW variability associated with the removal of orography and the reduction in the CEPG. Burpee (1972) and others have shown that the AEJ satisfies the Charney and Stern (1962) instability criterion, and that the jet supports westward propagating disturbances evolving through both barotropic and baroclinic energy conversions.

An analysis of the mean PV and θ structure for each of the experiments shows that for the three cases the Charney-Stern and Fjortoft necessary conditions for instability are satisfied. However, in the NO_ORO case the area of negative PV gradients is reduced in conjunction with the magnitude of the reversals, suggesting a weakening of barotropic energy conversions. Moreover, the structure of the surface θ is also different from that in CTRL, showing a reduction in the θ gradients north of 14°N. In the NO_CEPG case the distribution of negative PV and θ gradients is comparable to that on the CTRL case over land. Over the ocean, negative PV gradients are highly reduced relative to the CTRL case.

In the NO_ORO case, the resulting weaker AEJ leads to weaker PV reversals impacting the interactions of negative and positive PV gradients and the associated barotropic conversions that take place at the jet level over East and West Africa. At the lower level, the changes in the surface temperature distribution relative to the CTRL case, originate changes in the baroclinic energy conversion over land. These changes result in a weakening of barotropic conversions at the jet level and a weakening of baroclinic conversions at the lower level over land, consistent with a reduction of wind variance in the $2-6$ day band over East and West Africa. Right at the coast, the intensification of barotropic conversions at the jet level and baroclinic conversions at the lower level explain the maximum of variance observed in this region.

In the NO_CEPG case, the reduction of CEPG results in a displacement of the AEJ by about 3° to the south. A southward displacement of the jet implies a debilitation of

the interaction between the negative PV gradients at the jet level and the θ gradients at the surface, which results in a reduction of baroclinic conversions at the lower levels. At the jet level, the barotropic conversion is also weaker than in the CTRL case. The southward displacement of the jet is also related with a reduction in precipitation over West Africa. The reduction in the baroclinic conversions could also be associated with a decrease of latent heat release due to drier conditions over West Africa. This aspect grants further investigation.

The role of orography and the CEPG in African easterly wave genesis and maintenance was studied focusing on processes related to the dynamical stability of the jet and to the distribution of surface temperature gradients. Results show the importance of orography in creating meridional surface temperature gradients and a defined AEJ. The former determines the magnitude and structure of the baroclinic conversions and the latter controls the barotropic conversions. It has also been shown that the magnitude of the CEPG over the Eastern Atlantic Ocean regulates the location of the AEJ and as a result the magnitude of the energy conversions that lead to AEW growth.

Other aspects that are important in the generation of AEWs and need to be addressed in relation to the impact of the orographic features and the magnitude of the CEPG are: the association with the convective activity that takes place south of the jet, interactions with the surface ITCZ, and the behavior of the vertical Rossby wave propagation mechanism.

APPENDIX A

MONSOON INDICES

Table A.1: Definitions of monsoon indices used in this study

Index	Definition
AIMR	Seasonally averaged precipitation over all Indian subdivisions from June to September (Parthasarathy et al 1992)
WYI	Vertical zonal wind shear between 850 and 200-hPa, U850-U200, averaged over the south Asia region 0°-20°N, 40°-110°E (Webster and Yang 1992)
MHI	Vertical meridional wind shear between 850 and 200-hPa, V850 V200, averaged over 10°-30°N, 70°-110°E (Goswami et al. 1999)
WSI	Vertical zonal wind shear between 850 and 200-hPa, U850 U200, averaged over 5°-20°N, 40°-80°E (Wang and Fan 1999)
SOM1	Square root of the area mean wind speed at 850 hPa in the region 5°S - 20°N, 50°E - 70°E (Boos and Emanuel 2009)
SOM2	Area mean meridional wind at 925-hPa in the region 5°S- 5°N, 40°E-60°E
CEPG	Difference in sea level pressure between 20°N and 20°S along the 60°E longitude)

REFERENCES

Adler, R. F., G. J. Huffman, A. Chang, R. Ferraro, P. P. Xie, J. Janowiak, B. Rudolf, U. Schneider, S. Curtis, D. Bolvin, A. Gruber, J. Susskind, P. Arkin, and E. Nelkin, 2003: The version-2 global precipitation climatology project (gpcp) monthly precipitation analysis (1979-present). *Journal of Hydrometeorology*, **4**, 1147–1167.

Albignat, J. P. and R. J. Reed, 1980: The origin of african wave disturbances during phase iii of gate. *Monthly Weather Review*, **108**, 1827–1839.

Arkin, P. A. and B. N. Meisner, 1987: The relationship between large-scale convective rainfall and cold cloud over the western-hemisphere during 1982-84. *Monthly Weather Review*, **115**, 51–74.

Arnault, J. and F. Roux, 2009: Case study of a developing african easterly wave during namma: An energetic point of view. *Journal of the Atm*, **66**, 2991–3020.

Arpe, K., L. Dumenil, and M. A. Giorgetta, 1998: Variability of the indian monsoon in the echam3 model: Sensitivity to sea surface temperature, soil moisture, and the stratospheric quasi-biennial oscillation. *Journal of Climate*, **11**, 1837–1858.

Ashok, K., Z. Y. Guan, and T. Yamagata, 2001: Impact of the indian ocean dipole on the relationship between the indian monsoon rainfall and enso. *Geophysical Research Letters*, **28**, 4499–4502.

Betts, A. K. and M. J. Miller, 1993: The betts-miller scheme. *The representation of cumulus convection in numerical models*, K. A. Emanuel and D. J. Raymond, eds., American Meteorological Society, Boston, Mass., volume 46, 107–121.

Bjerknes, J., 1969: Atmospheric teleconnections from equatorial pacific. *Monthly Weather Review*, **97**, 163–172.

Bolvin, D., R. Adler, G. Huffman, E. Nelkin, and J. Poutiainen, 2009: Comparison of gpcp monthly and daily precipitation estimates with high-latitude gauge observations. *Journal of Applied Meteorology and Cimatology*, **48**, 1843–1857.

Boos, W. R. and K. A. Emanuel, 2009: Annual intensification of the somali jet in a quasi-equilibrium framework: Observational composites. *Quarterly Journal of the Royal Meteorological Society*, **135**, 319335.

Bracco, A., F. Kucharski, R. Kallummal, and F. Molteni, 2004: Internal variability, external forcing and climate trends in multi-decadal agcm ensembles. *Climate Dynamics*, **23**, 659–678.

Bracco, A., F. Kucharski, F. Molteni, W. Hazeleger, and C. Severijns, 2007: A recipe for simulating the interannual variability of the asian summer monsoon and its relation with enso. *Climate Dynamics*, **28**, 441–460.

Burpee, R. W., 1972: The origin and structure of easterly waves in the lower troposphere of north africa. *Journal of the Atmospheric Sciences*, **29**, 77–90.

— 1974: Characteristics of north african easterly waves during the summers of 1968 and 1969. *Journal of the Atmospheric Sciences*, **31**, 1556–1570.

— 1975: Some features of synoptic-scale waves based on a compositing analysis of gate data. *Monthly Weather Review*, **103**, 921–925.

Carlson, T. N., 1969a: Some remarks on african disturbances and their progress over the tropical atlantic. *Monthly Weather Review*, **97**, 716–726.

— 1969b: Synoptic histories of three african disturbances that developed into atlantic hurricanes. *Monthly Weather Review*, **97**, 256–276.

— 1979: Atmospheric turbidity in saharan dust outbreaks as determined by analyses of satellite brightness data. *Monthly Weather Review*, **107**, 322–335.

Chandrasekar, A. and A. Kitoh, 1998: Impact of localized sea surface temperature anomalies over the equatorial indian ocean on the indian summer monsoon. *Journal of the Meteorological Society of Japan*, **76**, 841–853.

Chao, W. C. and B. Chen, 2001: The origin of monsoons. *Journal of the Atmospheric Sciences*, **58**, 3497–3507.

Charney, J. and J. Shukla, 1981: Predictability of monsoon. *Monsoon Dynamics*, J. Lighthill and R. Pearce, eds., Cambridge University Press, 735.

Charney, J. G. and M. E. Stern, 1962: On the stability of internal baroclinic jets in a rotating atmosphere. *Journal of the Atmospheric Sciences*, **19**, 159–172.

Chung, C. E. and V. Ramanathan, 2006: Weakening of north indian sst gradients and the monsoon rainfall in india and the sahel. *Journal of Climate*, **19**, 2036–2045.

Cifelli, R., T. Lang, S. Rutledge, N. Guy, E. Zipser, J. Zawislak, and R. Holzworth, 2010: Characteristics of an african easterly wave observed during namma. *Journal of the Atmos*, **67**, 3–25.

Clark, C. O., J. E. Cole, and P. J. Webster, 2000: Indian ocean sst and indian summer rainfall: Predictive relationships and their decadal variability. *Journal of Climate*, **13**, 2503–2519.

Clark, C. O., P. J. Webster, and J. E. Cole, 2003: Interdecadal variability of the relationship between the indian ocean zonal mode and east african coastal rainfall anomalies. *Journal of Climate*, **16**, 548–554.

Cook, K. H., 1999: Generation of the african easterly jet and its role in determining west african precipitation. *Journal of Climate*, **12**, 1165–1184.

Das, P. K., 1986: Monsoon. *V.I.M.O. Lecture*, World Meteorological Organization, volume 613, 155.

Dash, S. K., R. K. Jenamani, S. R. Kalsi, and S. K. Panda, 2007: Some evidence of climate change in twentieth-century india. *Climatic Change*, **85**, 299–321.

Dash, S. K., M. A. Kulkarni, U. C. Mohanty, and K. Prasad, 2009: Changes in the characteristics of rain events in india. *Journal of Geophysical Research-Atmospheres*, **114**, 1–12.

Dash, S. K., J. R. Kumar, and M. S. Shekhar, 2004: On the decreasing frequency of monsoon depressions over the indian region. *Current Science*, **86**, 1404–1411.

Diedhiou, A. Diedhiou, Janicot, S. Janicot, Viltard, A. Viltard, F. de, and P. d. Flice, 2002: Energetics of easterly wave disturbances over west africa and the tropical atlantic: A climatology from the 1979-95 ncep/ncar reanalyses. *Climate Dynamics*, **18**, 487–500.

Diedhiou, A., S. Janicot, A. Viltard, and P. de Felice, 1998: Evidence of two regimes of easterly waves over west africa and the tropical atlantic. *Geophysical Research Letters*, **25**, 2805–2808.

Dudhia, J., 1989: Numerical study of convection observed during the winter monsoon experiment using a mesoscale two-dimensional model. *Journal of the Atmospheric Sciences*, **46**, 3077–3107.

Estoque, M. A. and M. S. Lin, 1977: Energetics of easterly waves. *Monthly Weather Review*, **105**, 582–589.

Fasullo, J. and P. J. Webster, 2002: Hydrological signatures relating the asian summer monsoon and enso. *Journal of Climate*, **15**, 3082–3095.

Fein, J. S. and P. L. Stephens, 1987: *Monsoons*. Wiley, New York.

Findlater, J., 1969a: Interhemispheric transport of air in lower troposphere over western indian ocean. *Quarterly Journal of the Royal Meteorological Society*, **95**, 400–403.

— 1969b: A major low-level air current near indian ocean during northern summer. *Quarterly Journal of the Royal Meteorological Society*, **95**, 362–380.

Flohn, H., 1957: Large-scale aspects of the "summer monsoon" in south and east asia. *Journal of the Metereological Society of Japan*, **35**, 180–186.

Flohn, H. and E. R. Reiter, 1968: Contributions to a meteorology of the tibetan highlands.

Frank, N. L., 1970: Atlantic tropical systems of 1969. *Monthly Weather Review*, **98**, 307–314.

Ghosh, S., V. Luniya, and A. Gupta, 2009: Trend analysis of indian summer monsoon rainfall at different spatial scales. *Atmospheric Science Letters*, **10**, 285–290.

Gibson, J. K., P. Kallberg, S. Uppala, A. Hernandez, A. Nomura, and E. Serrano, 1997: Ecmwf re-analysis. project report series. 1. era description. Technical report, European Centre for Medium-Range Weather Forecast, Reading (UK).

Gill, A. E., 1980: Some simple solutions for heat-induced tropical circulation. *Quarterly Journal of the Royal Meteorological Society*, **106**, 447–462.

Goswami, B. N., 2006: *The Asian monsoo: Interdecadal variability*, Springer, chapter 7. 295–327.

Goswami, B. N., V. Krishnamurthy, and H. Annamalai, 1999: A broad-scale circulation index for the interannual variability of the indian summer monsoon. *Quarterly Journal of the Royal Meteorological Society*, **125**, 611–633.

Grist, J. P., 2002: Easterly waves over africa. part i: The seasonal cycle and contrasts between wet and dry years. *Monthly Weather Review*, **130**, 197–211.

Grist, J. P. and S. Nicholson, 2002: Easterly waves over africa. part ii: Observed and modeled contrasts between wet and dry years. *Monthly Weather Review*, **130**, 212 – 225.

Grist, J. P. and S. E. Nicholson, 2001: A study of the dynamic factors influencing the rainfall variability in the west african sahel. *Journal of Climate*, **14**, 1337–1359.

Guhathakurta, P. and M. Rajeevan, 2008: Trends in the rainfall pattern over india. *International Journal of Climatology*, **28**, 1453–1469.

Hahn, D. G. and S. Manabe, 1975: Role of mountains in south asian monsoon circulation. *Journal of the Atmospheric Sciences*, **32**, 1515–1541.

Hall, N. M. J., G. N. Kiladis, and C. D. Thorncroft, 2006: Three-dimensional structure and dynamics of african easterly waves. part ii: Dynamical modes. *Journal of the Atmospheric Sciences*, **63**, 2231–2245.

Hart, J. E., 1977: Theory of east-african low-level jet stream. *Pure and Applied Geophysics*, **115**, 1263–1282.

Hirsch, R. M., J. R. Slack, and R. A. Smith, 1982: Techniques of trend analysis for monthly water-quality data. *Water Resources Research*, **18**, 107–121.

Hong, S.-Y., J. Dudhia, and S.-H. Chen, 2004: A revised approach to ice microphysical processes for the bulk parameterization of clouds and precipitation. *Monthly Weather Review*, **132**, 103–120.

Hong, S.-Y., Y. Noh, and J. Dudhia, 2006: A new vertical diffusion package with an explicit treatment of entrainment processes. *Monthly Weather Review*, **134**, 2318–2341.

Hoskins, B. J., M. McIntyre, and A. Robertson, 1985: On the use and significance of isentropic potential vorticity maps. *Quarterly Journal of the Royal Meteorological Society*, **111**, 877–946.

Hoyos, C. D. and P. J. Webster, 2007: The role of intraseasonal variability in the nature of asian monsoon precipitation. *Journal of Climate*, **20**, 4402–4424.

Hsieh, J.-S. and K. H. Cook, 2005: Generation of african easterly wave disturbances: Relationship to the african easterly jet. *Monthly Weather Review*, **133**, 1311–1327.

— 2007: A study of the energetics of african easterly waves using a regional climate model. *Journal of the Atmospheric Sciences*, **64**, 421–440.

Huffman, G. J., R. F. Adler, D. Bolvin, and G. Gu, 2009: Improving the global precipitation record: Gpcp version 2.1. *Geophysical Research Letters*, **36**, 1–5.

Janjic, Z. I., 1994: The step-mountain eta coordinate model: Further developments of the convection, viscous sublayer, and turbulence closure schemes. *Monthly Weather Review*, **122**, 927–945.

Joseph, P. and P. Xavier, 1999: Monsoon rainfall and frequencies of monsoon depressions and tropical cyclones of recent 100 years and an out look for the first decades of 21st century, meteorology beyond 2000. *Proceedings of Indian Meteorological Society*, TROPMET-99, 364371.

Joseph, P. V., 1976: Climate change in monsoon and cyclones 1891 1974. *Symp. Tropical Monsoons*, 378 – 387.

Joseph, P. V. and A. Simon, 2005: Weakening trend of the southwest monsoon current through peninsular india from 1950 to the present. *Current Science*, **89**, 687–694.

Kiladis, G. N., C. D. Thorncroft, and N. M. J. Hall, 2006: Three-dimensional structure and dynamics of african easterly waves. part i: Observations. *Journal of the Atmospheric Sciences*, **63**, 2212–2230.

Kripalani, R. H. and A. Kulkarni, 1997: Rainfall variability over south-east asia - connections with indian monsoon and enso extremes: New perspectives. *International Journal of Climatology*, **17**, 1155–1168.

Kripalani, R. H., A. Kulkarni, and S. V. Singh, 1997: Association of the indian summer monsoon with the northern hemisphere mid-latitude circulation. *International Journal of Climatology*, **17**, 1055–1067.

Kripalani, R. H., J. H. Oh, A. Kulkarni, S. S. Sabade, and H. S. Chaudhari, 2007: South asian summer monsoon precipitation variability: Coupled climate model simulations and projections under ipcc ar4. *Theoretical and Applied Climatology*, **90**, 133–159.

Krishna Kumar, K., B. Rajagopolan, and M. A. Cane, 1999: On the weakening relationship between the indian monsoon and enso. *Science*, **284**, 21562159.

Krishnakumar, K. N., G. Rao, and C. S. Gopakumar, 2009: Rainfall trends in twentieth century over kerala, india. *Atmospheric Environment*, **43**, 1940–1944.

Krishnamurthy, V. and B. N. Goswami, 2000: Indian monsoon-enso relationship on interdecadal timescale. *Journal of Climate*, **13**, 579–595.

Krishnamurti, T. N., 1971a: Observational study of the tropical upper tropospheric motion field during the northern hemisphere summer. *Journal of Applied Meteorology*, **10**, 1066–1096.

— 1971b: Tropical east-west circulations during northern summer. *Journal of the Atmospheric Sciences*, **28**, 1342–1347.

— 1985: Summer monsoon experiment - a review. *Monthly Weather Review*, **113**, 1590–1626.

Krishnamurti, T. N., P. Ardanuy, Y. Ramanathan, and R. Pasch, 1981: On the onset vortex of the summer monsoon. *Monthly Weather Review*, **109**, 344–363.

Krishnamurti, T. N. and H. N. Bhalme, 1976: Oscillations of a monsoon system .1. observational aspects. *Journal of the Atmospheric Sciences*, **33**, 1937–1954.

Krishnamurti, T. N., J. Molinari, and H. L. Pan, 1976: Numerical simulation of the somali jet. *Journal of the A*, **33**, 2350 – 2362.

Krishnan, R. and M. Sugi, 2003: Pacific decadal oscillation and variability of the indian summer monsoon rainfall. *Climate Dynamics*, **21**, 233–242.

Kucharski, F., A. Bracco, J. H. Yoo, and F. Molteni, 2007: Low-frequency variability of the indian monsoon-enso relationship and the tropical atlantic: The "weakening" of the 1980s and 1990s. *Journal of Climate*, **20**, 4255–4266.

— 2008: Atlantic forced component of the indian monsoon interannual variability. *Geophysical Research Letters*, **35**.

Kucharski, F., A. Bracco, J. H. Yoo, A. M. Tompkins, L. Feudale, P. Ruti, and A. Dell'Aquila, 2009: A gill-matsuno-type mechanism explains the tropical atlantic influence on african and indian monsoon rainfall. *Quarterly Journal of the Royal Meteorological Society*, **135**, 569–579.

Kucharski, F., F. Molteni, and A. Bracco, 2006: Decadal interactions between the western tropical pacific and the north atlantic oscillation. *Climate Dynamics*, **26**, 79–91.

Kuettner, J. P., 1974: General description and central program of gate. *Bulletin of the American Meteorological Society*, **55**, 712–719.

Kumar, K. R., G. B. Pant, B. Parthasarathy, and N. A. Sontakke, 1992: Spatial and subseasonal patterns of the long-term trends of indian-summer monsoon rainfall. *International Journal of Climatology*, **12**, 257–268.

Kuo, H. L. and Y. F. Qian, 1982: Numerical-simulation of the development of mean monsoon circulation in july. *Monthly Weather Review*, **110**, 1879–1897.

Kwon, H. J., 1989: A reexamination of the genesis of african waves. *Journal of the Atmospheric Sciences*, **46**, 3621–3631.

Laprise, R., 1992: The euler equations of motion with hydrostatic pressure as an independent variable. *Monthly Weather Review*, **120**, 197–207.

Lau, K. M. and S. Yang, 1997: Climatology and interannual variability of the southeast asian summer monsoon. *Advances in Atmospheric Sciences*, **14**, 141–162.

Lau, N. C. and M. J. Nath, 2000: Impact of enso on the variability of the asian-australian monsoons as simulated in gcm experiments. *Journal of Climate*, **13**, 4287–4309.

Li, S. L., J. Perlwitz, X. W. Quan, and M. P. Hoerling, 2008: Modelling the influence of north atlantic multidecadal warmth on the indian summer rainfall. *Geophysical Research Letters*, **35**, 1–6.

Li, T., B. Wang, C. P. Chang, and Y. S. Zhang, 2003: A theory for the indian ocean dipole-zonal mode. *Journal of the Atmospheric Sciences*, **60**, 2119–2135.

Li, T., Y. Zhang, C. Chang, and B. Wang, 2001: On the relationship between indian ocean sea surface temperature and asian summer monsoon. *Geophysical Research Letters*, **28**, 2843–2846.

Lorenz, E. N., 1955: Available potential energy and the maintenance of the general circulation. *Tellus*, **7**, 271–281.

Loschnigg, J., G. A. Meehl, P. J. Webster, J. M. Arblaster, and G. P. Compo, 2003: The asian monsoon, the tropospheric biennial oscillation, and the indian ocean zonal mode in the ncar csm. *Journal of Climate*, **16**, 1617–1642.

Lu, R. Y., B. W. Dong, and H. Ding, 2006: Impact of the atlantic multidecadal oscillation on the asian summer monsoon. *Geophysical Research Letters*, **33**, 1–5.

Mass, C., 1979: A linear primitive equation model of african wave disturbances. *Journal of the Atmospheric Sciences*, **36**, 2075–2092.

Matsuno, T., 1966: Quasi-geostrophic motions in the equatorial area. *Journal of the Metereological Society of Japan*, **44**, 25–43.

Medina, S., R. H. Houze, A. Kumarb, and D. Niyogic, 2010: Summermonsoon convection in the himalayan region: Terrain and land cover effects. *Quarterly Journal of the Royal Meteorological Society*, **136**, 593616.

Meehl, G. A., 1987: The annual cycle and interannual variability in the tropical pacific and indian-ocean regions. *Monthly Weather Review*, **115**, 27–50.

Meehl, G. A. and J. M. Arblaster, 2002a: Indian monsoon gcm sensitivity experiments testing tropospheric biennial oscillation transition conditions. *Journal of Climate*, **15**, 923–944.

— 2002b: The tropospheric biennial oscillation and asian-australian monsoon rainfall. *Journal of Climate*, **15**, 722–744.

Meehl, G. A., J. M. Arblaster, and W. D. Collins, 2008: Effects of black carbon aerosols on the indian monsoon. *Journal of Climate*, **21**, 2869–2882.

Mehta, V. M. and K. M. Lau, 1997: Influence of solar irradiance on the indian monsoon-enso relationship at decadal-multidecadal time scales. *Geophysical Research Letters*, **24**, 159–162.

Mekonnen, A., C. D. Thorncroft, and A. R. Aiyyer, 2006: Analysis of convection and its association with african easterly waves. *Journal of Climate*, **19**, 5405–5421.

Mlawer, E. J., S. J. Taubman, P. D. Brown, M. J. Iacono, and S. A. Clough, 1997: Radiative transfer for inhomogeneous atmospheres: Rrtm, a validated correlated-k model for the longwave. *J. Geophys. Res.*, **102**, 16663–16682.

Molinari, J., D. Knight, M. Dickinson, D. Vollaro, and S. Skubis, 1997: Potential vorticity, easterly waves, and eastern pacific tropical cyclogenesis. *Monthly Weather Review*, **125**, 2699–2708.

Molteni, F., 2003: Atmospheric simulations using a gcm with simplified physical parametrizations. i: Model climatology and variability in multi-decadal experiments. *Climate Dynamics*, **20**, 175–191.

Mooley, D. A. and B. Parthasarathy, 1984: Fluctuations in all-india summer monsoon rainfall during 1871-1978. *Climatic Change*, **6**, 287–301.

Mozer, J. B. and J. A. Zehnder, 1996: Lee vorticity production by large-scale tropical mountain ranges. part ii: A mechanism for the production of african waves. *Journal of the Atmospheric Sciences*, **53**, 539–549.

Murakami, T., T. Matsuno, and A. Yatagai, 1999: Similarities as well as differences between summer monsoons over southeast asia and the western north pacific. *Journal of the Meteorological Society of Japan*, **77**, 887–906.

Nicholson, S., 2009: A revised picture of the structure of the "monsoon' and land itcz over west africa. *Climate Dynamics*, **32**, 1155–1171.

Nicholson, S. E. and P. J. Webster, 2007: A physical basis for the interannual variability of rainfall in the sahel. *Quarterly Journal of the Royal Meteorological Society*, **133**, 2065–2084.

Normand, C., 1953: Monsoon seasonal forecasting. *Quarterly Journal of the Royal Meteorological Society*, **79**, 463–473.

Norquist, D. C., E. E. Recker, and R. J. Reed, 1977: The energetics of african wave disturbances as observed during phase iii of gate. *Monthly Weather Review*, **105**, 334–342.

Palmer, T. N., C. Brankovic, P. Viterbo, and M. J. Miller, 1992: Modeling interannual variations of summer monsoons. *Journal of Climate*, **5**, 399–417.

Parthasarathy, B., K. R. Kumar, and A. A. Munot, 1993: Homogeneous indian monsoon rainfall - variability and prediction. *Proceedings of the Indian Academy of Sciences-Earth and Planetary Sciences*, **102**, 121–155.

Parthasarathy, B., A. Munot, and D. Kothawale, 1995: Monthly and seasonal rainfall series for all-india homogeneous regions and meteorological subdivisions: 1871-1994. Research Report No. RR-065, Indian Institute of Tropical Meteorology.

Parthasarathy, B., A. A. Munot, and D. R. Kothawale, 1994: All-india monthly and seasonal rainfall series - 1871-1993. *Theoretical and Applied Climatology*, **49**, 217–224.

Parthasarathy, B., N. A. Sontakke, A. A. Monot, and D. R. Kothawale, 1987: Droughts floods in the summer monsoon season over different meteorological subdivisions of india for the period 1871-1984. *Journal of Climatology*, **7**, 57–70.

Parthasarathy, B., N. Sontkake, A. Munot, and D. Kothawale, 1990: Vagaries of indian monsoon rainfall and its relationships with regional/global circulations. *Mausam*, **41**, 301–308.

Philander, S. G., 1990: *El Nio, La Nia, and the Southern Oscillation*, volume 46 of *International geophysics series*. Academic Press, San Diego.

Pytharoulis, I. and C. Thorncroft, 1999: The low-level structure of african easterly waves in 1995. *Monthly Weather Review*, **127**, 2266–2280.

Rajeevan, M., J. Bhate, and A. K. Jaswal, 2008: Analysis of variability and trends of extreme rainfall events over india using 104 years of gridded daily rainfall data. *Geophysical Research Letters*, **35**, 1–5.

Rayner, N. A., D. E. Parker, E. B. Horton, C. K. Folland, L. V. Alexander, D. P. Rowell, E. C. Kent, and A. Kaplan, 2003: Global analyses of sea surface temperature, sea ice, and night marine air temperature since the late nineteenth century. *J. Geophys. Res.*, **108**, 4407.

Redelsperger, J., C. D. Thorncroft, A. Diedhiou, T. Lebel, D. J. Parker, and J. Polcher, 2006: African monsoon multidisciplinary analysis - an international research project and field campaign. *Bulletin of the American Meteorological Society*, **87**, 1739–1746.

Reed, R. J., E. Klinker, and A. Hollingsworth, 1988: The structure and characteristics of african easterly wave disturbances as determined from the ecmwf operational analysis/forecast system. *Meteorology and Atmospheric Physics*, **38**, 22–33.

Reed, R. J., D. C. Norquist, and E. E. Recker, 1977: The structure and properties of african wave disturbances as observed during phase iii of gate. *Monthly Weather Review*, **105**, 317–333.

Rennick, M. A., 1976: The generation of african waves. *Journal of the Atmospheric Sciences*, **33**, 1955–1969.

Reynolds, R. W., N. A. Rayner, T. M. Smith, D. C. Stokes, and W. Wang, 2002: An improved in situ and satellite sst analysis for climate. *Journal of Climate*, **15**, 1609–1625.

Richards, F. and P. Arkin, 1981: On the relationship between satellite-observed cloud cover and precipitation. *Monthly Weather Review*, **109**, 1081–1093.

Riehl, H., 1954: *Tropical Meteorology*. McGraw-Hill, New York.

Ross, R. S., T. N. Krishnamurti, S. Pattnaik, and A. Simon, 2009: Energy transformation and diabatic processes in developing and nondeveloping african easterly waves observed during the namma project of 2006. *Weather and Forecasting*, **24**, 1524–1548.

Rowell, D. P., C. K. Folland, K. Maskell, and M. N. Ward, 1995: Variability of summer rainfall over tropical north-africa (1906-92) - observations and modeling. *Quarterly Journal of the Royal Meteorological Society*, **121**, 669–704.

Saji, N. H., B. N. Goswami, P. N. Vinayachandran, and T. Yamagata, 1999: A dipole mode in the tropical indian ocean. *Nature*, **401**, 360–363.

Scheffe, H., 1959: *The Analysis of Variance*. Wiley, New York.

Schubert, W. H., P. E. Ciesielski, D. E. Stevens, and H.-C. Kuo, 1991: Potential vorticity modeling of the itcz and the hadley circulation. *Journal of the Atmospheric Sciences*, **48**, 1493–1509.

Shukla, J., 1975: Effect of arabian sea-surface temperature anomaly on indian summer monsoon - numerical experiment with gfdl model. *Journal of the Atmospheric Sciences*, **32**, 503–511.

— 1987: Interannual variability of monsoon. *Monsoons*, J. S. Fein and P. L. Stephens, eds., Wiley, New York, 399–464.

Shukla, J. and D. A. Paolino, 1983: The southern oscillation and long-range forecasting of the summer monsoon rainfall over india. *Monthly Weather Review*, **111**, 1830–1837.

Simmons, A. J., 1977: A note on the instability of the african easterly jet. *Journal of the Atmospheric Sciences*, **34**, 1670–1674.

Skamarock, W. C., J. B. Klemp, J. Dudhia, D. O. Gill, D. M. Barker, W. Wang, and J. G. Powers, 2005: A description of the advanced research wrf version 2. Technical report, ECMWF.

Slingo, J. M. and H. Annamalai, 2000: 1997: The el nio of the century and the response of the indian summer monsoon. *Monthly Weather Review*, **128**, 1778–1797.

Smith, T. M., R. W. Reynolds, T. C. Peterson, and J. Lawrimore, 2008: Improvements to noaa's historical merged land-ocean surface temperature analysis (1880-2006). *Journal of Climate*, **21**, 2283–2296.

Soman, M. K. and J. Slingo, 1997: Sensitivity of the asian summer monsoon to aspects of sea-surface-temperature anomalies in the tropical pacific ocean. *Quarterly Journal of the Royal Meteorological Society*, **123**, 309–336.

Srinivasan, J., S. Gadgil, and P. J. Webster, 1993: Meridional propagation of large-scale monsoon convective zones. *Meteorology and Atmospheric Physics*, **52**, 15–35.

Straus, D. M. and J. Shukla, 2000: Distinguishing between the sst-forced variability and internal variability in mid latitudes: Analysis of observations and gcm simulations. *Quarterly Journal of the Royal Meteorological Society*, **126**, 2323–2350.

Terray, P., P. Delecluse, S. Labattu, and L. Terray, 2003: Sea surface temperature associations with the late indian summer monsoon. *Climate Dynamics*, **21**, 593–618.

Thorncroft, C. and K. Hodges, 2001: African easterly wave variability and its relationship to atlantic tropical cyclone activity. *Journal of Climate*, **14**, 1166–1179.

Thorncroft, C. D., 1995: An idealized study of african easterly waves. iii: More realistic basic states. *Quarterly Journal of the Royal Meteorological Society*, **121**, 1589–1614.

Thorncroft, C. D. and B. J. Hoskins, 1994a: An idealized study of african easterly waves. i: A linear view. *Quarterly Journal of the Royal Meteorological Society*, **120**, 953–982.

— 1994b: An idealized study of african easterly waves. ii: A nonlinear view. *Quarterly Journal of the Royal Meteorological Society*, **120**, 983–1015.

Toma, V. and P. Webster, 2010a: Oscillations of the intertropical convergence zone and the genesis of easterly waves. part i: Diagnostics and theory. *Climate Dynamics*, **34**, 587–604.

— 2010b: Oscillations of the intertropical convergence zone and the genesis of easterly waves part ii: numerical verification. *Climate Dynamics*, **34**, 605–613.

Tomas, R. A., J. R. Holton, and P. J. Webster, 1999: The influence of cross-equatorial pressure gradients on the location of near-equatorial convection. *Quarterly Journal of the Royal Meteorological Society*, **125**, 1107–1127.

Tomas, R. A. and P. J. Webster, 1997: The role of inertial instability in determining the location and strength of near-equatorial convection. *Quarterly Journal of the Royal Meteorological Society*, **123**, 1445–1482.

Torrence, C. and G. P. Compo, 1998: A practical guide to wavelet analysis. *Bulletin of the American Meteorological Society*, **79**, 61–78.

Torrence, C. and P. J. Webster, 1999: Interdecadal changes in the enso-monsoon system. *Journal of Climate*, **12**, 2679–2690.

Trenberth, K. E., D. P. Stepaniak, and J. M. Caron, 2000: The global monsoon as seen through the divergent atmospheric circulation. *Journal of Climate*, **13**, 3969–3993.

Uppala, S. M., P. W. Kllberg, A. J. Simmons, U. Andrae, V. D. C. Bechtold, M. Fiorino, J. K. Gibson, J. Haseler, A. Hernandez, G. A. Kelly, X. Li, K. Onogi, S. Saarinen, N. Sokka, R. P. Allan, E. Andersson, K. Arpe, M. A. Balmaseda, A. C. M. Beljaars, L. V. D. Berg, J. Bidlot, N. Bormann, S. Caires, F. Chevallier, A. Dethof, M. Dragosavac, M. Fisher, M. Fuentes, S. Hagemann, E. Hlm, B. J. Hoskins, L. Isaksen, P. A. E. M. Janssen, R. Jenne, A. P. Mcnally, J.-F. Mahfouf, J.-J. Morcrette, N. A. Rayner, R. W. Saunders, P. Simon, A. Sterl, K. E. Trenberth, A. Untch, D. Vasiljevic, P. Viterbo, and J. Woollen, 2005: The era-40 re-analysis. *Quarterly Journal of the Royal Meteorological Society*, **131**, 2961–3012.

Viltard, A., P. de Felice, and J. Oubuih, 1997: Comparison of the african and the 6-9 day wave-like disturbance patterns over west-africa and the tropical atlantic during summer 1985. *Meteorology and Atmospheric Physics*, **62**, 91–99.

Wallace, J. M., 1970: Time-longitude sections of tropical cloudiness (december 1966 - november 1967). Technical report, NESC ESSA.

Wang, B. and Z. Fan, 1999: Choice of south asian summer monsoon indices. *Bulletin of the American Meteorological Society*, **80**, 629–638.

Waple, A. M., J. H. Lawrimore, M. S. Halpert, G. D. Bell, W. Higgins, B. Lyon, M. J. Menne, K. L. Gleason, R. C. Schnell, J. R. Christy, W. Thiaw, W. J. Wright, M. J. Salinger, L. Alexander, R. S. Stone, and S. J. Camargo, 2002: Climate assessment for 2001. *Bulletin of the American Meteorological Society*, **83**, 938–938.

Webster, P. and S. Yang, 1992: Monsoon and enso: Selectively interactive systems. *Quarterly Journal of the Royal Meteorological Society*, **118**, 877–926.

Webster, P. J., 1972: Response of tropical atmosphere to local, steady forcing. *Monthly Weather Review*, **100**, 518–&.

— 1983: Mechanisms of monsoon low-frequency variability - surface hydrological effects. *Journal of the Atmospheric Sciences*, **40**, 2110–2124.

— 1987: The elementary monsoon. *Monsoons*, J. S. Fein and P. L. Stephens, eds., Wiley, New York, 3–32.

Webster, P. J. and H. R. Chang, 1988: Equatorial energy accumulation and emanation regions - impacts of a zonally varying basic state. *Journal of the Atmospheric Sciences*, **45**, 803–829.

Webster, P. J., C. Clark, G. Cherikova, J. Fasullo, W. Han, J. Loschnigg, and K. Sahami, 2002: The monsoon as a self-regulating coupled ocean-atmosphere system. *Meteorology at the Millennium*, R. P. Pearce, ed., Academic press, San Diego, 198–219.

Webster, P. J. and J. Fasullo, 2003: Monsoon: Dynamical theory. *Encyclopedia of atmospheric sciences*, J. R. Holton, J. A. Curry, and J. A. Pyle, eds., Academic Press, Amsterdam; Boston, 1370–1386.

Webster, P. J., V. O. Magana, T. N. Palmer, J. Shukla, R. A. Tomas, M. Yanai, and T. Yasunari, 1998: Monsoons: Processes, predictability, and the prospects for prediction. *Journal of Geophysical Research-Oceans*, **103**, 14451–14510.

Webster, P. J., A. M. Moore, J. P. Loschnigg, and R. R. Leben, 1999: Coupled ocean-atmosphere dynamics in the indian ocean during 1997-98. *Nature*, **401**, 356–360.

Wicker, L. J. and W. C. Skamarock, 2002: Time-splitting methods for elastic models using forward time schemes. *Monthly Weather Review*, **130**, 2088–2097.

Wu, M.-L. C., O. Reale, S. D. Schubert, M. J. Suarez, R. D. Koster, and P. J. Pegion, 2009: African easterly jet: Structure and maintenance. *Journal of Climate*, **22**, 4459–4480.

Wu, R. G. and B. P. Kirtman, 2003: On the impacts of the indian summer monsoon on enso in a coupled gcm. *Quarterly Journal of the Royal Meteorological Society*, **129**, 3439–3468.

Xie, P. P. and P. A. Arkin, 1997: Global precipitation: A 17-year monthly analysis based on gauge observations, satellite estimates, and numerical model outputs. *Bulletin of the American Meteorological Society*, **78**, 2539–2558.

Yanai, M. and C. F. Li, 1994: Mechanism of heating and the boundary-layer over the tibetan plateau. *Monthly Weather Review*, **122**, 305–323.

Yanai, M. H., C. F. Li, and Z. S. Song, 1992: Seasonal heating of the tibetan plateau and its effects on the evolution of the asian summer monsoon. *Journal of the Meteorological Society of Japan*, **70**, 319–351.

Yang, S. and K. M. Lau, 1998: Influences of sea surface temperature and ground wetness on asian summer monsoon. *Journal of Climate*, **11**, 3230–3246.

— 2006: Interannual variability of the asian monsoon. *The Asian Monsoon*, B. Wang, ed., Praxis Publishing Ltd, Chichester, UK, Berlin, Heidelberg, 219–293.

Yang, S., P. J. Webster, and M. Dong, 1992: Longitudinal heating gradient: Another possible factor influencing the intensity of the asian summer monsoon circulation. *Advances in Atmospheric Sciences*, **9**, 397–410.

Yasunari, T., 1987: Global structure of the el-nio southern oscillation .2. time evolution. *Journal of the Meteorological Society of Japan*, **65**, 81–102.

— 1990: Impact of indian monsoon on the coupled atmosphere ocean system in the tropical pacific. *Meteorology and Atmospheric Physics*, **44**, 29–41.

— 1991: The monsoon year - a new concept of the climatic year in the tropics. *Bulletin of the American Meteorological Society*, **72**, 1331–1338.

Yasunari, T. and Y. Seki, 1992: Role of the asian monsoon on the interannual variability of the global climate system. *Journal of the Meteorological Society of Japan*, **70**, 177–189.

Yu, J. Y., S. P. Weng, and J. D. Farrara, 2003: Ocean roles in the tbo transitions of the indian-australian monsoon system. *Journal of Climate*, **16**, 3072–3080.

Zawislak, J. and E. Zipser, 2010: Observations of seven african easterly waves in the east atlantic during 2006. *Journal of the Atmospheric Sciences*, **67**, 26–43.

Zhang, C., D. S. Nolan, C. D. Thorncroft, and H. Nguyen, 2008: Shallow meridional circulations in the tropical atmosphere. *Journal of Climate*, **21**, 3453–3470.

Zipser, E., C. , Twohy, S. Tsay, K. Thornhill, S. Tanelli, R. Ross, T. Krishnamurti, Q. Ji, G. Jenkins, S. Ismail, N. Hsu, R. Hood, G. Heymsfield, A. Heymsfield, J. Halverson, H. Goodman, R. Ferrare, J. Dunion, M. Douglas, R. Cifelli, G. Chen, E. Browell, and B. Anderson, 2009: The saharan air layer and the fate of african easterly waves. *Bulletin of the American Meteorological Society*, **90**, 1137–1156.